Structure and magnetic properties of bulk and thin film nickel manganite (NiMn(_2)O(_4))

Ashcroft, Gwynfor Rhys

Structure and Magnetic Properties of Bulk and Thin Film Nickel Manganite ($NiMn_2O_4$)

by

Gwynfor Rhys Ashcroft

A Thesis submitted in partial fulfilment of the requirements for the degree of Doctor of Philosophy

Durham University

Department of Physics

2003

Acknowledgements

I would like to thank my supervisor, Dr. Ian Terry, for all his help and patience in the past few years, and helping with the VSM measurements.
I am grateful to Professor Tanner, and Professor Pennington, the heads of department during my work, for the use of their facilities.
Thanks to John Dobson and all the technicians, and workshop staff in the Department for their patience, and interpreting of scruffy sketches.
Thanks to Dr John Evans and his research group in the Chemistry department, for the use of the X–ray diffractometer, and for answering all my questions about crystallography.
Particular thanks go to Dr Richard Gover, for helping me out of an a awkward situation on more than one occasion
Thanks to Dan Read, for helping me on numerous occasions with matters cryogenical.
Thanks to the glass blowers in chemistry, for producing the right bits when I did not know what I needed.
Thanks to Simon Keys, for keeping me sane during the last months of late nights.
Everybody in the teaching labs, who allowed extended loans of vital pieces of equipment.
Thanks to Dr Gwaenelle Rousse, and the support staff at the ILL, for help with the neutron diffraction measurements, and Tadaaki Matsumura for the measurements at KEK, Japan.
Thanks to Rainier Schmidt, for providing me with the thin film samples, and his supervisor, Dr Brinkman for useful discussion, and use of facilities.
Andrew Yates, for SEM measurements on demand. Alton Horsfall for bringing me up to speed on AGFM's.
Thanks to my parents, for their concern over my wellbeing, and financial support.
I acknowledge the financial support provided by the EPSRC in the form of my grant.

Gwynfor Rhys Ashcroft

Structure and Magnetic Properties of Bulk and Thin Film Nickel Manganite ($NiMn_2O_4$)

Abstract

The structural and magnetic properties of nickel manganite ($NiMn_2O_4$) have been investigated, for bulk, and thin film samples. $NiMn_2O_4$ has partially inverted spinel structure, $Mn_\nu Ni_{1-\nu}[Ni_\nu Mn_{2-\nu}]O_4$, where ν is the inversion parameter. Bulk samples were produced from co-precipitated metal hydroxides at various firing times and temperatures. Particular attention was given to determining the optimum preparation route. Nickel oxide was the major impurity encountered due to sub-optimal preparation conditions, but was difficult to detect using diffraction, due to considerable Bragg reflection overlap with those $NiMn_2O_4$. Nickel oxide is believed to have been present in most samples studied by other researchers in the field. Pure material formed in air after firing for 48 hours in the region 780 °C to 820 °C; a much smaller range than previously reported. By controlling the cooling rate after firing, $0.7483(19) \leq \nu \leq 0.8830(22)$ was obtained; as determined by neutron diffraction measurements. Ferrimagnetic Curie temperatures (T_C) between 100 K and 147 K were obtained for the range of ν studied; somewhat lower than previously reported. The magnetisation below T_C exhibits *P*-type behaviour, which has hitherto not been observed in this compound. Evidence compatible with a local canted state at temperatures below ~10 K was observed using muon spectrometry.

The magnetic properties of electron-beam evaporated thin films of $NiMn_2O_4$ were investigated with a custom built Alternating Gradient Field Magnetometer. The AGFM was initially constructed for a study of Dilute Magnetic Semiconductor (DMS) materials, and was capable of temperatures down to 77 K, and resolution of 14 pJT^{-1}. This instrument used a mechanically resonant quartz fibre sample holder, and piezoelectric detection. The response of the instrument to temperature drift, applied magnetic field, and differing sample properties is reported. The T_C of a typical thin film sample was measured, and $\nu = 0.788(8)$ inferred from the relationship with T_C, as determined for bulk material.

Contents

Declaration

I declare that this thesis is original and that no part of it has been submitted previously for a degree at this or any other university. All work presented herein is my own unless otherwise stated. This thesis is within the word limit set by the examining body.

G. R. Ashcroft

Chapter 1
Introduction

There are a wide range of parameters of interest in the study and characterisation of magnetic materials, such as susceptibility, saturation moment, etc. Most of these can be obtained from a study of the variation of a sample's magnetic moment ($\underline{m}$), with changes in applied field ($\underline{H}$). In addition, it is useful in many cases to be able to take measurements as a function of temperature. More details about the various types of magnetic behaviour commonly encountered can be found in section 1.3 below.

A wide range of equipment is available to characterise the $\underline{m}$-$\underline{H}$ relationship of various materials in a range of applied magnetic fields, and number of comprehensive reviews of magnetic measurement techniques can be found in the literature [1-4]. Some of these measurement techniques, which are relevant to this work, are introduced in section 1.5. Many of these will be immediately familiar, such as the Vibrating Sample Magnetometer (VSM), and the Superconducting Quantum Interference Device (SQUID) magnetometer. The VSM is a very useful instrument, readily adaptable to work down to liquid nitrogen temperatures (77 K) or below, and offering a modest resolution. VSMs are commercially available with a sensitivity of 10^{-8} JT^{-1} [5], and are also relatively easy to build in a laboratory [6], giving a cost effective source of routine magnetic characterisation. The VSM is suitable for studying materials that have a relatively large magnetic response, or are available as large samples, and usually needs no cryogen supply for room temperature operation. SQUID magnetometers offer a much higher resolution, but the purchase and running costs are high as they are only available commercially, and due to the need for a continuous supply of liquid helium. However, a low cost instrument which provides a sensitivity approaching that of a SQUID magnetometer is the Alternating Gradient Field Magnetometer (AGFM), first demonstrated by Zijlstra [7] in 1970 with a room temperature resolution of 10^{-11} JT^{-1}. This instrument requires no cryogen for room temperature operation and therefore the running costs are very low compared to the SQUID magnetometer. In fact, there has been no other type of magnetometer reported in the literature, which is of a

comparable sensitivity and economy, that can accommodate such a wide range of samples, or can be so easily constructed in the laboratory.

The first part of the work reported in this thesis was the development of an AGFM. The original motivation for the construction of this instrument, was the study of low moment samples such as bulk and thin film dilute magnetic semiconductor (DMS) materials, and other samples of interest to the X-ray and magnetism group at Durham university, where high sensitivity measurements were necessary for magnetic characterisation. Examples of this can be found in Figure 3.23, where measurements on 26.7(2) mg of HgMnTe yielded a saturation magnetisation of 1.7(6) x 10^{-9} $JT^{-1}kg^{-1}$, and Figure 3.25, showing measurements on cobalt – platinum thin film recording media. The system had to be robust and able to measure samples of a range of masses and moments in general purpose use as a magnetometer, and obtain sufficient resolution for the more demanding samples. Details of the measurement aims, and the resolution required for some samples are outlined in section 1.1. In view of previous authors' difficulties in obtaining high resolutions at low temperatures [8], it was decided to develop a working instrument for ambient temperature operation in the first instance, with a view to subsequently tackling the challenge of operating at cryogenic temperatures. This was also done to enable characterisation of the instrument without the expense of a cryogen supply. Cost was also a major influence in many of the design decisions taken, with a limited budget available for development work.

The design of the AGFM is reported in chapter 2, along with a review of previously reported AGFM realisations. In order to have faith in the accuracy of any results obtained with the AGFM, it was necessary to thoroughly characterise the instrument, including the effect of any external influences on the operation. This is especially important for samples with small magnetic moments to be measured, as any disturbances will have a proportionally larger effect. The results of this characterisation are presented in chapter 3, and demonstrate the correct performance of the instrument. Representative data taken on a wide range of samples is to be found therein, and comparisons with other magnetometers show good agreement. One of the original aims of the project, to study DMS material was not fully achieved, due to the problems encountered with low temperature operation of the AGFM, a shift in research focus of the

magnetism group within the department, and significant deterioration of the available DMS samples. A few measurements were carried out, as shown in Figure 3.23, which yielded a figure for the small saturation magnetisation present in bulk samples. However, the AGFM was used to study a number of samples of interest to various research groups, such as the cobalt – platinum thin films discussed in chapter 3, and thin films of nickel manganite [9-14]. It was research into this latter set of films that initiated the detailed investigation of the structural and magnetic properties of nickel manganite that make up the bulk of the research work reported in this thesis.

Nickel manganite ($NiMn_2O_4$) is a partially inverted spinel [15], widely used for electronic applications [16] as it is a suitable material for negative temperature coefficient (NTC) thermistor devices. The strong temperature dependence of the conductivity is illustrated in Figure 1.1 and is known to be largely determined by the arrangement of cations in the compound [17, 18]. The electrical conduction is due to an electron jump between the Mn^{3+} and Mn^{4+} cations located on the B sites [19]. This hopping process will obviously be affected by the relative concentrations of these cation species.

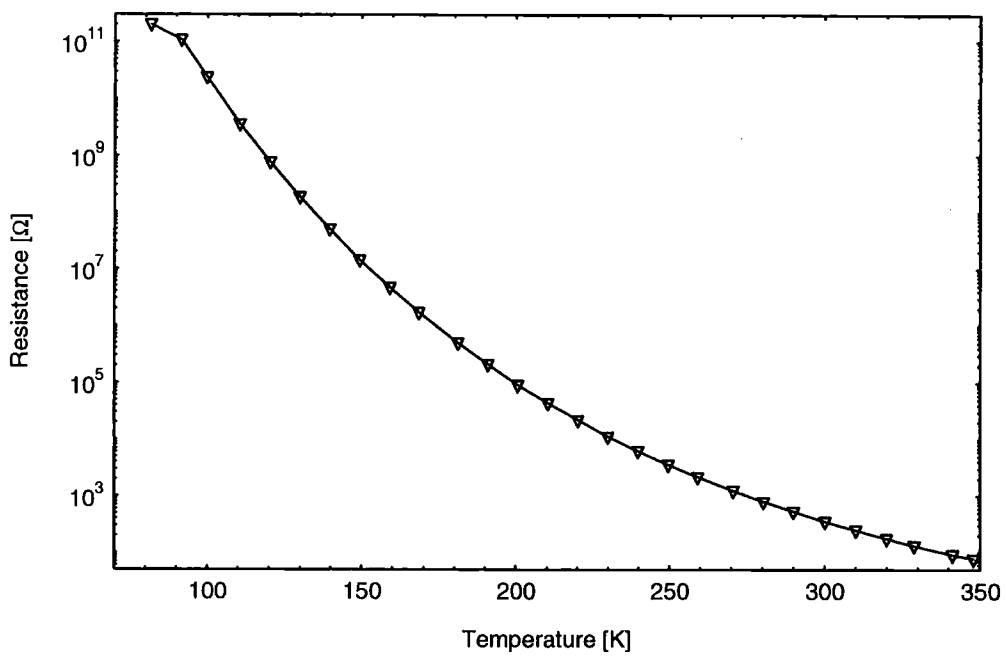

Figure 1.1. Temperature dependence of resistance of thin film nickel manganite (from Basu *et al.*, [13]).

The arrangement of cations is quantified by the inversion parameter and, as the cations have non-zero magnetic moment, the magnetic properties also vary with

the inversion parameter [24]. Fritsch *et al.*, [18] gives the effective number of charge carriers (assuming a random cation distribution across the B sites) as;

$$N_{eff} = \frac{\left[Mn_B^{3+}\right]\left[Mn_B^{4+}\right]}{\left[Mn_B^{3+}\right]+\left[Mn_B^{4+}\right]}$$

which, for a stoichiometric material with the cation distribution of Brabers [20] (see section 5.3), gives a conductivity maximum at an inversion parameter of $\nu = 0.59$. Recently, there has been interest in processing mechanisms to produce thin film devices, which requires an understanding of how the inversion parameter, and hence the electrical properties, vary with the growth techniques used. It is clear that in order to control device conductivity, a method of controlling the inversion parameter is necessary. Hence when attempting to optimise process techniques for device manufacture, a convenient way of measuring the inversion parameter is required. This has previously only been achieved for bulk samples using neutron diffraction [21-23], which is not applicable to thin film devices due to insufficient scattering cross section. Neutron scattering cannot be used as a routine characterisation technique in the laboratory, however, given the sensitivity of the magnetic properties of the material to the inversion parameter [21], the author decided that the problem of identifying the cation distribution of the thin films could be tackled by first relating the magnetic properties of a number of bulk samples to their inversion parameters obtained from neutron scattering measurements. Thus once the correlation between inversion parameter and magnetic properties had been confirmed, thin films of nickel manganite could characterised magnetically and the inversion parameters deduced. However, it soon became clear that the wide range of preparation routes for bulk nickel manganite used, had resulted in many of the published properties differing greatly between reports in the available literature. Most of the reported magnetic characterisation was performed on samples that contained significant amounts of other (magnetic) material phases. Therefore to provide an unambiguous link between inversion parameter, and magnetic properties, it was essential to be able to produce single phase, stoichiometric samples. Preliminary measurements on high purity samples showed different behaviour to that previously reported, and prompted an in depth study of the nickel manganite system.

A more detailed description of the properties of nickel manganite, and the motivation for this work can be found in section 1.2. Details about the spinel structure, and the magnetic properties resulting from this structure, are found in chapter 4. Included in chapter 4 is a derivation of the relationship between the spinel lattice parameter, oxygen position, and the effective radii of the ions present in a spinel crystal. To the best of the authors knowledge, this has not appeared in published form before now. A comprehensive review of the available literature, concerning the preparation and material properties of nickel manganite is given in chapter 5. A brief explanation of the relevant magnetism theory, and the experimental techniques used in the study of nickel manganite is given in section 1.3. The experimental data thus obtained is presented and discussed in chapter 6. Chapter 7 draws together the conclusions of the experimental work and contains suggestions for future studies of nickel manganite.

1.1 AGFM development

The original measurement aims when the AGFM was built, was the study of dilute magnetic semiconductor (DMS) materials. These consist of conventional II-VI semiconductor material, in which a fraction of the group II sublattice is replaced at random by a magnetic ion. The most extensively studied materials have manganese as the magnetic ion. Extensive electrical transport measurements have been carried out at the Physics Department at Durham, on $Hg_{1-x}Mn_xTe$ films grown by metal-organic vapour phase epitaxy [25, 26], and bulk $Cd_{1-x}Mn_xTe$:In [27]. The intention was to examine the magnetic behaviour of these materials for a number of phenomena. Part of the interest in these materials is the persistent photo-induced magnetism that they exhibit [28, 29], and the spin glass behaviour of $Cd_{1-x}Mn_xTe$ [30, 31] at low temperatures. All these effects require an instrument resolution of at least 10^{-5} J T^{-1} kg^{-1} to study adequately. A similar figure is needed to study the optically induced magnetisation in bulk $Hg_{1-x}Mn_xTe$ [32, 33]. To adequately study thin films, an improvement in available resolution of several orders of magnitude would be required. This improved sensitivity is also required, in order to accurately characterise these materials at ~300 K where they are only weakly magnetic. Such room temperature characterisation would be useful, in order to detect any

magnetic impurities, or possible manganese clusters [25]. A design target resolution of 10^{-8} J T^{-1} kg^{-1} was set, which necessitated the development of this magnetometer to a resolution much higher than conventional methods such as vibrating sample magnetometry (VSM). While it is accepted that commercially available SQUID magnetometers have the required resolution for this study, the purchase and running costs of such a system was not viable due to financial considerations.

1.2 Nickel manganite.

Nickel manganite exhibits the spinel structure, in common with many other oxides of transition metals. The spinel structure consists of an approximately close packed anion lattice, containing cations in two distinct environments. In common with many other spinels, it exhibits a partially inverted structure. This is important from the point of view of device properties, as the conductivity mechanism is believed to be short range hopping between mixed valency cations. The unusually high conductivity was presumed to be due to thermally activated electron exchange between Mn^{3+}, and Mn^{4+} by Larson *et al.*, [19], with an activation energy of 0.36 eV. This activation energy changes above 450 °C, giving an activation energy for high temperature cation mobility of 0.66 eV [17]. Work on thin films [34] found activation energies similar to bulk material, but the conductivity was found to be only 10% of the bulk value, due to low film density. Fritsch *et al.*, [18] found a change in conductivity arising from differing heat treatments, which was correlated with a change in cation distribution. The effective number of charge carriers was calculated to have a maximum at an inversion parameter of $\nu = 0.59$. Later work (Elbadraoui *et al.*, [35]) found a decrease in conductivity of ~40%, due to increased short range ordering in slowly cooled samples. Recent work on thin films (see Figure 1.1, Basu *et al.*, [12]) concluded that the conductivity mechanism was Efros-Shklovskii variable range hopping with a characteristic temperature of $T_0 = 2.3 \times 10^5$ K. The mixed valency state is strongly dependent upon the value of the inversion parameter, material stoichiometry, and short range order (see section 5.8). These factors are worthy of study, if only to facilitate the control of transport properties in commercial application. In addition, nickel manganite undergoes a number of

magnetic ordering transitions below room temperature. The transition is initially to a collinear ferrimagnetic structure, which displays complex magnetic behaviour at lower temperatures. The transition temperature, and details of the low temperature behaviour are also dependent on the inversion parameter. This low temperature magnetic behaviour is still not understood in detail despite several investigations, warranting a study of the bulk magnetic properties, presented in section 6.6.

There have been many reports of investigations into the properties of nickel manganite, using a wide range of sample preparation routes, and characterisation techniques. There has been some degree of confusion as to the precise conditions required to produce pure material, with a consequence that many of the earlier reports are contradictory. The need to produce pure, stoichiometric material is important when studying the magnetic properties, as impurities can have a disproportionate effect on the measured properties. It is clear that the sample quality of previously reported experiments is variable, in particular the presence of impurity phases that are difficult to detect using standard techniques such as X-ray, and neutron diffraction. This is particularly true of early neutron diffraction experiments, as resolutions achievable were limited. Recent work has concentrated on non-stoichiometric samples, with emphasis on device properties. A relatively new sample preparation route has been used in this study, which overcomes the limitations and disadvantages of many of the methods hitherto used. In view of the confusion present in published reports (as discussed in chapter 5), concerning the stability or otherwise of $NiMn_2O_4$ and related compounds, a study was made into the subject. The optimum preparation conditions applicable to this route have been systematically investigated, and are reported in sections 6.2, and 6.3.

In order to correlate the properties of this system to the inversion parameter, a way of varying, and measuring it has to be used. Investigations into methods of preparing pure samples with differing inversion parameters are reported on in sections 6.4, and 6.5. Neutron diffraction is the technique of choice to measure the inversion parameter of bulk material, as it is a relatively direct technique. X-ray diffraction suffers from a lack of contrast between nickel and manganese, as they have similar scattering factors. Neutron diffraction is unsuitable for characterisation of thin films however, due to the small sample volume.

Magnetic measurements present an alternative characterisation route, provided the relationship between magnetic properties and the inversion parameter is known. Therefore magnetic characterisation of bulk material was a necessary step, and is reported in section 6.6. Since the AGFM had been adapted to variable temperature measurements, this instrument enabled sensitive measurements on thin films of nickel manganite, as reported in section 6.7. The ferrimagnetic transition temperature of nickel manganite was determined, and from this, the inversion parameter was estimated, using the T_C vs. ν relationship obtained from bulk material. Muon spin relaxation was used to study the local dynamics of the magnetic states of nickel manganite, reported in section 6.8.

1.3 Material magnetisation

Magnetisation in a material is a result of the distribution of rotating currents and spin vectors of electrons in that material. It can be represented on a macroscopic scale by a vector, $\underline{M}$ that may or may not be identical over the volume of the sample. $\underline{M}$ can be regarded as being directly proportional to dipole moments (caused by either electronic orbits or spins).

$\underline{M}$ is related to the magnetic field, $\underline{H}$ and the magnetic induction, $\underline{B}$ in the following way; (Sommerfeld convention)

$$\underline{B} = \mu_0[\underline{H} + \underline{M}]$$

$\underline{H}$ in this case is the field experienced by the material, with any demagnetising field taken into account (This is the contribution caused by the effect of magnetisation at the surface of a sample, and is considered an external field). $\underline{B}$ is the only one of these quantities that can be directly measured. The magnetisation, $\underline{M}$, is defined per unit volume, so one can define a magnetic moment, $\underline{m}$ for a specific sample as: -

$$\underline{m} = \underline{M}V ,$$

where V is the volume of the sample. In general, $\underline{M}$ is a function of $\underline{H}$ and in some cases, also a function of the magnetic history of the material. The conventional way to indicate this is via the susceptibility, χ;

$$\underline{M} = \chi \underline{H}$$

It is clear that the susceptibility can be field dependent, so a differential susceptibility can be defined;

$$\chi' = \frac{d\underline{M}}{d\underline{H}}$$

As can be seen, $\underline{M}$ and $\underline{H}$ are vectors, and therefore χ is a tensor, however in nearly all cases $\underline{M}$ and $\underline{H}$ are parallel or antiparallel, so χ reduces to a scalar quantity. Furthermore, in many cases $\underline{M}$ is linear with $\underline{H}$ for attainable values of $\underline{H}$, so χ is field independent. A material with a positive, constant susceptibility is termed a paramagnet, whereas a negative constant susceptibility gives a diamagnet. In the case of insulating materials, these types of behaviour can be modelled by a collection of non-interacting moments (isolated ion magnetism). Interactions between ions within a sample can result in ordered arrangements of their magnetic moments.

1.3.1 Isolated ion magnetism

The magnetisation (M) and susceptibility (χ) of an isolated ion can be defined as;

$$M(H) = -\frac{1}{V}\frac{dF}{dH} \qquad\qquad \chi = -\frac{1}{V}\frac{d^2F}{dH^2},$$

where F is the Helmholtz free energy, and H the magnetic field experienced by the ion. At and below normal room temperatures, the ground state energy can be substituted for F. In order to compute the change in this ground state energy due to an applied field, modifications to the usual energy Hamiltonian have to be made.

The momentum is modified;

$$\underline{p_i} \rightarrow \underline{p_i} + e\underline{A}(\underline{r_i})$$

where $\underline{A}$ is the vector potential;

$$\underline{A} = -\tfrac{1}{2}(\underline{r} \times \underline{H})$$

In addition, the energy due to the directions of the electron spins (s^i_x) in a magnetic field (oriented along the x-axis), H is added;

$$\Delta\aleph = g_0\mu_0\mu_B H\sum_i s_z^i$$

Where the sum of the electron spins in the x direction can be written as;

$$\sum_i s_z^i = S_z$$

where g_0 is the Lande g-factor, μ_B the Bohr magneton, and μ_0 the permeability of free space.

Making these substitutions, the field dependent terms in the Hamiltonian can be expressed as;

$$\Delta \aleph = \mu_0 \mu_B (\underline{L} + g_0 \underline{S}) \cdot \underline{H} + \frac{e^2}{8m} |\underline{H}|^2 \sum_i (x_i^2 + y_i^2)$$

Where $\underline{L}$ is the electron orbital angular momentum, $\underline{S}$ the electron spin, and x_i, y_i the position co-ordinates. The resulting change in energy can be calculated using second order perturbation theory;

$$\Delta E_n = \mu_0 \mu_B \langle n | \underline{L} + g_0 \underline{S} | n \rangle \cdot \underline{H} \qquad 1)$$

$$+ \sum_{n \neq n'} \frac{\left| \langle n | \mu_0 \mu_B (\underline{L} + g_0 \underline{S}) \cdot \underline{H} | n' \rangle \right|^2}{E_n - E_n'} \qquad 2)$$

$$+ \frac{e^2}{8m} |\underline{H}|^2 \langle n | \sum_i (x_i^2 + y_i^2) | n \rangle \qquad 3)$$

Each of these terms gives a different contribution to the observed magnetism;

1) Paramagnetism due to angular momentum.

This effect is only present when the value of $\underline{J}$ (the total electronic angular momentum vector) for an ion is non zero. When present, this term is much larger than the other two.

2) Van Vleck paramagnetism.

This contributes when an electron shell is one short of being half full ($\underline{J} = 0$). The magnitude of this contribution is comparable to that of term 3.

3) Langevin diamagnetism.

This is present for all electrons, even those in full shells. It is usually masked by term 1.

1.3.2 Inter-ionic interactions

In almost all cases the predominant interactions between neighbouring magnetic ions in a material are those due to the orbitals of the electrons that give rise to the magnetic moment. Magnetic (dipole-dipole) interactions between adjacent ions are usually negligible. The interactions are termed exchange interactions, since the possible swapping of electrons between ions is the interaction mechanism which are discussed in detail in section 4.3.

Interactions can be grouped together as follows;

1. **Direct (overlap) exchange.**

   Direct Exchange is important when the orbitals of two ions overlap spatially (for instance if there is a chemical bond between them). The strength of the interaction is governed by the amount of wavefunction overlap, and so this is only usually important for adjacent ions.

2. **Superexchange.**

   Superexchange is propagated through intervening non-magnetic atoms. The sign, and strength of the interaction depend upon the electronic configuration of the magnetic ions, and the angles between the bonds to them.

3. **Itinerant exchange.**

   Itinerant exchange is only present in systems with a conduction band, where the conduction electrons play a significant role in the magnetic ordering. The interaction is between conduction electrons.

4. **RKKY exchange.**

   The RKKY coupling is transmitted through polarisation of conduction electrons, and has an oscillatory distance dependence.

If the interactions present are such that an ordered arrangement of moments has a lower energy than a disordered arrangement, the material will transform to this ordered state when the temperature is lowered sufficiently. The temperature at which this ordering takes place depends upon the energy difference between ordered and disordered states. These can vary between millikelvin temperatures for dilute weakly interacting systems, to several hundred degrees for some metals. Sometimes different ordered arrangements are stable at different temperatures, and a number of magnetic transitions are seen. These are sometimes accompanied by structural phase transitions. The bulk magnetic behaviour exhibited below the transition temperature depends upon many parameters, but can be distinguished by the nature of the ordered arrangement.

1.3.3 Ferromagnetism

Characterised by a (large) maximum value for the magnetisation, attainable in modest (or zero) applied fields, ferromagnetism is caused by the individual moments aligning parallel to one another. The maximum (saturation)

magnetisation is a material parameter, obtained when all the moments are perfectly aligned. The paramagnetic susceptibility (χ) rises sharply as the Curie (transition) temperature is approached. The behaviour of χ above the Curie temperature can be modelled using the mean field theory of Weiss. This assumes that every magnetic moment experiences an effective magnetic field, comprised of a component due to an external applied field, and a component due to interactions with other moments. The latter component is the product of the magnetisation, M, and an interaction term, λ. This gives an expression for χ, of;

$$\chi = \frac{C}{T - C\lambda},$$

where C is the Curie constant in the non-interacting limit. The inverse susceptibility ($1/\chi$) is therefore a linear function of temperature above the Curie temperature.

1.3.4 Antiferromagnetism

When the interactions are negative in sign, and the ions form two sublattices with equal and opposite moment, the ordered arrangement has no net magnetisation. The susceptibility is independent of applied field, like a paramagnet, but shows a maximum at the Néel (transition) temperature, as shown in Figure 1.2.

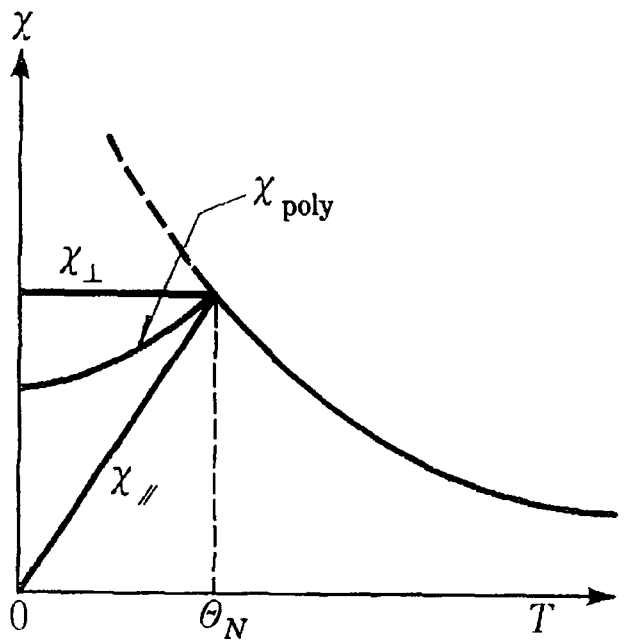

Figure 1.2. Temperature dependence of the magnetic susceptibility of antiferromagnetic materials. $\chi_{//}$ and $\chi_{\perp}$ are the magnetic susceptibilities measured by applying magnetic field parallel and perpendicular to the spin axis. χ_{poly} is the susceptibility for polycrystalline material calculated by averaging $\chi_{//}$ and $\chi_{\perp}$ (Figure 7.7 from Chikazumi [36]).

Like a ferromagnet, the inverse susceptibility ($1/\chi$) is a linear function of temperature above the ordering temperature.

1.3.5 Ferrimagnetism

Ferrimagnetism was named after the first materials that it was observed in, the ferrites (spinels containing iron). This ordering is the result of antiferromagnetic type interactions between magnetic cations on two sublattices with unequal moments. The resultant magnetisation is equal to the difference of the two magnetisations.

Nearly all of the spinel compounds containing magnetic ions on both sublattices are ferrimagnetic, caused by a superexchange interaction between the cation sublattices. The magnetic behaviour below the Curie (transition) temperature is similar to that of a ferromagnet, except that a magnetisation increase above 'saturation' is observed in high fields, due to the smaller moment rotating slightly towards the applied field direction. The inverse paramagnetic susceptibility ($1/\chi_p$) immediately above the Curie temperature is also not linear in temperature, as shown in Figure 1.3.

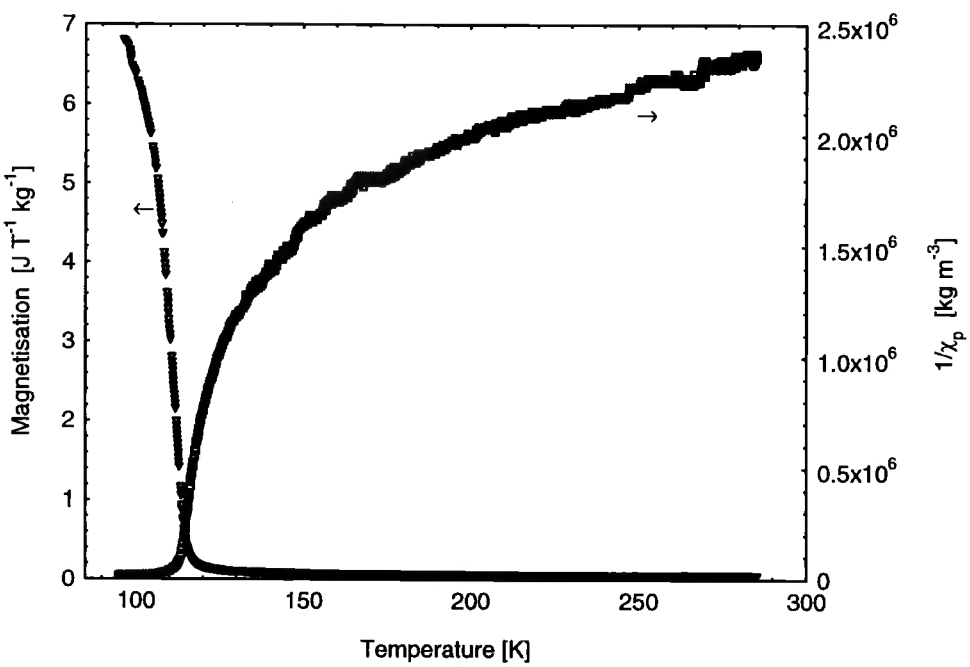

Figure 1.3. Plot of magnetisation and inverse susceptibility, as a function of temperature for ferrimagnetic nickel manganite, measured on a VSM.

The change in slope of the inverse paramagnetic susceptibility ($1/\chi_p$) is due to the competition between inter- and intra-sublattice interactions. The form of this can be derived from a Weiss mean field approximation [37], with two interpenetrating sublattices, labelled A, and B in the following treatment. The magnetisation of the A sublattice is assumed to take the form;

$$M_A = \frac{C_A}{T} H_A = \frac{C_A}{T}(H + \lambda_{AA} M_A + \lambda_{AB} M_B),$$

where C_A is the Curie constant of the A sublattice in the non – interacting limit, H is the applied field, λ_{AA} is the A intra-sublattice interaction term, and λ_{AB} is the inter-sublattice interaction term. The expression for the B sublattice magnetisation is similar.

Solving these pair of simultaneous equations, in a similar way to the case of a ferromagnet (see section 1.3.3), gives an expression for the susceptibility of;

$$\chi = \frac{T(C_A + C_B) - C_A C_B(\lambda_{AA} + \lambda_{BB} - 2\lambda_{AB})}{T^2 + T(C_A \lambda_{AA} + C_B \lambda_{BB}) - C_A C_B(\lambda_{AA}\lambda_{BB} - \lambda_{AB}^2)}.$$

This can be re-written in the more familiar form [36] by suitable substitutions;

$$\frac{1}{\chi} = \frac{T}{C} + \frac{1}{\chi_0} + \frac{A}{(T-\theta)}.$$

By comparing the above equation with data collected on a ferrimagnetic sample, values of the various parameters can be obtained. Since each of these parameters has a different dependence upon the various interactions, conclusions can be drawn about their relative strengths.

The dependencies can be broadly broken down into;

C	Combined Curie constant.
$1/\chi_0$	Inter-sublattice interactions.
θ	Difference between intra- and inter-sublattice interactions.
A	Difference between the sublattices.

To obtain reliable values for the above parameters, it is necessary to examine the behaviour of the susceptibility over a large temperature range, from the Curie temperature up to where conventional Curie-Weiss behaviour is observed (as shown in Figure 1.3). The spontaneous magnetisation below the transition temperature can take a number of forms. The reason for this is that the magnetisations of the two sublattices often have different temperature dependencies. These observed behaviours are designated as P, Q, R, and N type behaviour, as detailed in Figure 1.4.

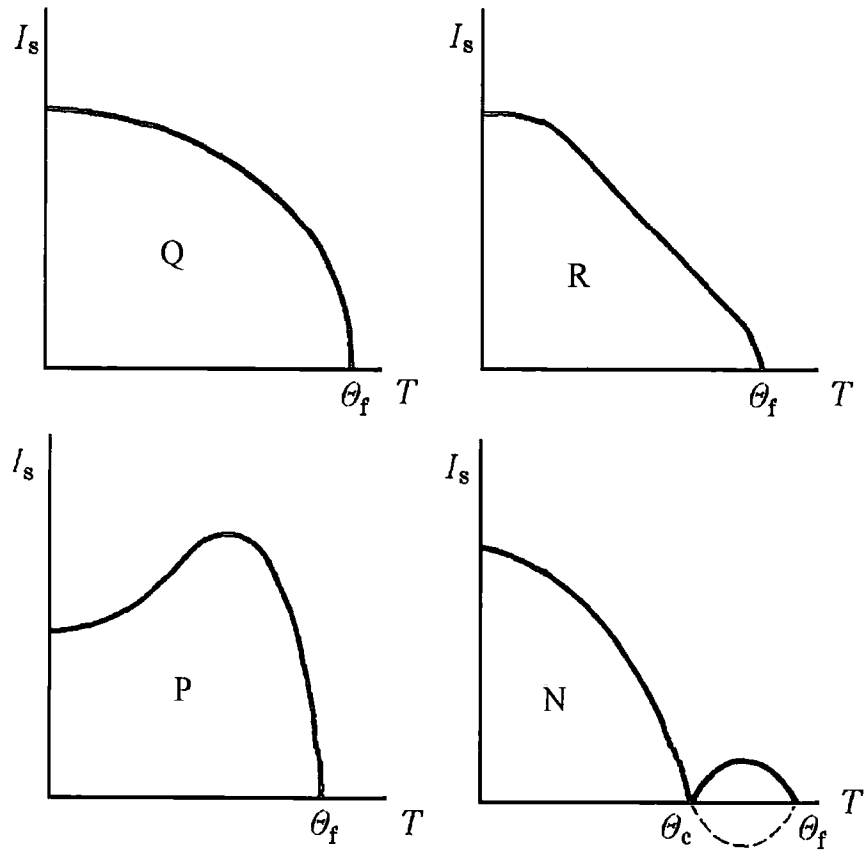

Figure 1.4. The four possible types of temperature dependence of the spontaneous magnetisation of ferrimagnetic materials. (Figure 7.12 from Chikazumi [36]).

Q type behaviour occurs when both sublattices are at saturation, and the spontaneous moment has the same temperature dependence as a ferromagnet. When one or other sublattice is unsaturated, more complicated behaviour results. If the sublattice with the larger moment is unsaturated, *N* or *R* type behaviour results, and *P* type results if the smaller moment sublattice is unsaturated. It has been claimed [38, 39] that the presence of either *N*, *P*, or *R* type ferrimagnetic behaviour in spinel oxides implies the presence of magnetic frustration on at least one sublattice. A frustrated system is one whose symmetry precludes the possibility that every pairwise interaction, or 'bond' in a system can be satisfied at the same time [40, 41].

1.3.6 Disordered magnetic systems.

In addition to the ordered magnetic states described above, various disordered magnetic states have been experimentally identified [42], of which the spin glass is probably the most well known. These states are characterised by localised

magnetic features that cannot be adequately described as a periodic spatial variation. The simplest spin glass systems are dilute magnetic impurities dispersed in a non magnetic host, such as the $Cu_{1-x}Mn_x$, and $Au_{1-x}Fe_x$ intermetallics with x~0.01 [43, 44]. These systems exhibit a spin 'freezing temperature', below which the spins are static. If such a sample is cooled in a zero applied field, the configuration that is frozen in has no net magnetisation. Upon warming such a frozen state through the spin glass freezing temperature in the presence of an applied field, the spins become mobile, and respond to the applied field to give an increase in the magnetisation. No such increase in the magnetisation is observed if the sample is cooled, and then warmed in a constant applied field. Spin glass magnetism has been observed in many metal oxide systems ([42, 45] and references therein), such as the $La_2Co_xCu_{1-x}O_{4+\delta}$ ($0.5 < x < 0.95$) layered oxides [46], and various spinels containing chromium [47-57], lithium [58-64], cobalt [65, 66], copper [67], and the $Mg_{1+x}Fe_{2-2x}Ti_xO_4$ system [44]. In the latter system, a transition from a paramagnetic state to a spin glass is observed for $0.68 < x < 0.83$.

In addition to spin glasses, many other forms of disordered behaviour have been observed, many of which are superimposed upon conventional long range ordered magnetic states. Examples include spin ices [68], localised canted states (LCS), and materials with a ferromagnetic wandering axes [42]. The pyrochlore system $Tb_2Ti_2O_7$ [69], displays 'spin ice' freezing, where upon lowering the temperature, the system becomes locked into one of the many degenerate groundstate configurations. This is analogous to a spin glass system [41], but with a much higher spin density. Similar systems have also shown fluctuating short range ordered 'spin liquid' behaviour superimposed upon a long range antiferromagnetic ordering [70].

LCS behaviour occurs where the direction or angle of canting of magnetic moments away from a conventional ordered state itself shows no long range ordering. This is in contrast to the model of Boucher *et al.,* [71], where the canting in nickel manganite shows long range order, and emerges from a collinear phase at higher temperatures. Features indicative of a LCS, have been observed in the system $Ni_xCd_{1-x}Mn_2O_4$ ($0.2 < x < 0.8$) at low temperatures [72].

The $Mg_{1+x}Fe_{2-2x}Ti_xO_4$ system [44] also undergoes a transition from a collinear ferrimagnet, to a LCS at low temperature for $x > 0.83$.

The 3 prerequesites for all such disordered magnetic behaviour are randomness, mixed interactions, and frustration [42, 73, 44]. All of these can be found in nickel manganite; a random spatial distribution of cations, mixed interactions between the various ionic species present, and frustration as shown from the magnetisation behaviour below the Curie temperature. Frustrated systems can have a disordered ground state with macroscopic degeneracy, i.e. a huge number of equivalent states with the same energy. Such an example is the low temperature proton disorder in ice, which was the first system where frustration was identified by Pauling [74]. The crystal structure of water ice, that of corner-shared tetrahedra, is analogous to the arrangement of B sites in the spinel structure [75].

1.4 Units of magnetism

The Sommerfeld convention for SI units was officially accepted for magnetic measurements by the International Union for Pure and Applied Physics shortly after 1960. The main points of this and the alternative unit systems are summarised in Table 1.1.

Quantity	SI (Sommerfeld)	SI (Kennely)	Gaussian (CGS)
Field, $\underline{H}$	Am^{-1}	Am^{-1}	Oersted
Induction, $\underline{B}$	Tesla	Tesla	Gauss
Magnetisation, $\underline{M}$	Am^{-1}	-	$EMUcm^{-3}$
Intensity of magnetisation, $\underline{I}$	-	Tesla	-
Flux, Φ	Weber (Vs)	Weber	Maxwell
Moment, $\underline{m}$	Am^2	Weber·m	EMU
pole strength, p	Am	Weber	$EMUcm^{-1}$
Field equation	$\underline{B}=\mu_0(\underline{H}+\underline{M})$	$\underline{B}=\mu_0\underline{H}+\underline{I}$	$\underline{B}=\underline{H}+4\pi\underline{M}$
Moment equation	$\underline{m}=V\underline{M}$	$\underline{m}=V\underline{I}$	$\underline{m}=V\underline{M}$
Energy of moment in free space	$E=-\mu_0\underline{m}\cdot\underline{H}$	$E=-\underline{m}\cdot\underline{H}$	$E=-\underline{m}\cdot\underline{H}$
Susceptibility (Volume)	$\chi=\underline{M}/\underline{H}$	$\chi=\underline{I}/\underline{H}$	$\chi=\underline{M}/\underline{H}$
Torque on moment in free space	$\underline{T}=\mu_0\underline{m}x\underline{H}$	$\underline{T}=\underline{m}x\underline{H}$	$\underline{T}=\underline{m}x\underline{H}$
Bohr magneton	$eh/4\pi m$	$\mu_0 eh/4\pi m$	$eh/4\pi mc$

Table 1.1. Units of Magnetism according to various conventions [76].

As can be seen the Sommerfeld and Kennely conventions are very similar, and the quantities $\underline{M}$ and $\underline{I}$ may be used in both systems with no contradictions

arising. Where they do differ however, is in their definition of magnetic moment, and Bohr magneton. The system adopted henceforth in this thesis is SI units, Sommerfeld convention. To give the reader some idea of the orders of magnitude involved, Table 1.2 contains data for some commonly encountered phenomena.

Earth's Magnetic field	$\underline{H} = 56\ \mathrm{Am}^{-1}$, $\underline{B} = 7 \times 10^{-5}\ \mathrm{T}$
Saturation Magnetisation of Iron	$\underline{M} = 1700\ \mathrm{kAm}^{-1}$
Large laboratory Electromagnet	$\underline{H} = 1600\ \mathrm{kAm}^{-1}$, $\underline{B} = 2\ \mathrm{T}$

Table 1.2. Strengths of commonly encountered phenomena [77].

1.5 Magnetic property measurement instrumentation

There is a wide range of equipment used to characterise the $\underline{m}$-$\underline{H}$ relationship of various materials. These can be split into 3 types, according to the method used for measuring $\underline{m}$. For a more detailed treatment of magnetic measurement techniques, the reader is directed towards one of the many reviews on the subject, such as Flanders and Graham [4], or others [1-3].

Force methods measure the force on a magnetic sample due to an applied magnetic field gradient. This is given by equation 1.1 for a sample with a uniform magnetisation $\underline{m}$, in a uniform field gradient, $\nabla\underline{H}$.

$$\underline{F} = \underline{m} \cdot \nabla \underline{H} \tag{1.1}$$

This force is most familiar as the force that causes permanent magnets to be attracted or repelled from one another. Examples of instruments using the force method are Faraday and Guoy balances, and the AGFM. The force measured can be static (Faraday balance [78]), or time varying (AGFM [7]).

Induction methods are essentially the inverse of force methods, measuring the voltage induced in one or more search coils, as a sample is moved, or its magnetic moment changes. Voltages induced in the coils are proportional to the rate of change of magnetic flux through the coils, and with suitable coil geometry and integration, information on the magnetic moment is obtained. $\underline{B} - \underline{H}$ loopers, permeameters, vibrating sample magnetometers (VSM), and induction susceptometers all utilise induction methods. Of these, the VSM [79, 6] is probably the most widely used for research.

Indirect methods utilise the effect of the magnetic moment on some other property of the sample. These methods are usually restricted to certain classes of

material, where the desired effects are observable, and repeatable. One example of such an effect is Kerr rotation, or the magnetisation dependent rotation of the polarisation of light reflected from a magnetised surface.

1.5.1 Vibrating sample magnetometer

The vibrating sample magnetometer is an induction method that utilises the fact that a sample is easily movable perpendicular to the field. This method has the advantage that the only material for which the magnetisation is measured is that which is vibrating, as the coils are stationary. The voltage, V produced in the detection coils is equal to the rate of change of flux through the coils multiplied by the number of turns on the coil;

$$V = -n\frac{d\Phi}{dt}.$$

The rate of change of flux is given by:-

$$\frac{d\Phi}{dt} = km\frac{dz}{dt},$$

where k is a factor determined by the coil geometry, m is the magnetic moment of the sample parallel to the applied field, and z is the position of the sample in the vertical direction. And as:-

$$z = z_0 \sin(\omega t),$$

the voltage produced in the pickup coils is sinusoidal, and 90° out of phase with respect to the vibration of the sample:-

$$V_{RMS} = nkmz_0\,\omega/\sqrt{2}.$$

The instrument installed in the Physics department at Durham university, and which was used for all the VSM measurements reported here, is similar to that described by Hoon [6], as shown in Figure 1.5. The magnetic measurements on various bulk samples of nickel manganite are reported in section 6.6. Some improvements have been made to the system, including the addition of a cryostat to enable low temperature measurements [80]. The cryostat used was a modified model CF1200 continuous flow cryostat, made by Oxford Instruments. The method for producing the large fields needed was to use a conventional laboratory electromagnet, with iron pole pieces, with a field of 1.2 T being possible. Sets of detection coils used were similar to the type described as Mallinson [81] geometry. Low temperature measurements were possible by

attaching a continuous flow cryostat to the vibrating head device, into which the sample rod extended.

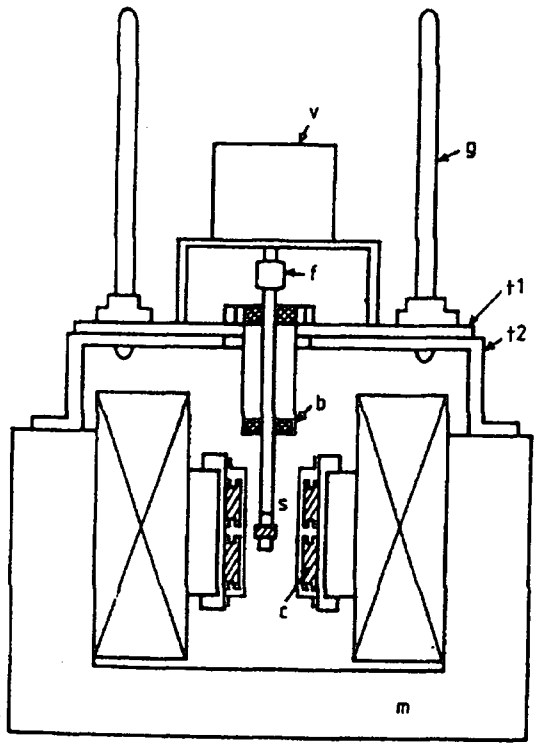

Figure 1.5. Schematic of a VSM similar to the one used. Principal elements are labelled: b; PTFE guide bushes, c; shrouded pickup coils, f; flexible coupling, g; guide rods, m; electromagnet, t_1; movable table, t_2; support table, v; electromagnetic vibrator; s; sample (From Hoon [6] Figure 2).

1.6 X-ray, and neutron diffraction

Both X-rays and thermal neutrons find application in the determination of crystal structures, despite a large difference in energies. For a wavelength of 1 Å, neutrons have an energy of 82 meV, whereas an X-ray photon has an energy of 12 keV. The typical atomic separation in a solid is of the order of 1 Å (10^{-10} m), and thus any probe of the structure must have a wavelength of this order. A source of X-rays is required that has a narrow emission linewidth. X-rays are typically produced by a number of different methods; a standard laboratory source will use the radiation emitted when high-energy electrons strike a metal target. The targets used are low atomic number metals, the most common is copper. The emitted photon energy spectrum, in addition to Bremstrahlung radiation, will contain intense spikes. These spikes are the result of electrons being excited out of low-lying orbitals, and electrons in higher energy states cascading down to fill the vacated level. The emitted photon has a characteristic

energy, according to the material. The most intense emission line from copper has a wavelength of 1.54056 Å. In addition, X-rays can be produced in synchrotron sources, as relativistic charged particles undergo acceleration caused by steering magnets. All of the X-ray diffraction work reported herein (chapter 6) has used a conventional copper laboratory source.

Neutrons are produced either by nuclear fission in a reactor (such as the one at the Institute Laue-Langevin (ILL), Grenoble, France), or by spallation (facilities at the Rutherford Appleton Lab, Oxon., UK). Spallation involves firing high-energy protons at either uranium or a tantalum target. Neutrons, along with many other particles such as muons are produced. The neutrons produced by either source need to be slowed to a usable wavelength, by inelastic collisions with a moderating material. These are then monochromated by reflection from a suitable crystal.

When a neutron or X-ray photon strikes an atom, it can be scattered either elastically, or inelastically. In an elastic scattering event, the phase and wavelength of the scattered particle are preserved, but not the direction. If the atom is in a periodic lattice, particles scattered from a family of planes of atoms can interfere constructively, giving a diffraction peak at a certain angle. The condition for this is illustrated in Figure 1.6, when the path difference is a multiple of the wavelength, as described by Bragg in 1913.

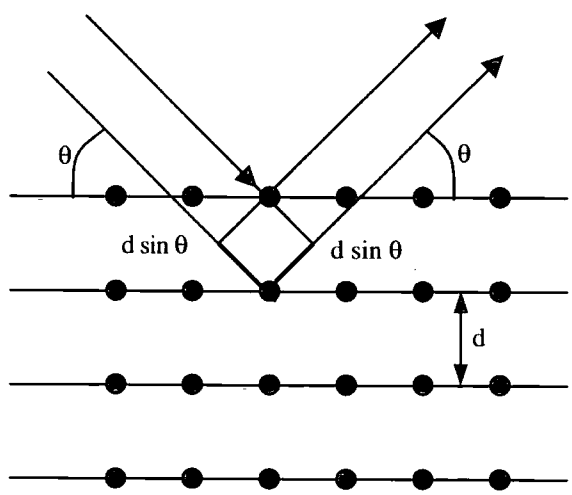

Figure 1.6. A Bragg reflection from a particular family of lattice planes.

This gives rise to the famous Bragg condition for radiation of wavelength λ, and plane spacing d;

$$n\lambda = 2d\sin\theta .$$

The Bragg condition is only satisfied for a particular angle between the incident radiation, and a given crystallographic plane. However, if a sufficiently fine powder is illuminated, the condition will be satisfied by some of the grains, giving a peak in scattered intensity at an angle of 2θ from the incident beam. For any crystalline sample, there will be many crystallographic planes, each with a different value of d, and thus a different scattering angle. Thus with suitable detectors, a plot of intensity against angle, or diffractogram can be obtained. Examples can be found in sections 6.2 onwards.

The intensity of the observed peaks is affected by a number of factors, such as the angular dependence of ordinary scattering, and any angular contribution from particular ions (such as scattering of neutrons by ions with magnetic moments [82]). In the general case of a crystal with more than one atom in the unit cell, scattering contributions from all these atoms must be taken into account. This is expressed in a quantity called the structure factor [83]. The relative phase of these contributions depends upon their position within the unit cell, and the angle of the incoming radiation. The structure factor has to be determined separately for each reflection, and can take on values of zero for crystals with certain symmetry operators. Examination of the intensity and position of the observed peaks can thus give information about the size, contents, and symmetry of the unit cell of a sample. If a sample is a mixture of more than one crystal phase, the peaks of both phases are present in the diffractogram. For a more thorough treatment of diffraction, and its uses in crystallography, the reader is advised to consult one of a number of books on the subject [82, 84].

1.7 Muon spin relaxation

μSR is a technique that has been used to probe the spin dynamics of many different classes of material. It is exceptional in that it is a local probe, the muons ($\mu_\mu = 3.18\ \mu_p$) interacting with the local magnetic field at the point where they comes to rest, via a dipole-dipole interaction. If the local fields contain an off-axis component, the spin of the muons will precess around this, at a rate

determined by γ_μ (1.36 x 10^8 s^{-1} T^{-1} [85]), the muon gyromagnetic ratio [86]. All experiments were carried out at the μSR spectrometer at the ISIS facility [87], housed at the Rutherford Appleton Labs, Didcot, Oxon., UK.

1.7.1 Muon production at ISIS

At ISIS, a pulsed 800 MeV proton beam is directed onto a graphite target. This produces (amongst other things) positive pions (π^+), which decay into positive muons (μ^+) with a half life of approximately 26 ns. Pions decaying in the rest frame of the graphite target produce muons, which have a momentum of 29.8 MeV c^{-1}, and are 100 % spin polarised. The polarisation vector is anti-parallel to the momentum vector. These muon pulses are then magnetically steered to impinge upon the sample material. The muons rapidly thermalise within the sample, while maintaining their spin polarisation. Muons have a half life of 2.2 μs, and decay into a positron and 2 neutrinos. The positron is preferentially emitted along the instantaneous muon spin direction, with energies of up to 53 MeV. Detection of these positrons will therefore give information on the time dependence of the muon spin, and therefore the local field experienced at the muon site.

1.7.2 Positron detection

Plastic scintillation counters attached to photomultiplier tubes are used to detect the positrons. The usual experimental geometry (as used at ISIS) is two banks of detectors, situated forward and backward of the initial muon polarisation, as shown in Figure 1.7. The difference in detection rates in these banks (after allowing for efficiency differences) is termed the asymmetry, $a_o(t)$. This is an average over all muon sites, so if there is any variation in the local magnetic field experienced by the muons, they will not precess coherently, and dephasing of the measured asymmetry will occur. The rate, and type, of this dephasing will depend upon the strength, and distribution of the local fields present. In general, the local fields encountered will not be static, and information on their fluctuation rate can be gained from measurements performed in a magnetic field parallel with the initial muon polarisation. The time window of observable

phenomena is approximately 10 ns < t < 10 μs, dictated by the response time of the detectors, and the muon half life.

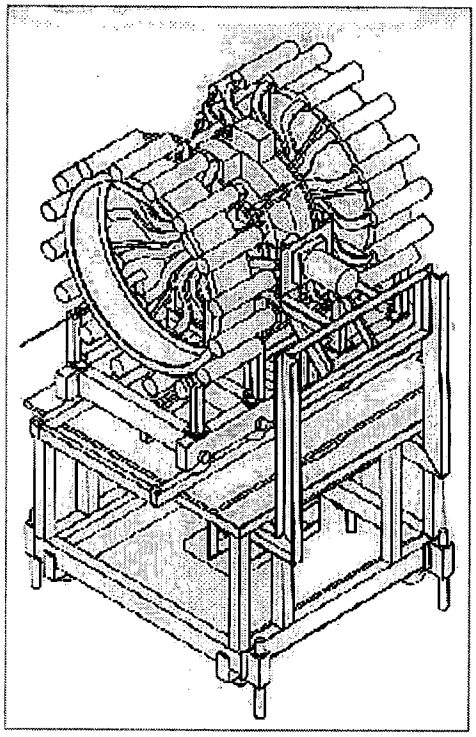

Figure 1.7. Diagram of the MuSR spectrometer at ISIS, showing the forward and backward detector banks [87].

1.7.3 Data collection and analysis

Since muons have a half life of 2.2 μs, the vast majority will have decayed, and emitted their positrons within a few multiples of this. As a result the data becomes increasingly noisy beyond this time, as each data point is the result of fewer and fewer decays. The data is the sum of positron detections over many muon pulses, in order to improve the error statistics. In a typical μSR experiment, approximately 10^7 events are detected for each combination of temperature and applied field. Low temperatures can be obtained with the use of a closed cycle refrigerator provided at ISIS. Data collected within 0.2 μs of the muon pulse is generally discarded, in order to eliminate effects due to the finite muon pulse length, and the decay of muons before coming to rest in the sample.

References

1. Foner, S., *J. Appl. Phys.* **38** (1967) 1510.
2. Schieber, M. M., *Experimental Magnetochemistry; Nonmetallic Magnetic Materials.* 1st Edition. selected Topics in Solid State Physics. Vol. 8, ed. Wohlfarth, E.P. Published by; North - Holland Publishing Company, Amsterdam (1967)
3. Bates, L. F., *Contemporary Phys.* **11** (1970) 301.
4. Flanders, P. J. and Graham Jr, C. D., *Rep. Prog. Phys.* **56** (1993) 431.
5. Princeton Measurements Corporation, 31 Air Park Road, Princeton, NJ 08540, USA, prnctnmeas@msn.com, Tel. No. (609) 924-7885. *MicroMag 3900 Vibrating Sample Magnetometer*, (1st July 1998),
6. Hoon, S. R., *Eur. J. Phys.* **4** (1983) 61.
7. Zijlstra, H., *Rev. Sci. Instrum.* **41** (1970) 1241.
8. Flanders, P. J., *J. Appl. Phys.* **63** (1988) 3940.
9. Hashemi, T. and Brinkman, A. W., *J. Mat. Res. Soc.* **7** (1992) 1278.
10. Parlak, M., *et al.*, *J. Mat. Sci. Lett.* **17** (1998) 1995.
11. Parlak, M., *et al.*, *Thin Solid Films* **345** (1999) 307.
12. Basu, A., *et al.*, *J. App. Phys.* **92** (2002) 4123.
13. Schmidt, R. and Brinkman, A. W., *Int. J. Inorg. Mat.* (2002) 1.
14. Schmidt, R., *et al.*, *Key Engineering Materials* **206-213** (2002) 1417.
15. Boucher, B., *C. R. Hebd. Seances Acad. Sci.* **249** (1957) 514.
16. Philips Components Limited, Philips House, 3 Kelvin Av., Cambridge, info@philips.co.uk, *NTC Thermistors, surface mounting devices*, Serial Number **2322 615 1...** (13 November 1997), Preliminary specification.
17. Brabers, V. A. M. and Terhell, J. C. J. M., *Phys. Stat. Sol. A* **69** (1982) 325.
18. Fritsch, S., *et al.*, *Solid State Ionics* **109** (1998) 229.
19. Larson, E. G., Arnott, R. J. and Wickham, D. G., *J. Phys. Chem. Solids* **23** (1962) 1771.
20. Brabers, V. A. M., *Phys. Stat. Sol. A* **12** (1972) 629.
21. Boucher, B., Buhl, R. and Perrin, M., *Acta Cryst.* **B25** (1969) 2326.
22. Baudour, J. L., *et al.*, *Physica B* **180 & 181** (1992) 97.
23. Gillot, B., *et al.*, *Solid State Ionics* **58** (1992) 155.
24. Boucher, B., Buhl, R. and Perrin, M., *J. Phys. Chem. Solids* **31** (1970) 363.
25. Hallam, T. D., *et al.*, *J. Crystal Growth* **146** (1995) 604.
26. Horsfall, A. B., *et al.*, *J. Crystal Growth* **159** (1996) 1085.
27. Leighton, C., Terry, I. and Becla, P., *Phys. Rev. B* **56** (1997) 6689.
28. Wojtowicz, T., *et al.*, *Phys. Rev. Lett.* **70** (1993) 2317.
29. Stankiewicz, J. and Palacio, F., *Phys. Rev. B* **56** (1997) 12077.
30. Galazka, R. R., Nagata, S. and Keesom, P. H., *Phys. Rev. B* **22** (1980) 3344.
31. Sawicki, M., *et al.*, *J Crystal Growth* **138** (1994) 900.
32. Krenn, H., Zawadzki, W. and Bauer, G., *Phys. Rev. Lett.* **55** (1985) 1510.
33. Anderson, J. R., *et al.*, *Phys. Rev. B* **33** (1986) 4706.
34. Lindner, F. and Feltz, A., *J. Eur. Ceramic Soc.* **11** (1993) 269.
35. Elbadraoui, E., *et al.*, *Phys. Stat. Sol. B* **212** (1999) 129.
36. Chikazumi, S., *Physics of Ferromagnetism.* 2nd Edition. The International Series of Monographs on Physics, ed. Birman, J., *et al.*,. Published by; Clarendon Press, Oxford (1997)
37. Goodenough, J. B., *Magnetism and the Chemical Bond.* 1st Edition. Interscience Monographs on Chemistry. Vol. 1, ed. Cotton, A.F. Published by; Interscience Publishers, John Wiley and Sons, New York (1963)
38. Coey, *J. App. Phys.* **49** (1978) 1646.
39. Antoshina, L. G., *et al.*, *J. Phys: Condens. Matter* **14** (2002) 8103.
40. Toulouse, G., *Commun. Phys.* **2** (1977) 115.
41. Bramwell, S. T. and Gingras, M. J. P., *Science* **294** (2001) 1495.
42. Dormann, J. l. and Nogues, M., *J. Phys.: Cond. Mat.* **2** (1990) 1223.
43. Campbell, I. A., *et al.*, *Phys. Rev. Lett.* **72** (1994) 1291.
44. Brabers, V. A. M., *Progress in Spinel Ferrite Research*, in *Handbook of Magnetic Materials*, Buschow, K.H., Editor. 1995, Elsevier Science: Amsterdam. p. 189.
45. Dormann, J. L., *Hyperfine Interact.* **68** (1991) 47.
46. Lappas, A., *et al.*, *J. Sol. State. Chem.* **145** (1999) 587.

47. Alba, M., Hammann, J. and Nogues, M., *Physica B & C* **107** (1981) 627.
48. Fiorani, D., *et al.*, *Phys. Rev. B* **30** (1984) 2776.
49. Ledang, K., Mery, M. C. and Veillet, P., *J. Magn. Magn. Mater.* **43** (1984) 161.
50. Agostinelli, E., *et al.*, *Solid State Commun.* **56** (1985) 541.
51. Leccabue, F., *et al.*, *J. Mater. Sci.* **28** (1993) 3945.
52. Leccabue, F., *et al.*, *J. Cryst. Growth* **128** (1993) 859.
53. Sagredo, V., *et al.*, *J. Magn. Magn. Mater.* **197** (1999) 423.
54. Afif, K., *et al.*, *Phys. Status Solidi B-Basic Res.* **219** (2000) 383.
55. Maksymowicz, L. J., Lubecka, M. and Jablonski, R., *J. Magn. Magn. Mater.* **215** (2000) 579.
56. Martinho, H., *et al.*, *Phys. Rev. B* **6402** (2001) 4408.
57. Muroi, M., Street, R. and McCormick, P. G., *Phys. Rev. B* **6305** (2001) 2412.
58. Endres, P., *et al.*, *Solid State Ion.* **89** (1996) 221.
59. Onoda, M., *et al.*, *Phys. Rev. B* **56** (1997) 3760.
60. Ueda, Y., Fujiwara, N. and Yasuoka, H., *J. Phys. Soc. Jpn.* **66** (1997) 778.
61. Fujiwara, N., Yasuoka, H. and Ueda, Y., *Phys. Rev. B* **59** (1999) 6294.
62. Jang, Y. I., Chou, F. C. and Chiang, Y. M., *Appl. Phys. Lett.* **74** (1999) 2504.
63. Jang, Y. I., *et al.*, *J. Appl. Phys.* **87** (2000) 7382.
64. Miyoshi, K., *et al.*, *Physica B* **281** (2000) 30.
65. Khan, M. N., *et al.*, *Journal of Materials Science* **27**:(20), (1992) 5676.
66. Mandrus, D., Keppens, V. and Chakoumakos, B. C., *Mater. Res. Bull.* **34** (1999) 1013.
67. Petrakovskii, G. A., *et al.*, *Phys. Rev. B* **6318** (2001) 4425.
68. Champion, J. D. M., *et al.*, *Europhys. Lett.* **57** (2002) 93.
69. Gardner, J. S., *Phys. Rev. Lett.* **82** (1999) 1012.
70. Mirebeau, I., *et al.*, *Nature* **420** (2002) 54.
71. Boucher, B., Buhl, R. and Perrin, M., *J. Phys. Chem. Solids* **31** (1970) 2251.
72. Bhandage, G. T., *et al.*, *J. Magn. Magn. Mater.* **166** (1997) 141.
73. Mydosh, J. A., *Spin Glasses, An Experimental Introduction.* Published by; Taylor and Francis, London (1993)
74. Pauling, L., *The Nature of the Chemical Bond.* 3rd Edition Published by; Cornell University Press, New York (1960)
75. Lee, S. H., *et al.*, *Nature* **418** (2002) 856.
76. Crangle, J., *Solid State Magnetism.* Published by; Edward Arnold, London (1991)
77. Jiles, D., *Introduction to Magnetism and Magnetic Materials.* Published by; Chapman and Hall, London (1991)
78. Dam, N.-E., Guldbrandsen, T. and Jacobsen, C. S., *Meas. Sci. Tech.* **4** (1993) 42.
79. Foner, S., *Rev. Sci. Instrum.* **27** (1956) 548.
80. Delap, M. R., PhD Thesis, Department of Physics, Durham University, Durham, (1990).
81. Mallinson, J., *J. Appl. Phys.* **37** (1966) 2514.
82. Bacon, G. E., *Neutron Diffraction.* 3rd Edition. Monographs on the Physics and Chemistry of Materials, ed. Bawn, C.E.H., *et al.*,. Published by; Clarendon Press, Oxford (1975)
83. Ashcroft, N. W. and Mermin, N. D., *Solid State Physics.* 1st Edition Published by; W. B. Saunders Company, Philadelphia (1976)
84. Hammond, C., *The Basics of Crystallography and Diffraction.* 1st Edition. IUCr Texts on Crystallography. Vol. 3 Published by; Oxford University Press, Oxford (1997)
85. Kilkoyne, S. H., *Lecture notes from the Training Course in Pulsed mSR techniques*, . 1996, CCLRC.
86. Lee, S. L., Kilkoyne, S. H. and Cywinski, R. *Muon Science: muons in physics, chemistry and materials.* in *Proceedings of the Fifty First Scottish Universities Summer School in Physics.* 1998. St Andrews, Scotland: IOP Publishing, Edinburgh, (July 1999)
87. King, P., http://www.isis.rl.ac.uk/muons/muonsIntro/isisMuons/isisMuons.htm (Accessed on; 20/10/2001)

Chapter 2

The Alternating Gradient Force Magnetometer

As noted in section 1.5, the AGFM is a force instrument, comprising of 3 component parts. Firstly, the instrument must be capable of applying a known magnetic field to the sample. Methods of generating fields of various strengths have been well covered in the literature [1, 2]. Secondly, the instrument must have a controllable source of alternating field gradient. This has conventionally been achieved with coils of appropriate geometry, carrying an alternating current and is described in more detail in section 2.2.1. Finally, the resulting oscillatory force on the sample has to be detected, usually by attaching the sample to a mechanically compliant system and measuring the displacement. Many of the previously reported systems have operated at a mechanical resonance, thereby greatly enhancing the displacement. This is covered in more detail in sections 2.2.2, and 2.2.3.

2.1 Review of AGFM literature

The physical forms of instruments that could be called AGFM's are diverse, as they have been used to study a range of samples under different conditions, and different geometries. A list of the instruments discussed in this section can be found in Table 2.1, along with details of the detection systems used, some design parameters, and the resolutions obtained. The discussion purposefully concentrates upon systems with similar form and function to the AGFM constructed by the author. The first demonstration of resonant operation of a force magnetometer was by Zijlstra [3] in 1970. He called his instrument a vibrating reed magnetometer; it was only later that AGFM became the preferred name. Zijlstra designed his instrument in order to study the hysteresis curves of microscopic (a few μm across) single domain particles. Using a fine (38 μm x 20 mm) gold wire as a resonant element, a resolution of 10^{-11} J T^{-1} was reported. Zijlstra's experimental set-up was configured so that the alternating gradient field was oriented vertically, in the same direction as the applied DC field. The resonant element was mounted perpendicular to the field

(i.e. horizontally). The displacement of the reed was measured visually, with the aid of a calibrated microscope, and a stroboscopic lamp to 'freeze' the motion of the fibre at its maximum deflection. The signal used to drive the stroboscope lamp was derived from the same source (an audio oscillator) as that used to drive the gradient coils, after passing through a phase shifting network.

Author	Year	Sample Size	Resolution [J T^{-1}]	Detection Method	Probe Material	Probe dimensions	Q factor	Gradient field [T m^{-1}]	Resonant frequency [Hz]
Zijlstra [3]	1970	~10 μm	10^{-11}	Stroboscope	Fine gold wire	38 μm x 20 mm	100	5	~170
Reeves [4]	1972	several grams	2 x 10^{-10}	Piezoelectric record player cartridge	Silica tubing (non resonant)	3.5 mm x 350 mm	10-100	0.1	167 (operated at ~70)
Roos *et al.*, [5]	1980	~10 μm	10^{-13}	Piezoelectric biomorph	Fine gold wire + glass fibre	18 μm x 10 mm, 150 μm x 70 mm	<70, 550 in vacuum	16.7	62, and 20
Schippan *et al.*, [6]	1982	~10 μm	10^{-13}	Piezoelectric biomorph	Hollow quartz fibre	150 μm OD, 100 μm ID x 30 mm	<70	16.7	151, 953 (harmonic)
Flanders [7]	1988	~0.5 mm	10^{-11}	Piezoelectric biomorph	Various	Various, 10 – 25 mm	25 - 250	0.4	10 – 100
Richter *et al.*, [8]	1988	~1 μm	10^{-14}	Piezoelectric biomorph	Compound hollow quartz fibre	100 μm OD, 20 μm ID x 9.8 mm, 780 μm OD, 350 μm ID x 35 mm	310	46.5	852
Frey *et al.*, [9]	1988	100 mm^3	10^{-10}	Piezoelectric biomorph	Double quartz fibre			2.5	40 – 80
Flanders [10]	1990	135 mg	10^{-11}	Piezoelectric biomorph	Quartz fibre (non resonant)	70 – 300 μm x 150 mm	20 - 100	0.4	200 – 550
Gibson *et al.*, [11]	1991	~10 μm	1.4 x 10^{-14}	Optical Interferometry	Magnetic force microscope tip (Si_3N_4)	-	43	50	24500
O'Grady *et al.*, [12]	1993	100 mg	2 x 10^{-11}	Piezoelectric biomorph		-		0.4	500
Wallace *et al.*, [13]	1995	0.5 mm	10^{-8}	Tunnelling current	Brass strip	-	30	0.001	217
Zimmer-mann *et al.*, [14]	1996	~1 μm	10^{-14}	Optical deflection (PSD)	Optic Fibre	125 μm	400	3.2	~1000
Asti *et al.*, [15, 16]	1996	~1 mm	5 x 10^{-10}	Piezoelectric record player cartridge	Tensioned tungsten wire	300 mm x 40 μm	1000	-	150
Hill *et al.*, [17]	1996	Thin films 4 mm x 4 mm	3.4 x 10^{-10}	Optical deflection (PSD)	Tungsten wire	20 mm x 250 μm	700	0.2	250
Ashcroft	2001	various	5 x 10^{-11}	Piezoelectric biomorph	Compound quartz fibre	120 mm x 650 μm	50 - 300	15	40 - 95

Table 2.1. Parameters of previous instruments reported in the literature, and the present work.

Major developments in the design of the AGFM were made by Flanders who changed to a different coil configuration [10], employing an alternating field with

a gradient perpendicular to the field vector. This is shown in Figure 2.1, and allowed the use of a non-resonant extension, similar to that used earlier by Reeves [4]. This was especially advantageous, as it allowed the resonant element and piezoelectric biomorph to remain at room temperature, while the temperature of the sample was varied in the range 77 to 900 K. This largely negated the need for a nulling coil (first used by Reeves [4], but impractical at 900 K), or excessive frequency tracking during experiments. The resonant properties were found to be nearly stable when using a long extension (100 – 150 mm), that had been suitably heat-shielded. Quartz fibres and capillary tubes were used as extensions, with diameters suited to the sample mass and sensitivity required, in the range 70 μm to 300 μm. The biomorphs used were the only resonant element present, and were of the order of 20 mm long and 0.6 mm thick.

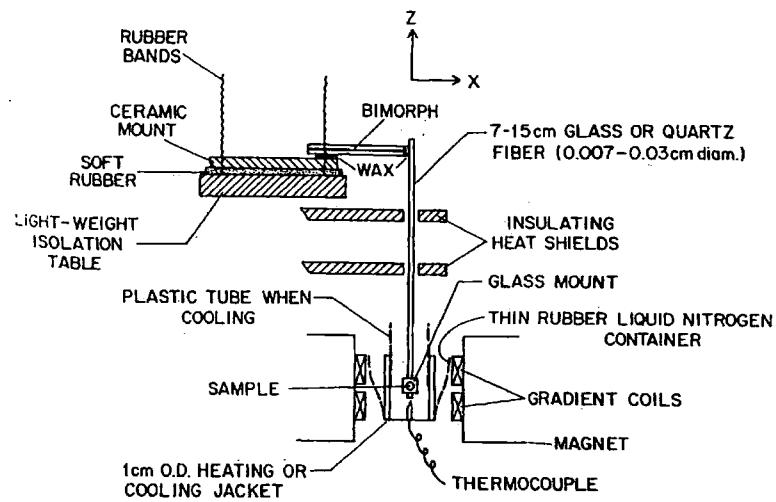

Figure 2.1. The instrument used by Flanders, configured for vertical force mode. (Figure 1 from Flanders [10])

Temperature was varied in a similar manner to that used in previous work [7], with higher temperatures being produced by a furnace of similar size to the cooling tube. Temperatures were measured using a thermocouple mounted just below the sample. The resonant frequency of the system was found to depend strongly on sample mass, decreasing from approximately 500 Hz unloaded, to approximately 200 Hz for a sample of 135 mg, and weakly dependent on temperature when using thin fibres. There was no measurable change in the Q factor with changes in sample temperature. Palladium foil was used to calibrate the system, and to check the resolution obtainable (10^{-11} J T^{-1}). Problems were

encountered when measuring superconducting samples, due to unwanted field gradient components in directions perpendicular to the one required. These unwanted components were a necessary consequence of the coil design employed. This meant that there were very large distortions in measured *M-H* loops when the sample was slightly displaced from the field centre, or for large samples of superconducting material.

In the late 1980's, Princeton Measurements Corp. started producing commercially available AGFM systems, one of which (the M2900 model) was the subject of a paper by O'Grady *et al.*, [12]. In this, a study of the resolution and reproducibility was reported, as well as the effect of the alternating gradient field on samples. This effect was reported to be considerable in the case of samples with a low coercivity, mainly due to sample positioning errors. Deviation of the sample from the centre of the alternating gradient region means that the sample experiences an additional alternating magnetic field component. The commercial system was similar in many respects to Flanders' instruments [7, 10], with a choice of probes corresponding to the two configurations outlined. The resolution was reported as 2×10^{-11} J T^{-1}, slightly worse than the manufacturer's quoted value of 10^{-11} J T^{-1}. Repeatability was within 6 %, deteriorating to 20 % for samples with low moments (towards the limit of resolution). In addition, a low temperature modification was detailed, allowing measurements down to 4 K. This was fabricated from a modified Oxford Instruments ESR continuous flow cryostat. The cooling was performed by a method similar to Flanders [7, 10], whereby a jet of cold gas was directed at the base of an aluminium cup surrounding the sample holder. The flow of helium introduced mechanical noise into the system, reducing the resolution to 2×10^{-8} J T^{-1} at 5 K.

Many authors indulged in calculations of the theoretical resolution of their instruments, limited by such factors as electrical noise in detectors, thermally induced noise in the resonant element, noise base of lock-in amplifiers, etc. In all cases, the actual performance fell considerably short of these predictions. Most authors attributed this to external mechanical vibrations being coupled to the system, despite many taking great care to isolate their systems from the environment. There seems to be at present no way of eliminating this source of noise completely.

2.2 AGFM design

The original motivation for construction of an AGFM has been detailed in section 1.1, resulting in a target resolution of 10^{-8} J T^{-1} kg^{-1} or better. It was decided to initially develop the instrument for ambient temperature operation, with a view to subsequently extending operation to cryogenic temperatures. This enabled initial characterisation of the instrument (reported in chapter 3), without the expense of a cryogen supply. Once a room temperature system was established, adaptation to enable measurements down to 77 K was attempted. Cost was also a major influence in many of the design decisions taken, with a limited budget available for development work. The $Hg_{1-x}Mn_xTe$ film samples available were ~0.5 mm thick (including substrate), between 3 and 10 mm across, and were all less than 0.3 grams in weight. The AGFM was therefore designed to accommodate such samples. A conventional iron yoke electromagnet was used, capable of generating homogenous fields up to 400 mT. A schematic of the AGFM is shown in Figure 2.2.

2.2.1 AC magnetic field gradient

The object of the AC gradient coils is to produce a homogenous, well-defined alternating field gradient at an accurately controlled frequency. Field gradient ($\nabla\underline{H}$) is a tensor of rank 2, and has 9 components. One of these components needs to be non zero, as the driving component. It is desirable for the other 8 components to be zero in the region of the sample. Generally this is not possible, so those components that could excite unwanted resonances should be minimised, ideally to a level below that which the instrument is able to detect. A comprehensive study of many coil configurations has been undertaken by Roos *et al.*, [5]. All the previous designs have used circular coils, except Zimmermann *et al.*, [14], where rectangular coils were used. There have been several problems reported [5, 8, 13, 14] of the gradient coils vibrating in a steady applied field, at the driving frequency. The coil winding therefore needed to be held rigid to minimise vibration, as this could disturb a sensitive detector. A rigid mounting to the pole pieces, and having small coils reduced this problem.

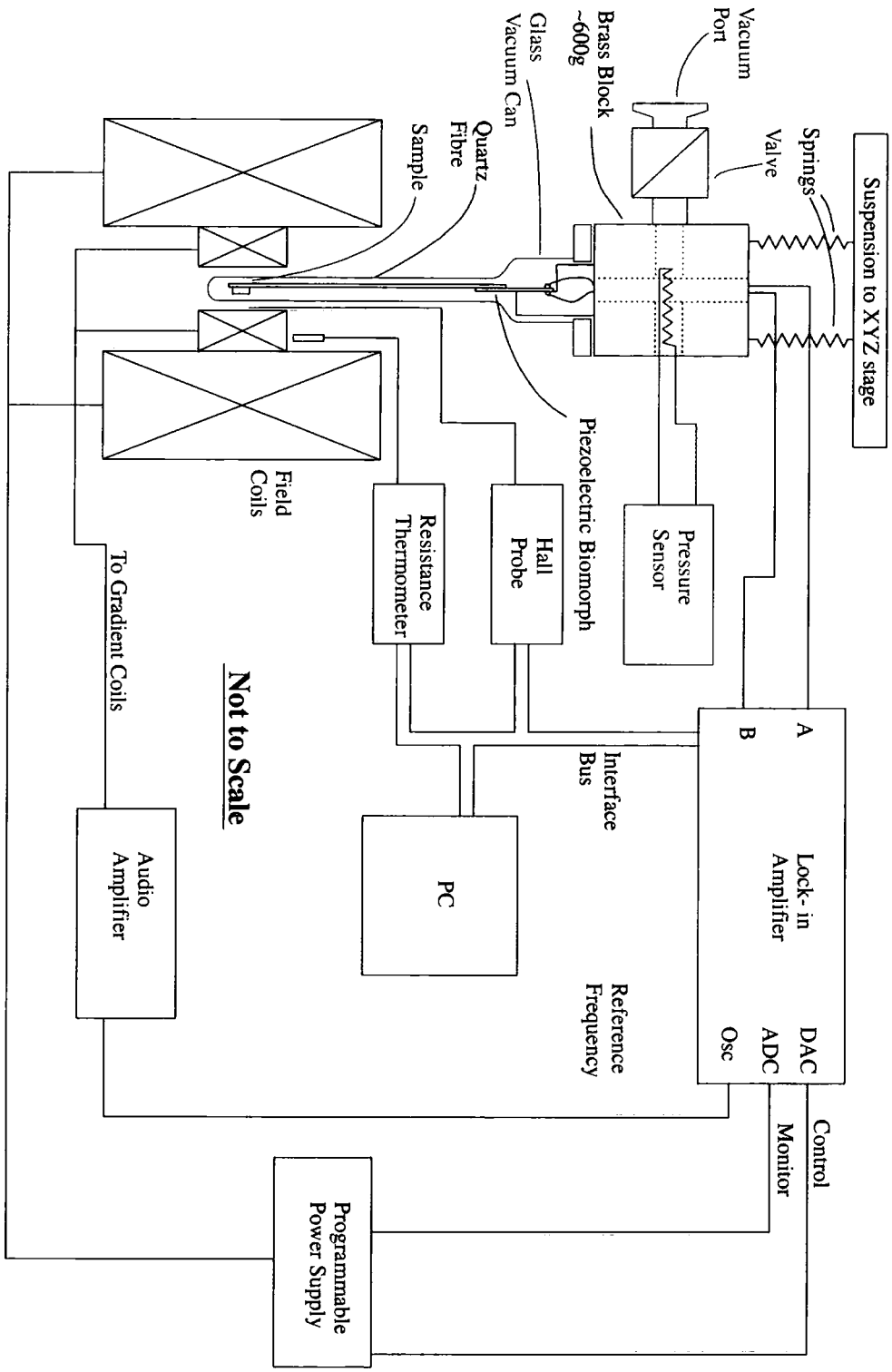

Figure 2.2. Schematic of the AGFM. The new vacuum system is outlined in red.

A pair of coils were designed, and manufactured in the departmental workshop. The formers were fabricated in Tufnol, with a low magnetic susceptibility, and is tough, durable, and cheap. It was decided to have a coil of outside diameter 25 mm, inside diameter 6 mm, and thickness 6 mm. The coil space had a volume

of 2.78 x 10^{-6} m^3, and contained 200 turns of 0.4 mm diameter insulated copper wire, secured with a varnish layer on the outside. The coils were wired in antiparallel, so that the field in the plane of symmetry of the two coils was zero, but the field gradient was non zero.

The coils were powered by a Quad™ audio frequency amplifier, fed from the internal reference of a lock-in amplifier. The coils were attached, and centred on the pole pieces with a 6.35 mm centred hole in the iron pole pieces. Proximity of the iron pole pieces has the effect of introducing a frequency dependence of the amplitude and phase of the gradient field. One way of overcoming this problem was to monitor the actual gradient field, with an additional set of coils, placed inside the coils used to generate the gradient [8, 14].

2.2.2 Resonant sample mount

The resonant system is the heart of the AGFM, which distinguishes it from conventional cantilever [18], or force magnetometry. It is advantageous to have high sensitivity, and mechanical gain (or Q factor). Design of the resonant element has received a great deal of attention in the literature, with many different solutions being proposed. All the previous designs have used a resonant cantilever, of some description, varying from 500 μm, to 200 mm long. An approximate mathematical treatment of the equations governing mechanical resonance led Zijlstra [3] to expressions for the mechanical quality factor (Q), and sensitivity (y_d/F_0) in terms of various physical quantities of the system. Given assumptions of light damping, and small displacements from equilibrium, these are;

$$Q \approx 0.3\left(\frac{d^3}{\eta l^2}\right)(\rho Y)^{1/2} \qquad (2.1) \qquad \left(\frac{y_d}{F_0}\right) \approx 2\left(\frac{l}{\eta d}\right)\left(\frac{\rho}{Y}\right)^{1/2} \qquad (2.2).$$

Here F_0 is the oscillatory force, y_d the dynamic displacement, η the dynamic viscosity of air, l the reed length, d the reed diameter, ρ the reed density, and Y is Young's modulus.

Sidles *et al.*, [19] gave expressions for the eigenfrequencies and effective spring constant of a simple clamped cantilever with thickness t, and mass m;

$$\omega_0 = \begin{bmatrix} 3.516 \\ 22.03 \\ 61.70 \\ 120.9 \end{bmatrix} \frac{t}{l^2}\sqrt{\left(\frac{Y}{12\rho}\right)} \qquad (2.3) \qquad k_{mech} = \frac{m}{4}\omega_0^2 \qquad (2.4).$$

The important characteristics that the resonant system of an AGFM should possess are discussed below.

High sensitivity and Q factor

The Q factor is the factor by which the sensitivity at resonance (S_R) is increased by, over the static sensitivity (S_S);

$$S_R = S_S Q$$

These should therefore be large enough to enable detection of the moment of small or weakly magnetic samples. From equations 2.1 and 2.2, the conditions for optimum performance of the instrument are, in the case of high sensitivity; a long thin, dense and flexible reed. For maximal Q factor, the conditions are changed to; a short wide, dense and stiff reed. These requirements have to be balanced against the need for a short length scale, in order to achieve a sufficiently high resonant frequency. Q also determines the width of the resonance peak, with an excessively high Q value meaning an extremely narrow (and difficult to find) resonant peak. This would then require a very precise and minutely adjustable oscillator to stay on resonance, and allow for frequency drifts with temperature. The Q factor can be expressed as a measure of energy loss per vibration period, so for a high Q all loss mechanisms should be minimised. Previous work [5] indicates that air damping is the major loss mechanism at atmospheric pressure. A modest vacuum reduces this, as does a small surface area resonant element. Other possible loss mechanisms are internal mechanical hysteresis in the material, and losses through the support. Very low internal losses are predicted for a cantilever made of pure defect free materials, such as single crystal silicon [20], and silicon nitride (Si_3N_4). Energy losses from the resonant element through the support are reduced as the stiffness of the support

increases. This can be achieved by making the resonant frequency of the support much lower (1-2 orders of magnitude) than the operating frequency [3].

Low magnetic moment

Since the sample mount is under the influence of the same fields as the sample, there will be an additional force acting upon it according to its magnetic moment, indistinguishable from those of interest. Obviously the lower the moment is, the better, so that large background contributions are not present. The background should be reproducible, to the resolution required to extract the signal due to a sample, and ideally linear with field, and temperature. For this reason, ferromagnetic materials are unsuitable.

Suitable resonant frequency

Experience and common sense indicates that operation of any sensitive detectors anywhere near a multiple of 50 Hz, produces excessive amounts of interference from nearby, mains powered equipment. In addition, the energy spectrum of environmental noise is inversely proportional to frequency, so it is advantageous to have a high resonant frequency. A higher frequency also means that for a given Q factor, the system is quicker to respond to a change in driving force. There are several factors that affect the resonant frequency of a system, as shown in equation 2.3. There are also geometrical factors, due to the shape of the system, detailed given by Zijlstra [3]. There is the possibility of operating a resonant element at a higher harmonic frequency. From equations 2.3 and 2.4, the second flexural mode is expected at 6.3 times the fundamental frequency, and the effective spring constant increases by roughly a factor of 40. This implies an increase in Q factor, and a decrease in static sensitivity of a factor of 6.3, from examination of equations 2.1, and 2.2, which should give the same dynamic sensitivity.

Resilience

Any sample mount needs to accommodate macroscopic samples, and still yield accurate data. Sample mass has an effect on the resonance properties of the sample holder [7], increasing for large samples. Increasing the mass and

thickness of the resonant sample mount reduces this effect, allowing larger samples to be measured. This would make the sample mounts less prone to breaking when changing sample. If it is intended to subject the sample to a range of temperatures, the properties of the sample holder must be suitable throughout the temperature range.

These individual requirements are not difficult to meet separately. However, when considered together, compromises had to be made to gain the best possible performance. The sample probes used were made from a number of quartz glass fibres, glued together with either cyanoacrylate or epoxy adhesive in a plane perpendicular to the axis of the magnets. The fibres were glued together at regular intervals, so that they vibrated together. Quartz was chosen, as the resonant properties are not affected by magnetic fields [21], and thin fibres were readily available at no cost, from a glassblowing workshop on site. The sample holder consisted of a piece of thin glass cut to size and glued to the end of the sample probe. The glass sample holder was also aligned in this plane for most of the probes. The samples were mounted onto the glass plates using a small amount of vacuum grease. For large thin samples, such as nickel foil, two pieces of glass, with the foil sandwiched between them. This was because thin samples had a tendency to twist so that the field was in the plane of the sample, rather than perpendicular to it. The probes were very fragile, and many were broken during the experiment, despite great care being taken when they were being removed or inserted into the apparatus. The quartz fibres used in the construction of the probes were noticeably tapered, with one end of a larger diameter than the other. An attempt was made to reduce the effect of this on the vibration by arranging fibres together in the completed probes so that the tapers of adjoining fibres ran in opposite directions. Due to this, and the fact that the average fibre diameters varied slightly, no two sample rods were identical, each having different resonant frequencies and Q factors. A photograph of the completed apparatus is shown in Figure 2.3, with a sample rod in place.

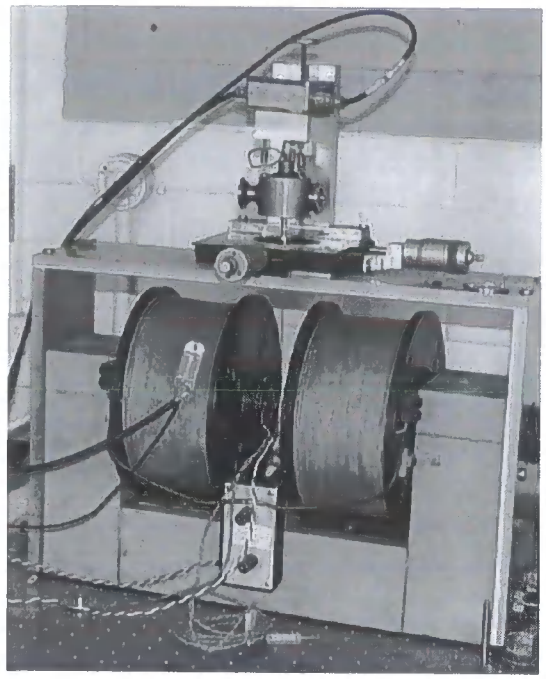

Figure 2.3. Photograph of the completed AGFM, set up for room temperature operation. The x-y-z stage can be seen above the magnet coils, with the brass damping block in place.

2.2.3 Vibration detection

A method of detecting the vibrations of the resonant sample mount was needed, robust enough to handle the mass of the sample and sample mount, and the stresses involved in changing the sample. Ideally it should be unaffected by both the applied field, field gradient, and changes in temperature.

Piezoelectric biomorph

The vibration-sensing element in the experimental system was a piezoelectric biomorph. This consisted of a thin ceramic plate, with a thin film of piezoelectric crystal deposited on both sides. The material used was lead-zirconium titanante (PZT), one of the most common piezoelectrics. Piezoelectric materials produce electrical signals when they are deformed, and conversely deform when electrical signals are applied to them. They form the basis of quartz oscillators, and many types of electronic transducers. The devices used were supplied by RS Components Ltd, stock number 285-784, were 35 mm long, 1.5 mm wide, 0.6 mm thick, and had a response of 4 V peak-to-peak for a 0.01 mm vibration at the biomorph tip [22]. The actual deformation experienced in use was orders of magnitude smaller. Signals were typically of the order of

0.2 mV (corresponding to a calculated deformation of 5 Å at the biomorph tip). The sample probe was glued to the tip of a biomorph, with roughly 10 mm overlap. The position of the biomorph is shown in Figure 2.3.

Vibration isolation

It was impossible to find a location free from external sources of mechanical vibration, so isolating the instrument from these sources was necessary. The level of isolation should be such that levels of vibration at the measurement frequency are reduced as far as is possible. This will depend upon the measurement frequency used, and the bandwidth of the detection circuitry (e.g. dictated by the time constant on a lock in amplifier). Also present were vibrations at the measurement frequency from the gradient coils. The isolation was chosen to adequately screen noise of a broad bandwidth, from sub-Hertz building noise, to audio frequency ambient noise. It was therefore decided to have a number of layers of vibrational isolation. These took the form of a large brass block, suspended on three extension springs, as shown in Figure 2.3. This was designed to have a resonant frequency much lower than that used in the instrument. Additional isolation was provided by liberal use of rubber isolators, and placing the instrument on an optical bench. An attempt to reduce vibration by enclosing the sample and detector in an evacuated enclosure was unsuccessful, due to the extra vibrations introduced by the vacuum pump.

2.3 Vibrations of the AGFM probe

2.3.1 Resonant conditions

Due to the need to drive the AGFM probe to mechanical resonance, it was necessary to determine the exact resonance frequency, Q factor, and relative phase of the system before each measurement. The motion of the quartz fibre can be described using the equations of forced (or driven), damped harmonic motion, as given in equation 2.5. It was assumed that the deflections are small enough so that any restoring forces are linear with deflection.

$$z'' + 2\zeta z' + \Omega^2 z = a\sin(\omega t) \tag{2.5}$$

Where z is the deflection of the tip of the quartz fibre from its equilibrium position, and Ω is the resonant frequency of the undamped system (a measure of the restoring force towards equilibrium). ζ is a resistive term, due to losses in the fibre, and drag forces acting on the probe. The reduced driving force is $a \cdot \sin(\omega t)$, at a frequency $f = \omega / 2\pi$. The solution to this equation has two parts, a steady state solution, and an exponentially decaying solution. It is the steady state solution that is of interest;

$$z = P' \sin(\omega t) + Q' \cos(\omega t).$$

Substituting this into equation 2.5, and solving for P' and Q' gives;

$$P' = \frac{-a\left(\Omega^2 - \omega^2\right)}{\left(\Omega^2 - \omega^2\right)^2 + 4\zeta^2\omega^2}, \qquad Q' = \frac{2a\zeta\omega}{\left(\Omega^2 - \omega^2\right)^2 + 4\zeta^2\omega^2}.$$

Combining these into a single oscillating term of general phase δ' gives;

$$z = \frac{a\sin(\omega t + \delta')}{\sqrt{\left(\Omega^2 - \omega^2\right)^2 + 4\zeta^2\omega^2}}, \qquad \delta' = \tan^{-1}\left(\frac{Q'}{P'}\right). \tag{2.6}$$

To find the resonant frequency, one needs simply to find the value of ω that gives a maximum in z. This is calculated by;

$$\omega_C^2 = \Omega^2 - 2\zeta^2.$$

If the AGFM is well designed, the damping term, ζ will be much smaller than Ω, the restoring term. Therefore, the resonant frequency would be only slightly lower than the case without any damping at all. The maximum amplitude of vibration is found by substituting the resonant frequency, ω_c into the general term for z (equation 2.6), giving;

$$z_{max} = \frac{a}{2\zeta\sqrt{\Omega^2 - \zeta^2}}. \tag{2.7}$$

The phase of the oscillation with respect to the driving force is given by;

$$\delta_c' = \tan^{-1}\left(\frac{-\omega_c}{\zeta}\right).$$

This tends to –90 °, as the damping is reduced towards zero (i.e. as P' approaches zero). The Q factor can be found by comparing the maximum value of the displacement at resonance (equation 2.7) with the static displacement away from resonance. The static displacement (response to a constant force, or an

oscillating force well removed from resonance) can be obtained either by disregarding all differentials of z in equation 2.5, or by constraining ω to zero in equation 2.6. This gives in the limit of small damping (large Q factor);

$$z_s = \frac{a}{\Omega^2}, \qquad Q = \frac{\Omega^2}{2\zeta\sqrt{\Omega^2 - \zeta^2}} \approx \frac{\Omega}{2\zeta}.$$

This allows an expression for P' and Q' in terms of resonant frequency, and Q factor.

$$P' = \frac{-a\left(\omega_c^{\,2} - \omega^2\right)}{\left(\omega_c^{\,2} - \omega^2\right)^2 + \frac{\omega_c^{\,2}\omega^2}{Q^2}} \quad (2.8), \qquad Q' = \frac{a\frac{\omega_c\omega}{Q}}{\left(\omega_c^{\,2} - \omega^2\right)^2 + \frac{\omega_c^{\,2}\omega^2}{Q^2}}. \quad (2.9)$$

As can be seen from equations 2.8, and 2.9, the component in phase with the driving force, P' disappears when at the resonant frequency. This gives a potentially useful indicator as to when the system is on resonance. However, since these expressions are approximations, this is not the case in reality (the expression for the phase when on resonance is $\neq 90$ °). To find the frequency at which P' is zero, for the case where damping is taken into account fully is a little more complex. The exact expression for P' is found to be;

$$P' = \frac{-a\left(\frac{\omega_c^{\,2}Q}{\sqrt{Q^2 - 1}} - \omega^2\right)}{\left(\omega_c^{\,2} - \omega^2\right)^2 + \frac{\omega_c^{\,2}\omega^2}{\left(Q^2 - 1\right)}}. \quad (2.10)$$

As can be seen, this is non zero when on resonance, with a value of;

$$P' = -\frac{a}{\omega_c^2}\left(1 + Q\sqrt{Q^2 - 1} - Q^2\right). \quad (2.11)$$

This can be simplified by replacing the term inside the brackets of equation 2.11 with its Maclaurin series [23] in powers of $1/Q$. Neglecting terms of order $1/Q^4$ and higher yields an approximation of;

$$P' \approx -\frac{a}{2\omega_c^2}\left(1 - \frac{1}{Q^2}\right) \approx -\frac{a}{2\omega_c^2}$$

For an expected operating frequency of the order of 100 Hz, this is negligible compared to the peak amplitude.

Also using the exact expression for P' (equation 2.10), the point at which it is exactly zero is when;

$$\omega = \frac{\omega_c}{\sqrt[4]{1-\frac{1}{Q^2}}} \approx \omega_c\left(1+\frac{1}{4Q^2}\right).$$

Using a frequency of 100 Hz, and a Q factor of 200, the calculated deviation of the zero crossing point from resonance is 0.625 mHz, which is below the resolution of the frequency source in the lock-in amplifier. At much lower Q factors and frequencies, these factors may become important, but the approximation of zero crossing of P' at resonance has been taken to be valid in normal operation. This treatment can be extended, to cover the higher order resonances. Flanders [7] gives solutions for a general resonance order;

$$X = af_0 f \frac{\left(\frac{f_n f}{Q}\right)}{\left(\frac{f_n f}{Q}\right)^2 + (f_n^2 - f^2)^2} \quad (2.12), \quad Y = af_0 f \frac{(f_n^2 - f^2)}{\left(\frac{f_n f}{Q}\right)^2 + (f_n^2 - f^2)^2} \quad (2.13)$$

Where X and Y are the in phase and quadrature signals respectively. These correspond to equations 2.8, and 2.9 from the treatment above. f_0 is the centre frequency of the first (fundamental) resonance peak, and f_n is the centre frequency of the resonant peak in question. These equations assume that the resonant element is of uniform density and stiffness along its length, the deflection along the element can be approximated as the sum of travelling waves, and the support is immovable. None of these assumptions are valid for an AGFM, as the sample mass is localised at one point on the resonant element. The travelling wave model assumes that the free end of the rod has an angular deflection of zero, whereas the angular deflection is maximised at the free end. In addition, Flanders used a biomorph detector, between the resonant element, and the support; thus, the support presented to the resonant element was not infinitely stiff.

2.3.2 Resonant peak fitting

As far as the author is aware, the resonant analyses outlined below, and the subsequent data correction procedure (detailed in section 2.3.3) is unique to this

work. No similar corrections have been reported in the analysis of data from any other AGFM, or related magnetic measurement system.

A signal is said to be in phase, if the X component is maximised at the resonant frequency. Knowledge of the above equations, and data for the X, and Y signals in the region of the resonant frequency allows an optimisation routine to be used. This fits a number of parameters to a dataset, such as resonant frequency, Q factor, peak height, etc. Unfortunately, there is a phase change inherent in the response of the system due to the audio amplifier and pole piece effects, so not only does the centre frequency need to be found, but this phase lag needs to be found also. In general, the lock-in signal outputs will be as follows,

$$X^* = X\cos(\theta) + Y\sin(\theta), \qquad Y^* = X\cos(\theta + \pi/2) + Y\sin(\theta + \pi/2).$$

To find the correct phase and frequency for measurements, both the in-phase, and out of phase components are measured, over a narrow frequency range centred on the frequency of interest, an example of which is given in Figure 2.4.

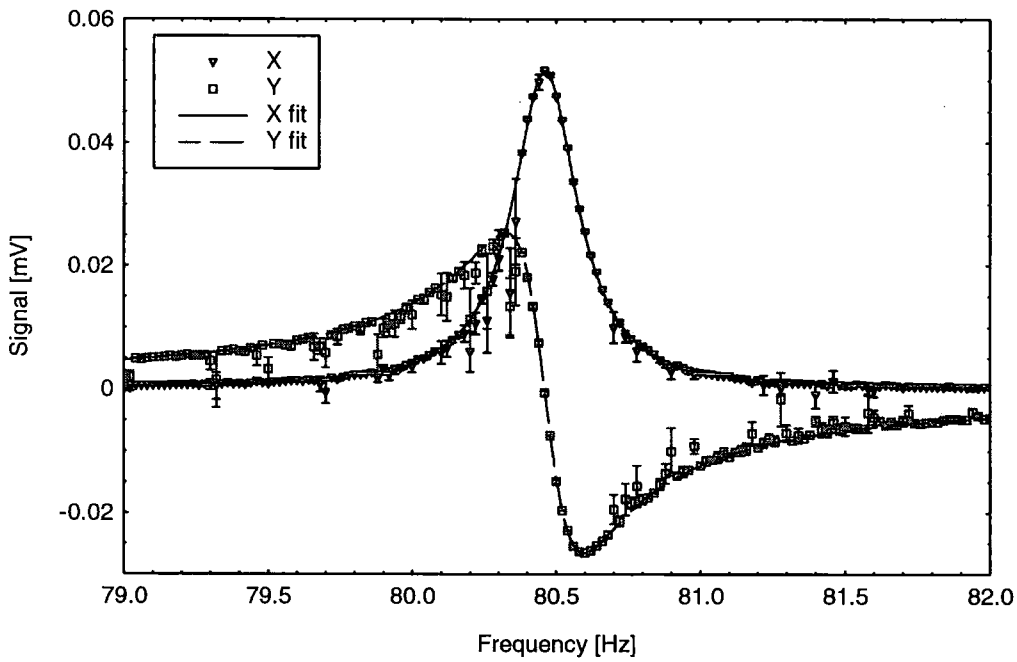

Figure 2.4. Illustration of the uneven errors encountered when looking at small signals. Lines are fits to the data points.

These curves are modelled simultaneously, in a spreadsheet application. This also gives information about any instrument offsets present, and the quality factor of the resonance. The application accepts data in 5 columns, corresponding to frequency, X^* signal, X^* noise, Y^* signal, Y^* noise. The noise values are the

standard deviation of a number of measurements taken under identical conditions, separated in time by a delay of at least 5 times the time constant of the lock – in amplifier. The variable parameters are; phase, resonant frequency, vibration amplitude, Q factor, and offsets in the X^*, and Y^* signals. A trial fit dataset is constructed from the initial values of the variable parameters, and a difference table calculated. From the difference table, a fitting parameter, F is obtained;

$$F = \sum_f \frac{|X^*(f) - X_{FIT}^*(f)|}{\sigma_X + \sigma_A} + \sum_f \frac{|Y^*(f) - Y_{FIT}^*(f)|}{\sigma_Y + \sigma_A} \qquad (2.14)$$

Where $X^*(f)$, $X^*_{FIT}(f)$, and σ_X are the data point, trial fit, and data noise respectively. A weighting of $1/(\sigma_X + \sigma_A)$ was applied in order to minimise the influence of rogue data points from noisy datasets. These points were found away from the main curve, and were caused by some transient vibration source (such as a door slamming). The addition of σ_A is necessary for the case where the noise present is below the resolution of the lock-in amplifier, and a value of zero for σ_X would result in an infinite term in the series. σ_A is the average noise value for the entire dataset.

A new set of the variable parameters are chosen, that reduce the value of the fit parameter F. The process is repeated until no further improvement is possible, within a set tolerance. The fitting procedure is automated within the spreadsheet, including choosing of sets of variable parameters. It was found that the initial guesses needed to be reasonably accurate for the automatic fitting procedure to commence. The fitting procedure was found to be robust, allowing 'difficult' datasets to be analysed, such as in Figure 2.4, where the noisy data points were displaced to lower amplitude values. The cause of this particular type of error is unknown. This has been successfully analysed, due to the greater weighting of points with smaller noise values. The same is true for the data in Figure 2.5, where the increased electrical noise due to interference from mains powered equipment is clearly visible around 100 Hz. The resonant peak height is approximately an order of magnitude lower than the one shown in Figure 2.4. The signal offsets are now clearly visible.

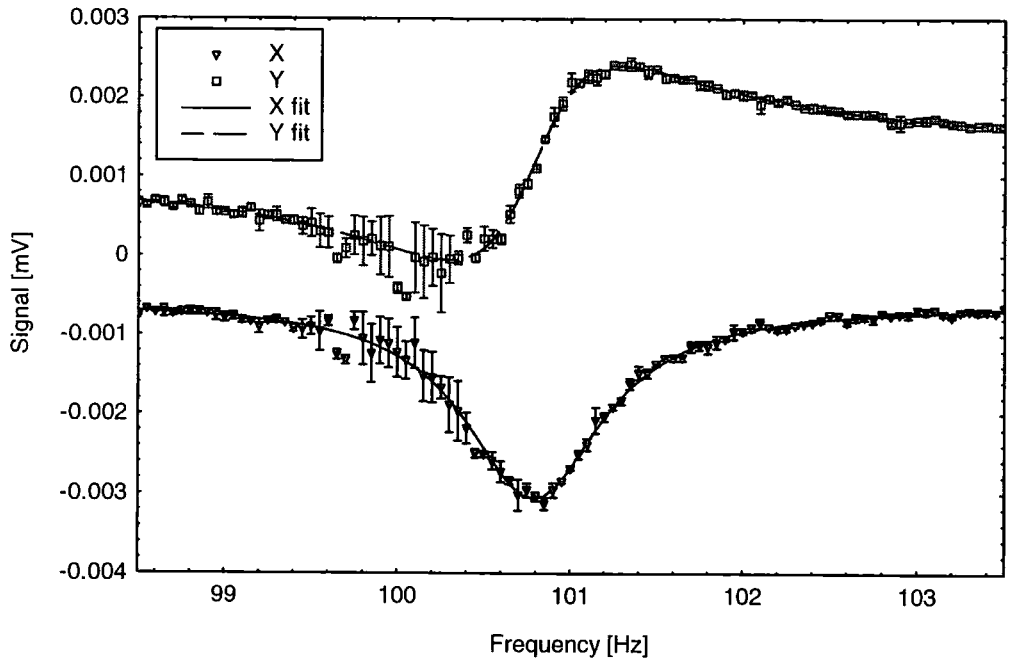

Figure 2.5. The effect of noise at 100 Hz. The lines are fits to the resonant function. The offsets are large compared with the signal.

These are caused by biasing errors in amplifier stages, and crosstalk from leads supplying the gradient coils, to the biomorph connections. Once the correct frequency and phase are known, it is possible to obtain the maximum output signal, working on the peak of the in-phase component (i.e. at f_n). The peak value of X is;

$$X_{MAX} = \frac{af_0Q}{f_n} . \tag{2.15}$$

Usually, there is no reason not to operate at the fundamental frequency, f_0. However, it was soon found that once determined, the resonance frequency was not stable from hour to hour, and day to day. This was noticed because of the sensitivity of the out of phase signal to small changes in resonant frequency, due to it having maximum gradient at resonance, where it crosses through zero. The reasons for this are discussed in section 3.2. There are two possible approaches to eliminating the errors produced when the resonant frequency changes. One can attempt to continuously alter the frequency of the signal applied to the gradient coils, and stay on resonance, or the measurement frequency can remain fixed, and corrections be made to the data according to the calculated resonant frequency. Initial attempts to continuously update the measurement frequency

during data collection proved difficult, especially as the field was varied through zero. The increased number of measurements necessary to determine resonance conditions slowed data collection to a considerable degree. It was decided to operate at fixed frequency for all but a few experiments thereafter.

2.3.3 Off-resonance corrections

This procedure enables the variation in resonant frequency to be tracked as an experiment is being run, or later when the data is being analysed. Starting from any point on the resonance curve, one can, with knowledge of both X, and Y components of the data, find the height, and centre frequency of the resonance. These calculations are assuming Q factor, and phase stay unchanged throughout the experimental run. From inspection of the equations given by Flanders, (equations 2.12 and 2.13), and the expression for the maximum height of the resonance peak (equation 2.15), it can be seen that this is given by;

$$X_{MAX} = X(f_0) = X(f) + \frac{(Y(f))^2}{X(f)}. \qquad (2.16)$$

By dividing equation 2.13 by equation 2.11, and re-arranging, the centre frequency can be expressed as;

$$f_0 = \frac{f}{2}\left(\sqrt{4+\left(\frac{Y(f)}{QX(f)}\right)^2} + \left(\frac{Y(f)}{QX(f)}\right)\right)$$

The only variables needed in these equations are the values of X, and Y, and the Q factor. In practice, knowledge of the experimental offsets is also required. Examples of data that have been treated in this way are shown in section 3.4. The assumptions that the phase and Q factor remain approximately stable are borne out by experiment (see section 3.3). In order to obtain any meaningful results from this technique, the measurement frequency needs to be within the main part of the resonant peak. If this is not the case, the errors become very large as is illustrated in Figure 2.6. This was obtained from resonance curve data, similar to that in Figure 2.4. The resonance curve was first fitted, using the procedure outlined above, to get accurate values for the Q factor, and the peak amplitude.

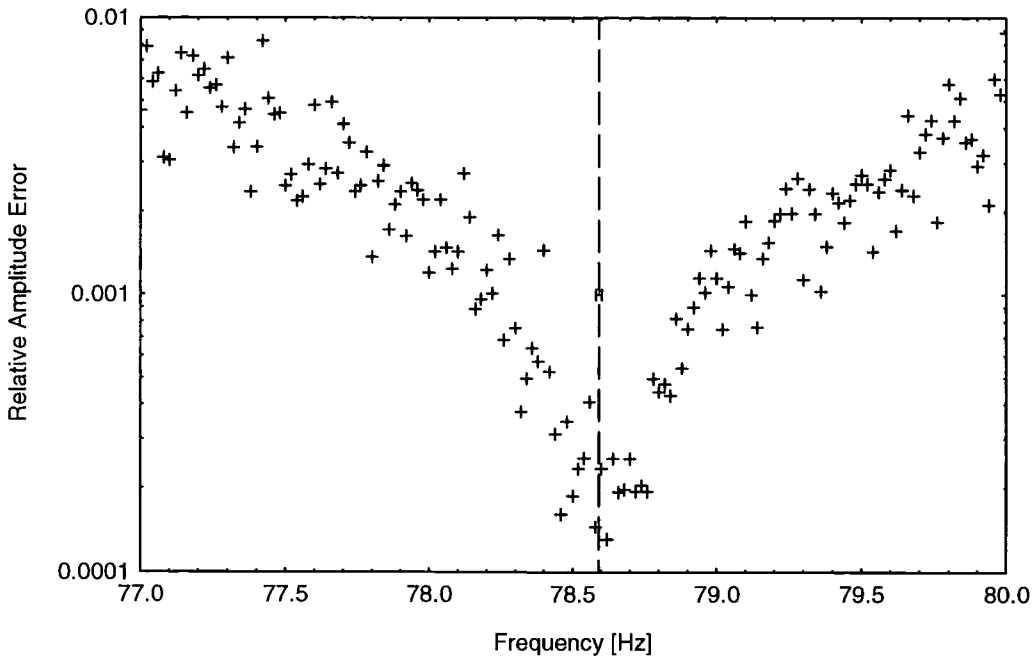

Figure 2.6. Standard error on the reconstructed peak amplitude. The resonant frequency, as determined from a fit to the resonant curve is marked (78.952(10) Hz). The error on the plotted points lies within the data markers.

Then taking the individual X and Y values collected at each measurement frequency, and the Q value already obtained, a calculation of the reconstructed peak height was made using equation 2.16. The error on this quantity was also calculated, due to the uncertainty in the precise values of X, Y, Q, and the calibration constant for the probe, C. Uncertainties in the values of X, and Y were obtained from the standard deviation of the collected data points. The uncertainty in Q was estimated from the variation of fitted values to a number of resonant curves measured with the same sample mounted. The sample used for these measurements was 31.7(8) mg of quartz glass. The largest contribution to the uncertainty in the calibration constant, C was due to the uncertainty on the measurement of the sample mass. The formula for the standard error on the reconstructed peak amplitude is;

$$\frac{\sigma_{X_{MAX}}}{X_{MAX}} = \frac{\sqrt{\left[\left(\left|\sigma_X\left(1-\left(\frac{Y}{X}\right)^2\right)\right|+\left|2\sigma_Y\frac{Y}{X}\right|\right)C\right]^2+\left[\frac{X_{MAX}\sigma_C}{C}\right]^2}}{X_{MAX}}.$$

Similarly, the standard error on the reconstructed resonant frequency is;

$$\frac{\sigma_{f_n}}{f_n} = \frac{\left|\left(\frac{fY}{2XQ}\right)\left(1+1\Big/\sqrt{1+\left(\frac{2QX}{Y}\right)^2}\right)\left(\left|\frac{\sigma_X}{X}\right|+\left|\frac{\sigma_Y}{Y}\right|+\left|\frac{\sigma_Q}{Q}\right|\right)\right|}{f_n}.$$

The uncertainty in f, the measurement frequency is quoted as 10^{-3} Hz in the manual for the lock-in amplifier. This is insignificant compared to the other sources of error, and so has been ignored. As can be clearly seen from Figure 2.6, the uncertainties associated with the fitting technique increase rapidly as the measurement frequency diverges from the resonant frequency. The data presented here was taken under optimal conditions, in a steady applied magnetic field. The sample mass was small, so environmental noise was reduced. The ambient temperature was stable during data collection, the DC field coils having been left powered for a number of hours before the measurement took place.

2.4 Summary

The available literature concerning the development and evaluation of various AGFMs shows many varied attempts, the first being Zijlstra [3]. Many more followed, refining and adapting that which had gone before. Amongst these, of note is the design of Richter *et al.*, [8], who achieved an optimum magnetic moment resolution of 10^{-14} JT^{-1}, although only when measuring micron sized particles. Richter *et al.*, and most before, used piezoelectric detection elements, but Gibson *et al.*, [11] used optical interferometry to achieve a comparable resolution, albeit with a similar limit upon sample sizes. All of those instruments that allowed the study of macroscopic samples (Reeves [4], Frey *et al.*, [9], and the commercially available system evaluated by O'Grady *et al.*, [12]) obtained somewhat lower resolutions. A number of authors successfully demonstrated variable temperature operation, unfortunately with an accompanying loss of resolution. The limiting factor in terms of resolution of nearly all instruments reported seems to be the effects of ambient vibration on the detection elements. In view of the previous work done, and the expertise available to the author, it was decided to use piezoelectric detection for the present instrument. These also had the advantage of being readily available, and easily interfaced to a lockin

amplifier. The resonant element was chosen to be quartz, as this was readily available, and had been successfully used in many of the previous instruments, in various sizes of drawn fibre. Attention was paid to the dimensions of the resonant fibre, in order to obtain a suitable stiffness, resonant frequency, and Q factor. In order to eliminate as much as possible the environmental vibrations that have been the limiting factor in improving resolution of other instruments, attention was paid to the vibration isolation employed. Several methods were used to screen the detection mechanism from both acoustic (airborne), and structural ambient vibrations.

The DC magnetic field, and alternating field gradient were realised in a conventional manner, using an electromagnet, and opposition wound air cored coils respectively. Both of these elements were placed under automated computer control, as was the lockin amplifier used to measure the output of the piezoelectric element. A block diagram of the control equipment is given in Figure 2.2.

A thorough mathematical treatment of the mechanical vibration is presented in section 2.3 above. Due to the mechanical resonant frequency not being sufficiently stable during a sequence of measurements, it was found necessary to correct the measured signals for frequency error. This entailed measuring the resonant curves to establish the correct phase and Q factor, and applying a correction term to the measured signals. The correction term needed has been determined from the relevant equations of motion, and a treatment of the ensuing uncertainties of measurement has been given. As expected, the lowest measurement uncertainties are obtainable when the measurement frequency is the same as the mechanical resonant frequency. The application of correction factors, and associated measurement uncertainties has been routinely applied to all the measured data from the AGFM, by means of a standard measurement procedure, and analysis spreadsheets.

References

1. Flanders, P. J. and Graham Jr, C. D., *Rep. Prog. Phys.* **56** (1993) 431.
2. Chikazumi, S., *Physics of Ferromagnetism.* 2nd Edition. The International Series of Monographs on Physics, ed. Birman, J., *et al.,*. Published by; Clarendon Press, Oxford (1997)
3. Zijlstra, H., *Rev. Sci. Instrum.* **41** (1970) 1241.
4. Reeves, R., *J. Phys. E* **5** (1972) 547.
5. Roos, W., *et al.*, *Rev. Sci. Instrum.* **51** (1980) 612.
6. Schippan, R. and Hempel, K. A., *J. Appl. Phys.* **53** (1982) 7867.
7. Flanders, P. J., *J. Appl. Phys.* **63** (1988) 3940.
8. Richter, H. J., Hempel, K. A. and Pfeiffer, J., *Rev. Sci. Instrum.* **59** (1988) 1388.
9. Frey, T., Jantz, W. and Stibal, R., *J. Appl. Phys.* **64** (1988) 6002.
10. Flanders, P. J., *Rev. Sci. Instrum.* **61** (1990) 839.
11. Gibson, G. A. and Schultz, S., *J. Appl. Phys.* **69** (1991) 5880.
12. O'Grady, K., Lewis, V. G. and Dickson, D. P. E., *J. Appl. Phys* **73** (1993) 5608.
13. Wallace, J. L. and Espinoza-Faller, F. J., *Meas. Sci. Tech.* **6** (1995) 1221.
14. Zimmermann, G., *et al.*, *IEEE Trans. Mag.* **32** (1996) 416.
15. Asti, G. and Solzi, M., *IEEE Trans. Mag.* **32:**(5), (1996) 4893.
16. Asti, G. and Solzi, M., *Rev. Sci. Instrum.* **67:**(10), (1996) 3543.
17. Hill, E. W., Nazran, P. and Tailor, P., *IEEE Trans. Mag.* **32** (1996) 4899.
18. Dam, N.-E., Guldbrandsen, T. and Jacobsen, C. S., *Meas. Sci. Tech.* **4** (1993) 42.
19. Sidles, J. A., *et al.*, *Rev. Mod. Phys.* **67** (1995) 249.
20. Witek, A. and Onn, D. G., *J. Vac. Sci. Tech.* **B9** (1991) 639.
21. Spassov, L., *et al.*, *Sensors and Actuators A* **62** (1997) 484.
22. RS Components, http://www.rs.co.uk/home (Accessed on; 12 July 2001)
23. Jeffrey, A., *Mathematics for Scientists and Engineers.* 4 Edition Published by; Chapman and Hall, London (1989)

Chapter 3

AGFM performance

It was noted in chapter 2 that the AGFM consists of the following components:

1) A source of known magnetic field.
2) A controllable source of alternating field gradient.
3) A method of detecting the oscillatory force on the sample by attaching the sample to a mechanically compliant system at a mechanical resonance, thereby greatly enhancing the displacement.

In the present chapter the performance of each of these components is described in detail.

3.1 DC field homogeneity

It was found that the positioning of the magnet pole pieces had a large effect on the homogeneity of the applied field. This is shown in Figures 3.1 and 3.2.

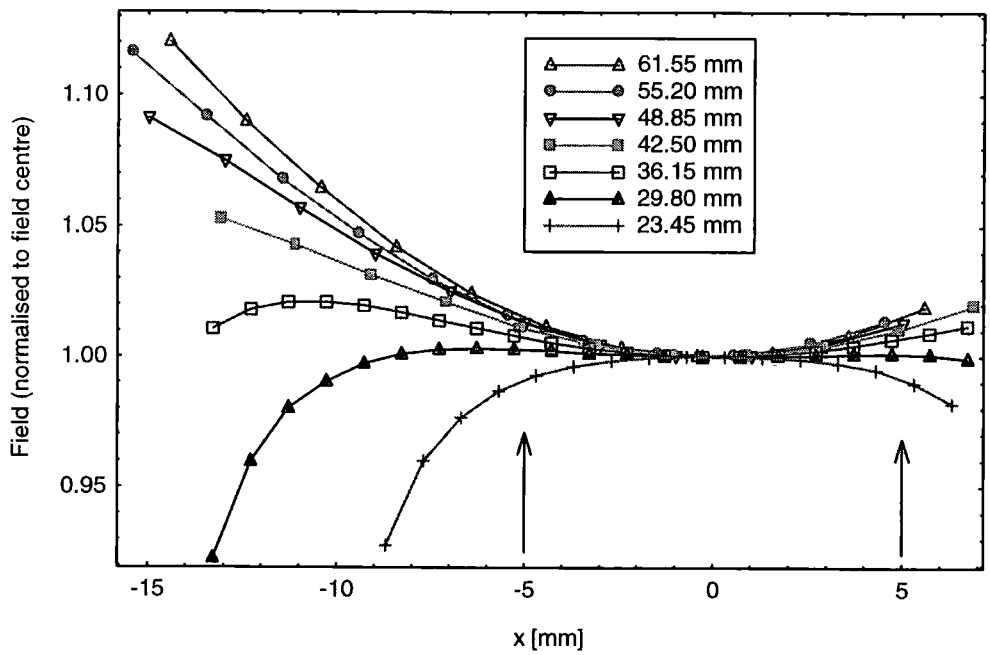

Figure 3.1. Variation in magnetic field with distance from field centre (along axis of magnet). All field plots have been normalised to 1 at the field centre.

As can be seen, the variation of field with distance on the magnet axis is at a minimum when there is a spacing of approximately 30 mm between the pole pieces. The estimated field variation at this spacing is 0.25 % over 10 mm,

increasing for spacings above and below this. Thus, a spacing of 30 mm was used for all AGFM measurements.

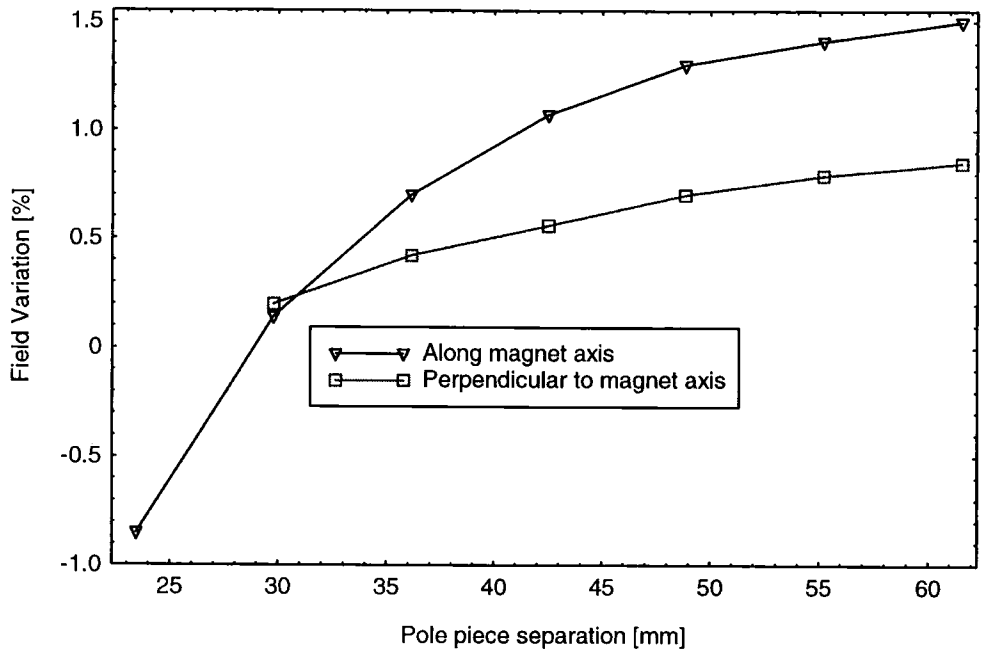

Figure 3.2. Variation in magnetic field over 10 mm, as a function of pole piece separation. All variations were measured relative to the field centre. Lines are guides to the eye.

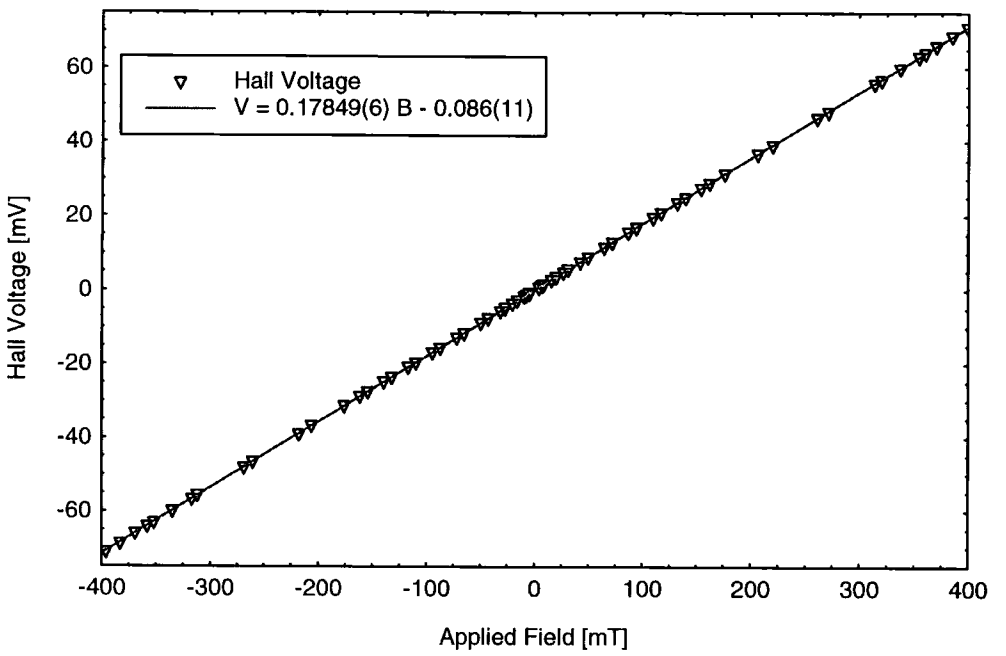

Figure 3.3. Calibration curve for Hall effect probe, field measured with a Hirst Teslameter situated at the sample position. The maximum deviation from linearity is 0.29 mV.

The off-axis variation was found to reduce as the spacing was reduced. To measure the field between the pole pieces, a small Hall device was attached to

the face of one of the gradient coils. This was calibrated using another Hall probe, placed in the centre of the field, where the sample usually sits. The relationship between the measurements was accurately linear, as shown in Figure 3.3. This was despite one Hall probe being much nearer the pole pieces than the other. The calibration constant was incorporated into a computer programme, so that Hall voltage was converted into magnetic field values without any intervention from the user.

3.2 AC gradient field homogeneity

The spacing of 30 mm between pole pieces was adequate to fit a set of thin gradient coils entirely inside, thus minimising any problems due to the complex permeability of the pole pieces. The resultant AC field is shown in Figure 3.4. This data was taken using a frequency of 82.00(1) Hz, and the gradient field was detected with a search coil consisting of a pair of 6 mm diameter coils, separated by 3 mm. The coils were connected in series-opposition (the same as the alternating gradient coils). The voltage from these coils was measured using the lock-in amplifier usually used to measure the signal from the biomorph. The coil was scanned through the sample area with the aid of a travelling microscope stage.

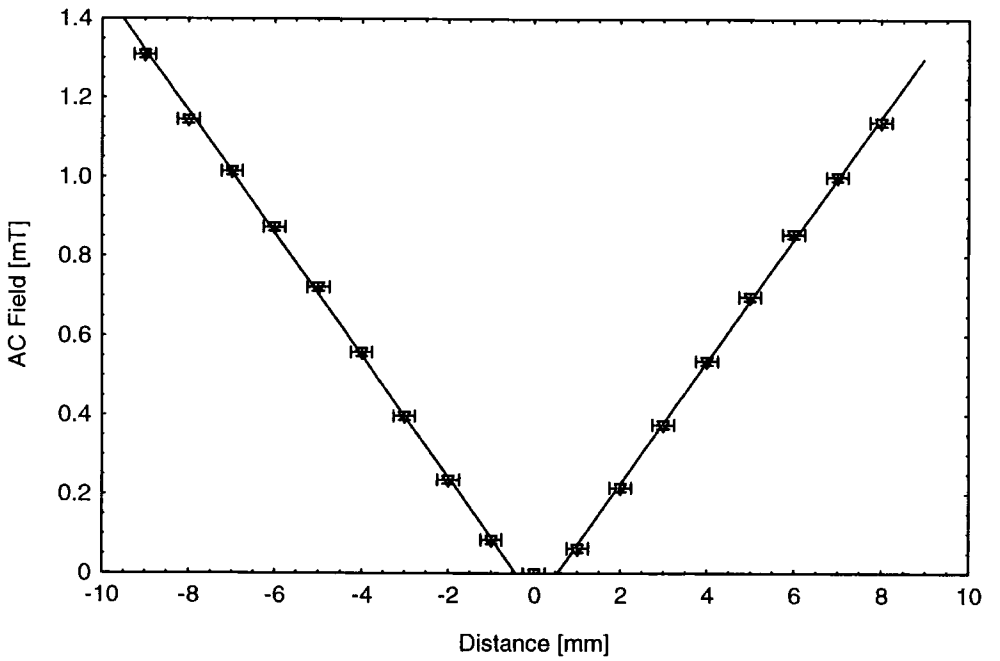

Figure 3.4 Alternating magnetic field (due to the gradient coils), as a function of on- axis distance from the field centre. The lines are straight-line fits to the data.

The AC gradient field appears to have a region of zero field around the midpoint of the coils. This is an experimental artefact, caused by the finite size of the search coils. As can be seen, the AC field is at a minimum at the field centre, and increases approximately linearly away from this. The value of the AC field gradient calculated from the data in Figure 3.4 is 0.152(2) T m^{-1}.

The response of the audio amplifier and gradient coils was investigated as a function of frequency. The results of this are shown in Figure 3.5. Neither the signal magnitude, nor the phase are constant around the frequencies of interest. The data was collected using a set of thin monitor coils; one of each attached to the inside face of the alternating gradient coils. The variation in phase of the signal is attributed to the effect of the soft iron pole pieces, and the magnitude of vibration could be also due to this, or a change in the output impedance of the audio amplifier with frequency.

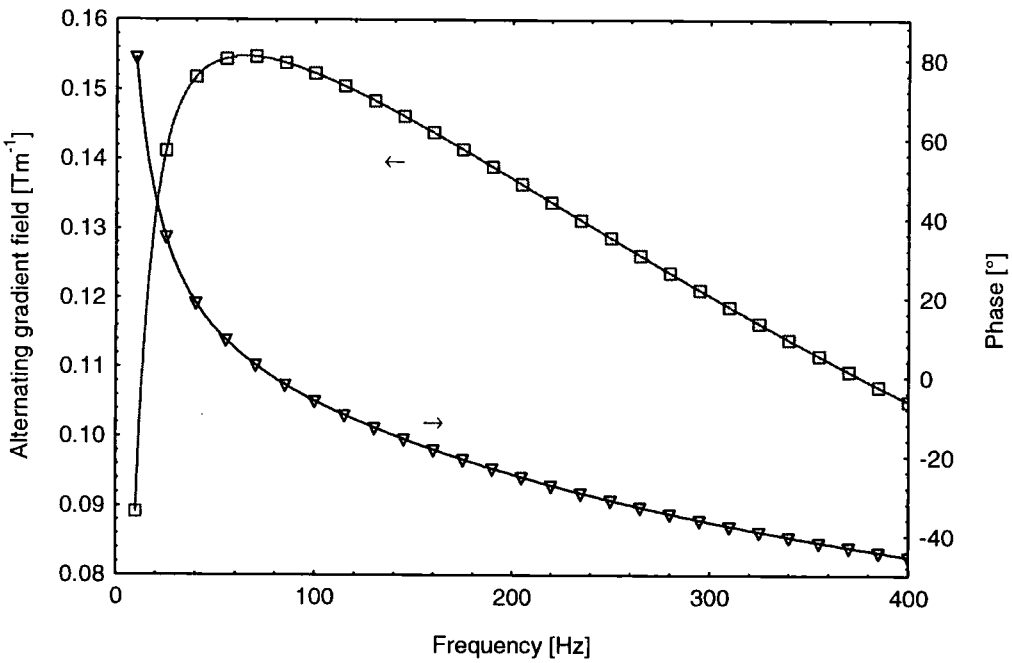

Figure 3.5. The measured amplitude and phase of the alternating gradient field at the sample position. The changes are due to the non-linearity in the audio amplifier, and the effect of the complex permittivity of the pole pieces. V_{osc} = 0.5 V.

The variable gradient means that the characteristics of different probes, having different resonant frequencies cannot be directly compared. However, the field gradient is approximately constant at the operating frequency of many of the probes constructed, 60-90 Hz. This means that a calibration of one of these probes should remain reasonably accurate for the small changes in resonant

frequency caused by samples of differing mass. The characteristics of the audio amplifier were investigated further, as shown in Figure 3.6. The output of the amplifier was connected directly to the input on the lock-in amplifier. The output voltage is accurately linear with input, however there is a small phase difference, becoming more pronounced at lower input voltages. The reason for this is unclear. The input voltage was therefore fixed at 0.5 V for all measurements.

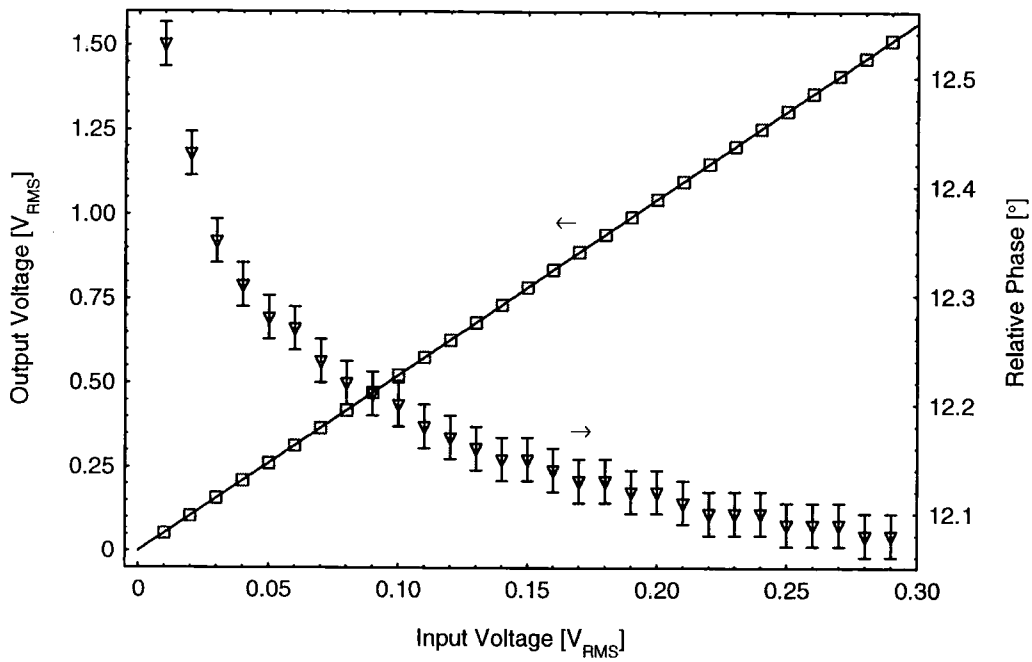

Figure 3.6. Response of the Audio amplifier to varying input signals. Frequency = 90 Hz. Measurements were taken with a lock in amplifier.

3.3 Temperature dependent effects

It was found that the resonant frequency was not stable for long periods. Typical variation in the resonant frequency over three days is shown in Figure 3.7. The resonant frequency was determined using the procedure detailed in section 2.3, with continuous adjustment of the measuring frequency. A lock-in time constant of 10 s was used, in order to reduce the noise present. The air temperature was continuously measured with a platinum resistance thermometer. The frequency variation is attributed to variations in ambient temperature, and a good correlation was observed, modelled by;

$$f = 96.564(77) - 0.0134(77) \text{ x } T.$$

A more obvious change in resonant frequency was observed when the probe was subjected to a larger temperature change, as shown in Figure 3.8.

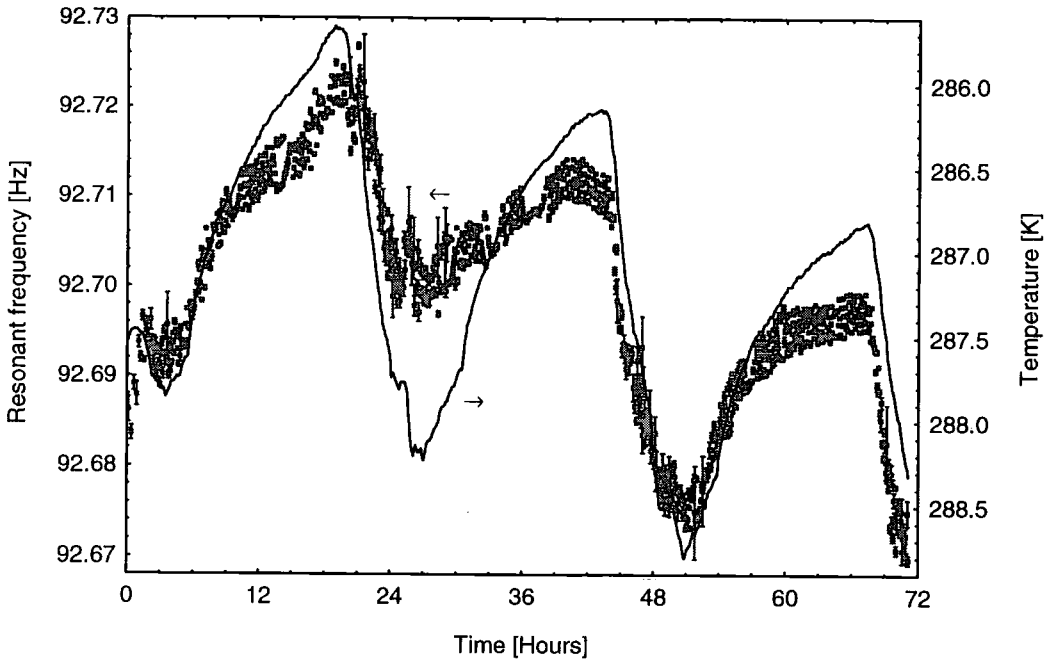

Figure 3.7. Long term drift in the resonant frequency, over a period of 3 days. The variation in ambient temperature is also plotted (the axis has been inverted).

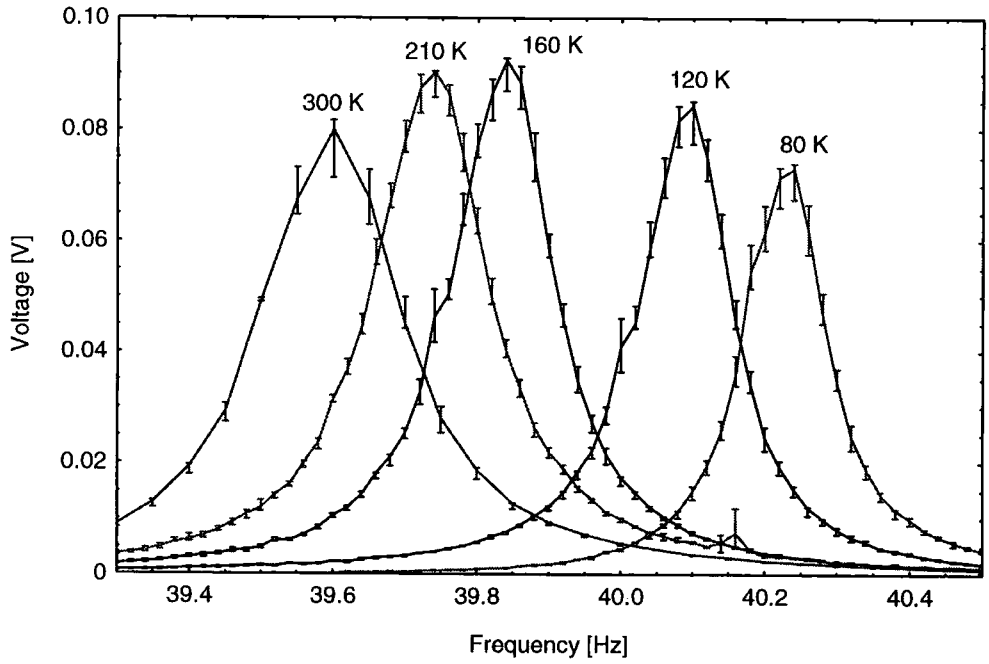

Figure 3.8. Variation of the in-phase resonant peak with changes in temperature for the cryostat system.

Only the in-phase components are plotted, as the variation was large. Several of the resonant peaks showed signs of a double resonance, at slightly different

frequencies. The AGFM was modified to fit inside a nitrogen continuous flow cryostat, mounted between the pole pieces of an iron-cored electromagnet. The temperature was monitored with a miniature platinum resistance thermometer, mounted on a thick quartz fibre lying parallel to the sample probe. Problems were encountered with this design, due to the unacceptably large background contribution due to the stainless steel cryostat. The data in Figure 3.8 (including the out of phase signals not shown), were analysed as detailed in section 2.3, to yield accurate values for the frequency, phase and Q factor, shown in Figure 3.9. The phase was not found to vary in any systematic manner, but both the frequency and Q factor increased as the temperature dropped. The rate of change of frequency with temperature, at room temperature was -0.0016 Hz K^{-1}, much less than that found for ambient temperature variations. The relative change was 5×10^{-5} K^{-1}, which compares well to the value reported by Spassov *et al.*, [1], of 3.8×10^{-5} K^{-1}, in the range 170 K-300 K.

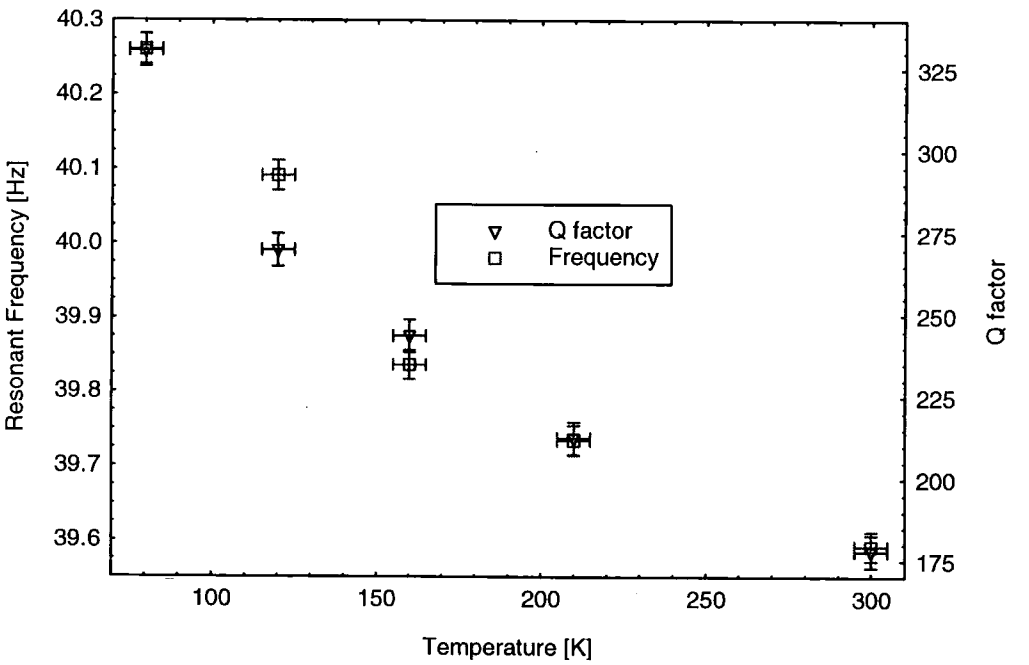

Figure 3.9 The variation of the resonant frequency and Q factor with temperature. Values have been derived from fits to the data in figure 3.8.

The variation of Q factor with temperature is approximately –0.4 K^{-1}, which is not enough to detect from ambient temperature changes. The inaccuracy due to the instability of the Q factor is small, of the order of 0.2 % per degree.

However, it was soon found that the variation in the Q values obtained from fitting to resonant curves using the same probe and sample was sometimes a few percent. In order to test if this was a real effect, two resonance scans were taken one after the other with no sample attached, in a small field. The first scan was taken in the conventional order, increasing in frequency, but the second was taken decreasing in frequency. Each scan took roughly 20 minutes to acquire. The values of the Q factor, and resonant frequency obtained from these scans are reported in Table 3.1. As can be seen, there was an increase in resonant frequency between the two scans. It was assumed that this was due to temperature fluctuations, and the increase was reasonably steady throughout the period of the experiment. Therefore the first scan will be elongated in the frequency axis slightly, and the second scan compressed, due to the time it takes to complete a scan.

Scan Order	Resonant Frequency [Hz]	Q factor
Increasing frequency	87.419	265.6
Decreasing frequency	87.436	273.2

Table 3.1. Values of Q factor, and resonant frequency obtained from consecutive resonance scans.

Consequently, the Q factor obtained from the first scan should be slightly lower than the correct value, similarly the value obtained from the second scan should be slightly higher. This prediction agrees with the observations, the difference being approximately 2.8 %. The correct Q factor was estimated to be the mean value, 269.4.

There is another way to determine the Q factor, by looking at the decay of vibrations of the sample rod under freely oscillating conditions. The number of vibrations taken for the vibration amplitude to decrease by a factor e^1 (~2.718) is proportional to the Q factor. A measurement of this dependence was taken, looking at the decay when the AC field was removed, and the resurrection of the signal after the AC field was re-established. This is shown in Figure 3.10. This was performed using a different probe to the measurements in Figure 3.9, so the Q factors will be correspondingly different. The decay constants for the two fits shown in Figure 3.10, are 0.5961(18), and 0.6121(23). This combined with the resonant frequency of 40.310 Hz, give calculated Q factors of 212.4(6), and 206.9(8) respectively. The weighted mean, and combined error of these two

values is 210.0(28), which agrees well with the Q factor obtained from fitting to a resonance peak. Fitting to a frequency scan gave a Q value of 210.8.

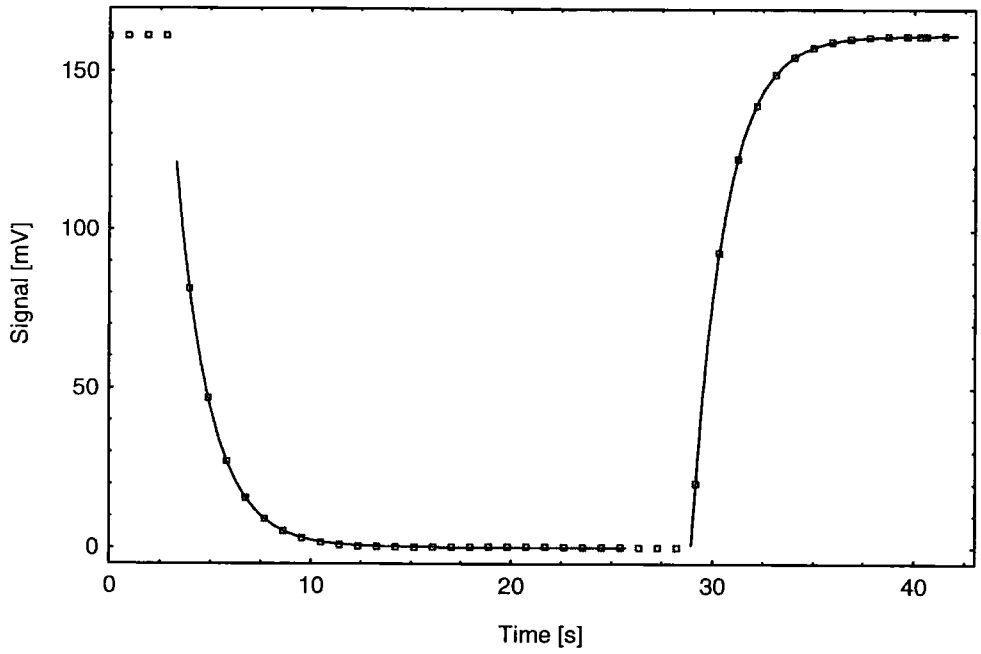

Figure 3.10. Decay of probe vibrations after the AC field is removed, and later re-established. Lines are exponential fits to the data. The data was taken on a resonance peak of 40.310 Hz, using a time constant of 50 ms on the lock-in amplifier.

3.4 Sample mass dependent effects

In order to investigate the effect of changing the sample mass on the resonant properties, the susceptibility of various sized pieces of palladium were measured. Palladium is a paramagnet, with a mass susceptibility of 6.8 x 10^{-8} m^3 kg^{-1} at 298 K [2]. This enabled the mass of the palladium samples to be established from magnetisation measurements, and the resonant properties were obtained from fits to resonant curves. The only parameter that showed any significant change was the resonant frequency, of 646(8) Hz g^{-1}, as shown in Figure 3.11. The sample masses plotted in Figure 3.11 were calculated from the observed gradient of the *m-H* curve, and the susceptibility of palladium at 298K. The masses obtained from magnetisation data agreed to within 5% with values obtained from weighing the samples. The errors in the actual sample masses might be quite significant, as there was no way of determining the mass of vacuum grease used to mount the palladium onto the probe. It is worth noting that approximately 1.8 mg of palladium is sufficient to cancel out the diamagnetic contribution to the background at room temperature. The noise

present showed a marked increase with increasing sample mass, again this is not altogether unexpected.

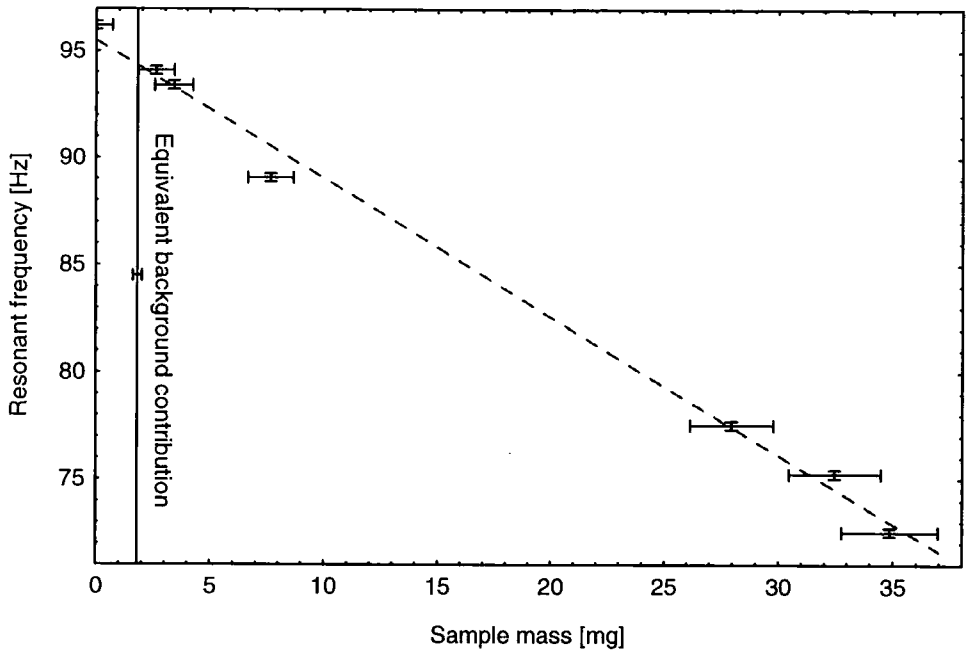

Figure 3.11. Graph showing the dependance of resonant frequency on sample mass. The dashed line is a straight line fit to the data. The vertical line marks the amount of palladium required to cancel the diamagnetic background contribution.

3.5 Applied field and sample moment dependent effects

In addition to the changes with temperature, and sample mass, marked changes in resonant frequency were observed when measuring certain high moment samples. This is demonstrated in Figure 3.12, which shows the *m-H* loop, and the change in resonant frequency for a sample of Yttrium-Iron-Garnet. Two *m-H* loops are shown, with different step sizes. The repeatability of both the data and the frequency shift is demonstrated. To investigate this effect systematically, a series of frequency scans were taken, at different applied fields (and therefore different sample moments). The sample used was a piece of 4 μm electro-deposited nickel foil, mounted so that the applied DC field was perpendicular to the plane of the foil. The resonant peaks are shown in Figure 3.13. As can clearly be seen from the data, the resonant frequency is not constant from run to run. There is a slight drift downwards, as the applied field (and therefore moment) is increased.

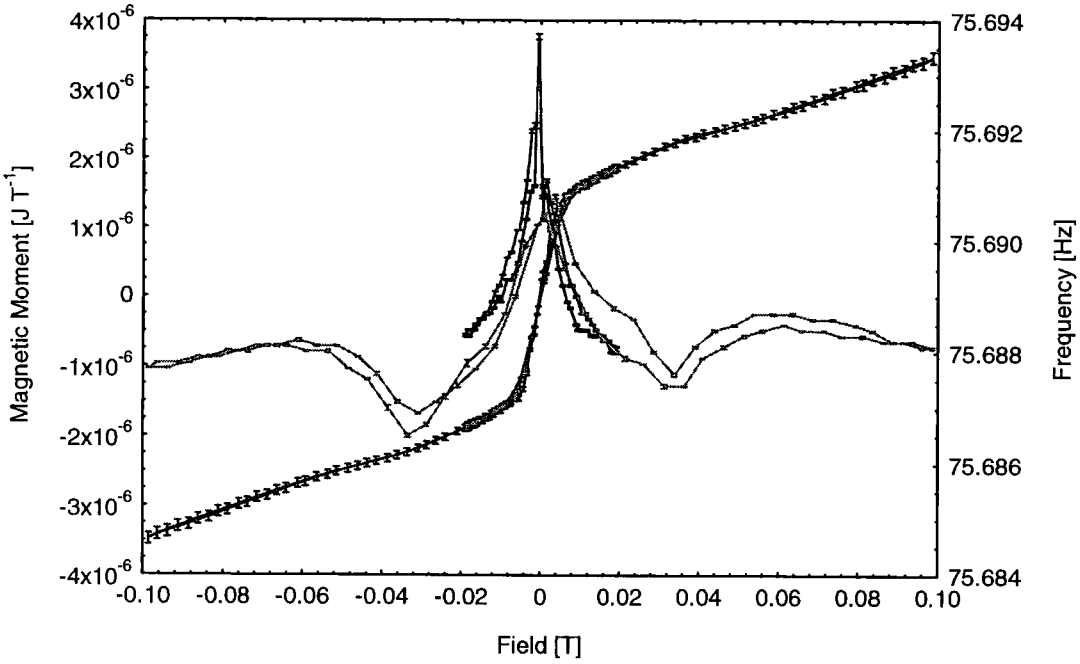

Figure 3.12. *m-H* loop for Yttrium iron garnet in low fields. Two consecutive scans are shown, with different field steps.

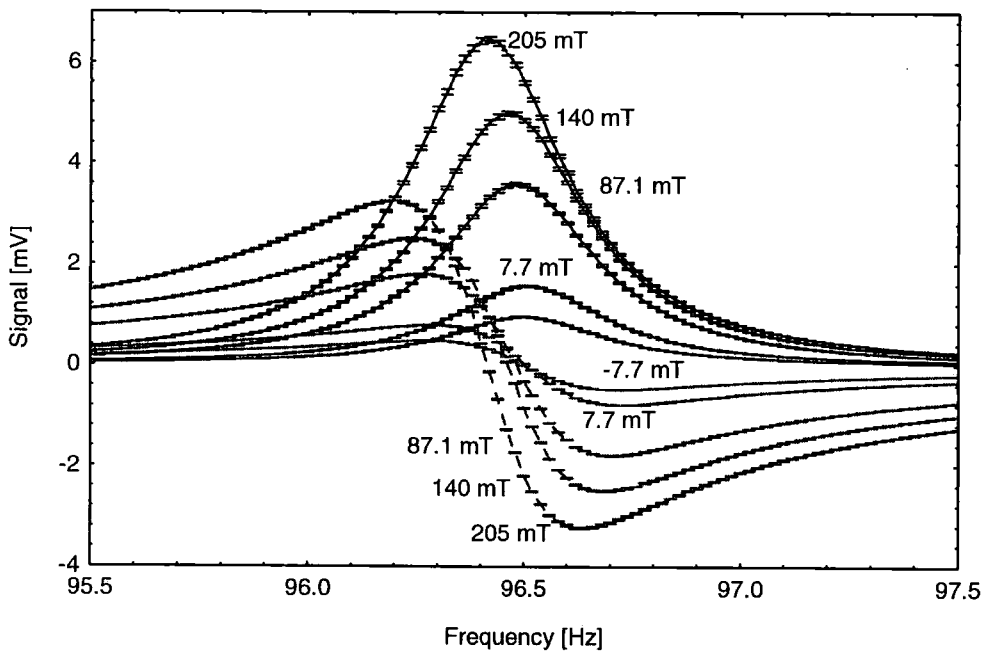

Figure 3.13. Resonant peaks for the same nickel foil sample, measured at different values of applied field. Runs were carried out consecutively, and each took approximately 25 minutes.

This effect is repeatable, and not just a result of the variation of resonant frequency with temperature (see section 3.3), as the coils heat up. Fitting of ideal resonant peaks to the data in Figure 3.13 was carried out, giving the variation in frequency, Q factor, and phase. The variations in these parameters are shown in

Figure 3.14. It is unclear whether these variations were due to the changing moment of the sample, or the applied field. The variation is approximately 0.1 %, 0.8 %, and 0.2 % for frequency, Q factor, and phase respectively. However, the effect of these variations will be different, as the signal amplitude varies linearly with a change in Q factor, whereas a small difference between the resonant frequency and the measurement frequency is enough to affect seriously the measured signal.

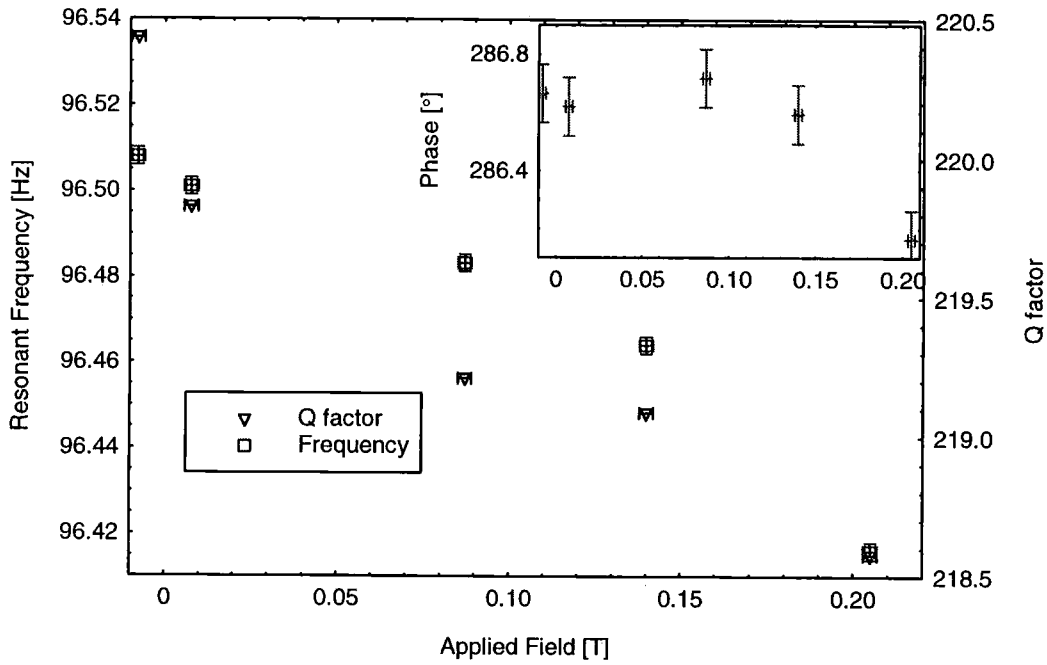

Figure 3.14. Variation of resonant frequency and Q factor (obtained from fitting to the data in Figure 3.13), with applied field. Inset; variation of Phase with applied field.

The effect of changes in resonant phase of the order observed is negligible. However, the apparent change in Q factor may not be a true representation of the properties of the system, due to the reasons outlined in section 3.3. However, it is unlikely that this effect will have masked any larger changes in Q factor in all the runs shown in Figure 3.13. It is therefore reasonably safe to assume that the true variation in Q factor is somewhat smaller than that observed. In conclusion, the only significant change in system properties with a change in field, is the change in resonant frequency. The other parameters can be assumed constant, so the signal recovery process detailed in section 2.3 can still be said to be valid. From consideration of the data in Figures 3.12 to 3.14, it is still unclear whether the resonant frequency changes with moment or applied field, or some other

unknown variable. Therefore, tests were carried out with a small wire loop mounted on the probe, in the same location as a sample would be. The coil was made from 1 turn of thin copper wire, approximately 3 mm diameter. A small current could be passed through the coil, to generate a moment independent of applied field. Data collected for a variety of currents is presented in Figures 3.15 to 3.17. The *m-H* loops for various coil currents are shown in Figure 3.15.

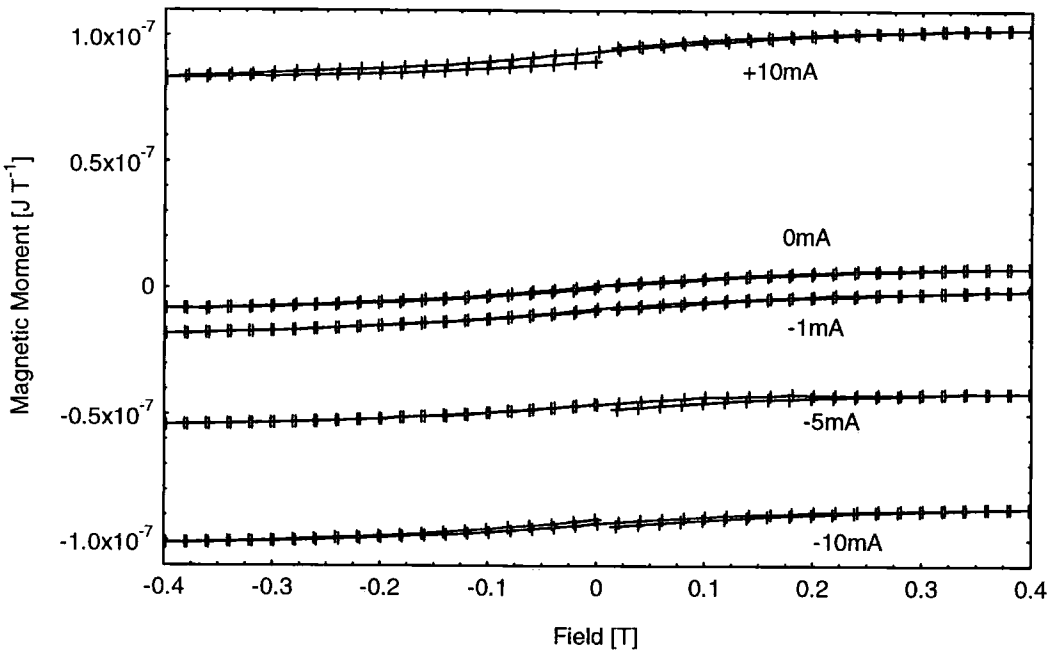

Figure 3.15. *m-H* loops for a 1 turn coil of copper wire, ~3 mm diameter, for different currents through the wire. In all cases, the background signal has been subtracted. The mass of copper wire in the loop was 0.24 mg. The error bars are smaller than the symbols in all cases.

The offsets generated by this technique are limited to fairly small values, as the current capacity of the coil wire is limited. The estimated mass of the copper coil was 0.24 mg, but it was still possible to detect ferromagnetic impurities present. The estimated impurity mass, based on easily saturated iron impurities, was ~ 30 ng. No conclusive variation of the resonant frequency was observed for any of these runs. The calculation of resonant frequencies for such small samples gives rise to large errors. A zero field measurement of the moment due to the loop was carried out, using a longer time constant for the smaller current values. This was possible as no significant amount of heat was being generated anywhere in the system. Measurements with a higher coil current had to be performed quickly though. The resultant datasets are shown in Figure 3.16.

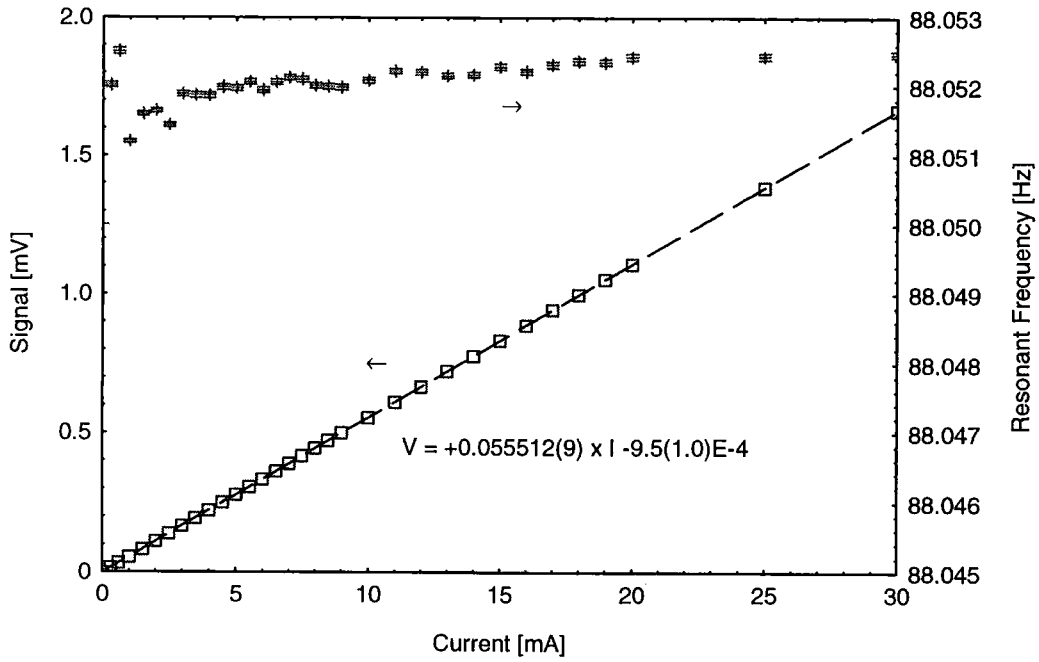

Figure 3.16. The signal due to a current in the 1 turn coil, in zero applied field. The measurement frequency was estimated to be 88.05(1) Hz. Any variations in the resonant frequency are within the instrument accuracy. The dashed line is a linear fit to the data.

As can be seen, the out of phase component stays almost at zero throughout the measurements, and so the corrected datasets are essentially the same as the in phase component. The calculated variation in the resonant frequency is smaller than the quoted frequency stability of the signal source used. The linearity of the response to a generated moment is good, with a maximum deviation of 0.25%. This is confirmed by Figure 3.17, showing all the *m-H* loops measured with the coil in place. The offsets due to the coil current have been removed. The repeatability was found to be good. The slight variation in the datasets is attributed to minute amounts of ferromagnetic dust settling onto the sample holder over the course of time. There was no measurable change found in the resonant frequency, with a change in sample moment induced by a current in a small coil. It is postulated that the changes in frequency are due to twisting of samples disrupting the resonant properties slightly, as the effect is most noticeable in anisotropic (thin in one direction) samples, and the magnitude of the effect does not depend upon the moment of the sample for samples of differing material.

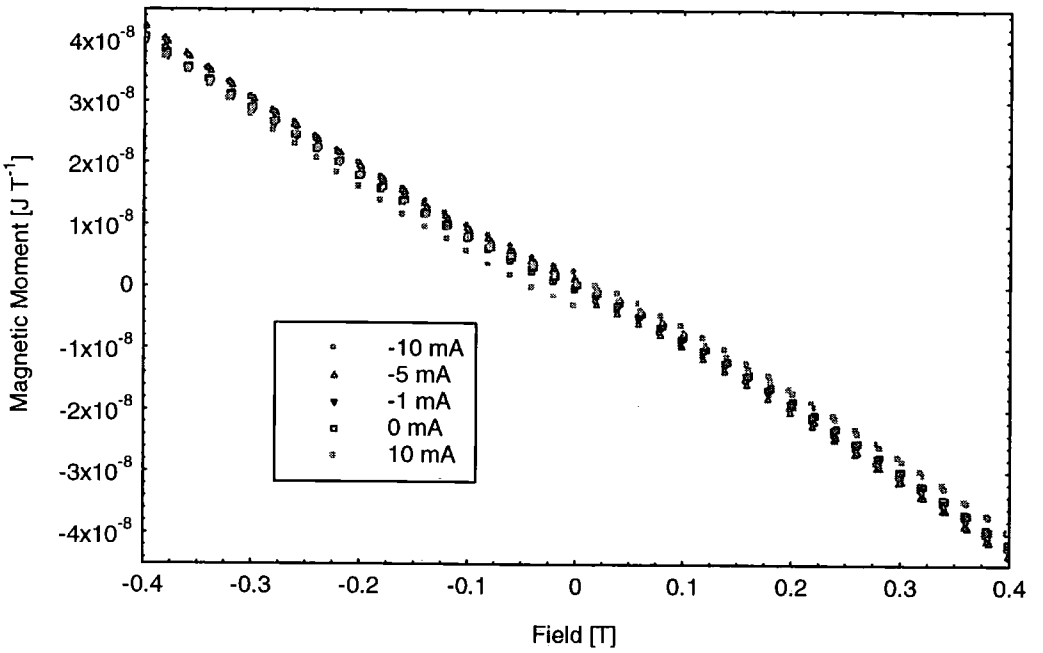

Figure 3.17. The signal due to the current loop, with any offsets due to current having been removed. The slight increase in ferromagnetic contribution is attributed to atmospheric contamination.

3.6 Calibration

In order to determine the response of the instrument, each time the quartz fibre was changed, it was necessary to re-calibrate the instrument. Since the quartz fibre probes were very fragile, they often broke when changing samples. The probes were calibrated with small pieces of polycrystalline nickel. Nickel foil is no longer used for calibration, due to suspected problems with torque, and a large shape demagnetising factor. Some success has been achieved using fine nickel powder in a grease binder. A typical calibration trace is shown in Figure 3.18. The corrected signal was re-constructed using the treatment outlined in section 2.3. The value of the saturation magnetisation of nickel was taken to be 55.37 A m^2 kg^{-1}, at 298 K, as reported by Pauthenet, and Graham [3, 4]. The variation of the saturation magnetisation with room temperature fluctuations was considered insignificant, when compared with variations due to sample purity (99 % +). Once the system had been calibrated (and assuming the probe was still intact), the nickel had to be removed. In the case of nickel powder in grease, this has to be done very thoroughly, using an ultrasonic bath. If this was not done, significant magnetic contamination resulted.

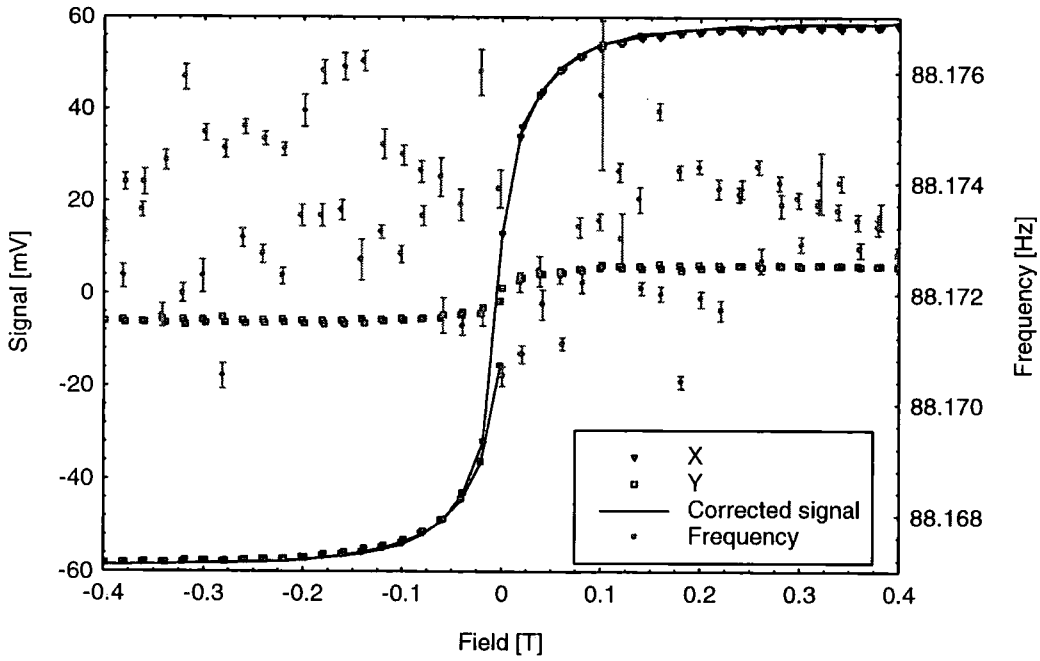

Figure 3.18. A typical calibration curve, obtained using a sample of 1.10(5) mg electro-formed nickel foil. The saturation magnetisation of the sample was taken to be 60.9(28) x 10^{-6} J T^{-1}, corresponding to a mean signal level of 58.59(10) mV, resulting in a calibration constant of 1.040(47) x 10^{-6} J T^{-1} mV^{-1}. As indicated by the non-zero out of phase signal, the measurement frequency (88.153 Hz) was set slightly away from the resonant frequency (calculated).

In order to check both the accuracy of the calibration, and the linearity of the response of the instrument, a piece of palladium with a mass of 36(1) mg was measured at room temperature. Palladium is a paramagnet, with a mass susceptibility of 6.8 x 10^{-8} m^3 kg^{-1} at 298 K [2]. The resulting curve is shown in Figure 3.19. The measured mass susceptibility was 6.6(2) x 10^{-8} m^3 kg^{-1}, which is in good agreement with the reported value. The curve shows no significant deviation from linearity, demonstrating correct instrument performance.

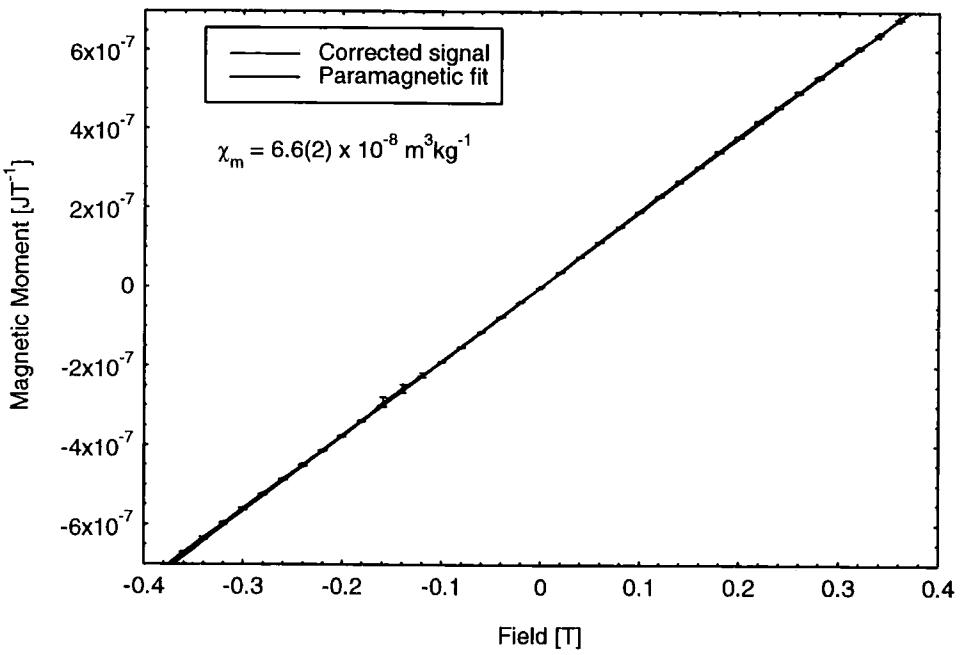

Figure 3.19. An *m-H* loop, obtained using a sample of 36(1) mg palladium. Also shown is a paramagnetic fit to the data. The curve has been corrected for background contributions.

3.7 Background signal

A background run is shown in Figure 3.20. There remained on the sample holder (a small piece of microscope cover slide), a small amount of vacuum grease, which had been used to mount a sample.

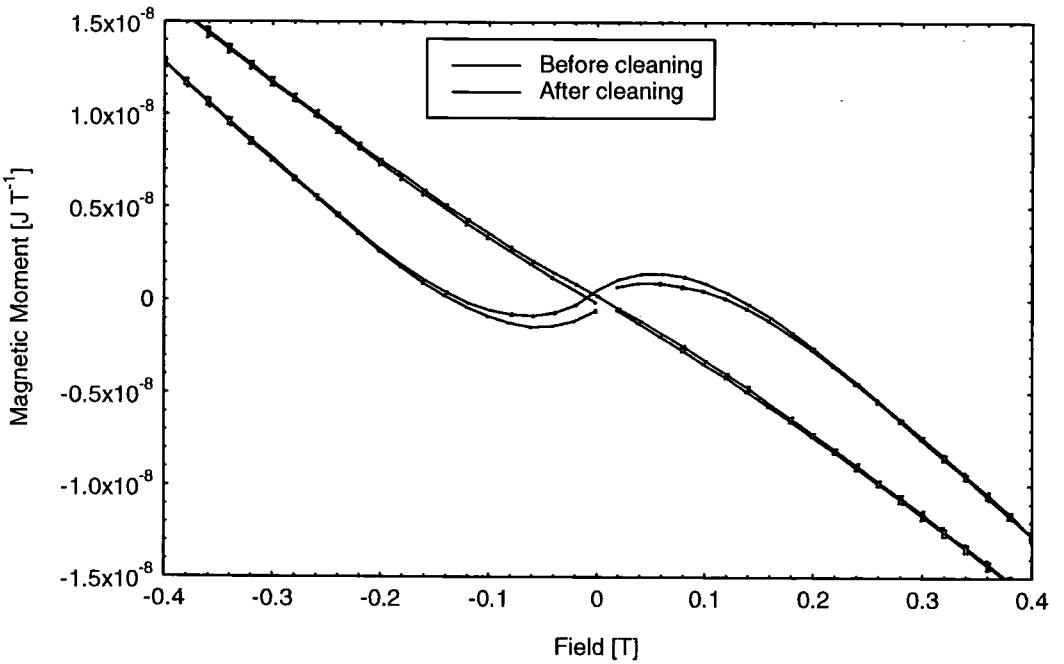

Figure 3.20. Background signal, before and after cleaning. The error bars are ~10^{-11} JT^{-1}.

As can be seen, there is some ferromagnetic contamination, probably left over from nickel used to calibrate the probe. To obtain a saturation moment such as this would require only 0.14(2) μg of nickel. The grease was then thoroughly removed by cleaning in toluene and an ultrasonic bath, and as can be seen the majority of the ferromagnetic background has been eliminated.

The accumulation of small amounts of dust onto any probe left in the AGFM for a few days had an adverse effect on the repeatability of the background measurements. Figure 3.21 shows all the background runs taken with one particular probe over a period of 3 months in between measuring various samples.

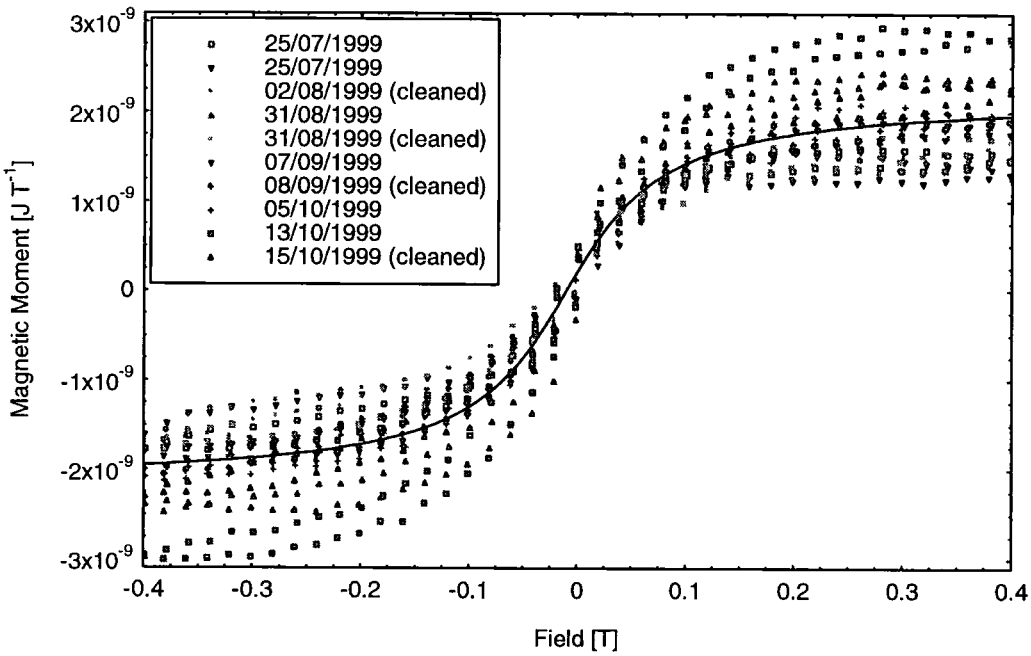

Figure 3.21. Ferromagnetic contributions to various background runs taken using the same probe. The line is an empirical fit to all the datasets.

The diamagnetic background contributions have been removed from all datasets. Since many samples that were measured had magnetic moments comparable to the background contribution, this variability introduces errors that are sometimes significant. The line plotted in Figure 3.21 is an empirical fit to all of the background datasets simultaneously. The resultant fit was used in a spreadsheet programme to subtract the background contributions from the data. It was found that the background contributions from different probes differed wildly, sometimes by up to a factor of 10, but the signal was invariably diamagnetic. A

background run from one of the better probes is shown in Figure 3.22. This does not show any noticeable ferromagnetic component, unlike most other probes.

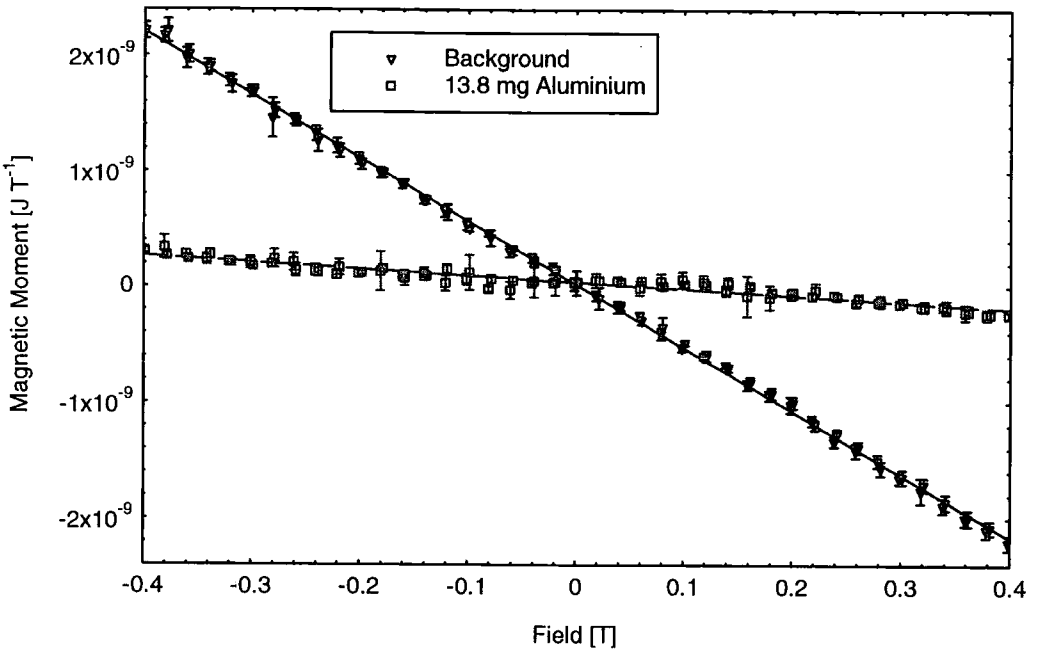

Figure 3.22. A background *m-H* loop. The lines are diamagnetic fits to the data.

An attempt was made to cancel out the measured background signal, by permanently attaching small pieces of paramagnetic material to the end of the probes. An example of a trace obtained is given in Figure 3.22, for a probe with 13.8 mg of pure aluminium wire attached. This technique had drawbacks, as the increase of mass meant a lower sample mass capacity. The addition of the aluminium changed the slope of the background from -5.473(18) x 10^{-9} J T^{-2}, to -5.71(19) x 10^{-10} J T^{-2}, an order of magnitude improvement. The error bars on both datasets were approximately 4 x 10^{-11} J T^{-1}.

3.8 Noise measurements

The noise base of the system has been measured as 1.4 x 10^{-11} JT^{-1} under optimum conditions, with no sample on the probe, and a lock-in time constant of 10 s. Under normal operation, a noise base of 4 x 10^{-11} JT^{-1} was routinely attainable, as demonstrated by the data in Figures 3.20, and 3.22.

3.9 Applications of the AGFM

3.9.1 Measurements on mercury manganese telluride

Presented here is a measurement on a sample of bulk $Hg_{(1-x)}Mn_xTe$, ($x = 0.13(1)$), intended to illustrate a typical measurement using the AGFM. Mercury manganese telluride is a spin glass at low temperatures, the dominant interaction being antiferromagnetic superexchange [5]. The sample was grown from melt, so should be homogenous. The corrected signal obtained is shown in Figure 3.23, and the frequency change calculated is shown in Figure 3.24.

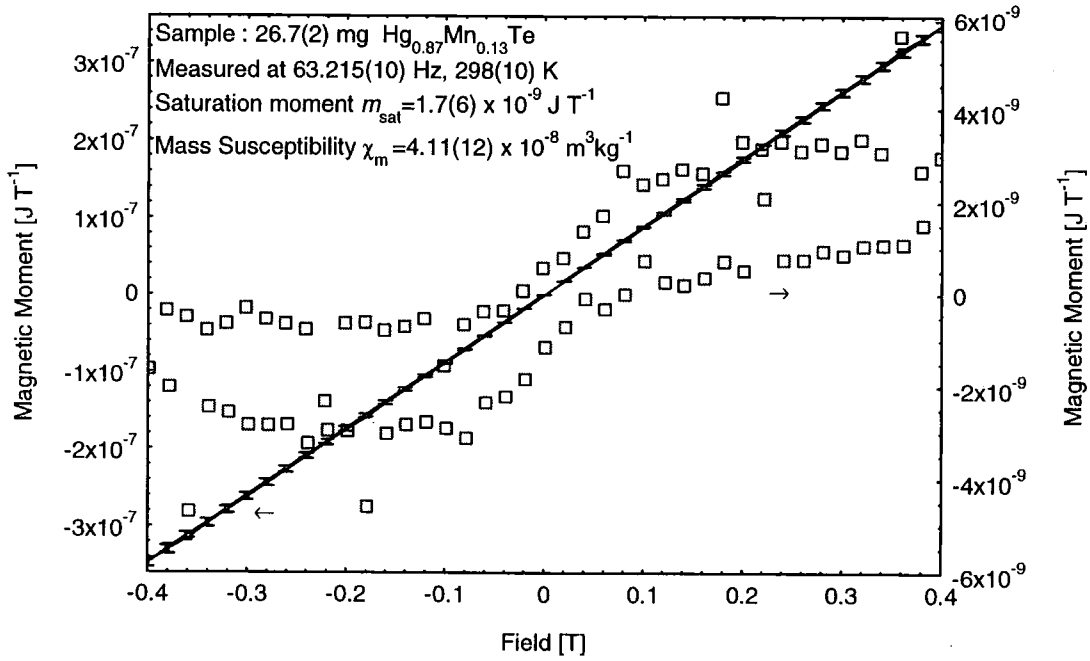

Figure 3.23. Magnetic moment of a sample of mercury manganese telluride, corrected for off resonance frequency. The extracted ferromagnetic component is plotted on the right hand axis.

The temperature in the sample space was monitored with a platinum resistance thermometer during the experiment, and a linear fit to this is shown in Figure 3.24. The agreement between the changes in temperature and resonant frequency is good, when the different thermal masses of the sample probe and thermometer are taken into account. The magnetisation curve was separated into paramagnetic (linear), and ferromagnetic components. The ferromagnetic component was a very small proportion of the total signal, comparable to the background ferromagnetic component, shown in Figure 3.21. This signal may have been due to contamination either in the sample, or sample probe.

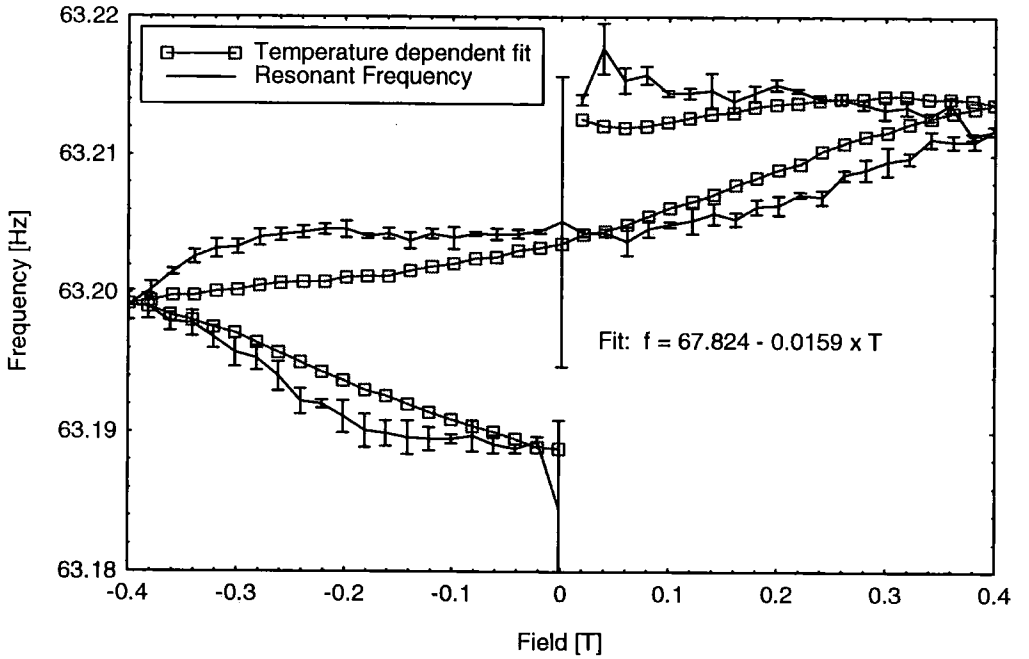

Figure 3.24. Calculated resonant frequency, while taking the readings in Figure 3.22.

An upper limit of the saturation magnetisation of 6.4(22) x 10^{-5} J T^{-1} kg^{-1} corresponds to 3.5(12) x 10^{-6} μ_B per molecule, or 2.7(10) x 10^{-5} μ_B per manganese atom assuming $x = 0.13$. Bulk manganese displays antiferromagnetic order at 298 K [6], but small clusters may display a finite net magnetisation. The mass susceptibility determined from the slope of the data in Figure 3.23, and the manganese concentration, allows a value for the effective paramagnetic moment per manganese ion (p_{eff}) can be calculated. Using the following expression for the paramagnetic susceptibility;

$$p_{eff} = \frac{1}{\mu_B}\sqrt{\frac{3\chi_m k_B (T-\theta)m}{x\mu_0}},$$

with mass per molecule m (= 5.135 x 10^{-25} kg), and the paramagnetic Curie-Weiss parameter, θ (assuming nearest neighbour interactions only) given by [5];

$$\theta = 70xJ, \qquad J = -7 \text{ K},$$

which for $x = 0.13$, gives θ = -63.7 K. This yields an effective paramagnetic moment per manganese ion of 4.7(4) μ_B, which is lower than the calculated value of 5.92 μ_B for the expected charge state (Mn^{2+}). The magnetic moment of various states of manganese can be found in Table 4.8. This low value determined from the experiment may be a consequence of clustering of some

manganese ions which are exchange coupled so that their total spin is smaller than $S = 5/2$. Such a phenomenon has been observed in the literature [5], but the effect of such clustering is usually observed at temperatures $T \approx -J$.

3.9.2 Measurements on thin film magnetic recording media

The data in Figure 3.25 is also intended to illustrate use of the AGFM to study thin films. The samples investigated were alternating layers of 4 Å cobalt, and 12 Å platinum, covered by a 50 Å platinum buffer layer, deposited on silicon by magnetron sputtering [7]. The number of bilayer repeats, n, ranged from 5 to 20.

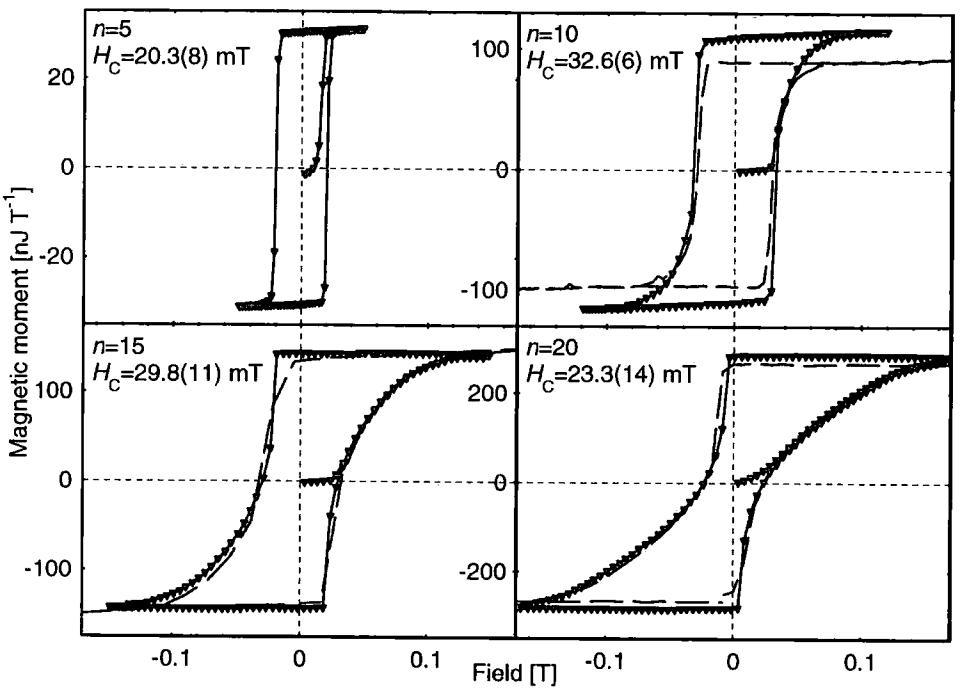

Figure 3.25. *m-H* loops for a number of Co-Pt multilayers [7], with 5, 10, 15, and 20 bilayer repeats. All of these thin film samples were measured perpendicular to the plane of the film. Coercivity values have been determined for all the samples. The dashed lines are VSM data, taken on larger samples from the same wafers. The *n=5* sample was not measured on the VSM.

These types of material are candidates for high-density magnetic and magneto-optical recording media. They exhibit perpendicular magnetic anisotropy (PMA), such that the magnetisation vector is perpendicular to the plane of the film. These materials have the potential to enable much higher areal storage density than conventional in-plane magnetic storage media. The mechanism that leads to PMA is still incompletely understood, but it has been established that it is associated with the interface between magnetic and non magnetic layers. PMA in Co/Pt multilayers is not observed for cobalt layers thicker than 8 Å. The

multilayers measured with the AGFM were also studied with a VSM, torque magnetometry to measure the anisotropy, and grazing incidence X-ray scattering (GIXS) to measure the interface roughness [7]. It was possible to calculate the effective anisotropy, K_{eff}, in two ways, from an analysis of torque magnetometry curves, and by the difference in the areas enclosed under $M - H$ loops measured in the plane and perpendicular to the plane of the samples. Values from both calculations agreed well, giving a maximum effective anisotropy of $1.1(1) \times 10^5$ Jm^{-3} at 15 bilayer repeats. This was correlated with an increase in the dimensionality of the interface roughness for larger numbers of bilayer repeats, as determined from grazing incidence X-ray scattering. The VSM measurements were performed by Amir Rotazian on large samples from the same wafers as the samples studied with the AGFM. The VSM data in Figure 3.25 have been normalised to take account of the differing sample masses. The agreement between the VSM, and AGFM data is good, any differences being ascribed to non-uniformity across the sample wafers, and the uncertainties in measuring the sample areas. GIXS allowed the correlated, and uncorrelated roughness to be determined for each film. The correlated roughness, and lateral roughness correlation lengths were 2.6(2) Å, and 64(8) Å respectively for all the films, and there was no detectable interdiffusion at the Co/Pt interfaces. The coercivity was greatest for the sample with 10 bilayers.

The *m-H* loops in Figure 3.25 look promising from the perspective of magnetic recording media. The loop squareness is good for samples with fewer bilayers, and there is no significant change in magnetisation from saturation to remenance. The coercivity is similar to that found in conventional recording media. For comparison, AGFM measurements on a piece of conventional flexible magnetic recording tape are presented in Figure 3.26. The hysteresis loop in the plane has been differentiated to obtain the switching field distribution, which shows narrow peaks centred on the coercivity (29.9(11) mT). The ratio of remenant to saturation magnetisation was 0.79, which is clearly inferior to the Co/Pt multilayers. The out of plane magnetisation plot shows the effect of the large shape anisotropy in this sample. The film areas of both the Co/Pt multilayers, and the recording tape were similar, and the larger magnetisation values of the latter reflect the greater thickness of this sample.

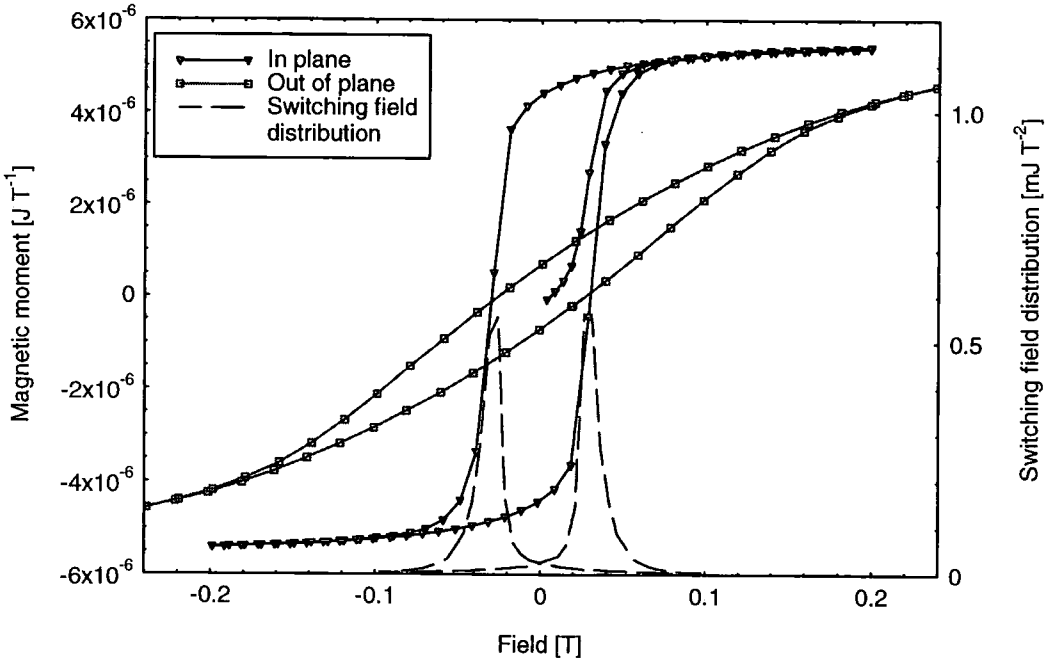

Figure 3.26. *m-H* loop for a disk of conventional magnetic recording tape, measured in the plane and perpendicular to the tape. Also shown is the switching field distribution for the in plane magnetisation.

These measurements have confirmed that the Co/Pt multilayers have a strong PMA, suitable for magnetic storage applications, that peaks at approximately 15 bilayer repeats, while loop squareness is greatest for thinner multilayers. The in-plane magnetisation data in Figure 3.26 shows excellent agreement with that in Figure 3.27, which was measured using a commercially available AGFM (Princeton Measurements Corporation model M2900). All the features of the initial magnetisation curve, hysteresys loop, and switching field distribution are faithfully reproduced. The commercial system was the subject of a paper by O'Grady *et al.*, [9], who reported a resolution of 2 x 10^{-11} J T^{-1}, and a repeatability of within 6 % for high moment samples. A fuller discussion of this instrument can be found in section 2.1.

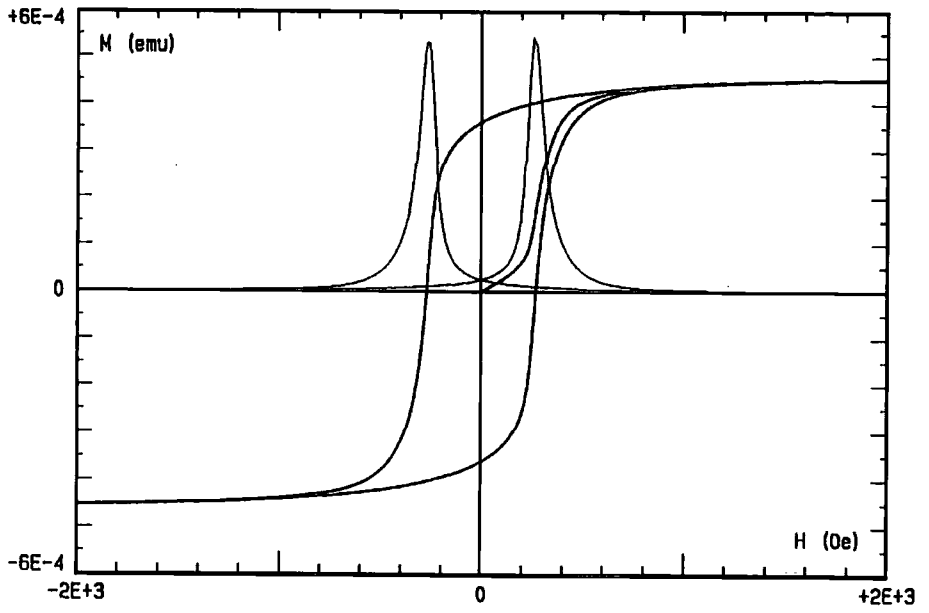

Figure 3.27. *m-H* loop for conventional magnetic recording tape, measured in the plane using a MicroMag AGFM, made by Princeton Measurements Corporation [8]. Also shown is the switching field distribution.

3.9.3 Low temperature measurements on nickel manganite

Using the AGFM as modified to enable low temperature measurements, a check was made on a sample which was also measured at low temperatures in a VSM, shown in Figure 3.28. The sample used was a mixture of nickel and manganese hydroxides that had been fired at 700 °C, as detailed in section 6.1. The sample consisted of a mixture of mainly $NiMn_2O_4$, and $NiMnO_3$ with small amounts of other oxides. Both these compounds show magnetic ordering at 77 K (see Appendix 1 for more details). Unfortunately due to the sample being a powder, it was necessary to mix a small amount with a grease binder for the AGFM measurements. Therefore the mass of material measured in the AGFM could not be accurately determined. The two curves show good agreement between the responses of the two instruments, subject to the field resolution of the VSM. The VSM data has been corrected to equalise the positive and negative coercive fields, H_C. A fuller discussion of this, and other nickel manganite low temperature magnetisation data can be found in chapter 6.

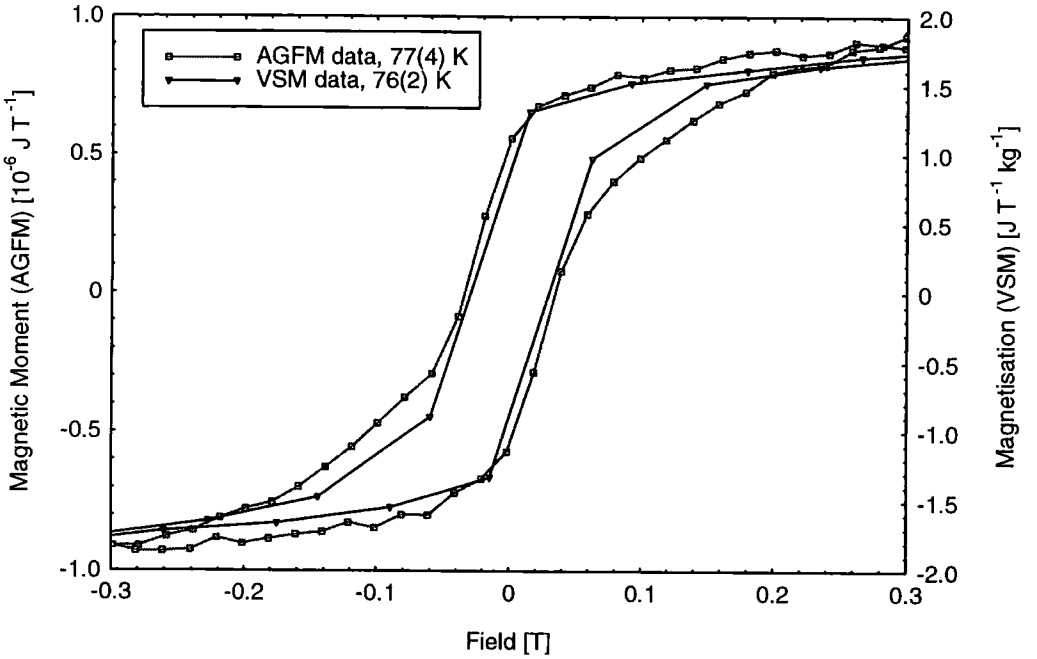

Figure 3.28. Comparison of *m-H* loops for a nickel manganite sample, measured using the AGFM, and the VSM detailed in chapter 1.

3.10 Summary

The AGFM as constructed has been thoroughly investigated, and the various influences upon the applied field, and measured magnetic moment quantified. A summary of the investigations is given in Table 3.2, which shows excellent performance in most areas.

Quantity	Performance
DC Field Homogeneity	± 0.25% within $(10mm)^3$
Hall Probe linearity	± 0.4% up to 0.4 T, relative to Hirst GM04
AC field gradient	0.152(2) Tm^{-1} at 82.00(1) Hz
Resonant frequency temperature coefficient	-0.013(8) Hz K^{-1} at 298 K
Q factor temperature coefficient	-0.4 K^{-1} at 298 K
Resonant frequency mass coefficient	646(8) Hz g^{-1}
Signal linearity with moment	± 0.25% up to 3 x 10^{-7} JT^{-1}
Typical Sensitivity	1.04(5) x 10^{-6} JT^{-1} mV^{-1}
Calibration accuracy (Estimated)	± 3%
Background signal at 0.4 T	1.6 x 10^{-8} JT^{-1} (Typical), 2 x 10^{-9} JT^{-1} (Optimum), 3 x 10^{-10} JT^{-1} (Compensated)
Noise base	4 x 10^{-11} JT^{-1} (Typical), 1.4 x 10^{-11} JT^{-1} (Optimum)

Table 3.2. Results of the characterisation of the AGFM.

For many aspects of the AGFM, the amount of absolute characterisation that could be done was limited by a lack of suitable instrumentation, such as a

calibrated Hall probe, voltmeter, or frequency counter. The values quoted in Table 3.2 are subject to the linearity and accuracy of the various instruments used, such as the lockin amplifier, and voltmeter used to measure the Hall voltage. For an absolute measurement of a low mass, high moment sample, the measurement uncertainty is expected to be dominated by the AGFM calibration uncertainty, and the variation of AC field gradient with frequency (Figure 3.5). Relative measurements (either of the same sample at different applied fields, or similar mass samples at the same field), will be unaffected by the calibration error. Increasing the mass of the sample affects the measurement as the noise base increases and the resonant frequency changes. Measurements on low moment samples will be less accurate, as the lockin amplifier will be measuring smaller voltages (16 μV for a measurement of the typical background at 0.4 T), and the variations in the background signal will become significant (Figure 3.21). The performance of the AGFM is sufficient to produce reliable data on a wide range of samples, from highly magnetic materials, to thin films, and small weakly magnetic samples.

A number of measurements on various samples of interest are detailed in section 3.9, intended to demonstrate this performance. In many cases comparisons are made with data obtained on other magnetometers, and agreement is found in all cases. A sample of bulk mercury manganese telluride was measured, and found to display paramagnetic behaviour at room temperature, as expected, but with a small ferromagnetic signal superimposed. This was ascribed to a small impurity content, possibly small clusters of elemental manganese. The effective paramagnetic moment per ion was calculated as 4.7(4) μ_B, slightly lower than the value for Mn^{2+}, possibly due to a slightly lower manganese concentration, or a varying charge state. Comparisons of several magnetic recording media were made using measurements from the AGFM under discussion, a VSM, and a commercially available AGFM. This commercially available AGFM was a Princeton Measurements Corporation Model M2900 system with a minimum resolvable moment of 2×10^{-11} JT^{-1}, comparable with the system described herein. The agreement was good between all three instruments. Evaluation of the cobalt – platinum multilayers studied revealed several promising characteristics in terms of recording media

performance, such as the remnant magnetisation not differing much from the saturation value. Low temperature operation of the AGFM was checked by comparison to data taken using a low temperature VSM on a sample from the same batch as that used in the AGFM. The shape of the curves agreed well, and demonstrated qualitatively the correct performance of the AGFM.

References

1. Spassov, L., *et al.*, *Sensors and Actuators A* **62** (1997) 484.
2. Foner, S., Doclo, R. and McNiff Jr, E. J., *J. App. Phys.* **39** (1968) 551.
3. Graham Jr, C. D., *J. Appl. Phys.* **53** (1982) 2032.
4. Pauthenet, R., *J. Appl. Phys.* **53** (1982) 2029.
5. Oseroff, S. and Keesom, P. H., *Semiconductors and Semimetals.* Vol. 25, ed. Furdyna, J.K. and Kossut, J. Published by; Academic Press, London (1988)
6. Crangle, J., *Solid State Magnetism.* Published by; Edward Arnold, London (1991)
7. Rotazian, A. S. H., *et al.*, *Submitted to J. Mag. Magn. Mat.* (2002)
8. Princeton Measurements Corporation, 31 Air Park Road, Princeton, NJ 08540, USA, prnctnmeas@msn.com, Tel. No. (609) 924-7885. *MicroMag 2900 Alternating Gradient Magnetometer*, (1st July 1998),
9. O'Grady, K., Lewis, V. G. and Dickson, D. P. E., *J. Appl. Phys* **73** (1993) 5608.

Chapter 4

Theory relating to spinel structures

There has been a great deal of interest in the spinel structure, as it is the structure taken by the ferrites, an industrially important class of materials. The ferrites were also the first compounds found to display ferrimagnetism. In the following sections some of the theory of spinels pertinent to the study of nickel manganite is discussed. In some cases, this is compared with experimental data from the literature. In section 4.2.1, a relationship between the lattice parameter, and the cation – oxygen distances is derived for cubic spinels. As far as the author is aware, this calculation is novel and cannot be found elsewhere in the published literature.

4.1 The spinel crystal structure [1]

The unit cell of the spinel structure consists of a face centred cubic (FCC) lattice of oxygen (32 atoms in the unit cell) with the cations situated in the spaces between them, as shown in Figure 4.1.

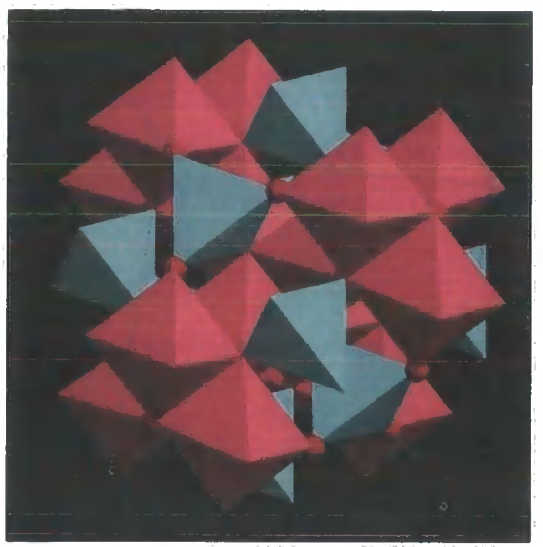

Figure 4.1. The spinel unit cell. Oxygen ions and co-ordination polyhedra are shown; oxygen ions in red, tetrahedral (A) sites in green, and octahedral (B) sites in pink. The B sites form continuous edge bonded chains through the structure.

There are two types of cation sites, octahedral, and tetrahedral. There are 64 tetrahedral sites, and 32 octahedral sites, of which 8 and 16 respectively are occupied. The local environment of the cation sites is shown in Figure 4.2. The

arrangement of the surrounding anions influences the relative energies of the cation electron orbitals. In a perfect FCC lattice, the tetrahedral sites are smaller than the octahedral sites (see section 4.2.1 for a discussion of distortion of the oxygen lattice).

(a) (b)

Figure 4.2. Arrangements of oxygen ions surrounding (a) tetrahedral, and (b) octahedral sites. The co-ordination polyhedra are shown.

In addition, compounds with anions other than oxygen can take up the spinel structure e.g. $CuTi_2S_4$, $NiLi_2F_4$. A list of the metallic ions found in oxidic spinels has been compiled by Gorter *et al.*, [2]. The lattice parameter is approximately 8.4 Å for most spinel structures. This structure can be indexed in the space group *Fd3m* [1] (no 227). For a more complete treatment, the reader is advised to consult the international tables for crystallography [3], or *Crystal Structures*, by Wyckoff [4]. The multiplicity of a general site for this space group is 192, but as all the atoms in the spinel structure are situated in positions of high symmetry, their multiplicities are much smaller. Atoms at these positions are given a notation (after Wyckoff [4]), according to their multiplicity. There are two choices of origin for this space group (1 or 2 [3]). The choice will affect the location of the special positions, and the centre of symmetry. The tetrahedral and octahedral sites are variously designated as A (Wyckoff notation 8a), and B (Wyckoff notation 16c) sites respectively, and the oxygen atoms sit on 32e sites. The co-ordinates of these are given in Table 4.1, for both choices of origin. In the present work, origin choice 2 has been adopted.

Origin Choice	1	2
A site (8a) co-ordinates	0,0,0	1/4, 1/4, 1/4
B site (16c) co-ordinates	5/8, 5/8, 5/8	1/2, 1/2, 1/2
Oxygen co-ordinates	*u*, *u*, *u*	*x*, *x*, *x*
Centre of symmetry	1/8, 1/8, 1/8	0, 0, 0

Table 4.1. Atom positions for the spinel structure, for both origin choices of space group *Fd3m*.

By using the properties of the symmetry operators, and the effect on the atomic positions, it is possible to produce a set of rules for allowed diffraction peaks/reflections. These vary for different Wyckoff positions, so that some peaks are composed of reflections from just one constituent atom, or site (A, B, or oxygen), and others have contributions from more than one. Knowledge of these allows an analysis of diffraction patterns, giving information on the positions and relative abundance's of atoms within the crystal structure, as demonstrated in chapter 6. A listing of the allowed reflections for the spinel structure is given in Appendix 1.

4.2 Atom positions in the spinel structure

There are a number of possible variations in position and abundance of atoms in the spinel structure. Some of these are confined to a small subset of compounds, (such as vacancy ordering), while others are present to varying degree in the majority of spinels studied. Study of these (usually by X-ray or neutron diffraction), gives important information on the environment of ions, which can be used to make predictions about the bonding mechanisms, magnetic interactions, electrical transport properties, etc. Those of relevance to nickel manganite are detailed below.

4.2.1 Oxygen position parameter

The oxygen has a variable atomic position in the spinel structure, deviating slightly from ideal FCC positions. The position of the oxygen ion in relation to its neighbours is shown in Figure 4.3. Study of the oxygen position allows the distances between it and the cations on the A, and B sites to be determined (with knowledge of the lattice parameter). These distances can then be compared with values obtained from other compounds with known ionic valencies, to give an indication of the likely cation distribution in nickel manganite. The symbols used for the oxygen position in the different origin choices are as adopted in the literature (see Table 4.1). The δ parameter ($\delta = x\text{-}1/4 = u\text{-}3/8$) is used here to simplify matters. The inter-ionic distances and angles, in terms of x and δ are presented in Tables 4.2, and 4.3 along with values assuming a lattice parameter of 8.395 Å, and $\delta = 0$. For most spinels, u is just over 3/8, and x just over 1/4.

The oxygen are slightly distorted away from the FCC lattice positions of (1/4, 1/4, 1/4), due to the proximity of the A sites.

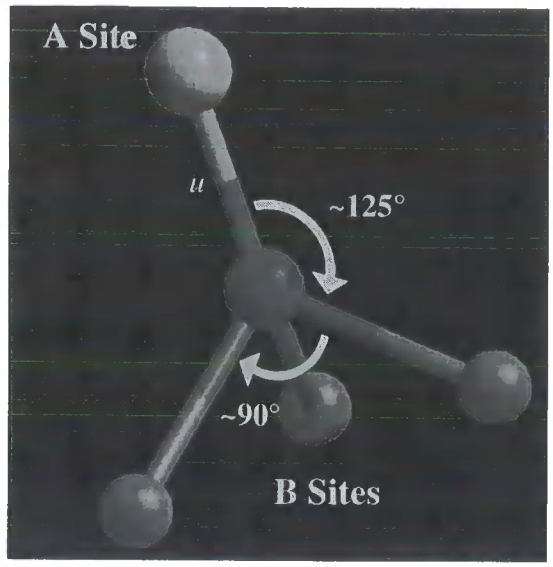

Figure 4.3. Position of the oxygen ion in a spinel.

Bond	Multiplicity	Distance as a function of x	Distance as a function of δ	Distance (fractional co-ordinates)	Distance [Å]
A - O	A:4 O:1	$\sqrt{3}\left(x-\frac{1}{8}\right)$	$\sqrt{3}\left(\delta+\frac{1}{8}\right)$	0.2165	1.818
A - O	A:12 O:3	$\sqrt{3x^2-\frac{5}{4}x+\frac{19}{64}}$	$\sqrt{3\delta^2+\frac{\delta}{4}+\frac{11}{64}}$	0.4146	3.481
B - O	B:6 O:3	$\sqrt{3x^2-2x+\frac{3}{8}}$	$\sqrt{3\delta^2-\frac{\delta}{2}+\frac{1}{16}}$	0.2500	2.099
B - O	B:2 O:2	$\sqrt{3x^2-x+\frac{1}{4}}$	$\sqrt{3\delta^2+\frac{\delta}{2}+\frac{3}{16}}$	0.4330	3.635
O - O	O:12 (split to 6 when $\delta \neq 0$)	$\sqrt{2}\left(\frac{3}{4}-2x\right)$, $\sqrt{2}\left(2x-\frac{1}{4}\right)$	$\sqrt{2}\left(\frac{1}{4}-2\delta\right)$, $\sqrt{2}\left(\frac{1}{4}+2\delta\right)$	0.3536	2.968
A - A	A:4	$\frac{\sqrt{3}}{4}$	$\frac{\sqrt{3}}{4}$	0.4330	3.635
A - B	A:12 B:6	$\frac{\sqrt{11}}{8}$	$\frac{\sqrt{11}}{8}$	0.4146	3.481
B - B	B:6	$\frac{\sqrt{2}}{4}$	$\frac{\sqrt{2}}{4}$	0.3536	2.968

Table 4.2. Lengths and multiplicities of various bonds in the spinel structure, and the effect of the oxygen parameter upon them. Values of fractional distances given assuming $x = 0.25$, and distances in Angstroms assuming a lattice parameter of 8.395 Å.

The direction of distortion is away from the A sites, in a [111] direction, making the size of the A, and B sites more nearly equal. The values of u reported in the literature vary from 0.375, to 0.392 [1]. The A-O, and B-O distances are

approximately equal for observed values of the oxygen position, x, as the cations present are of similar size.

Bonds	Angle as a function of x	Angle as a function of δ	Angle at $\delta = 0$
A-O-B	$\cos^{-1}\left(\frac{\sqrt{3}x - 1/\sqrt{3}}{\sqrt{3x^2 - 2x + 3/8}}\right)$	$\cos^{-1}\left(\frac{3\delta - 1/4}{\sqrt{3}\sqrt{3\delta^2 - \delta/2 + 1/16}}\right)$	125.26
B-O-B	$\cos^{-1}\left(\frac{3x^2 - 2x + 5/16}{3x^2 - 2x + 3/8}\right)$	$\cos^{-1}\left(1 - \frac{1}{(48\delta^2 - 8\delta + 1)}\right)$	90

Table 4.3. Angles between various bonds in the spinel structure, and the effect of the oxygen parameter upon them. Values of the angles given are for the case of $x = 0.25$.

With knowledge of the ionic radii of the various species present, expected values of the structural parameters can be calculated, using the nearest neighbour anion-cation distance equations from Table 4.2;

$$d_A = a\sqrt{3}\left(\delta + 1/8\right), \quad (4.1), \qquad d_B = a\sqrt{3\delta^2 - \delta/2 + 1/16}. \quad (4.2)$$

Where a is the lattice parameter. Solving these for a gives;

$$\sqrt{33/25\, d_B^2 - 8/25\, d_A^2} = \sqrt{3}a\left(3/20 - \delta\right) \text{ for } \delta < 0.15.$$

This can be assumed to be universally valid, as observed values of δ are of the order of 0.01. Eliminating δ gives;

$$a = \frac{40}{11\sqrt{3}} d_A + \sqrt{64/11\, d_B^2 - 512/363\, d_A^2} \quad (4.3)$$

This calculation assumes that the ions can be treated as hard spheres, with invariant radii. It is acknowledged that this is not the case in practice, and that there is some finite force-distance relationship between the two ions sharing a bond. However, the result above presents a useful starting point to account for the observed behaviour. The lattice parameter is most affected by the sum of the metal-oxygen distances. Knowing the lattice parameter, δ can be obtained from equation 4.1. It was found that δ can be expressed as a function of the ratio of the metal-oxygen distances, as expected. Values for the metal-oxygen distances can be calculated, given the assumption that ionic radii are valid parameters (i. e. the material has a close packed structure). This calculation requires knowledge of the cation distribution, and ionic radii of the species present.

4.2.2 Cation distribution in nickel manganite

The chemical formulae for normal and inverse oxide spinels respectively containing metal ions Me, and Me', are;

$$Me[Me'_2]O_4, \qquad Me'[MeMe']O_4,$$

The square brackets denoting ions on octahedral sites. Structures intermediate to these limiting cases occur, known as partially inverted spinels, with structure;

$$Me'_{\nu}Me_{1-\nu}[Me'_{2-\nu}Me_{\nu}]O_4,$$

where ν is known as the degree of inversion. For example, manganese ferrite has an inversion parameter of approximately 0.2.

For binary spinels (those containing two cations with definite charge states), the equilibrium distribution is determined by a Boltzmann expression according to Gorter [2];

$$kT \ln\left(\frac{(1-\nu)^2}{\nu(\nu-1)}\right) = E,$$

in which E is the energy involved in the interchange of a Me ion on a B site, and a Me' ion on an A site. A similar expression was used by Navrotsky *et al.*, [5] when fitting to experimental data;

$$\ln\left(\frac{\nu^2}{(1-\nu)(2-\nu)}\right) = -\frac{\Delta G^0}{RT} = \frac{\Delta S^0}{R} - \frac{\Delta H^0}{RT}.$$

The value of ΔS^0 (entropy change of cation exchange) was found to be approximately zero for all the systems studied.

The co-ordination numbers of A, and B sites are 4, and 6 respectively, so the occupation of A sites by divalent cations, and B sites by trivalent cations, will minimise the local electrostatic energy. Other configurations, such as tetravalent ions on A sites, and divalent ions on B sites have been observed. Mixed valency is also possible, where the occupation of the sites is split between two or more species, either the same atomic type with different charge, or of different atomic types. This was first suggested by Barth and Posnjak [1] in 1931, for the mineral spinel. There are several other effects to take into account when predicting the occupation of the sites in a spinel, which can be combined, and expressed as an octahedral site preference energy. Basic calculations of different configurations were carried out by Verwey *et al.*, in 1951 [6]. These calculations used only the

charges on the ions (q_1 and q_2) and the lattice parameter, a. The expression given for the difference in energy between normal and inverse configurations was;

$$\Delta V = 100.1(q_1 - q_2)^2 \frac{e^2}{a}.$$

These simple calculations did not take into account variations in u, the oxygen parameter. Figure 2 in Verwey *et al.*, [6] gives an indication of the dependence of energy difference on u. Goodenough *et al.*, [7] gave a summary of the experimental evidence available in 1955, which tentatively supported the predictions of Verwey *et al.*,. Goodenough *et al.*, also proposed that the readiness of cations to form partially covalent bonds had an influence on site preference. A preference for A sites was expected in ions with a full d shell, that have empty s, and p shells close in energy, due to hybridisation of sp^3 orbitals. This is also true for ions with a half full d shell that is spherically symmetric, such as Mn^{2+} [7]. Ions with configuration $3d^3$ and $3d^6$ were expected to favour B sites due to hybrid $d^2 sp^3$ orbitals. Similarly ions with configuration $3d^4$, $3d^8$, and $3d^9$, due to formation of coplanar dsp^2 orbitals. $3d^8$ ions (such as Ni^{2+}) would have to reverse one electron spin (and become diamagnetic), to form covalent bonds, so it was assumed that Ni^{2+} always formed ionic bonds in spinels. The same was not assumed of $3d^4$ ions (such as Mn^{3+}) which can form partially covalent square bonds (such as when involved in Jahn-Teller type distortions) without any reduction in moment.

Dunitz *et al.*, [8] calculated site preference energies of transition metal ions due to the crystal field using an ionic one electron model. The results are shown in Table 4.4, along with the predictions of Blasse [9] based upon ligand theory.

Number of 3d electrons	Ion	Calculated Octahedral site preference energy, Dunitz *et al.*, [8] [kJ mol^{-1}]	Experimental Octahedral site preference energy, Navrotsky *et al.*, [5] [kJ mol^{-1}]	Preferred Site [9]
3	Mn^{4+}	157.7	-	Octahedral
4	Mn^{3+}	95.4	60.9	No Preference
5	Mn^{2+}	0	-17.4	Tetrahedral
8	Ni^{2+}	86.2	51.9	No Preference

Table 4.4. Octahedral site preference energies for transition metal ions.

Note that the values given take no account of factors such as ionic size, oxygen parameter, electrostatic stability, etc. Navrotsky *et al.*, [5] reported values of site preference energies obtained purely from experiment, thus including all relevant

factors. The values for the various ions of nickel and manganese reported by Navrotsky *et al.*, are on the whole consistent with the predictions of Dunitz *et al.*, but not with those of Blasse. The concept of site preference energy is only strictly valid when the ions present have a definite charge state, since redox reactions between ions on different sites readily occur. This is the case with nickel and manganese, which are both found in a number of different oxidation states in spinel compounds. However, from the values given, a number of tentative predictions can be made about the cation distribution in nickel manganite. Firstly, any Mn^{2+} present is likely to be found on the A sites, and any Mn^{4+} will be on the B sites. The octahedral site preferences of Ni^{2+}, and Mn^{3+} are similar, so it is expected that these ions will co exist on the same site to some extent. There have been several different cation distributions for nickel manganite proposed in the literature, as listed below (for a fuller discussion, see section 5.3).

$Mn^{2+}_{0.65}Mn^{3+}_{0.35}[Ni^{2+}Mn^{3+}_{0.35}Mn^{4+}_{0.65}]O_4$	Larson *et al.*, [10]
$Ni^{2+}_{1-v}Mn^{3+}_{v}[Ni^{2+}_{v}Mn^{3+}_{2-v}]O_4$	Boucher *et al.*, [11-13]
$Mn^{2+}[Ni^{2+}Mn^{2+}_{0.1}Mn^{3+}_{0.9}]O_{3.95}$	Bhandage *et al.*, [14]
$Ni^{2+}_{1-v}Mn^{2+}_{v}[Ni^{2+}_{v}Mn^{3+}_{2-2v}Mn^{4+}_{v}]O_4$	Brabers [15]

It is now generally assumed the distribution given by Brabers is approximately correct, owing to the preference of Mn^{3+} for octahedral sites due to square planar covalent bond formation. There have been suggestions by several authors that there is a small amount (a few percent) of Mn^{3+} on the A sites. The value of v, the inversion parameter varies from approximately 0.7 to 0.95, depending upon thermal history. For a fuller discussion of the inversion parameter, see section 5.3.

The distribution of Brabers has 3 ions on the B sites in variable concentrations. These have differing ionic radii (see Table 4.5), Ni^{2+} being larger than Mn^{3+} or Mn^{4+}. Two adjacent Ni^{2+} ions would be expected to distort the local crystal structure, and therefore be energetically unfavourable. This leads to an effective local ordering interaction, which has been observed experimentally (see section 5.7). The absence of long range order in partially inverse structures was explained by the fact that the B sites form what is known as an anomalous lattice [16], meaning that a state with perfect nearest neighbour order still has

finite entropy. In other words, long range order does not follow from local interactions. However, long range order is found in some spinels, such as $Li_{0.5}Fe_{2.5}O_4$, where a 1:3 ordering occurs on the B sites. This is attributed to the effects of magnetic anisotropy [17].

There are several reports of ionic radii in the literature. Poix [18, 19], in 1965 looked at the spinels specifically, giving values for the metal-oxygen distances directly, which are reproduced in Table 4.5. A more general set of ionic radii were reported by Shannon [20] in 1976, this time distinguishing a separate radius for individual ions, and differing spin states. Some of these values were updated by O'Neill [21] in 1983, again specifically for spinel structures, and are also listed in Table 4.5.

Species	Tetrahedral site M-O distance [Å]	Octahedral site M-O distance [Å]	Radius in Tetrahedral site [Å]	Radius in Octahedral site [Å]
Ni^{2+}	1.970	2.088	0.705	0.83
Mn^{2+}	2.041	2.220	0.795	0.81 (0.94 High Spin)
Mn^{3+}	-	2.045	-	0.72 (0.785 High Spin)
Mn^{4+}	-	1.843	0.53	0.67
O^{2-}			1.24	1.28

Table 4.5. Selected values of metal-oxygen distances in spinels as reported by Poix [18, 19], and ionic radii as reported by Shannon [20], updated by O'Neill [21]. The ionic radii values are based upon a fluorine ionic radius of 1.14 Å.

Gillot *et al.*, [22] reported an experimental value for the $Mn^{3+}{}_A$-O distance of 1.891Å, which would enable calculations based upon the distributions reported by Larson *et al.*, [10] and Boucher *et al.*, [11, 12, 23, 13].

4.2.3 Effect on the lattice parameter

The theoretical treatment of the oxygen position parameter above allows calculations to be made of the lattice parameter of nickel manganite, using reported values of ionic radii. Taking an average of the ions present on the respective sites and assuming a high spin configuration throughout, the effective radii for the A, and B sites are;

$$r_A = 0.69 + 0.11\nu, \qquad r_B = 0.785 - 0.07\nu$$

These values were calculated using the latest radius values available, and assuming the cation distribution as reported by Brabers [15]. As a starting point for calculations, we take the value for the oxygen radius in a tetrahedral

environment (1.24 Å) as more appropriate, as the oxygen is known to distort away from the A-sites. Therefore, the cation-oxygen distances are;

$$d_A = 1.93 + 0.11\nu \qquad d_B = 2.025 - 0.035\nu$$

If these expressions are inserted into the derived formula (equation 4.3) for the lattice parameter, this then approximates (in the range $0.6 < \nu < 1$) to;

$$a \approx 8.3702 - 0.040712\nu$$

This is shown in Figure 4.4 (labelled $R_O = 1.24$ Å, High spin), along with experimental points reported in the literature (for a fuller discussion of the literature, see section 5.2). The extremal values of Meenakshisundaram [24], and all the reports that assumed an inversion parameter of 1 have been disregarded. As can be seen, there is some variation in the position and accuracy of the reported values. The gradient of the calculated line is comparable to that of the experimental points (obtained from diffraction experiments) but the predictions are consistently too small by approximately 0.06 Å.

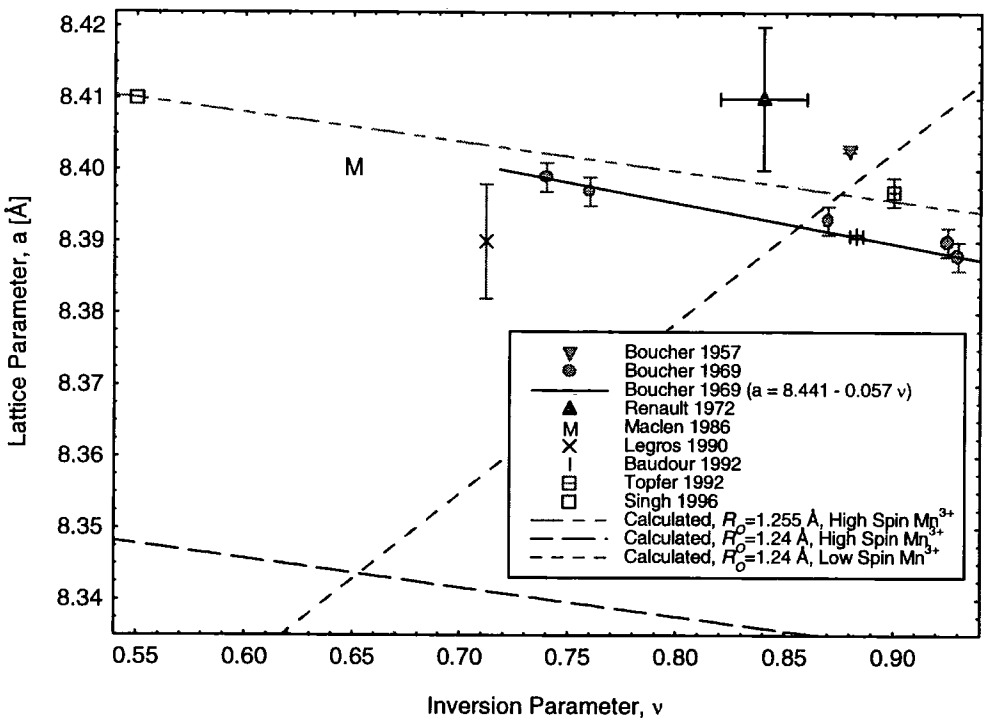

Figure 4.4. Literature values of inversion parameter and lattice parameter, and calculated relationships based upon different ionic radii. The solid line is a fit to the data of Boucher *et al.*

If the value of the oxygen radius found in an octahedral environment (1.28 Å) is used instead, then the following expression is obtained;

$$a \approx 8.5373 - 0.040616\nu$$

The modelled relationship is now approximately 0.10 Å too large and is not plotted in Figure 4.4. Assuming a value of 1.255 Å for the oxygen radius mid-way between the limiting cases of tetrahedral, and octahedral environment, gives;

$$a \approx 8.4324 - 0.040665\nu ,$$

which fits the data as well as can be expected. For comparison, if we use the low spin state values of the manganese radius, the expression becomes;

$$a \approx 8.1876 + 0.2389\nu ,$$

which is at odds with what is observed. One can therefore conclude (assuming the invariant nature of ionic radii) that the majority of the manganese on the B sites is in the high spin state.

4.2.4 Effect on the oxygen position

Using the value for the oxygen radius (1.255 Å) estimated from the calculations above, and the high spin manganese radius values, an approximation can be made (in the range $0.6 < \nu < 1$), of;

$$\delta \approx 0.00815 + 0.00824\nu , \qquad u \approx 0.38315 + 0.00824\nu .$$

This prediction is plotted in Figure 4.5 (upper line), along with reported values from the literature (for a fuller discussion of the literature, see section 5.4). All the reports that assumed an inversion parameter of 1 have been disregarded. There is quite a variation in the position and accuracy of the reported values.

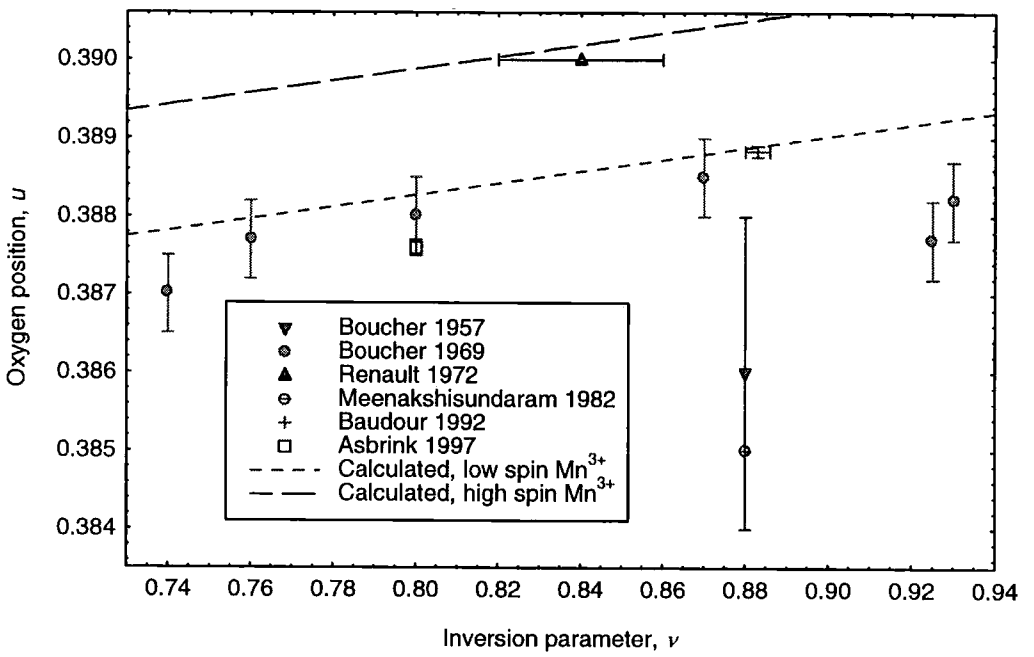

Figure 4.5. Reported values for the oxgyen position parameter, u, and inversion parameter, ν.

The values reported by Boucher *et al.*, [11] represent the only systematic study, and are therefore considered representative of any trends that might be present. As can be seen, the calculated values are consistently too high. There is good agreement with the slope of the data from Boucher *et al.*, apart from the two points with the highest inversion parameter. This suggests that the variation of the bond lengths with ν is correct, but there is a constant discrepancy in one or both. A variation in the value of the oxygen radius has the same effect on both inter-atomic distances, so varying this will not improve the agreement between the prediction and experimental results. Also plotted in Figure 4.5 is a prediction with the ions in low spin states, which fits the oxygen parameter well, but not the lattice parameter (see Figure 4.4). This shortcoming of the fixed-radius ionic model was mentioned by Poix [18], who suggested that A-O distances may be up to 5 % shorter than B-O distances for similar ions. Such an effect would explain the discrepancy between theory and experiment illustrated in Figure 4.5. An alternative explanation could be an error in the cation distribution. The presence of small amounts of manganese with a 3+ oxidation state on the A sites has been suggested by Padalia *et al.*, [25], from analysis of X-ray extended fine structure data. The formation of a Mn^{3+} ion on an A site from the oxidation of an Mn^{2+} ion, requires the reduction of a B site Mn^{4+} ion to an Mn^{3+} ion. This electron transfer results in a decrease of the average A site radius, and an increase in the average B site radius, and therefore a drop in the oxygen parameter, but little change of lattice parameter. It was expected that the amount of Mn^{3+} ions present on the A sites to be quite small, as this ion has a known preference for B sites (see section 4.2.2 for a discussion of site preference energies). Also, there is no bulk tetragonal distortion present for any value of the inversion parameter, ν. This indicates an upper limit on the amount of Mn^{3+} ions present on the B sites, as these are believed to be the cause of such distortion (see section 4.2.5). However the presence of larger amounts of A site Mn^{3+} ions at high values of inversion parameter could also explain the low values of oxygen parameter reported by Boucher *et al.*, [11]. These samples were slowly cooled to obtain high inversion parameters, so this apparent deviation could be due to impurity phases affecting the diffraction pattern. Boucher *et al.*, also reported short range

ordering on the B sites in these samples, which could also be a contributing factor.

4.2.5 The Jahn-Teller effect in $NiMn_2O_4$

Cations with a degenerate ground state (i.e. that has not been lifted by spin – orbit coupling) in an environment with cubic symmetry may have the degeneracy removed by distortion to lower symmetry [26]. Removal of the degeneracy involves lowering the ground state energy at the expense of an increase in the elastic energy of the crystal. The bonding then becomes partly covalent in nature [7, 27]. The Jahn-Teller effect is of importance for d^1 and d^6 states in tetrahedral sites, and d^4 and d^9 states in octahedral sites. Mn^{3+} ($3d^4$) on B sites often exhibits the Jahn-Teller effect; the distortion observed being an elongation of the oxygen polyhedra, as shown in Figure 4.6. If the spinel is not completely normal or inverse, or has a small amount of manganese present, the concentration of Jahn-Teller active ions is low enough so that they do not interact, and the directions of the elongated axes are distributed along random [100] directions. The result is the absence of any distortion from cubic symmetry. As the concentration is increased, the interactions between the distorted octahedra become important. It is favourable for the distortion axes of adjacent Jahn-Teller ions to align parallel with one another [28, 29] due to the minimisation of the elastic energy of the crystal [7].

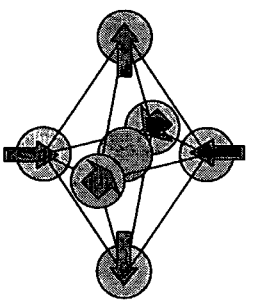

Figure 4.6. One of a number of possible distortions of an oxygen polyhedron due to the Jahn-Teller effect. The effect is exaggerated in the diagram.

The crystal will then order, and exhibit a preferred distortion direction in the bulk, leading to a distortion away from cubic symmetry to tetragonal, as detailed above. The concentration of Mn^{3+} required on the B sites for this bulk distortion has been investigated for a number of systems [30-32], and found to vary

somewhat with the differences in other ions present. The reported Mn^{3+} occupation values necessary for bulk distortion range between 55 % and 65 % of the B sites. The disordered distortions present below this value have been observed in splitting of IR absorption lines [32], and anomalously high isotropic displacement (temperature) factors derived from diffraction data [33], as predicted by Dunitz *et al.*, [28] (see section 1.5). Many systems that exhibit Jahn-Teller distortions revert to cubic symmetry at high enough temperatures, and the transitions are completed over a small temperature range. The highest occupied energy band is the square bond forming dsp^2 covalent band. With increasing distortion, the energy of this band is reduced due to increasing orbital overlap (decreased bond length). At high temperatures, some of the electrons are thermally excited from the covalent band, and the resultant bonds become partially ionic. This decreases the distortion, and in turn increases the band energy, making it easier to thermally promote an electron to a higher energy state. Thus the loosening of the square bonds from the plane perpendicular to the *c* axis is a co-operative phenomenon, explaining the sharp transition [7]. This also explains the thermal hysteresis commonly observed in the transition.
Given the lack of tetragonal distortion in nickel manganite, the lower limit on the inversion parameter is $\nu \geq 0.45$ (assuming the cation distribution of Brabers [15], along with a tetragonal distortion occurring at 55% $Mn^{3+}{}_B$ occupation). The suggested cation distribution of Boucher *et al.*, [11-13] which gives a $Mn^{3+}{}_B$ occupation of 53% to 63% for $\nu = 0.75$ to 0.95 is inconsistent with this lack of tetragonal distortion.

4.3 Magnetism in $NiMn_2O_4$ [17]

4.3.1 Magnetic interactions

The interactions between magnetic ions in spinels can be split into several types, a summary of which is given below. The resultant exchange constants between ions are generally negative (antiferromagnetic) in sign, but as the magnetic moments on the ions are generally unequal, ferrimagnetism (or some more complex arrangement) results.

Superexchange

Superexchange is generally agreed to be dominant in most spinel compounds. It is an indirect interaction between a pair of cations, the intervening anions being involved as intermediaries. In the following, it is assumed that the anion is oxygen, but the model is equally applicable to other anions. The strength of a superexchange interaction is dependent on the amount of overlap of the electron orbitals of an anion – cation pair. Generally, this will only be significant for nearest neighbour pairs. The distances involved in all other cases being too large for any appreciable overlap of electron orbitals [9]. The interactions of the anion with both cations are generally treated simultaneously. The configuration;

$$Me^{n+} - O^{2-} - Me^{n+}$$

can be treated as the ground state of the system (Me^{n+} = metal cation). The method used by Anderson [34], was to consider a second order perturbation to this, caused by excited states such as;

$$Me^{(n-1)+}\text{-}O^{1-}\text{-}Me^{n+} \quad \text{and} \quad Me^{n+}\text{-}O^{1-}\text{-}Me^{(n-1)+}, \tag{4.4}$$

where an electron hops from the oxygen ion to a cation. A mathematical formalism of this is contained in Goodenough [26], which give a resultant interaction constant J_{MO} for the metal-oxygen bond;

$$J_{MO} \propto \frac{b_{MO}^2}{U}$$

where U is the energy of an excited state (equation 4.4), and b_{MO} is a transfer integral, proportional to the orbital overlap; this must act twice to return the system to the ground state. The transfer integrals carry an electron without a change of spin, and the Pauli exclusion principle limits the population of an orbital to 2 electrons of opposite spin. Therefore, the interacting electrons must have spins antiparallel. The transfer of an electron with spin parallel to that of the receiving ion implies an excited state with much larger energy, as the electron must transfer to a higher energy state. It is the 2p orbitals of the oxygen that take part in this interaction, as they have a 'dumbbell' shaped spatial distribution, which maximises overlap with the 3d orbitals of the metal ions, as is shown in Figure 4.7. This filled 2p orbital becomes spin polarised, as the electron with suitable spin to transfer to a cation will preferentially orbit closer to that cation. Due to electrostatic repulsion, the other 2p electron will shift away. Therefore, if the two cations are sited on either side of the oxygen ion, they will experience

interactions from electrons of opposite spin. The overall interaction between the cations is therefore negative (favouring an antiparallel alignment).

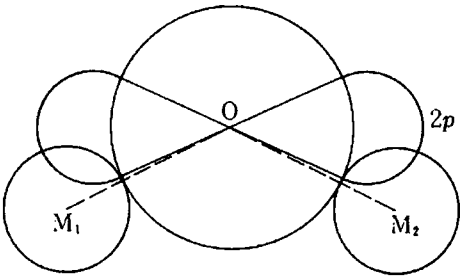

Figure 4.7. Diagram of the p orbital of an O^{2-} ion through which the superexchange interaction acts between the spins on magnetic ions M_1 and M_2. (Figure 7.5 from Chikazumi [17])

The strengths of these interactions are expected to diminish as the cation-anion-cation bond angle is reduced from 180 °, as the orbital overlap will decrease. The strength of the interaction increases with an increase in the covalent nature of the bond [26]. The sign and strength of the interaction can be estimated with knowledge of the outer electron configuration of the cations, and bond angles. This has been done by Goodenough, for 180 °, and 90 ° bonds (Table XII in [26]), reproduced in Tables 4.6, and 4.7, for some of the species present in nickel manganite. Estimated ordering temperatures range from 750 K (Strong ↑↓), to 100 K (Very Very Weak ↑↓). Blanks in Tables 4.6, and 4.7 represent negligible or variable interactions, and Mn^{III} refers to covalently bonded manganese.

A Site Ion\ B Site Ion	Mn^{4+} ($3d^3$)	Mn^{3+} ($3d^4$)	Mn^{III} ($3d^4$)	Ni^{2+} ($3d^8$)
Mn^{2+} ($3d^5$)	Mod. ↑↑	-	Mod. ↑↑	Strong ↑↓
Ni^{2+} ($3d^8$)	Mod. ↑↑	-	Mod. ↑↑	Strong ↑↓

Table 4.6. Estimated strengths of 180 ° superexchange between various ions (from Goodenough [26] Table XII). The $3d^5$-$3d^3$ (Mn^{2+}-Mn^{4+}) superexchange interaction is expected to be negative at an angle of 125 °.

Ion\ Ion	Mn^{4+} ($3d^3$)	Mn^{2+} ($3d^5$)	Ni^{2+} ($3d^8$)
Mn^{4+} ($3d^3$)	Weak ↑↓	V.V. Weak ↑↓	-
Mn^{2+} ($3d^5$)	V.V. Weak ↑↓	V. Weak ↑↓	-
Ni^{2+} ($3d^8$)	-	-	-

Table 4.7. Estimated strengths of 90 ° superexchange between various ions (from Goodenough [26] Table XII).

As expected, the strengths of 90 ° interactions are weaker than 180 ° interactions. There is evidence that anions taking part in 180 ° interactions will have enhanced negative 90 ° interactions [26]. The strengths of intermediate angle interactions

are expected to lie between the 90 °, and 180 ° values. The arrangement of cations around an anion is shown in Figure 4.3 for the spinel structure. There are two possible interactions mediated by the oxygen, A-O-B (125 °), and B-O-B (90 °). These angles will be modified slightly by any distortion of the oxygen lattice (see section 4.2.1 for details). The strength and nature of the interaction depends upon the electronic configuration of the ions present, as shown above. The A-O-B interactions are diminished by local Jahn-Teller distortions [27], particularly in the plane perpendicular to the distortion axis. From the qualitative predictions above, and assuming the cation distribution of Brabers [15], a number of predictions can be made about the properties of nickel manganite. Since the observed values of the inversion parameter are well above 0.5, the majority of the A sites will contain Mn^{2+}, and the B sites will contain equal amounts of Ni^{2+}, and Mn^{4+}, with a lesser amount of Mn^{3+}. The dominant interactions will therefore be antiferromagnetic between the A sites and B sites, as expected and observed. Assuming that the strength of these interactions is proportional to the numbers of ions involved, the strength should increase with an increase in inversion parameter. Similarly the competing ferromagnetic interaction of A sites with B site Mn^{III} should decrease in strength with increasing inversion parameter. A higher strength interaction should lead to an increase in ordering temperature as noted above. This prediction is contrary to what is observed, both by previous workers, and in the present study (Figure 6.73). Some other mechanism must then be responsible for the observed change in Curie temperature, or the predictions of Goodenough [26] must be in error for the case of nickel manganite.

Since there is a considerable difference between the 90 °, and 180 ° superexchange interactions, a change in the A-O-B angle would be expected to have a considerable effect on the Curie temperature. The oxygen position in the spinel structure is variable, depending upon the relative sizes of the ions present on the A, and B sites (for more details, see section 4.2.4). A larger oxygen parameter, u, indicates a displacement away from the A sites, and a decrease in the A-O-B angle. From the predictions in Tables 4.6, and 4.7, this implies a weaker interaction, and a lower Curie temperature. The observed dependence of T_C on u is plotted in Figure 4.8. There is considerable scatter in the datapoints,

due to the small changes in u involved, and the probable errors due to impurity phases in most of the reports. From the expressions given in Table 4.3, the angles can be calculated for the range of oxygen parameters reported. The A-O-B angle decreases by 0.72 °, from 121.19 ° to 120.47 °, and the B-O-B angle increases by 0.95 °, from 95.61 ° to 96.56 °, by increasing u from 0.387 to 0.389. These changes are considered much too small to be the cause of the observed range of Curie temperatures. Therefore there must be another mechanism by which the strength of the A-O-B is reduced, or a competing interaction that is important at high inversion parameter.

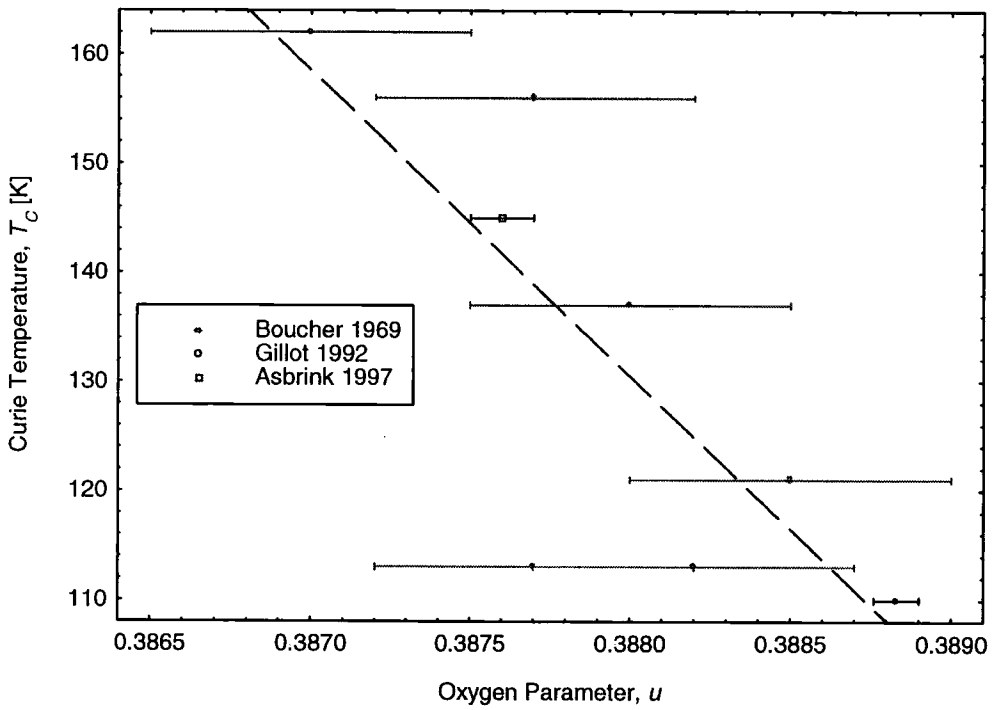

Figure 4.8. Reported values of oxygen parameter, u, and Curie temperature, T_C from the literature. The dashed line is a linear fit to the datapoints.

Direct exchange

Direct exchange is only of importance when the cations are close enough to one-another so that there is overlap of electron clouds. In the spinel structure, this is true for the B sites (~2.9 Å), but not the A sites (~3.7 Å). The proposed direct B-B interactions are the subject of several theoretical studies. The first by Anderson [16], points out that the B-sites form an anomalous lattice, such that it is possible to have perfect order due to nearest neighbour interactions, and simultaneously have a finite entropy (more than one lowest energy

configuration). This neglects any effects due to anisotropy, the mechanism to which the long-range order in certain spinels (e.g. $Li_{0.5}Fe_{2.5}O_4$) is attributed. Wickham *et al.*, [27] goes into some detail on the mechanism of the B-B interaction, suggesting that it is due to the t_{2g} orbitals of B site cations pointing towards neighbouring B sites. If the B site t_{2g} orbitals are half filled or less, then direct B-B interactions are possible. These B-B interactions are increased when Mn^{3+} is present due to the partially covalent nature of the bonding, and the resultant Jahn-Teller distortion. The interactions in the plane perpendicular to the axis of distortion are increased, while those out of the plane are decreased. Goodenough [35] generalises these direct interactions to other crystal structures, and points out that for an antiferromagnetic B-B interaction, the required electronic configuration on the B sites is $3d^m$ ($m \leq 5$). This is satisfied for Mn^{3+} ($3d^4$), and Mn^{4+} ($3d^3$) but not Ni^{2+} ($3d^8$). Therefore a high value of inversion parameter (Ni^{2+} on the B sites) would be expected to decrease the average strength of the antiferromagnetic B-B interaction. This interaction would be expected to act in opposition to the dominant A-O-B superexchange, as the latter acts to align all the moments on B sites ferromagnetically. This interaction is therefore not a candidate for causing the observed decrease in Curie temperature with increasing inversion parameter.

Double exchange

Double Exchange is due to mobile electrons in a crystal. As the electrons propagate, they interact with nearby moments, which affects their spin. In spinels, there is no conduction band as there is in a metal. Instead, conduction happens by hopping of charge carriers from one cation to an adjacent one (see section 5.3). The electrons do not change the spin orientation while they are hopping, and therefore the interaction is ferromagnetic. The range of this interaction is limited to the size of the electron hop. In spinels the hopping is primarily between B sites due to the shorter B-B distance (~2.9 Å), and is fixed range (nearest neighbour hopping). De Gennes [36] looked at the effect of double exchange (due to mobile electrons moving between sites) in crystals with existing antiferromagnetic coupling present due to another mechanism. In this

case, the theoretically most stable state at low temperature is a non-collinear moment arrangement.

At first sight, this interaction would seem to be a candidate for causing an increase in Curie temperature at low values of inversion parameter, as the hopping transport is assumed to take place via manganese on the B sites only. The resultant ferromagnetic B-B interaction would act in concert with the dominant antiferromagnetic A-O-B superexchange. However, the hopping (and therefore the exchange interaction) is a thermally activated process in nickel manganite, which becomes insignificant when samples are cooled to near the observed Curie temperatures.

4.3.2 Magnetic sublattices

It should be noted that each of the cations is connected to a number of other oxygen atoms, such that through a chain of interactions, long-range order can result. In particular, this is the reason why the A sites can be considered a distinct magnetic sublattice, despite the A-A interaction being negligible. Due to differences in the symmetry of the respective ionic environments, the A sites can be split into 2 sublattices, and the B sites into 4 sublattices. The B site sublattices are subject to trigonal fields, each along a different <111> direction. This may lead to a situation where the moments grouped on different sublattices are non-collinear.

4.3.3 Moments of ions in spinels

With knowledge of the quantum numbers L, S, and J, for an isolated ion (see section 1.3.1) it is possible to calculate the magnetic moment associated with this ion. Unfortunately, due to the environment that ions experience in crystals (the 'crystal field') L is no longer a valid quantum number. The contribution from orbital motion is reduced, or said to be quenched. This can be partial, or complete, and depends upon the symmetry of the ion position, and other factors. Wickham *et al.*, [27] mentions in a footnote (but without justification), that the quenching of orbital moment is incomplete for Mn^{2+} when situated on an A site, and Ni^{2+} when on a B site. The moments quoted are 4.6 μ_B, and 2.2 μ_B respectively. Several other authors have predicted the moments of various ions

in different sites in the spinel structure. A summary of reported and calculated values for the z component of magnetic moment is given in Table 4.8. A Jahn-Teller distortion on a particular site has been found to quench the orbital moment on that site completely [37]. Mn^{3+} on octahedral sites, and Ni^{2+} on tetrahedral sites are both Jahn-Teller active, so would be expected to have a value similar to the $L = 0$ calculated value. However the M_{SAT} value of 4.2 μ_B reported for Ni^{2+} by Mehandjiev [38] is significantly higher than the 2 μ_B expected.

Ion	Ni^{2+}	Ni^{3+}	Mn^{2+}	Mn^{3+}	Mn^{4+}
Electronic configuration	$3d^8$	$3d^7$	$3d^5$	$3d^4$	$3d^3$
L	3	3	0	2	3
S	1	1.5	2.5	2	1.5
J	4	4.5	2.5	0	1.5
Saturation Moment	5 μ_B	6 μ_B	5 μ_B	0 μ_B	0.6 μ_B
$L = 0$ Saturation Moment	2 μ_B	3 μ_B	5 μ_B	4 μ_B	3 μ_B
Wickham [27] value (Tetrahedral)	-	-	4.6 μ_B	-	-
Wickham [27] value (Octahedral)	2.2 μ_B	-	-	-	-
Mehandjiev [38] value (Tetrahedral)	4.2 μ_B	-	5.92 μ_B	-	-
Mehandjiev [38] value (Octahedral)	3.1 μ_B	-	5.92 μ_B	4.9 μ_B	3.75 μ_B
Effective Paramagnetic Moment (Table 31.4, [39])	5.59 μ_B	6.54 μ_B	5.92 μ_B	0 μ_B	0.77 μ_B
$L = 0$ Effective Paramagnetic Moment [39]	2.83 μ_B	3.87 μ_B	5.92 μ_B	4.90 μ_B	3.87 μ_B
Measured Paramagnetic Moment [39]	3.2 μ_B	-	5.9 μ_B	5.0 μ_B	4.0 μ_B

Table 4.8 Summary of reported and calculated values for the z component of magnetic moment.

The following equations were used to obtain the values calculated in Table 4.8;

$$M_{SAT} = Jg\mu_B, \qquad p_{eff} = \sqrt{J(J+1)}g\mu_B,$$

$$g = 1 + \frac{J(J+1) + S(S+1) - L(L+1)}{2J(J+1)}.$$

The values in Table 4.8, along with the cation distribution of Brabers, can be used to make predictions of the average saturation moments on the A, and B sites, assuming a collinear moment arrangement. Using the $L = 0$ value for Ni^{2+}, and the Wickham value for Mn^{2+}, the A site moment is;

$$M_A = 2 + 2.6v.$$

Similarly from the Wickham value for Ni^{2+}, and the Mehandjiev values for Mn^{3+}, and Mn^{4+}, the B site moment (per molecule) is;

$$M_B = 9.8 - 3.85v.$$

For an antiferromagnetic ordering between the A, and B sites, the total moment per molecule is;

$$M = 7.8 - 6.45v,$$

with the B site moment larger for all values of inversion parameter. This is contrary to what has been reported by Boucher *et al.*, [40], and others, with the A sites dominating at high inversion parameters, and a compensation point in the region of $v = 0.83$. Comparing the calculated values with experiment (as is done with values obtained from neutron diffraction experiments at 2 K in section 6.5.4), gives a good agreement for the A site moment, but a large discrepancy over the B site moment. A reversal of the moment of the nickel on the B sites would give;

$$M_B = 9.8 - 8.25v, \text{ and } M = 7.8 - 10.85v,$$

which means that the A sites would dominate at large values of inversion parameter, with a compensation point at $v = 0.719$. The possible mechanism that would bring about such a reversal is far from obvious, and certainly not expected from the predictions of Goodenough [26] as summarised in Table 4.6, and Table 4.7.

4.4 Summary

Nickel manganite crystallises in the spinel structure, which allows for some variation in the position of the oxygen ions. This distortion is predominantly driven by the differing ionic radii of the cation species present on the various crystallographic sites. In section 4.2.1, a new relationship between the lattice parameter, and the cation – oxygen distances has been derived. As far as the author is aware, this calculation is not to be found elsewhere in the published literature. The distribution of the cations over the various sites has been modelled with some success by the concept of site preference energies. The reported values of these site preference energies are in broad agreement with the cation distribution of Brabers [15], which is generally accepted to be approximately correct. Using the derived structural relationship from section 4.2.1, and reported experimental values for the various ionic radii present, good agreement has been found with the lattice parameters in published literature, and the present study. From the modelling process, it was concluded that the average

oxygen radius was approximately 1.255 Å, and that the majority of the Mn^{3+} on the octahedral (B) sites was in a high spin state. The reported behaviour of the oxygen position, u with changing inversion parameter, ν was also consistent with the model, and the ideas of Poix [19], that the effective oxygen radius is smaller for tetrahedral, than octahedral bonds. A small amount of Mn^{3+} ions on the tetrahedral (A) sites could explain the decrease in u at high inversion parameter values, however the possible amount is limited by the lack of a co-operative Jahn-Teller type distortion.

The magnetic behaviour is dominated by a superexchange interaction between the A, and B sites, giving ferrimagnetic ordering. The Curie temperature is lower than expected from the interaction strengths proposed by Goodenough, due to the A – O – B angle being less than 180 °, and various competing interactions between adjacent B sites. The observed trend in Curie temperature with inversion parameter was not consistent with the various interactions expected in nickel manganite. The B-B interactions vary in sign and strength, depending upon the ions present. Since there are believed to be a number of different ions present on the B sites in varying proportions, mixed interactions affecting individual ions are virtually inevitable. Following the cation distribution of Brabers [15], and using various reported values for the moments of the ions present, predictions have been made, and checked with the available published data regarding the moment arrangement in the ferrimagnetic state. The suggestion of Boucher *et al.*, [40] that the moment of the nickel on the B sites is antiparallel with that of the manganese is consistent with the published data, but not with the expected magnetic interactions.

References

1. Megaw, H. D., *Crystal Structures: A Working Approach.* 1st Edition. Studies in Physics and Chemistry. Vol. 10, ed. Stevenson, R. and Whitehead, M.A. Published by; W. B. Saunders Company, Philadelphia (1973)
2. Gorter, E. W., *Phillips Res. Rep.* **9** (1954) 295.
3. International Union of Crystallography, *International Tables for X - Ray Crystallography.* Vol. 1, ed. Henry, N.F.M. and Lonsdale, K. Published by; Kynoch Press, Birmingham (1952)
4. Wyckoff, R. W. G., *Crystal Structures.* 2nd Edition. Vol. 1-4 Published by; Wiley, New York (1962-1966)
5. Navrotsky, A. and Kleppa, O. J., *J. Inorg. Nucl. Chem.* **29** (1967) 2701.
6. Verwey, E. J. W., *et al.*, *Z. Phys. Chem.* **198** (1951) 6.
7. Goodenough, J. B. and Loeb, A. L., *Phys. Rev.* **98** (1955) 391.
8. Dunitz, J. D. and Orgel, L. E., *J. Phys. Chem. Solids* **3** (1957) 318.
9. Blasse, G., *Phillips Res. Reps.* **19:**(Supplement 3), (1964) 1.
10. Larson, E. G., Arnott, R. J. and Wickham, D. G., *J. Phys. Chem. Solids* **23** (1962) 1771.
11. Boucher, B., Buhl, R. and Perrin, M., *Acta Cryst.* **B25** (1969) 2326.
12. Boucher, B., Buhl, R. and Perrin, M., *J. Phys. Chem. Solids* **30** (1969) 2467.
13. Boucher, B., Buhl, R. and Perrin, M., *J. Phys. Chem. Solids* **31** (1970) 363.
14. Bhandage, G. T. and Keer, H. V., *J. Phys. C* **9** (1976) 1325.
15. Brabers, V. A. M., *Phys. Stat. Sol. A* **12** (1972) 629.
16. Anderson, P. W., *Phys. Rev.* **102** (1956) 1008.
17. Chikazumi, S., *Physics of Ferromagnetism.* 2nd Edition. The International Series of Monographs on Physics, ed. Birman, J., *et al.*,. Published by; Clarendon Press, Oxford (1997)
18. Poix, P., *Bull. Soc. Chim. Fr.* **5** (1965) 1085.
19. Poix, P., *C. R. Hebd. Seances Acad. Sci.* **268** (1969) 1139.
20. Shannon, R. D., *Acta. Cryst.* **A32** (1976) 751.
21. O' Neill, H. S. C. and Navrotsky, A., *American Mineralogist* **68** (1983) 181.
22. Gillot, B., *et al.*, *Solid State Ionics* **58** (1992) 155.
23. Buhl, R., *J. Phys. Chem. Solids* **30** (1969) 805.
24. Meenakshisundaram, A., *et al.*, *Phys. Stat. Sol. A* **69** (1982) K15.
25. Padalia, B. D. and Krishnan, V., *Phys. Stat. Sol. A* **25** (1974) K177.
26. Goodenough, J. B., *Magnetism and the Chemical Bond.* 1st Edition. Interscience Monographs on Chemistry. Vol. 1, ed. Cotton, A.F. Published by; Interscience Publishers, John Wiley and Sons, New York (1963)
27. Wickham, D. G. and Goodenough, J. B., *Phys. Rev.* **115** (1959) 1156.
28. Dunitz, J. D. and Orgel, L. E., *J. Phys. Chem Solids* **3** (1957) 20.
29. Novak, P., *J. Phys. Chem. Solids* **30** (1969) 2357.
30. Wickham, D. G. and Croft, J. W., *J. Phys. Chem. Solids* **7** (1958) 351.
31. Aoki, I., *J. Phys. Soc. Japan* **17** (1962) 53.
32. Brabers, V. A. M., *Phys. Stat. Sol.* **33** (1969) 563.
33. Cervinka, L., *J. Phys. Chem. Solids* **26** (1965) 1917.
34. Anderson, P. W., *Phys. Rev.* **79** (1950) 350.
35. Goodenough, J. B., *Phys. Rev.* **117** (1960) 1442.
36. De Gennes, P.-G., *Phys. Rev.* **118** (1960) 141.
37. Schieber, M. M., *Experimental Magnetochemistry; Nonmetallic Magnetic Materials.* 1st Edition. selected Topics in Solid State Physics. Vol. 8, ed. Wohlfarth, E.P. Published by; North - Holland Publishing Company, Amsterdam (1967)
38. Mehandjiev, D. and Angelov, S., *Magnetochemistry of Solid State.* Published by; Nauka; Ikustro, Sofia (1979)
39. Ashcroft, N. W. and Mermin, N. D., *Solid State Physics.* 1st Edition Published by; W. B. Saunders Company, Philadelphia (1976)
40. Boucher, B., Buhl, R. and Perrin, M., *C. R. Hebd. Seances Acad. Sci.* **263** (1966) 344.

Chapter 5

Review of literature on nickel manganite

The body of published material concerning nickel manganite is quite extensive, and spans nearly half a century from the first recorded synthesis by Sinha [1], in 1957, to recent papers on catalytic activity [2]. In this chapter, the various experimental methods used to produce nickel manganite are examined, in terms of the quality of the resultant material. In addition, the reported properties of nickel manganite are compared and discussed. There is some degree of disagreement over a number of key issues in the literature, and the remaining questions are identified, and form the motivation for much of the experimental work presented in chapter 6. A chronological summary of the published papers on nickel manganite is included in Table 5.1. This list only includes those papers that report one or more of the material parameters. There are a number of papers that report the production of nickel manganite, but contain no evidence as to the quality or otherwise of the samples. These papers have been largely disregarded as they impart no useful information to the reader, due to the possible errors in the determination of material properties when inferior preparation routes have been employed.

5.1 Fabrication routes

In the following section, the various approaches taken to produce nickel manganite are discussed, and judgements made as to their utility. Much of the early work on nickel manganite was carried out on samples that were (with hindsight) obviously of low quality, with significant impurity content and deviations from correct stoichiometry [3, 1, 4-6]. These shortcomings have only become apparent after later work highlighted the importance of sample purity in obtaining correct physical properties [7-12]. Despite the improved preparation routes latterly available, some recent investigations [13, 2] have not taken advantage of the current state of knowledge. Table 5.1 summarises the previous work in the field that used the fabrication routes discussed below, and reported values of key material parameters where appropriate.

First Named Author	Year	Preparation Route[8]	Inversion Parameter	Lattice Parameter, [Å]	Oxygen Parameter	T_C [K]	Quench Temperature [°C]	Nickel Deficiency	Oxygen Occupation
Sinha [1]	1957	O	1	8.37	0.381(4)		700-900		
Boucher [3]	1957	O	0.88	8.4028(3)	0.386(2)		900		
Baltzer [4]	1958	O	1	8.39	0.3835(20)	100[1]			
Azaroff [14]	1959	C	1			100[1]			
O'Keefe [15]	1961		1[1]						
Larson [16]	1962	O	1	8.396(1)					
Wickham [17]	1964	Ox	1	8.399(2)					
Villers [18] and Boucher[2] [7, 19, 8]	1965 to 1969	O	0.74	8.399(2)	0.3870(5)	162	940	0.02	3.97(4)
				8.398(2)		162	850		3.98(2)
			0.76	8.397(2)	0.3877(5)	156	750	0.037	4.03(4)
				8.395(2)		146	650		3.99(2)
			0.8		0.3880(5)	137	600	0.01	4.00(2)
				8.394(2)		127	550		3.98(2)
			0.87	8.393(2)	0.3885(5)	121	450	0.02	4.05(5)
			0.925	8.390(2)	0.3877(5)	113	350	0.026	4.03(3)
			0.93	8.388(2)	0.3882(5)	113	20	0.031	4.02(9)
Renault [5]	1972	O, N	0.84(2)	8.41(1)	0.39		800		
Brabers [20]	1972	Ox		8.39					
Bhandage [21]	1976	O	1	8.37(1)		100	900		3.95
Meenakshisundaram [6]	1982	H	0.88	8.45	0.385		850		
Brabers [10]	1982	Ox	0.9				400		
Brabers [11]	1983	N	0.86						
Maclen [12]	1986	O	0.65[3]	8.4006(9)			900		
Gillot [22]	1989	H	1						
Tang [23]	1989	Ox		8.390(2)			600		4.01
				8.398(2)			800		4.01
				8.383(3)[4]			370		4.17
Legros [24]	1990	Ox	0.712	8.39(8)				0.01	
Gillot [25]	1990	Ox	0.74	8.399			1200		
Jung [26]	1990	Ox, C		8.399(8)			800		4.00
Topfer [27]	1992	Ox	0.9	8.397(2)					
Gillot [28], Baudour [29]	1992	Ox	0.883(3)	8.3908(2)	0.38883(7)	110	20		
Martin de Vialdes [30]	1994	B		5.773(1),[5] 9.331(3)					
Singh [13]	1996	O	0.55	8.41					
Åsbrink [31]	1997	O	0.80[6]		0.3876(1)	145			
Åsbrink [32]	1998	O		8.65(8)[7], 7.88(15)					
Mehandjiev [2]	2001	C	0.80						

Table 5.1. Summary of fabrication routes, and material parameters reported in the literature.

Notes;
(1) Predicted.
(2) Boucher gives (Lattice Parameter = 8.441 - 0.057 ν) as a fit to their data.
(3) Found that at equilibrium, $\nu = 1 - 0.0005\ (T - 200)$ (Temperature in Centigrade).
(4) Low temperature (<400 °C) form.
(5) Tetragonal low temperature (200 °C) phase.
(6) Changing to $\nu = 0.87$ at 115 K.
(7) Tetragonal high-pressure phase, stable upon decompression.
(8) O – oxide, Ox – oxalate, C – carbonate, N – nitrate, H – hydroxide, B – n-butylamine.

5.1.1 Oxide route

The procedure adopted by Sinha *et al.*, [1] is hereafter referred to as the oxide route. As first reported, it involved heating a mechanically mixed, equimolar mixture of NiO and Mn_2O_3, and quenching to room temperature in air. The temperatures involved, and the lengths of time were not given to any more accuracy than 700-900 °C, and several hours. It was inevitable that such a poorly controlled procedure would lead to insufficiently pure end products, and therefore the physical parameters determined (inversion parameter, lattice parameter, oxygen position, etc) are obviously in error when compared to modern reports (see Table 5.1). Refinements to the method of Sinha have been adopted by many other groups. Workers at Saclay, France [3] reported making samples by firing for 'plusieurs heures' (many hours) at 900 °C which, while an improvement of the procedure of Sinha *et al.*, [1], were still of inferior quality. It was Larson *et al.*, [16] that made the first documented systematic investigation into the optimum preparation conditions of the mixed oxide route. They encountered difficulties, due to the conversion of Mn_2O_3 to Mn_3O_4 at high temperatures, and the tendency of this latter compound not to absorb any remaining NiO. An upper limit of approximately 1100 °C was found for the stability of $NiMn_2O_4$. The procedure followed was, starting from an equimolar mixture of oxides, repeated grinding and firing at 900 °C for 18 hours. This was followed by heating at 1000 °C for 3 days, and slow cooling to 600 °C. If the cooling rate was too slow (no figures were given), then Mn_2O_3 was found. Later reports from this group [17] indicate a move to the oxalate route (see below). The Saclay group persisted with the oxide route [18, 8, 33, 9], undertaking a thermogravimetric study, from which they obtained an optimum preparation temperature of 940 °C. This had to be sustained for about 3 days for the samples to homogenise, and crystallise. This group also made samples quenched from different (lower) temperatures, after firing at 940 °C. Renault *et al.*, [5] commented that samples made this way contained NiO as well as $NiMn_2O_4$. The reason NiO had not been detected previously, was that the X-ray diffraction lines of NiO overlap almost completely with those of $NiMn_2O_4$. A neutron diffraction study of these samples [9] confirmed that a nickel deficiency of between 2 and 7 % existed in the nickel manganite structure. Despite this warning, later

authors [34, 21, 35] continued to fabricate material at temperatures in excess of 900 °C. During a careful study of oxygen loss at different temperatures, and oxygen pressures, Macklen [12] concluded that $NiMn_2O_4$ made from mixed oxides began to lose oxygen above 810 °C in air, and 863 °C in an atmosphere of pure oxygen. In view of the difficulties encountered, this route has largely been abandoned by most researchers who are concerned with sample purity. However, for studies of thermistor device properties [36-39], it is still considered the most convenient. Preliminary experiments were carried out by the present author and confirmed the problems with the oxide route; this work is detailed in section 6.1.1. It is thought unlikely that any of the attempts to make pure stoichiometric nickel manganite by the oxide route were entirely successful, including the work at Saclay [3, 18, 7-9] upon which much later work has been based.

5.1.2 Carbonate route

Azaroff [14] adopted a slightly different preparation method, taking appropriate ratios of metal carbonates, milling thoroughly, then heating to 1000 °C to convert to oxides. The resulting oxides were then milled again, formed into pellets, and subjected to the following heat treatment; 16 hours at 900 °C, 3 minutes at 1250 °C, and 1 hour at 850 °C. This was deemed necessary to form single phase, stoichiometric material, although it was probable that the majority of the precursors had reacted after the initial firing at 1000 °C. The justification for the use of this method was that oxides prepared this way would be more finely divided and intimately mixed than material mixed from separate oxides, although why this would be the case is not immediately clear. The use of high firing temperatures would have inevitably lead to significant NiO, and Mn_3O_4 content, which would not have reacted to form nickel manganite after such a short anneal at 850 °C. Carbonates were also used as starting materials in a recent study of the catalytic activity [2] of $NiMn_2O_4$, where samples were held at 750 °C for 5 hours. Jung *et al.*, [26] appear to be the only authors who directly compared the carbonate route with another method (the oxalate route in this case). In the context of preparing dense sintered samples of pure nickel manganite the carbonate route was found to be inadequate. This was due to the segregation of

nickel oxide at high temperatures, which required further processing to eliminate. There appears to be no easy solution to this problem, as the high temperatures were necessary to sustain the mobility necessary for the solid state reaction to reach completion in a mechanically mixed sample.

5.1.3 Oxalate route

The oxalate route was first reported by Wickham [17] in an extension to the investigations of Larson *et al.*, [16]. It seeks to overcome the problems of the oxide and carbonate routes by providing an intimate mix of nickel, and manganese oxalates by coprecipitation from aqueous solution. The precipitated oxalates form a solid solution;

$$Ni_yMn_{1-y}(C_2O_4)\cdot 2H_2O,$$

resulting in mixing on the molecular level. The oxalates were decomposed to oxides by slow ignition in an oxygen atmosphere at 400 °C to 500 °C. The resulting mixtures were then heated at temperatures of between 600 °C and 1150 °C for 'periods of time long enough to bring about equilibrium among the solid phases' [17], however no actual timescales were reported. At the lower end of this temperature range, the reactions have subsequently been found to progress extremely slowly, so equilibrium may not have been reached. It was found that pure $NiMn_2O_4$ was formed in air only in the region 730 °C to 875 °C. In an oxygen atmosphere, the upper limit increased to roughly 1100 °C. Despite these findings, later groups [20, 10, 24, 28] persisted in preparing material in air at 900 °C or above, leading to inevitable impurity phases. The temperature range for stability of the spinel in oxygen was subsequently found to be between 975 °C [26], and 750 °C [23], a slightly larger range than in air. Co-precipitation seems to be a necessity, in order to form precursor materials that are sufficiently mixed to undergo reaction to completion at temperatures where pure nickel manganite is the equilibrium state. Accordingly co-precipitation was used to produce starting material in the present study (details of which can be found in chapter 6). However, coprecipitation of oxalates from aqueous solution presented problems in terms of controlling the precise ratio of nickel to manganese in the samples. This was due to the tendency of manganese oxalate to form supersaturated solutions [17], which was compensated for by preparing

solutions with a slight excess of manganese oxalate. It was found that the amount of manganese lost varied between samples, between 0.75 % and 1.9 %, so samples were in general non-stoichiometric.

Xiao-Xia Tang *et al.,* [23] reported the formation of a cation deficient (oxygen rich) spinel (equation 5.1) formed from oxalates between 250 °C and 500 °C in 5 x 10^4 Pa oxygen.

$$NiMn_2O_{4+\gamma} \qquad (5.1)$$

This low temperature, non-stoichiometric form reverted to a stoichiometric high temperature spinel (from now on referred to as LT, and HT spinels) when heated in an inert atmosphere at 600 °C for 1 day. The HT spinel did not recapture oxygen at a cooling rate of 1 $Kmin^{-1}$ from 800 °C, whereas the LT spinel altered oxygen content more readily. This has been shown to be due to kinetic (surface area, particle size) and not thermodynamic reasons. Gillot *et al.,* [25] reported the formation of stoichiometric $NiMn_2O_4$ from oxalates at 400 °C and above, in an atmosphere with an oxygen partial pressure of 100 Pa. In air, a LT spinel was formed between 350 °C and 500 °C. Above 500 °C, the spinel takes up more oxygen and decomposes. Several other authors [40, 27, 36] have confirmed this low temperature non-stoichiometric formation.

The oxalate route seems a promising possibility, were it not for the insufficient control of the co-precipitation stage.

5.1.4 Nitrate route

The nitrate route was first employed by Renault *et al.,* [5], with a similar justification to that of the carbonate route; finely divided starting materials compared to the oxide route. The reaction proceeded at 800 °C, a much lower temperature than the temperature at which the mixed oxide route was effective. However Brabers *et al.,* [11] reverted to higher temperatures (940 °C) and an oxygen atmosphere. Both authors reported the formation of pure samples, but gave no supporting evidence for this, so the state of their samples can only be estimated. In view of the difficulties encountered by most other workers, and the difficulty in identifying impurities, such claims must be viewed with some scepticism. The similarity between the nitrate and the carbonate route is noted, with mechanical mixing of powders being employed in both cases. Therefore the

problems reported using the carbonate route might be expected to also affect the nitrate route in a similar manner.

5.1.5 Hydroxide route

The hydroxide route, an alternative to the oxalate route, was first used by Meenakshisundaram *et al.*, [6]. It also employs coprecipitation from aqueous solution, in order to obtain intimate mixing. The mix of precipitated hydroxides was then fired at 850 °C for 24 hours. This technique avoids the main problem of the oxalate route; the tendency for manganese oxalates to form a supersaturated aqueous solution [17]. A similar technique was employed by Gillot *et al.*, [22], heating for between 4 and 48 hours, at temperatures between 900 °C and 1200 °C, which a study of the literature available at the time would have highlighted as too high. Despite this obvious error, and the error in the lattice parameter obtained by Meenakshisundaram *et al.*, [6], both papers reported the formation of pure material. Neither claim was backed up with experimental evidence, an unfortunate and recurring problem encountered when researching the available literature. Despite this, the method appears to be sound, and was chosen as suitable for further investigation. This route has no reported problems identified with it, provided the limits on the sintering temperature are observed. This is confirmed by the extensive investigations reported in chapter 6.

5.1.6 Permanganate route

The decomposition of a nickel complex permanganate (equation 5.2) at 750 °C leads directly to $NiMn_2O_4$, as reported by Feltz *et al.*, [40] in a comparison of different preparation routes for thermistor materials.

$$[Ni(OH_2)_6](MnO_4)_2 \qquad (5.2)$$

This route avoids the possibility of incomplete mixing of precursor material. However, inconsistencies in prepared samples caused this route to be abandoned without further investigation. The permanganate is not available commercially, and is not trivial to prepare by wet chemistry procedures.

5.1.7 n-Butylamine route

The decomposition of n-Butylamine gels [30] is distinguished from the other preparation routes, as it yields $NiMn_2O_4$ that is tetragonally distorted ($c / a > 1$) (see section 5.2 below). This phase was prepared by heating at 200 °C for 13 hours, gels obtained by addition of 1 M n-butylamine to mixed $NiCl_2$, and $MnCl_2$ solutions. It has been suggested that hydrated α-$Ni(OH)_2$ and Mn_3O_4 are formed as intermediate compounds at temperatures as low as 100 °C. The tetragonal spinel reverts to a cubic form upon heating at 800 °C for 13 hours, however a significant amount of Mn_2O_3 was observed to have formed as well. The reason for this was unclear, but suggests that this route is not suited to production of the cubic spinel in pure form.

5.1.8 Single crystal

There have been relatively few reports of attempts to grow single crystals of $NiMn_2O_4$. Brabers *et al.,* [10] reported success using HCl vapour as a transport agent at temperatures between 800 °C and 920 °C. The crystals obtained were of the order of 2 mm across, but were slightly nickel deficient. Smaller crystals (0.12 mm) were obtained from mixed oxides [31], prepared by heating for 45 days in a sealed evacuated silica tube, and then quenching. Attempts to replicate this experiment were not successful (see section 6.3).

5.1.9 High pressure phase

Mention should be made of the existence of a tetragonal high-pressure phase ($c / a < 1$). This phase was formed from cubic $NiMn_2O_4$ above approximately 12 GPa [32], and was found stable upon decompression.

5.2 Crystal structure and lattice parameter

All the reported values of lattice parameter are to be found in Table 5.1, along with all other relevant parameters. Sinha *et al.,* [1] reported a cubic spinel structure, and a lattice parameter of 8.37 Å from X-ray diffraction, for $NiMn_2O_4$ prepared above 700 °C. Later, more accurate lattice parameter values produced a discrepancy between samples quenched from 900 °C (Boucher [3], from neutron diffraction studies), and slow cooled samples (Larson *et al.,* [16]).

Villers *et al.*, [18] studied a range of samples quenched from different temperatures, and found a range of lattice parameters depending upon quench temperature. The explanation offered for this was due to the changing inversion parameter, ν (see below).

This was confirmed [8], as an almost linear relationship;

$$a = 8.441 - 0.057 * \nu.$$

Most later authors give similar values, apart from Meenakshisundaram *et al.*, [6], who reported 8.45 Å. The LT spinel made by Xiao-Xia Tang *et al.*, [23] was found to have a slightly lower lattice parameter (8.383(3) Å) than HT spinel fabricated by the same author (8.390(2) Å). The low temperature n-butylamine route [30] gives a tetragonal spinel, with a = 5.773(1) Å and c = 9.331(3) Å, whereas the high-pressure tetragonal spinel [32] has $a > c$. A single group has reported making $MnNi_2O_4$ [41], finding it a normal spinel, with a lattice parameter of 8.38(1) Å. This has not been repeated, despite an attempt by Xiao-Xia Tang *et al.*, [23], so may be in error. None of the reports of lattice parameter mentioned the inclusion of a nickel oxide phase in the refinement model, which has been shown to lead to significant errors in reported parameters (see section 6.2.5 for more details) where present. Therefore, a consideration of the purity of samples has implications for the reliability of reported values of lattice parameter, and all other parameters derived from diffraction data. In particular, the oxide preparation route (as used by many authors, including Larson *et al.*, [16], and the researchers at Saclay [3, 18]) is now known to leave appreciable quantities of nickel oxide in samples. Therefore the absolute values reported by these researchers are probably in error, but the reported trends with cooling rate may still be realistic. Figure 5.1 contains the values of inversion parameter (see section 5.3) and lattice parameter reported in the literature.

5.3 Inversion parameter and cation distribution.

The first report of the inversion parameter of $NiMn_2O_4$ was in 1957 [1], who found an inverse configuration (equation 5.3), based upon a visual estimation of reflection intensities from an X-ray powder diffractogram.

$$Mn^{2+}[Ni^{2+}Mn^{4+}]O_4 \qquad (5.3)$$

This conclusion must be regarded as suspect due to the proximity of nickel and manganese in the periodic table, and therefore the similarity in their X-ray scattering cross sections. Attempts to determine the inversion parameter from modern X-ray powder diffractograms by Rietveld analysis (as detailed in chapter 6), gave incorrect results for this reason.

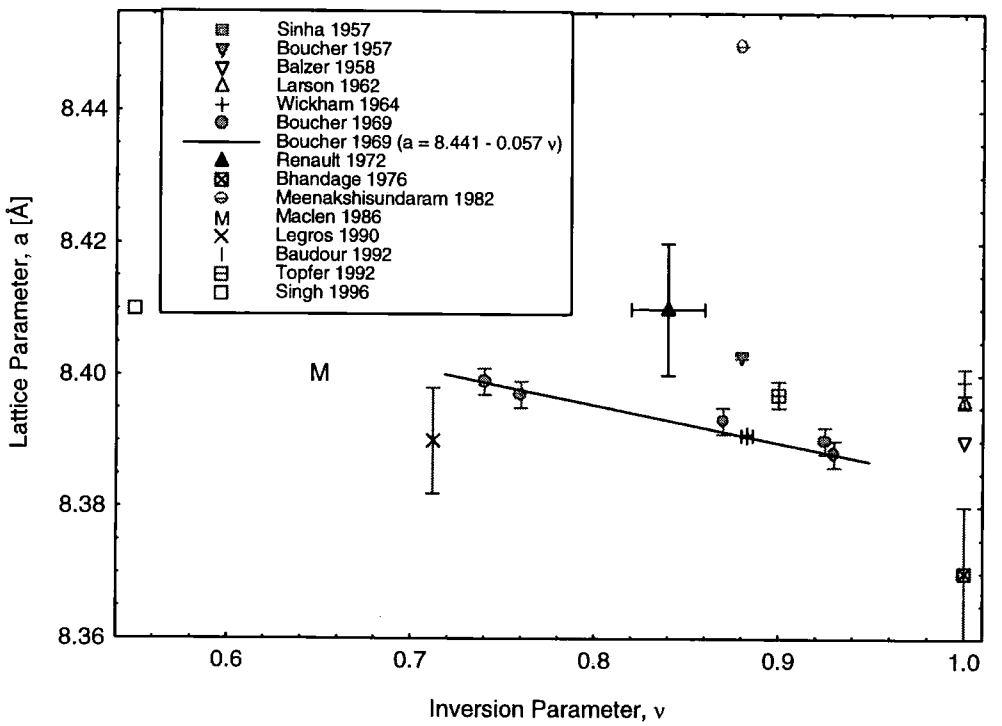

Figure 5.1. Reported values of inversion parameter and lattice parameter. Only those reports which include both parameters are included.

Nevertheless, this structure was confirmed later that year by Boucher [3], with neutron diffraction experiments yielding a more accurate inversion parameter. The neutron scattering cross sections of nickel and manganese are sufficiently different to enable a realistic determination of the inversion parameter. The reasons for the failure of Boucher to correctly determine the inversion parameter are unclear. This conclusion was again confirmed in 1958 [4] from magnetic measurements, in 1959 [14], based on neutron diffraction data, and in 1961 [15] by simple crystal field theory. A further X-ray diffraction study [16, 17], combined with a number of other techniques, found a mixed valence state on both sites;

$$Mn^{2+}_{0.65}Mn^{3+}_{0.35}[Ni^{2+}Mn^{3+}_{0.35}Mn^{4+}_{0.65}]O^{2-}_{4}. \qquad (5.4)$$

but again assumed a completely inverse structure. Shortly afterwards, magnetic measurements were made [18] at Saclay on samples quenched from different temperatures, showing variations in saturation moment, and Curie temperature. The inversion parameter was not measured, but it was acknowledged that it could vary from 1. Reports by the Saclay group [8, 33, 9] from 1969 made a leap in understanding. From a series of neutron diffraction experiments, inversion parameters of $0.74 < \nu < 0.93$ were measured. However, nickel deficiencies of between 2 and 7 % were reported for all the samples measured, and the presence of nickel oxide must be presumed. Due to the overlap of nickel oxide diffraction peaks with those of nickel manganite, and the low angular resolution then achievable in neutron diffractometers, significant errors in these inversion parameters cannot be ruled out. The charge state of manganese was assumed to be 3+ throughout;

$$Ni^{2+}{}_{1-\nu}Mn^{3+}{}_{\nu}[Ni^{2+}{}_{\nu}Mn^{3+}{}_{2-\nu}]O_4. \qquad (5.5)$$

However, this arrangement would not account for the high conductivity seen by previous authors. The variations of inversion parameter and lattice parameter (see section 5.2) were correlated to thermal histories. A study of IR absorption spectra by Brabers[20] led to a postulated formula;

$$Ni^{2+}{}_{1-\nu}Mn^{2+}{}_{\nu}[Ni^{2+}{}_{\nu}Mn^{3+}{}_{2-2\nu}Mn^{4+}{}_{\nu}]O_4. \qquad (5.6)$$

This, in common with equation 5.5 has no mixed valence on the A sites, although another contemporary XRD study [5] contradicts this, as does a later XAFS study [34]. The arrangement of equation 5.6 is now considered approximately correct. Both report inversion parameters in the range obtained by the Saclay group. Bhandage *et al.*, [21] favoured a different cation distribution, an inverse arrangement (equation 5.7) on the basis of electrical, magnetic, and ESR measurements.

$$Mn^{3+}[Ni^{2+}Mn^{2+}{}_{0.1}Mn^{3+}{}_{0.9}]O_{3.95} \qquad (5.7)$$

A further attempt at determining the inversion parameter [6], by investigating the intensity ratios of (220) and (440) XRD reflections, gave a value of $\nu = 0.88$. An absence of Mn^{4+} was assumed, with a distribution similar to that shown in equation 5.5. However, this result must be treated with caution as contamination by NiO can modify the apparent intensity of the (440) reflection. A high

temperature conductivity study [10] found features best explained by the onset of cation mobility above 400 °C. The enthalpy (E) for the reaction;

$$Ni^{2+}_B + Mn^{4+}_B + Mn^{2+}_A \leftrightarrow Ni^{2+}_A + 2Mn^{3+}_B - E \quad (5.8)$$

(Where the subscripts A, and B refer to the Tetrahedral, and Octahedral sites respectively) was determined to be ~ 0.6 eV. X-ray photoelectron spectroscopy by the same author [11] found an inversion parameter of 0.9, and added support to the configuration in equation 5.6. An oxygen loss study by Macklen [12] gave the lowest yet reported inversion parameter, of 0.65 at 900 °C. Macklen also gave an empirical expression relating the equilibrium inversion parameter to temperature (in °C), while noting that the time to gain equilibrium can be considerable at low temperatures;

$$\nu = 1 - 5 \times 10^{-4} (T - 200). \quad (5.9)$$

In a theoretical study using computer simulation techniques, Islam *et al.,* [42] suggested that the formula;

$$Ni^{2+}_{1-\nu}Mn^{3+}_{\nu}[Ni^{2+}_{\nu}Mn^{3+}_{2-\nu}]O_4 \quad (5.10)$$

would be likely due to ionisation energies, with an inversion parameter ~ 0.9. Despite [16, 17] conductivity data, Gillot [22] concluded a completely inverse state. Several other authors [24, 29, 27, 2], and later Gillot *et al.,* [28] found inversion parameters consistent with the findings of the Saclay group (see above). All favoured the distribution whereby most (if not all) of the manganese on A sites was in the 2+ state (equation 5.6), and conductivity occurs via B sites. In an unexpected development, Åsbrink *et al.,* [31], reported an increase in inversion parameter from 0.80 to 0.87 upon cooling from room temperature to 115 K. However, this change is within the reported error on the inversion parameter at 115 K. No error value for the room temperature value was given. This contradicted the findings of Brabers *et al.,* [10], who observed the onset of ion mobility at approximately 400 °C. Both tetragonal phases (see above) have been found (or assumed to be) completely inverse [30, 32].

In conclusion, there has been a wide range of cation distributions proposed, in order to account for a wide range of sample characteristics. Some of the measured sample characteristics were undoubtedly due to impurities, or non-stoichiometry, and so this has served to further confuse matters. The distribution that seems to be most widely favoured is that of equation 5.6, possibly with the

addition of a small amount of Mn^{3+} present on the A sites, although this is far from certain.

5.4 Oxygen parameter

The first report of Sinha *et al.*, in 1957 [1], found an oxygen parameter of 0.381(4). This was confirmed later that year [3], with neutron diffraction yielding a more accurate oxygen parameter of 0.386(2). A confirmation of this value was reported by 1959 [14] and indeed, this is one of the few things that most reports agree on. Boucher [8] commented that oxygen parameter stayed almost constant as inversion parameter varied. This is a surprising result, as the ionic radii of the cations involved changes substantially with inversion parameter (see section 4.2.3). The oxygen parameter, as obtained from analysis of peak intensities in diffraction data is subject to the effects of nickel oxide impurities, as discussed above. Figure 5.2 contains the values of oxygen parameter reported in the literature, plotted against lattice parameter.

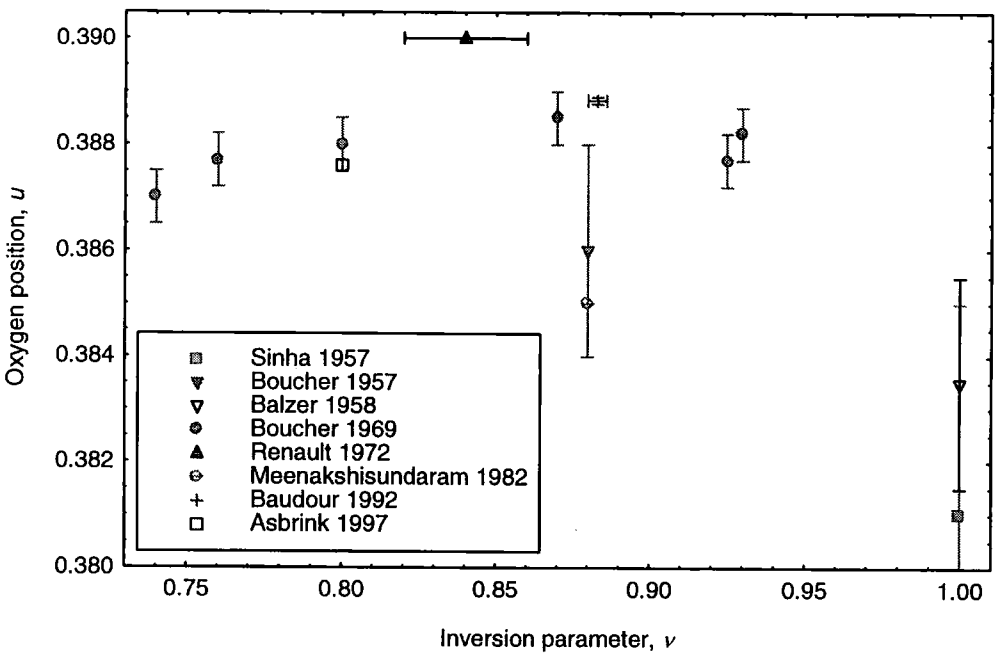

Figure 5.2. Reported values of oxygen parameter and lattice parameter. Only those reports which include both parameters are included.

5.5 Vacancies

Since the oxygen in the spinel structure is approximately close packed, any variation of the metal:oxygen ratio from 3:4 has almost universally been reported as vacancies in either the A, B or oxygen sites. The compounds Mn_2O_3, and

γ-Fe_2O_3 are considered spinels with ordered or partially ordered metal site vacancies [43]. Villers *et al.*, [18], and Boucher *et al.*, [8] reported small (less than 1 %) deviations from ideal oxygen content, concluded from neutron diffraction data. However, no systematic trend was observed, and all the variations from stoichiometry were within the quoted uncertainties.
Bhandage *et al.*, [21] was the first to report significant oxygen deficiencies. This was in an attempt to reconcile a presumed completely inverse structure (now known to be incorrect), with conductivity and ESR data, so may be in error.
Oxygen loss was reported from nickel manganite above 810 °C in air [12]. This important result puts most of the previous work (and much carried out afterwards) in doubt due to the high preparation temperatures used therein. This maximum temperature for stability of stoichiometric material was found to increase with oxygen partial pressure, up to approximately 865 °C at 1 atmosphere oxygen. A loss of oxygen up to 12.2 mg g^{-1} was found to be accommodated as oxygen vacancies in the spinel structure.
Anything above this value resulted in a partial reduction of $NiMn_2O_4$ by the reaction;

$$NiMn_2O_4 \rightarrow NiO + 2/3(Mn_3O_4) + 1/3(O_2).$$

It was found that stoichiometric $NiMn_2O_4$ was unable to take up excess oxygen at 800 °C. Gillot *et al.*, [22] also found no evidence for material with cation vacancies, in a study of oxidation kinetics below 800 °C. They found a direct oxidation of $NiMn_2O_4$ by the reaction;

$$NiMn_2O_4 + 1/4(O_2) \rightarrow NiMnO_3 + 1/2(\alpha - Mn_2O_3) .$$

In contrast to this, the LT spinel was found to be oxygen rich (contain cation vacancies) by many of the groups that studied it [23, 25, 40]. The effect of this on the inversion parameter, and cation distribution has not been studied, but Tang *et al.*, [23] assumed that the vacancies lie on the A sites;

$$NiMn_2O_{4+\gamma} \equiv Ni^{2+}_{1-v-3\gamma/8}Mn^{2+}_{v-3\gamma/8}V_{3\gamma/4}[Ni^{2+}_{v+\gamma/8}Mn^{3+}_{2-2v-15\gamma/8}Mn^{4+}_{v+14\gamma/8}]O_4 .$$

The 'V' represents a cation vacancy. This arrangement being due to the strong octahedral site preference of Ni^{2+}, Mn^{3+}, and Mn^{4+} ions. {N.B. The formula above is corrected from formula (7) in Tang *et al.*, [23], to bring the Ni:Mn ratio to 1:2}. Gillot *et al.*, [25] gave a more general formula, in terms of the oxidation

degree, D (the proportion of Mn^{2+} converted to Mn^{3+} to maintain charge neutrality);

$$Ni^{2+}{}_{s}Mn^{2+}{}_{sv(1-D)}Mn^{3+}{}_{s(2-2v+Dv)}\ Mn^{4+}{}_{sv}V_{3sDv/8}O_4$$

where $s = 8 / (8 + D\ v)$. The distribution of vacancies among sites is not determined; however, mention is made that vacancies are found on B sites in other cation deficient spinels (Reference 20 in Gillot *et al.,* [25]).

5.6 Magnetism

5.6.1 Initial investigations, and the $NiMn_2O_4$-Mn_3O_4 system

A great deal of interest has been shown in the magnetism of spinel type structures in the past, although mostly focussing on ferrites (iron-containing spinels). Indeed many of the theories of magnetic interactions were first developed in an attempt to explain the sometimes complex magnetic behaviour of spinel compounds. These include Néel's ferrimagnetism [44], Yafet-Kittel structures [45], and important work on double exchange [46]. The assumption that nickel manganite was ferrimagnetic below the Curie temperature has been demonstrated satisfactorily, however there are a number of lower temperature features that have been observed, the nature of which remain uncertain.

A non-collinear spin arrangement was postulated by Boucher [3], to explain a neutron diffraction pattern at 4.2 K. The pattern observed was not that expected from a simple antiferromagnetic coupling between A, and B site moments. However, he was unable to determine the precise nature of the arrangement, other than to postulate that the spins on the 4 B-site sub lattices were non-collinear. There were assumptions that no manganese was present in the 4+ oxidation state and that a pure sample was made, both of which are now known to be wrong. The presence of impurities undoubtedly affected the interpretation of the neutron diffraction data, as discussed at length above.

Baltzer *et al.,* [4] also performed some magnetic measurements, down to 77 K, but suffered from lack of resolution. The Curie temperature was estimated to be approximately 100 K. From a study of the $NiMn_2O_4$-Mn_3O_4 system (which becomes tetragonally distorted when the amount of nickel falls below 0.42), Larson *et al.,* [16] postulated that antiferromagnetic interactions between adjacent

B sites played an increasingly important role as the amount of nickel was reduced. This interaction is due to t_{2g} orbitals being directed towards neighbouring B site cations. The presumed 2+ oxidation state of nickel present on the B sites has a fully occupied t_{2g} orbital, and therefore is not expected to play any part in interactions of this type. Although Larson *et al.,* [16] assumed a completely inverse structure, and varying the B site nickel content by differing the starting materials, it seems probable that a change in inversion parameter would have a similar effect, as discussed in chapter 4, and below. This finding is in agreement with the observed decrease in Curie temperature with increasing inversion parameter, as an antiferromagnetic B – B interaction would be expected to interfere with a simple ferrimagnetic ordering. Changes in the magnetisation at 4.2 K with changing composition were interpreted as a rapid decrease in the total moment on the B sites (which was found to be larger than the moment on the A sites in $NiMn_2O_4$). This approximately coincided with the phase transition from cubic to tetragonal symmetry, as the amount of nickel present was reduced. Such a phase transition would involve considerable change in bond lengths, angles, and character (ionic or covalent), and it was unclear as to the mechanism for the change in moment.

The Saclay group then made further progress, [18] finding a variation in the saturation moment and Curie temperature for samples with different quenching temperatures. The samples used were still being made by the oxide route however, so were not of the highest quality. Samples quenched from 940 °C (the firing temperature) had a much reduced moment, and increased Curie temperature (0.35 μ_B, and 162 K respectively) compared with slow cooled samples (1.75 μ_B, and 113 K). This was attributed to a change in the inversion parameter, although how this altered the Curie temperature was not explored thoroughly. The Curie temperatures determined for these samples were higher than found in later work by Baudour *et al.,* [29], and in the present study. This could be due to a nickel deficiency in the samples changing the relative influence of the B – B antiferromagnetic interactions, as postulated by Larson *et al.,* [16] (see above). All of the Saclay group's samples measured were found to be non-stoichiometric (have an excess of manganese) by between 2 and 7 %. The

ordering transition at the Curie temperature was found to be purely magnetic (no associated structural phase change).

5.6.2 Neutron scattering and the non-collinear state

Neutron diffraction measurements [7] made at low temperatures and in applied fields apparently supported the non-collinear magnetic state first proposed by Boucher [3]. This non-collinear state was concluded to exist up to a transition at approximately 70 K, with a collinear state existing to the Curie temperature. The lower transition was found to be much broader than the upper transition, and almost independent of the inversion parameter. This is in contrast to the findings presented in chapter 6, showing this transition at lower temperatures, and varying with inversion parameter. The nickel deficiency noted above could be responsible for the higher temperatures found by the Saclay researchers.
The low temperature non-collinear state was reported as follows [7];

1) Sum of the B site moments at an angle (158.5 ° for an inversion parameter $\nu = 0.93$) to the sum of the A site moments.
2) 4 distinct FCC sublattices on the B sites, differentiated by crystallographic positioning.
3) The 4 B site sublattices have their moments non-collinear with respect to one another. The arrangement is described as 2 pairs of sublattices with some (unspecified) angle between their moments, as shown in Figure 5.3 (second configuration).
4) The sum of the A site moments (3.9 μ_B) is greater than the sum of the B site moments (2.65 μ_B), in contrast to the work of Larson *et al.*, [16]. The sample used to determine this had a reported inversion parameter of $\nu = 0.93$, and was slow cooled.
5) The moments of nickel and manganese ions on equivalent sites were aligned in the same direction.

The canting angle described in point 1) above increased the total moment from 1.25 μ_B (no canting), to 1.73 μ_B, which were in better agreement with the measured value of 1.75 μ_B.

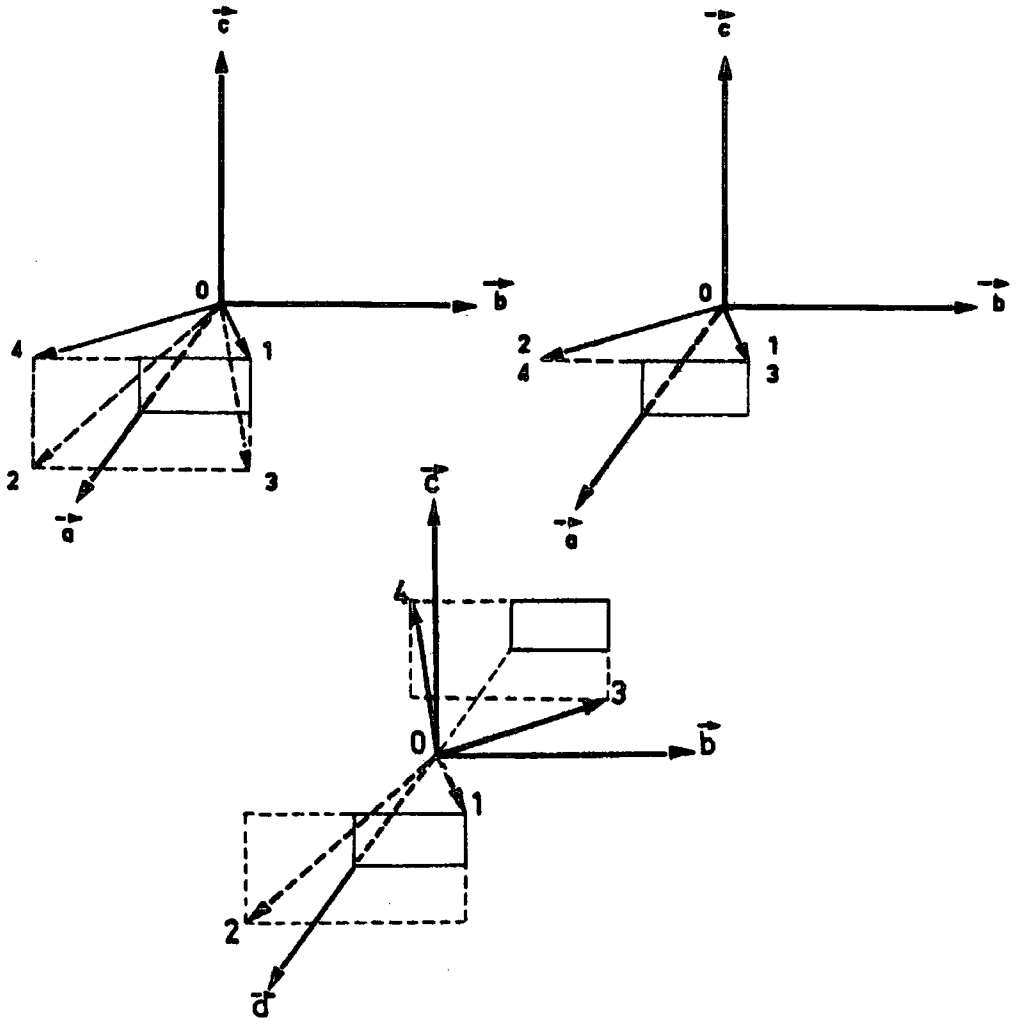

Figure 5.3. Possible arrangements of the 4 sublattices on the B sites of nickel manganite, as suggested by Boucher *et al.*, (Figure 8, [9]).

Using the moments for the various ions present (after Brabers [20]), as calculated in section 6.5.4 (see Figure 6.52), a value for the total moment with an inversion parameter of $\nu = 0.93$, is 1.76(11) μ_B, without the need for any canting angle between A, and B sites. Boucher *et al.*, [7], did assume that all of the manganese was present in a 3+ oxidation state, which is now known to be incorrect. The moment of Mn^{4+} is considerably smaller than that of Mn^{3+}, so their discrepancy between the B site moment as measured by neutron diffraction, and calculated from the expected ionic moments (detailed in Table 4.8), is reduced but not eliminated. The analysis of neutron diffraction data in section 6.5.4 confirms that the A site moment is greater for samples with similar inversion parameters, and gives some evidence of an angle between the moments on the A, and B sites. It was reported by the Saclay researchers [7] that the magnetic anisotropy became weaker for larger values of the inversion parameter (this is in agreement with

Blazer *et al.*, [4], who stated that Mn^{3+} on B sites is responsible for an increase in anisotropy in the <100> direction). Later publications (Boucher *et al.*, [9]), reported the temperature dependence of the A-site moment (via the (220) peak in neutron diffraction data). From this, in conjunction with bulk magnetisation measurements, they inferred that the B sites were split into a nickel lattice, and a manganese lattice, as shown in Figure 5.4.

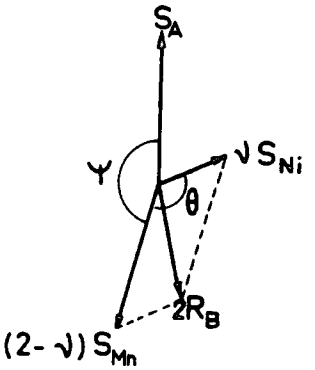

Figure 5.4. Diagram showing the relative directions of the moments of the A site ions (S_A), the B site nickel ions (S_{Ni}), and the B site manganese ions (S_{Mn}) in the arrangement proposed by Boucher *et al.*, (Figure 11, [9]).

The magnetic moments of the A, and two B sub-lattices were found to vary essentially independently of one another below the Curie temperature [47] (in a similar fashion to Néel's 2 sub-lattice model of antiferromagnetism [44]). A further conclusion was that all of the interactions between the moments on the various sub lattices were negative (antiferromagnetic) in the case of nickel manganite. This agrees with the predictions of Goodenough, outlined in section 4.3.1, and the *P* type behaviour of the magnetisation below the Curie temperature found in the present study (section 6.6.3). Boucher *et al.*, [19] hypothesised that, in the collinear region (just below the ferrimagnetic Curie temperature), the manganese moment on the B sites aligns antiparallel to the A site moments, but the B site nickel moment is aligned parallel. Below the lower transition temperature, the relative strengths of the interactions between the various sublattices produces the non-collinear state.

In the case of a sample with inversion parameter $\nu = 0.93$, Boucher *et al.*, [19] calculated the angles between the sub-lattice moments to be;

A site moment-B site manganese	= 143 °
A site moment-B site nickel	= 59 °

These conclusions were soon extended to samples with different inversion parameters [9], and measurements of the specific heat and Curie temperature (shown in Figure 5.5) were made. Peaks in the specific heat measurements confirmed the presence of 2 transitions.

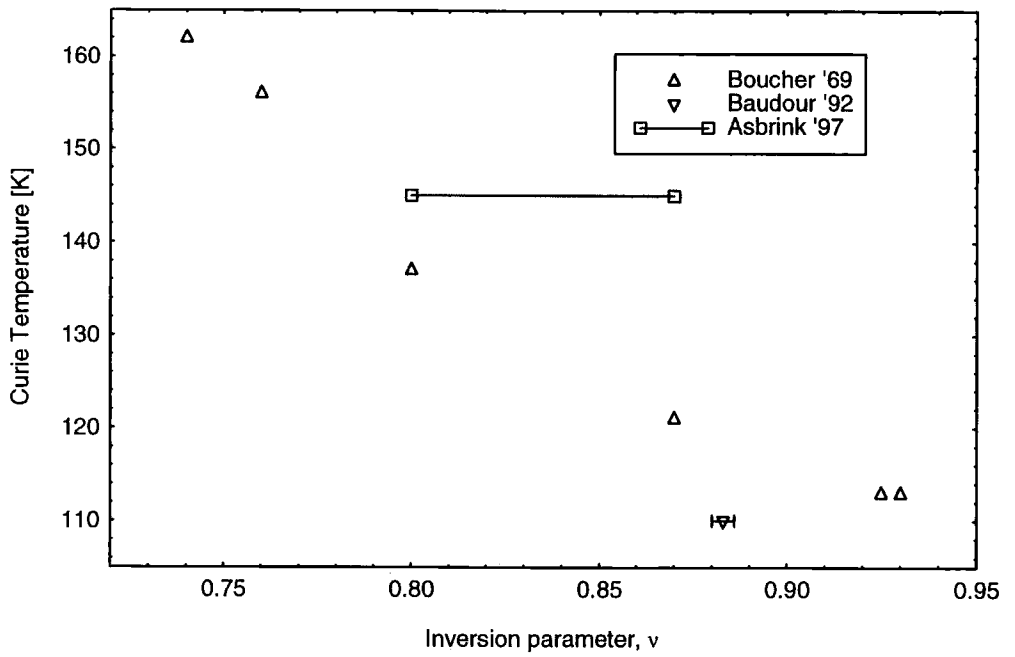

Figure 5.5. Variation of Curie temperature with inversion parameter, Data from Boucher *et al.*, [9], Baudour *et al.*, [29], and Asbrink *et al.*, [31]. Both Asbrink's inversion parameter values are plotted.

The splitting of the B sites, this time into 4 sub-lattices with non-collinear moments (as shown in Figure 5.3) was again considered, but rejected on the grounds of the absence of a field dependence of the (222) reflection in neutron diffraction data. This implied that the moments on the B sites were all parallel. This statement was apparently contradicted later in the same paper, in an attempt to explain the deviation of measured and calculated values for the B-site moments. Thus the splitting of the B sites into separate nickel and manganese moment directions was again favoured, but with no nuclear (spatial) long range order discernible.

The B site total moment was apparently further reduced by variations in the local 'crystal field' caused by the local site disorder, contributing to directional disorder of the moments. This effect was much reduced in the A sites, as the nearest neighbour B sites are further away (3.46 Å compared with a B – B distance of 2.97 Å) and more numerous (12 compared to 6). The experimental

values for A site, B site and total magnetic moments obtained at 4.2K by Boucher *et al.*, are given in Table 5.2.

Inversion Parameter, ν	A Site Moment	B Site Moment	Deviation Angle	Total Moment
0.74 (Boucher *et al.*, 1970)	3.48 μ_B	3.82 μ_B	3.4 °	0.39 μ_B
0.80 (Boucher *et al.*, 1970)	3.65 μ_B	3.84 μ_B	9.0 °	0.6 μ_B
0.88 (Baudour *et al.*, 1992)	3.83 μ_B	2.76 μ_B	25 °	1.77 μ_B
0.93 (Boucher *et al.*, 1970)	3.90 μ_B	2.66 μ_B	21.5 °	1.73 μ_B

Table 5.2. Magnetic data reported by Boucher *et al.*, [47], and Baudour *et al.*, [29].

As can be seen, the B site moments are the larger for lower values of inversion parameter, ν (quenched samples). This is therefore in agreement with the findings of Larson *et al.*, [16].

From this data a prediction can be made that the magnitude of the moments on both sites will be approximately equal for $\nu = 0.83$. It was reported that the sample with $\nu = 0.80$ could be driven from a collinear to a non-collinear state above the usual transition temperature by the application of an external magnetic field. This was ascribed to the exchange interactions between the various sub-lattices being of the same order as the energy of the total moment in the applied field.

5.6.3 Recent investigations

Following the work of the Saclay group, Bhandage *et al.*, [21] reported a Curie temperature of 100 K, for a sample believed (incorrectly) to be completely inverse, and oxygen deficient. More recent reports (Baudour *et al.*, [29]) found a lower Curie temperature of 110 K, for $\nu = 0.88$. These later values of the Curie temperature agree somewhat better with the present findings. Baudour *et al.*, also reported low temperature (1.5 K) neutron diffraction data, in good agreement with Boucher *et al.*, [9] for the moments present (see Table 5.2). However, a different cation distribution was determined (with 10% Mn^{3+} on the A sites), so that a conclusion of non-collinearity on both A, and B sub-lattices was made. Following Boucher *et al.*, [47], they supposed either a pyramidal arrangement (4 equal B site sublattices, as shown in Figure 5.3, first configuration), or a splitting of nickel and manganese moments (as shown in Figure 5.4) to account for the reduced B site moment. In common with

Boucher *et al.*, [47] the canting hypothesis was made in order to reconcile measured magnetisation values with expected values (Table 4.8, $L = 0$), but no other experimental data was offered in support of this. Åsbrink *et al.*, [31] found a Curie temperature of 145 K, for a single crystal with $\nu = 0.80$ ($\nu = 0.87(8)$ at 115 K), a little higher than the values of Boucher *et al.*, [9].

Thus even recent studies into the magnetism of nickel manganite have not been able to result in a clear understanding of the low temperature magnetic state of nickel manganite, with several conflicting models having been proposed. The work reported in this thesis goes some way to resolve the nature of the magnetism of nickel manganite.

5.7 Short range nuclear ordering

Boucher *et al.*, [7] reported being unable to discern any long range nuclear ordering of the nickel and manganese on the B sites, concluded by the absence of any superstructure peaks in neutron diffraction data. However, they found short-range order, over a length of approximately 6 Å, between B site atoms. The absence of any long range ordering on B sites is in agreement with the comments of Anderson [48] concerning anomalous lattices, described in greater detail in section 4.2.2. The lack of long range order on the A sites is expected due to the larger inter-site distance, and the long interaction paths via intervening atoms. However, the ideas of Anderson [48] do not preclude a short range ordering driven predominantly by nearest neighbour interactions.

The short range ordering seen by Boucher *et al.*, [7] manifests as a broad, low intensity modulation superimposed upon neutron diffraction data between 2θ angles of approximately 6 ° and 45 °. A similar signature has been observed in the present study. Later work [8] described this as a modulation of the background noise, independent of temperature, and stronger for samples with high inversion parameters.

The dependence upon inversion parameter was expected, due to there being a more similar amount of nickel and manganese on each of the sublattices for high inversion parameters, and therefore more opportunity to display ordering. The short B-B distance (2.97 Å), lead to a conclusion that the ordering was on the B sites as already mentioned.

A detailed analysis of this modulation after Cowley [49] gave values of the Warren-Cowley correlation coefficients, α_i, defined as;

$$\alpha_i = 1 - \frac{n_{12}^i}{C_2} = 1 - \frac{n_{21}^i}{C_1}.$$

Where C are the fractional concentrations of atoms of type 1 and 2 (nickel and manganese in this case), and n^i_{12} is the proportion of type 2 i-th nearest neighbours of a type 1 atom. A disordered arrangement would have all $\alpha_i = 0$, whereas $\alpha_i = \pm 1$ represents complete ordering. The values reported by Boucher *et al.*, [9] are reproduced in Table 5.3. All higher order terms were indistinguishable from zero. As can be seen, there is a relatively strong ordering of unlike nearest neighbours, increasing with inversion parameter, and a rapid decline in correlation with increased distance.

Inversion Parameter	0.74	0.80	0.93
α_1	-0.126(36)	-0.159(34)	-0.230(30)
α_2	0.091(32)	0.090(31)	0.267(25)
α_3	0.033(40)	0.032(38)	-0.055(32)

Table 5.3. Short-range ordering parameters for $NiMn_2O_4$, from Boucher *et al.*, [9].

This type of short range ordering can be explained purely in terms of the ionic radii of the species present. Mn^{4+}, thought to be the dominant manganese ion present (especially at high inversion parameters) has a much smaller radius (see Table 4.5 for a comparison of reported values) than either Mn^{3+}, or Ni^{2+}. Therefore the local lattice distortions around a pair of adjacent Ni^{2+}, or Mn^{4+} ions would be larger than if they were more widely separated. Study of IR absorption spectra by Brabers [20], confirmed the short range ordering, with both cations preferring unlike neighbours. This was used as evidence for the conclusion that most of the manganese was in a 4+ oxidation state, as Mn^{3+} ions have a tendency to form clusters [50] (thereby destroying the ordering). In later publications, the same authors commented that the driving force for the ordering may be anion polarisation if the manganese is predominantly tetravalent [10], and that the ordering is less pronounced in quenched samples [28]. This was confirmed by Elbadraoui *et al.*, [51], in a study of non-stoichiometric materials. The magnitude and signs of the Warren-Cowley coefficients obtained broadly agree with those of Boucher *et al.*, [7]. The increase in the α_i's at high inversion parameter can be explained by a combination of effects, the ionic radius argument as explained

above, and that slow cooling of samples is necessary to obtain such high values of inversion parameter. A slow cooling rate means a greater likelihood that nickel manganite will crystallise in a configuration that minimises the local distortions in the lattice, thereby increasing the short range ordering observed.

5.8 Conductivity mechanism.

O'Keefe [15] sought to explain the high conductivity of nickel manganite by a mixed valence state of manganese on the A sites, leading to thermally activated hopping. The conductivity was later found by Larson *et al.*, [16] to be *n*-type, from the sign of thermoelectric voltages, and was presumed to be due to electron exchange between Mn^{3+}, and Mn^{4+} on the B sites. This electron exchange was again assumed to be phonon activated, according to the formula;

$$\sigma = \sigma_0 \exp(-E_a / k_B T) \qquad (5.11)$$

with σ_0 approximately independent of temperature, and an activation energy, $E_a = 0.36$ eV. A mixed valence state on both sites (equation 5.4) was concluded by Larson *et al.*, however, the contribution to the conductivity from the A sites was ignored, because of the large distances between ions. Freud [52] studied the dependence of conductivity upon electric field, and asserted that the observed dominant linear term could not be explained by thermally activated hopping of localised charge carriers. Brabers and Terhell [10] adopted equation 5.11 as a model for the conductivity mechanism, but found different values of E_a of 0.59 eV, and 0.37 eV, above and below 450 °C respectively. From this, they deduced that the activation energy associated with cation mobility above 450 °C was approximately 0.66 eV. Maclen [12] observed a similar behaviour, with values of E_a of 0.45 eV, and 0.33 eV, above and below 352 °C. Islam *et al.*, [42] suggested that conductivity due to small polaron hopping occurs between Mn^{2+} and Mn^{3+} on B sites. The formation of the Mn^{2+} required for this would be due to thermal excitation of the charge transfer reaction;

$$Mn_B^{3+} + Ni_A^{2+} \rightarrow Mn_B^{2+} + Ni_A^{3+}.$$

This reaction is endothermic, calculated at 0.36 eV, which is similar to the activation energy obtained from experiment [16, 17].

In a study of prototype thermistor devices, Feltz *et al.*, [40] found a similar activation energy to Maclen [12] by fitting to equation 5.11, but found that the data was better approximated by;

$$\sigma = \frac{\sigma_0}{T^b}\exp(-E_a / k_B T)$$

in the range 0 °C < T < 70 °C. The activation energy was found to be 0.2458(13) eV, and b = 2.91(5). Significant variation of σ_0 between samples was encountered, and attributed to porosity differences. The conductivity was observed to decrease slightly over a number of days in samples held at 150 °C. Later work (Lindner and Feltz [36]) on electrophoresis deposited thin films reverted to analysis using equation 5.11. Activation energies similar to bulk material (0.339(3) eV) were found for film thickness between 21 and 95 μm. However, σ_0 was found to be only 10% of the bulk value, due to the lower density of the films studied.

In a study of non-stoichiometric bulk samples, Fritsch *et al.*, [53] found a change in conductivity arising from differing heat treatments, with quenched samples showing an increased conductivity compared with slow cooled samples. This was correlated with a change in cation distribution, determined from neutron diffraction experiments. The effective number of charge carriers was given (assuming a random distribution across B sites) as;

$$N_{eff} = NC(1-C) = \frac{[Mn_B^{3+}][Mn_B^{4+}]}{[Mn_B^{3+}]+[Mn_B^{4+}]}$$

which, for a stoichiometric material with the cation distribution of Brabers [20] (see section 5.3), gives;

$$N_{eff} = \frac{2\nu(1-\nu)}{2-\nu}$$

which has a maximum at an inversion parameter of $\nu = 0.59$.

Later work (Elbadraoui *et al.*, [51]) found an additional contribution to conductivity changes of ~40%, due to increased short range ordering on the B sites in slowly cooled samples. This partial ordering (see section 5.7) acted to decrease the observed conductivity.

Schmidt and Brinkman [54] found evidence for variable range hopping in non-stoichiometric samples, modelled by;

$$\sigma = \sigma_0 \exp(-(T_0/T)^n),$$

with $n = 0.28$.

Recent work on thin films (Basu *et al.,* [55]) concluded that the conductivity mechanism was Efros-Shklovskii variable range hopping (see Figure 1.1);

$$\sigma = \frac{\sigma_0}{\sqrt{T}} \exp(-(T_0/T)^{0.5}),$$

with a characteristic temperature of $T_0 = 2.3 \times 10^5$ K.

5.9 Summary

The numerous experimental methods used to produce nickel manganite have been examined, in terms of the quality of the resultant material. Those routes involving mechanical mixing of precursor material (oxide, carbonate, nitrate) have been found inadequate in the context of preparing samples with sufficient purity for further study. Of the remaining routes, the oxalate route suffers from an incomplete precipitation reaction, leading to non-stoichiometric samples. The approaches using n-butylamine gels, and decomposition of permanganate complexes both involve complex wet chemical methods. Therefore the hydroxide route was considered the most suitable for the present study, as there have been no problems yet reported in its implementation.

The various reported properties of nickel manganite have been compared and discussed. There is some variation in the values for various parameters reported in the literature. The great majority of these can be ascribed to the poor preparation routes used in the studies involved. Much of the early work on nickel manganite was carried out on samples that had significant amounts of nickel oxide impurities, and deviations from correct stoichiometry. These shortcomings have only become apparent after later work highlighted the importance of sample purity in obtaining correct physical properties. The fact remains however, that the number and scope of studies that were considered to offer valid conclusions on properties of pure material was small. This was due in no small part to the persistent use of inadequate methods, particularly by those researchers investigating prototype device properties.

The various parameters relating to the crystal structure of nickel manganite have been determined relatively consistently by most researchers, with a lattice parameter and oxygen parameter of approximately $a = 8.39$ Å, and $u = 0.388$ respectively. Both these parameters have been found to be slightly dependent upon the cation distribution, characterised by the inversion parameter, ν. The inversion parameter has in turn, been found dependent upon the preparation conditions, notably the cooling rate. The charge state of the cations has been studied extensively, as it has a bearing on the industrially important transport properties. The configuration of Brabers [20] has been generally accepted.
The significant remaining questions about nickel manganite are largely concerned with the magnetic behaviour at low temperatures, and therefore form the motivation for much of the experimental work presented in chapter 6. Several things are not in doubt; nickel manganite is a ferrimagnet below a Curie temperature between 100 K and 160 K, the dominant interaction is between the A, and B sites, and a further transition occurs at lower temperatures. The relationship between the Curie temperature and other sample parameters has not been determined conclusively, due mostly to the imperfect preparation conditions described above. There is obviously some doubt as to the nature of the low temperature magnetic state, with several conflicting models having been proposed. The evidence in support of these models is often doubtful, and some is based upon assumptions now know to be in error. In particular, much of the work of the Saclay group (Boucher *et al.*, Buhl *et al.*, [3, 18, 19, 7, 8, 33, 9]), was based upon the assumption that orbital contributions to moment of the various ions are completely quenched by the crystal field, and all of the manganese was in the 3+ oxidation state ($3d^4$), with a moment of 4 μ_B. This is now not thought to be the case (see section 5.3). Many of the details of the low temperature magnetic structures proposed by the Saclay group seem to be attempts to accurately reconcile the measured magnetic moment, with that expected by the proposed models. In particular the overall angle between the A and B site total magnetic moments seems to be at odds with the high symmetry of the spinel crystal structure. No attempt was found in the many papers published by this group, to explain the origin of this non-collinear state in terms of interactions between the various ionic species present.

To further complicate matters, short range ordering has been observed in nickel manganite, also dependent upon preparation conditions, and thought to have an influence on both the conductivity mechanism, and possibly the magnetic properties.

References

1. Sinha, A. P. B., Sanjana, N. R. and Biswas, A. B., *Acta Cryst.* **10** (1957) 439.
2. Mehandjiev, D., *Applied Catalysts A* **206** (2001) 13.
3. Boucher, B., *C. R. Hebd. Seances Acad. Sci.* **249** (1957) 514.
4. Baltzer, P. K. and White, J. G., *J. App. Phys.* **29** (1958) 445.
5. Renault, N., Baffier, N. and Huber, M., *J. Solid State Chem.* **5** (1972) 250.
6. Meenakshisundaram, A., *et al.*, *Phys. Stat. Sol. A* **69** (1982) K15.
7. Boucher, B., Buhl, R. and Perrin, M., *C. R. Hebd. Seances Acad. Sci.* **263** (1966) 344.
8. Boucher, B., Buhl, R. and Perrin, M., *Acta Cryst.* **B25** (1969) 2326.
9. Boucher, B., Buhl, R. and Perrin, M., *J. Phys. Chem. Solids* **31** (1970) 363.
10. Brabers, V. A. M. and Terhell, J. C. J. M., *Phys. Stat. Sol. A* **69** (1982) 325.
11. Brabers, V. A. M., Van Setten, F. M. and Knapen, P. S. A., *J. Solid State Chem.* **49** (1983) 93.
12. Macklen, E. D., *J. Phys. Chem. Solids* **47** (1986) 1073.
13. Singh, J. and Ram, R. S., *Phys. Stat. Sol. A* **158** (1996) 73.
14. Azaroff, L. L., *Z. Kristallographie* **112** (1959) S33.
15. O'Keefe, M., *J. Phys. Chem. Solids* **21** (1961) 172.
16. Larson, E. G., Arnott, R. J. and Wickham, D. G., *J. Phys. Chem. Solids* **23** (1962) 1771.
17. Wickham, D. G., *J. Inorg. Nucl. Chem.* **26** (1964) 1369.
18. Villers, G. and Buhl, R., *C. R. Hebd. Seances Acad. Sci.* **260** (1965) 3406.
19. Boucher, B., Buhl, R. and Perrin, M., *C. R. Hebd. Seances Acad. Sci.* **263** (1966) 785.
20. Brabers, V. A. M., *Phys. Stat. Sol. A* **12** (1972) 629.
21. Bhandage, G. T. and Keer, H. V., *J. Phys. C* **9** (1976) 1325.
22. Gillot, B., *et al.*, *Mat. Chem. Phys.* **24** (1989) 199.
23. Tang, X., Manthiram, A. and Goodenough, J. B., *J. Less Comm. Metals* **156** (1989) 357.
24. Legros, R., Metz, R. and Rousset, A., *J. Mat. Sci.* **25** (1990) 4410.
25. Gillot, B., *et al.*, *Mat. Chem. Phys.* **26** (1990) 395.
26. Jung, J., *et al.*, *J. Eur. Ceramic Soc.* **6** (1990) 351.
27. Topfer, J., *et al.*, *Phys. Stat. Sol. A* **134** (1992) 405.
28. Gillot, B., *et al.*, *Solid State Ionics* **58** (1992) 155.
29. Baudour, J. L., *et al.*, *Physica B* **180 & 181** (1992) 97.
30. Martin de Vialdes, J. L., *et al.*, *Mat. Res. Bulletin* **29** (1994) 1163.
31. Asbrink, S., *et al.*, *J. Phys. Chem. Solids* **58** (1997) 725.
32. Asbrink, S., *et al.*, *Phys. Rev. B* **57** (1998) 4972.
33. Buhl, R., *J. Phys. Chem. Solids* **30** (1969) 805.
34. Padalia, B. D. and Krishnan, V., *Phys. Stat. Sol. A* **25** (1974) K177.
35. Csete de Gyorgyfalva, G. D. C., *et al.*, *J. Eur. Ceramic Soc.* **19** (1999) 857.
36. Lindner, F. and Feltz, A., *J. Eur. Ceramic Soc.* **11** (1993) 269.
37. Parlak, M., *et al.*, *J. Mat. Sci. Lett.* **17** (1998) 1995.
38. Parlak, M., *et al.*, *Thin Solid Films* **345** (1999) 307.
39. Schmidt, R., *et al.*, *Key Engineering Materials* **206-213** (2002) 1417.
40. Feltz, A., Topfer, J. and Schirrmeister, F., *J. Eur Ceramic Soc.* **9** (1992) 187.
41. Devale, A. B. and Kulkarni, D. K., *J. Phys. C* **15** (1982) 899.
42. Islam, M. S. and Catlow, C. R. A., *J. Phys. Chem. Solids* **49** (1988) 119.
43. Megaw, H. D., *Crystal Structures: A Working Approach.* 1st Edition. Studies in Physics and Chemistry. Vol. 10, ed. Stevenson, R. and Whitehead, M.A. Published by; W. B. Saunders Company, Philadelphia (1973)
44. Néel, L., *Ann. Phys.* **3** (1948) 137.
45. Yafet, Y. and Kittel, C., *Phys. Rev.* **87** (1952) 290.

46. De Gennes, P.-G., *Phys. Rev.* **118** (1960) 141.
47. Boucher, B., Buhl, R. and Perrin, M., *J. Phys. Chem. Solids* **30** (1969) 2467.
48. Anderson, P. W., *Phys. Rev.* **102** (1956) 1008.
49. Cowley, J. M., *J. App. Phys.* **21** (1950) 24.
50. Novak, P., *J. Phys. Chem. Solids* **30** (1969) 2357.
51. Elbadraoui, E., *et al.*, *Phys. Stat. Sol. B* **212** (1999) 129.
52. Freud, P. J., *Phys. Rev. Lett.* **29** (1972) 1156.
53. Fritsch, S., *et al.*, *Solid State Ionics* **109** (1998) 229.
54. Schmidt, R. and Brinkman, A. W., *Int. J. Inorg. Mat.* **3** (2001) 1215.
55. Basu, A., *et al.*, *J. App. Phys.* **92** (2002) 4123.

Chapter 6

Experimental work on $NiMn_2O_4$

6.1 Study of the optimum preparation conditions for $NiMn_2O_4$

It is clear from even a cursory examination of the published literature (see chapter 5), that there was a wide variety of preparation routes employed, and samples were subjected to many different firing schedules. Serious problems in terms of sample purity have been identified with the majority of preparation routes, and also the temperatures used. In many cases, these problems were only identified comparatively recently, with the advent of improved analysis tools, and in particular the greater resolution achievable in diffraction experiments. This has lead to a great deal of confusion present in published reports, concerning the stability or otherwise of $NiMn_2O_4$ and related compounds [1-34]. The contaminated samples that must have been produced in the majority of studies have given rise to a wide range of reported material characteristics (reviewed in chapter 5). In many cases the published data is not sufficient to determine the quality of the samples used, so it is not possible to determine which of the range of reported characteristics are those of pure nickel manganite. Due to this situation, a great deal of effort was directed towards producing pure samples in the present study, by the best possible method. This enabled the definite determination of material characteristics from samples of verified purity.

6.1.1 Precursor material

Mixed oxide route

A preliminary investigation was carried out using the mixed oxide route, following the procedure of Schmidt and Brinkman [35]. An X-ray diffraction pattern of the resulting compound is shown in Figure 6.1. All X-ray diffraction data was taken using a Siemens D5000 diffractometer situated in the Department of Chemistry, University of Durham. The data was collected in the range $10\,° \leq 2\theta \leq 120\,°$, with a step size of 0.02 °. All of the patterns that were analysed by the Rietveld technique were recorded over a period of 12 hours, and the height of the most intense peak ranged from approximately 5000 to

16000 counts. The radiation source was a copper X-ray tube, with a main wavelength of $K_{\alpha 1}$ = 1.54056 Å, and a subsidiary wavelength of $K_{\alpha 2}$ = 1.54439 Å.

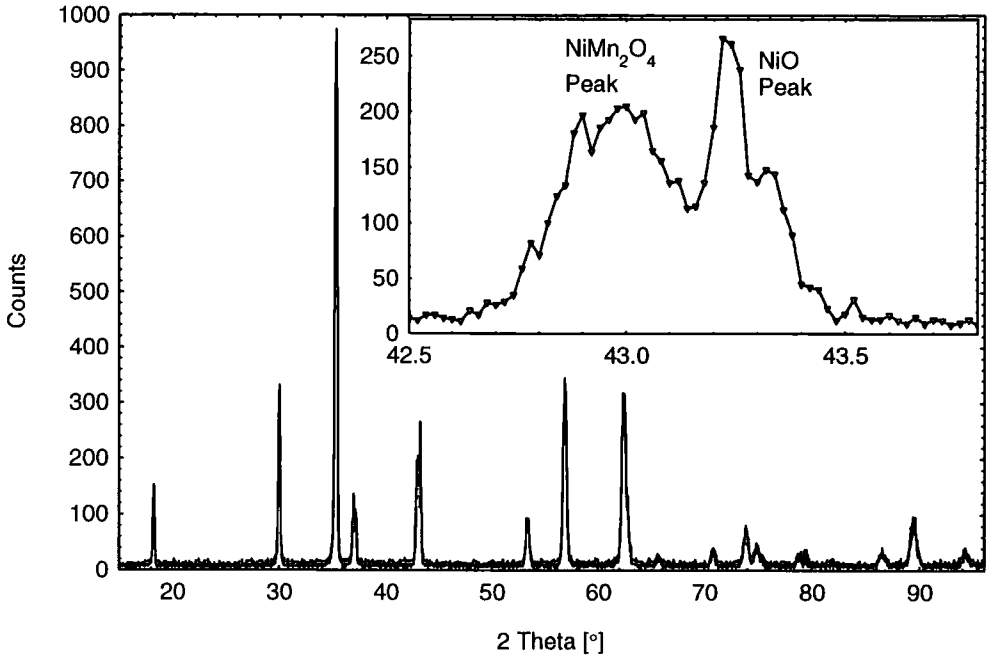

Figure 6.1. X-ray diffraction pattern for $NiMn_2O_4$ prepared from mixed oxides. The sample was fired at 1200 °C for 24 hours, followed by 24 hours at 800 °C. Data was taken over a period of 1 hour. Inset; Detail of the (400) peak, showing the impurity peak from NiO.

All the obvious peaks shown correspond to allowed reflections for $NiMn_2O_4$, however closer inspection of a number of peaks show the presence of NiO impurities. Detail of the (400) peak is shown, and similar impurity peaks are found adjacent to the (222), (440), and (444) peaks. The mixed oxide route was rejected due to the persistent presence of nickel oxide impurities in samples prepared at the temperatures reported in the literature (~ 800 °C). This was thought to be due to the incomplete mixing of the nickel and manganese oxides, and the low mobility of the metal atoms at the relevant growth temperatures. This leads to incomplete reactions, even after long firing times, most noticeably the continued presence of NiO. If the firing temperature is increased to 1200 °C, in order to speed up the reaction, NiO segregates out, and shows little tendency to be re-absorbed by annealing at 800 °C [5].

In view of the reported problems inherent in the mixed oxide route (see section 5.1.1), and results of these preliminary investigations, it was decided to

use a different preparation route. The available literature was investigated, as reported in chapter 5. It was decided that the routes involving mechanical mixing of solid precursors (oxide, carbonate, or nitrate) were unsuitable, and the oxalate route was rejected due to the inability to obtain an accurate metals ratio. Of the other procedures described, the permanganate, and n-butylamine routes, involved chemical preparation that was impractical due to cost, and lack of expertise. Therefore, the hydroxide route was selected as most suitable for preparing $NiMn_2O_4$. The procedure in section 6.1.2 was followed to make all of the samples (apart from preliminary work using a mixed oxide route). The quantities of starting materials were made as large as possible, for a number of reasons;

Uniformity.

Since a comparative study was to be undertaken, it was advantageous to have the starting materials of each experiment identical. Therefore, it was advantageous that large amounts of mixed hydroxide were prepared as one, then split into many smaller units.

Error reduction.

In order to reduce the effect of any errors or inaccuracies in weighing the raw materials. The masses required were 4 orders of magnitude above the resolution of the balance used at all times.

Convenience.

To speed up the progress of the series of experiments. Each batch of mixed hydroxides took 3-4 days to make, so making enough for one experiment only would have caused unacceptable delays.

6.1.2 Preparation conditions

In order to co-precipitate nickel and manganese hydroxides a suitable, soluble source of nickel and manganese ions was required. Also required, was some way of precipitating them from aqueous solution. Acetates were available in suitable quantities, at reasonable cost and purity, and were very soluble in water. The precipitation reaction used was;

$$Ni(CH_3CO_2)_2 + 2(Mn(CH_3CO_2)_2) + 6(NaOH) \rightarrow$$
$$Ni(OH)_2\downarrow + 2Mn(OH)_2\downarrow + 6(Na(CH_3CO_2))$$

Hydrated acetates were used as starting material. The most hydrated form was chosen if applicable, to minimise any errors due to absorption of additional water. This was the tetra-hydrate in both cases. The metal acetates were obtained from Aldrich chemicals, and the quoted purity was 99 + %. Sodium hydroxide was obtained from Fisher Chemicals, with a purity of 99 + %. Formula weights for $Ni(CH_3CO_2)_2{\cdot}4(H_2O)$, and $Mn(CH_3CO_2)_2{\cdot}4(H_2O)$, were 248.86 g, and 245.09 g respectively. It was decided to make batches of 0.0279 mol (nickel basis), as this gave approximately 6.3 g of mixed hydroxide precipitate after washing and drying. This was then split into 5 lots of 1.25 g (with a small amount of excess). The calculated masses of acetates needed were 6.9432 g of nickel acetate, and 13.3970 g manganese acetate. The resolution of the chemical balance used was 0.1 mg, and quantities were weighed to an accuracy of 1 mg. The weighed acetates were dissolved in 0.5 litres of distilled water. A slight excess (8 g) of sodium hydroxide in solution (0.5 litres) was used in order to ensure complete precipitation. This was slowly added from a burette to the continuously stirred acetate solution. This process took between 4 and 8 hours. The resulting mixture was stirred for a further 4-8 hours, and then suction filtered. The filtrate was repeatedly washed with distilled water to remove any remaining sodium acetate or unreacted sodium hydroxide. Once this was complete, the mixed hydroxides were dried at 120 °C overnight. These were then ground in a pestle and mortar, washed with distilled water, and dried overnight again. An analysis of the resulting intimately mixed hydroxides by X-ray diffraction is presented in Figure 6.2. The absence of any well-defined Bragg reflections indicates that the crystal size is extremely small, or that the sample is amorphous. Comparing this with the X-ray pattern obtained from commercial nickel and manganese oxides (shown in Appendix 1), it is clear that the crystallite size in the oxides is much larger. A small crystallite size is advantageous, as this implies a large surface area, and therefore a much higher reactivity.

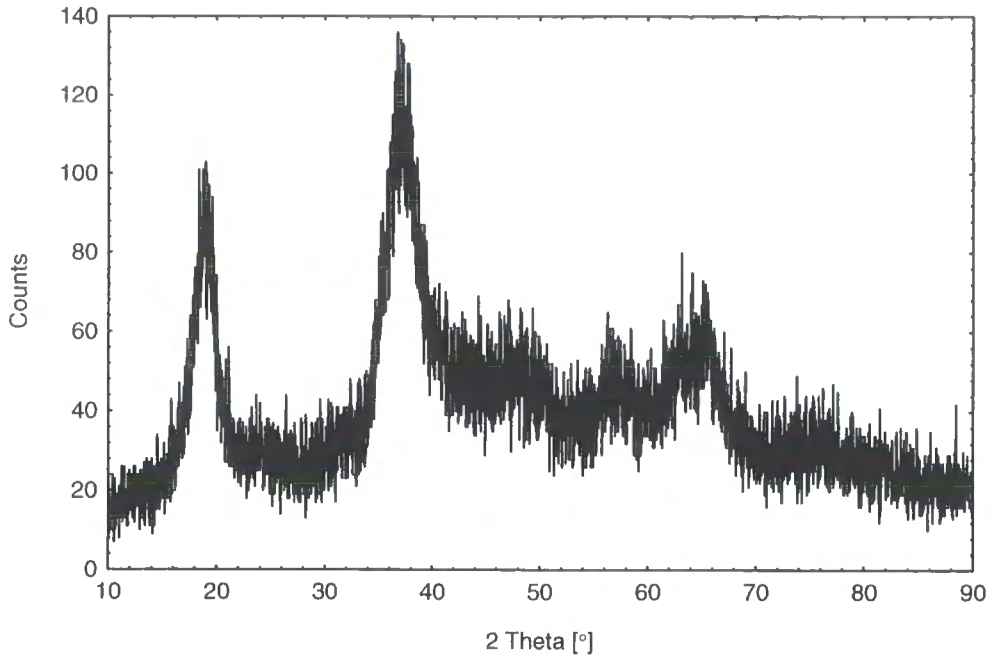

Figure 6.2. X-ray diffraction pattern for the mixed hydroxide precursor material (batch 1).

6.2 Determination of the correct preparation temperature for single phase $NiMn_2O_4$

6.2.1 Firing temperatures

In order to determine the optimum preparation temperature using mixed hydroxides, samples of the mixed hydroxides were fired at a range of different temperatures. The size of sample used was 1.25 g of dried mixed hydroxide. This was found to produce enough material, once fired, to fill a standard sample holder for use in X-ray diffraction. The samples were produced in an essentially random order, to eliminate any effects due to different batches of starting material having different properties, or any build up of contaminants in the crucibles used. All the samples were prepared in the same manner;

1. Load approximately 1.25 g mixed hydroxide precursor powder in a ceramic crucible, into a furnace at room temperature.
2. Heat to the required temperature at a rate of 10 °C per minute.
3. Dwell at the required temperature for 20 hours.
4. Remove the sample and crucible from the furnace, and leave to cool to room temperature.

The samples were then analysed by X-ray diffraction, scanning electron microscopy, and vibrating sample magnetometry (reported in section 6.6). The temperatures and originating precursor batches of the first set of samples is shown in Table 6.1.

Sample Firing temperature [°C]	Precursor batch used	Sample sequence number
200	3	13
400	1	5
600	1	1
700	1	6
750	1	7
770	7	14
780	2	9
800	1	3
800	2	8
820	2	10
850	2	11
900	1	4
1000	1	2
1100	2	12

Table 6.1. Firing schedule for temperature dependent experiments.

6.2.2 X-ray diffraction

X-ray diffraction was used to study the composition of the samples. In particular, if there were any identifiable impurities present, and to confirm that the crystal structure of nickel manganite agreed with past reports in the literature [5, 9]. The limit of detection for impurity phases was expected to be 1 ~ 3%, for crystalline impurities. Nickel oxide was a possible impurity phase at high temperatures (above 800 °C) [6], however the expected diffraction patterns from this, and nickel manganite, have a large amount of overlap. From reports in the literature [5, 9], it was expected that 800 °C would be close to the optimum firing temperature for the production of pure nickel manganite. It was also expected that a number of different impurities would be found at lower temperatures. This can be seen by inspection of the data shown in Figure 6.3, showing a part of the powder diffraction patterns collected from the samples fired at 600 °C, 800 °C, and 1100 °C. From this data, it can be concluded that the reaction has not gone to completion in the sample fired at 600 °C, as there are peaks present that cannot be assigned to the known structure of nickel manganite. This can be seen in Figure 6.4, which shows a part of the diffraction pattern from

the sample fired at 600 °C. There are peaks visible in the data that can be accounted for by the reflections from $NiMn_2O_4$, α-Mn_2O_3 [36], Mn_3O_4 [37], and $NiMnO_3$ [38].

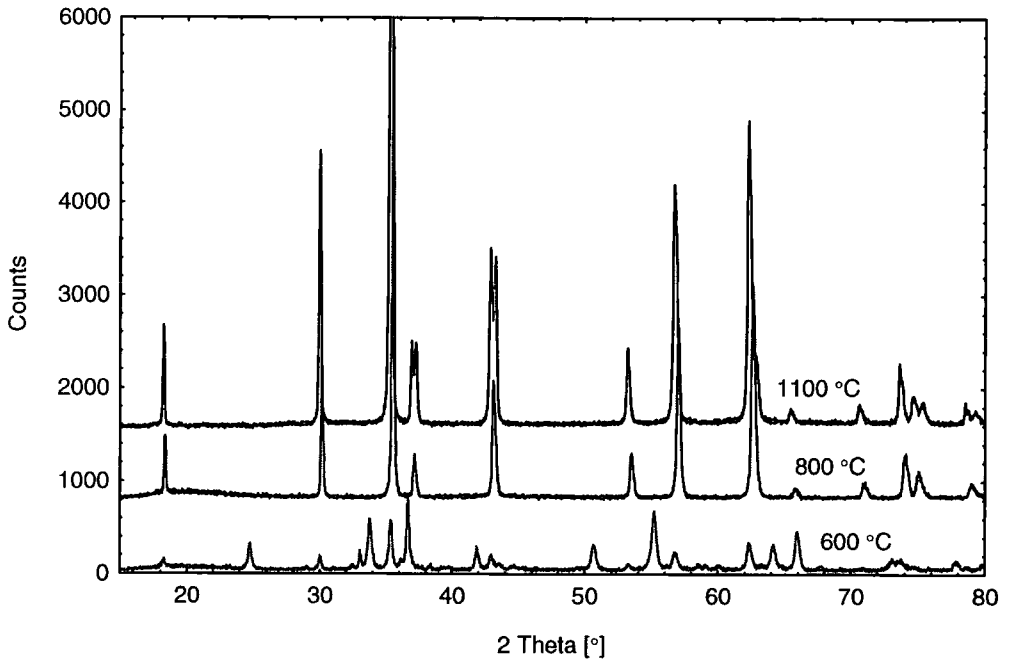

Figure 6.3. X-ray diffraction patterns for samples fired at 600 °C, 800 °C, and 1100 °C. The 1100 °C and 800 °C data have been offset for clarity.

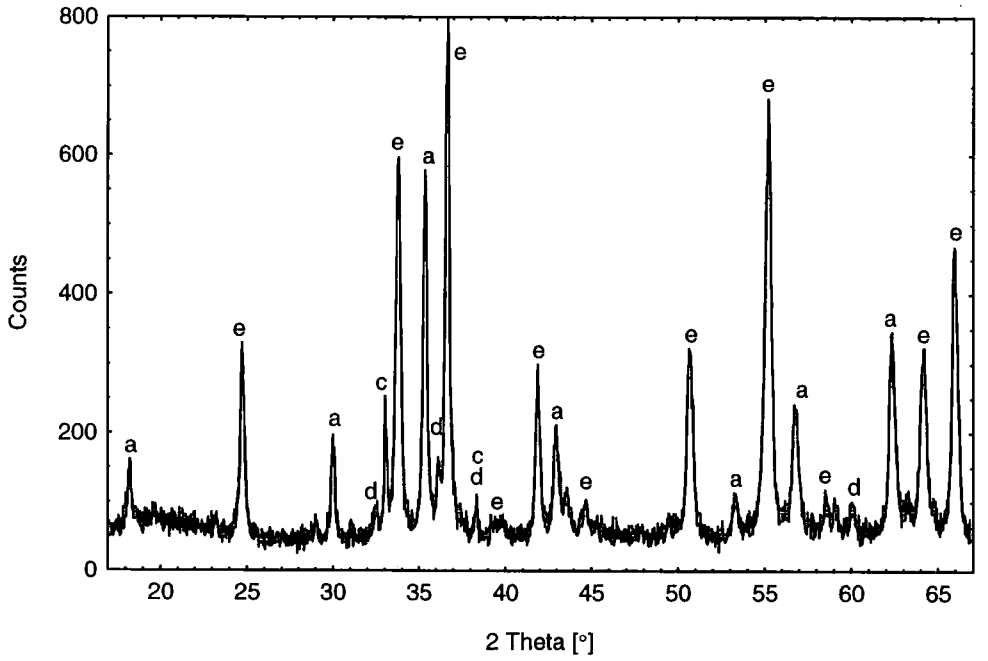

Figure 6.4. Detail of part of the X-ray diffraction pattern for a sample fired at 600 °C. The peaks are labelled accordingly; a – $NiMn_2O_4$, c – Mn_2O_3, d – Mn_3O_4, e – $NiMnO_3$.

The diffraction peaks are of lower intensity compared to the other datasets shown in Figure 6.3, and the measured peak widths are larger. This gives an indication of some combination of small crystallite size, mixed phase regions, and low crystallinity. All of these factors lead to the conclusion that chemical equilibrium had not been reached for the temperature (600 °C), in the time allowed (20 hours). Thus, it was inferred that the correct temperature for the formation of single-phase material was much higher than 600 °C. The 800 °C and 1100 °C data exhibit a much higher crystallinity, with well-defined peaks even at higher angles. This indicates that the relevant reactions have proceeded sufficiently, probably to a point not far from thermodynamic equilibrium. A close inspection of the 1100 °C dataset reveals that this sample shares the problem encountered in preliminary experiments, that of nickel oxide ($Ni_{(1-\delta)}O$ [39]), segregating out, thus forming a nickel-deficient spinel. This is expected from a published phase diagram [6], which shows the region of temperature in which the spinel is stable, increasing with manganese concentration. It is highly unlikely that the spinel would re-absorb any of this nickel oxide if held at such high temperatures for extended periods. The nickel oxide peaks are narrower than the spinel peaks, at a similar scattering angle. This indicates that the nickel oxide has formed into long-range ordered crystallites. The tendency for these to be re-absorbed at a lower temperature is probably low, as the nickel would have to then diffuse a considerable distance in order to establish a homogenous distribution. This has been reported in the literature [40], as one of the problems of the mixed oxide route.

6.2.3 Pattern decomposition

From inspection of the diffraction patterns obtained from various samples, the pattern taken from a sample fired at 800 °C showed the smallest number of identifiable diffraction peaks. This pattern was thus analysed first, as it appeared to be the simplest. There were 21 peaks identified, which were all modelled using a pseudo-Voigt profile function, $h(\theta)$ [41]. This function consists of a linear combination of Gaussian, G, and Lorentzian, L, profiles;

$$h(\theta) = \eta L + (1-\eta)G$$

The mixing parameter, $0 \leq \eta \leq 1$, was allowed to vary independently for each

peak. The other parameters necessary to describe the reflection profiles were the integrated intensity, I, profile width, Γ, and diffraction plane separation, d, for each peak. The background was described using a 4th order polynomial in diffraction angle, θ. All these parameters were initially treated as independent, giving 88 unknown variables. The only other inputs to the model were the wavelengths of the $K_{\alpha 1}$, and $K_{\alpha 2}$, emission lines of the copper X-ray tube, and the intensity ratio of these lines. The difference between the observed and calculated diffraction pattern was minimised using the least squares method.
The resulting fit to the data is shown in Figure 6.5, along with a plot of the difference between the calculated and observed data.

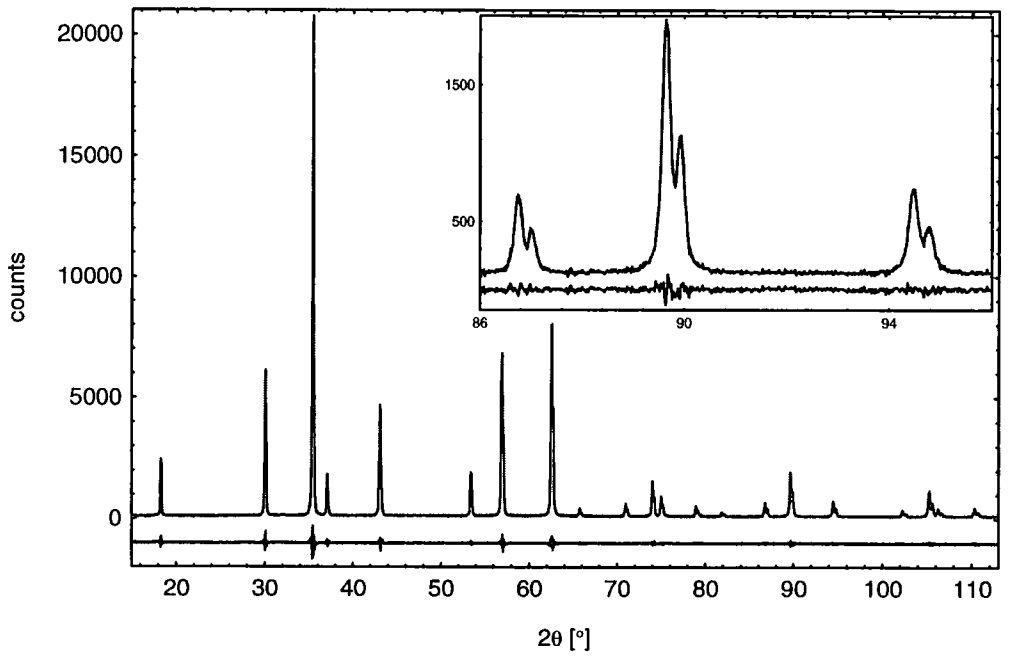

Figure 6.5. X-ray powder diffraction pattern for a sample of mixed nickel, and manganese hydroxides fired at 800 °C for 20 hours. Also shown is a fit to this data, and a plot of the difference between the model and fit. This latter curve has been offset for clarity.

The R-values of this fit are given, using the standard notation as described in section 1.4 of Young [41], as R_p = 6.03 %, R_{wp} = 8.34 %, R_e = 6.70 %, giving a 'goodness of fit', S = 1.244. These values were considered to indicate a satisfactory fit to the observed data, according to the criterion of Young (p 21 [41]). The values of the profile width, Γ, arrived at from the fitting process are shown in Figure 6.6. The solid line shown is a model of the Γ behaviour commonly used in Rietveld refinement, after Caglioti *et al.*, [42]. This was obtained by a least squares fit to the datapoints shown, giving equal weight

to each. The Caglioti model for Γ was incorporated into the data analysis, and the values of the parameters U, V, and W shown in Figure 6.6 were used as starting values.

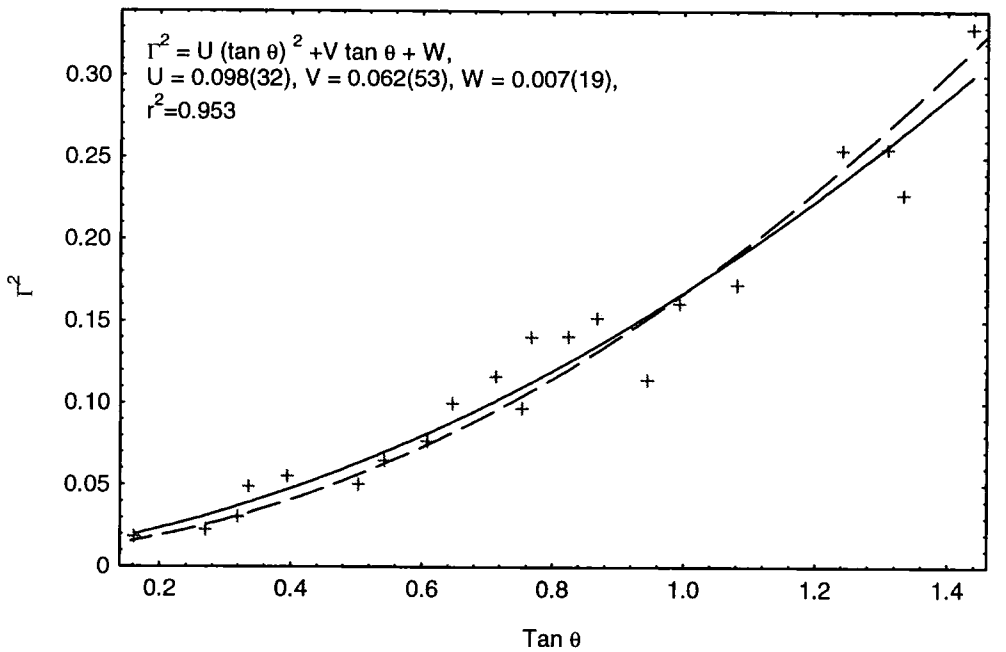

Figure 6.6. Profile width values for all diffraction peaks, estimated using the least squares method. The solid line is a least squares fit to the datapoints shown, after Caglioti *et al.*, [42], and the dashed line is that obtained from a least squares fit to the data shown in Figure 6.5.

This resulted in a reduction of the number of independent variables in the model from 88 to 70. The least squares minimisation was performed again, yielding R-values of; R_p = 6.07 %, R_{wp} = 8.38 %, R_e = 6.73 %, giving a 'goodness of fit', of S = 1.247. These values are slightly increased compared to the model with 88 parameters, and were again considered to indicate a satisfactory fit to the data. The refined parameters U, V, and W were found to have values of 0.126, 0.0340, and 0.007 respectively. The resulting behaviour of Γ is shown in Figure 6.6 as the dashed line. The reason for the slight difference in the parameters U, V, and W was ascribed to the differing integrated intensities of the various peaks in the data, giving a different weighting to each value of Γ in the respective fitting procedures. Similarly, replacing the 21 individual values of the mixing parameter, η, with the function;

$$\eta = \eta_0 + \eta_1(2\theta)$$

as suggested by Young (p9) [41], meant a further reduction to 51 independent variables, and a slight increase in R-values, to; R_p = 6.37 %, R_{wp} = 8.87 %,

R_e = 6.80 %, giving a 'goodness of fit', S = 1.305. The parameters η_0, and η_1, were 0.66, and –0.0025 respectively when fitting to the data shown in Figure 6.5. The observed dependence of Γ, and η, on diffraction angle has no particular physical significance, i.e. there is no physical process implicit in the model. This is not the case for values of d, which are the inter-plane spacings in various sets of directions in the crystalline phase(s) present in the sample. Therefore, in order to model the distribution of values of d, reference has to be made to lattice parameters, and space group information. A detailed summary of the available reports of the structure of nickel manganite produced at temperatures around 800 °C is given in chapter 5, but numerous authors [3, 5-7, 9, 22, 26] give the space group as *Fd3m* (number 227 in the International Tables for X-ray crystallography [43]), and report values of the lattice parameter between 8.390 Å and 8.399 Å. Using the information in the space group description, the wavelength of the radiation employed ($\lambda_{K\alpha 1}$ = 1.540560 Å), and the median value of lattice parameter reported, a list of the calculated peak positions is given in Table 6.2 for various reciprocal space directions (*hkl*). Also shown in Table 6.2, is the list of observed peak positions, which have been matched up to the nearest calculated values, and the difference calculated. In all cases, the difference is no more than 3 times the step size of the observed data (0.02 °), has a mean of -0.037 °, and standard deviation of 0.011 °. There were no peaks observed that did not match closely to an expected peak position. However, there were a number of peaks expected, that were not observed. This was ascribed to the intensities being insufficient to observe. The above information was incorporated into the model used to analyse the data shown in Figure 6.5. For each peak, the d spacings were calculated from the lattice parameter, a, and the reciprocal lattice vector associated with that peak (as in Table 6.2);

$$d = \frac{a}{|hkl|}.$$

There was also a parameter added to account for any misalignment of the diffractometer used to take the data. This took the form of a zero offset parameter, θ_0;

$$\theta = \theta_0 + \sin^{-1}\left(\frac{\lambda}{2d}\right).$$

(*hkl*)	2θ [°] calculated	2θ [°] observed	$2\theta_{cal} - 2\theta_{obs}$ [°]
111	18.289	18.322	-0.033
220	30.083	30.120	-0.037
311	35.434	35.473	-0.039
222	37.066	37.119	-0.053
400	43.064	43.115	-0.051
331	47.150	-	-
422	53.424	53.463	-0.039
511, 333	56.949	56.985	-0.036
440	62.536	62.577	-0.041
531	65.752	65.784	-0.032
442	66.806	-	-
620	70.944	70.979	-0.035
533	73.980	74.007	-0.027
622	74.981	75.028	-0.047
444	78.943	78.999	-0.056
551, 711	81.879	81.908	-0.029
642	86.728	86.748	-0.020
553, 731	89.624	89.652	-0.028
800	94.452	94.484	-0.032
733	97.362	-	-
660, 822	102.259	102.273	-0.014
555, 751	105.238	105.264	-0.026
662	106.241	106.279	-0.038
840	110.316	110.372	-0.056

Table 6.2. Observed and calculated peak positions for the data shown in Figure 6.5. The peak positions were calculated using the symmetry operations for space group *Fd3m*, a lattice parameter of 8.3950 Å, and an incident X-ray wavelength of 1.540560 Å.

These steps meant a further reduction to 32 independent variables, and another slight increase in *R*-values, to; R_p = 6.43 %, R_{wp} = 9.06 %, R_e = 6.83 %, giving a 'goodness of fit', of S = 1.326. The resulting lattice parameter, a, and zero offset θ_0, were found to be 8.3903(2) Å, and 0.020(1) ° respectively when fitting to the data shown in Figure 6.5.

6.2.4 Rietveld analysis of the sample fired at 800 °C

Analysis by the Rietveld method consists of the last step in the analysis process started in the preceding section, in which an expression for the integrated intensity of the peaks is introduced into the model. This is usually by far the most complex of the peak parameters to model, due to the large number of variables that can affect the calculated intensities, and the differing dependencies of each peak intensity on these variables. The factors that sum to produce the observed integrated intensities are [41] (The subscript K represents the Miller indices, *h, k, l,* for a Bragg reflection);

L_K, which contains the Lorentz, polarisation, and multiplicity factors,

$|F_K|^2$, the square of the structure factor for the K^{th} Bragg reflection,

P_K, the preferred orientation function, and

A, the absorption factor (which is constant for the diffraction geometry used).

This stage in the analysis was carried out using the dedicated computer programs, FULLPROF, and WinPLOTR [44]. These programs were chosen above others such as GSAS [45], and RIETAN [46], due to the fact that both X-ray, and neutron diffraction data could be analysed, and they ran on Windows™ based PC hardware, which was readily available. The various parameters determined in the preceding section were directly transferable to the models used in FULLPROF, and were used as the initial parameters in the analysis by the Rietveld method. The background function was transferred directly, and not refined further, and the inversion parameter was fixed at a value of 0.8. The value of the inversion parameter was not believed to have a large effect on the calculated intensities, as the contrast in the scattering cross sections of nickel and manganese is small. The value of 0.8 was used as a value representative of those reported [6, 7, 9, 22, 26]. Details of the various steps in the refinement are shown in Table 6.3.

	Initial	Cycle 1	Cycle 2	Cycle 3	Cycle 4	Cycle 5	Cycle 6	Cycle 7
a	8.3903	-	8.39046(9)	8.39043(9)	8.39045(8)	-	-	-
U	0.127	-	-	-	-	-	0.178(12)	0.115(14)
V	0.0351	-	-	-	-	-	0.004(11)	0.046(12)
W	0.0072	-	-	0.00263(39)	0.00261(39)	0.00254(38)	0.0067(22)	0.0042(23)
η_0	0.651	-	-	-	-	-	-	0.351(30)
η_1	-0.0023	-	-	-	-	-	-	0.00256(57)
x (O)	0.264	-	-	0.26408(17)	0.26394(19)	0.26396(19)	0.26400(19)	0.26407(17)
B (8a)	0.6	-	-	-	-	0.588(29)	0.551(29)	0.554(26)
B (16d)	0.6	-	-	-	-	0.353(20)	0.335(21)	0.373(21)
B (32e)	0.6	-	-	-	0.845(63)	0.863(61)	0.832(61)	0.827(54)
Disp.	0	-0.0338(3)	-0.0311(6)	-0.0314(6)	-0.0312(5)	-	-	-
R_p		7.11	7.06	6.82	6.78	6.68	6.47	5.96
R_{wp}		9.42	9.35	9.27	9.05	9.0	8.69	8.27
S		1.43	1.42	1.37	1.37	1.31	1.30	1.29

Table 6.3. Results from the first 7 cycles of the Rietveld refinement carried out on the data in Figure 6.5.

The parameter turn-on sequence was in accord with that suggested by Young [41]. The standard deviations in Table 6.3 have not been corrected for correlated residuals, the factor required being 2.72, reported from FULLPROF. The correlation matrix at the 7th step in the refinements is shown in Table 6.4.

	B(8a)	Scale	B(16d)	B (32e)	W	x (O)	U	V	η_0	η_1
B(8a)	100	64	41	41	-2	-12	6	0	29	-30
Scale	64	100	73	41	-2	-10	4	-1	34	-29
B(16d)	41	73	100	25	-5	0	4	1	37	-39
B (32e)	41	41	25	100	-7	-43	0	5	17	-18
W	-2	-2	-5	-7	100	14	76	-93	12	-11
x (O)	-12	-10	0	-43	14	100	10	-12	5	-4
U	6	4	4	0	76	10	100	-91	51	-55
V	0	-1	1	5	-93	-12	-91	100	-36	36
η_0	29	34	37	17	12	5	51	-36	100	-93
η_1	-30	-29	-39	-18	-11	-4	-55	36	-93	100

Table 6.4. Correlation Matrix resulting from cycle 7 of the Rietveld refinement procedure outlined in Table 6.3.

This reveals a number of large correlations between refined parameters. The largest correlations are those between; η_0 - η_1 , $W - V$, and $U - V$. These were not altogether unexpected, as the origin of the functional forms of both the profile width, Γ, and the mixing parameter, η, both are centred on $2\theta = 0$ °. A close inspection of the plotted difference between the data, and calculated fit reveals several features, as shown in Figure 6.7a.

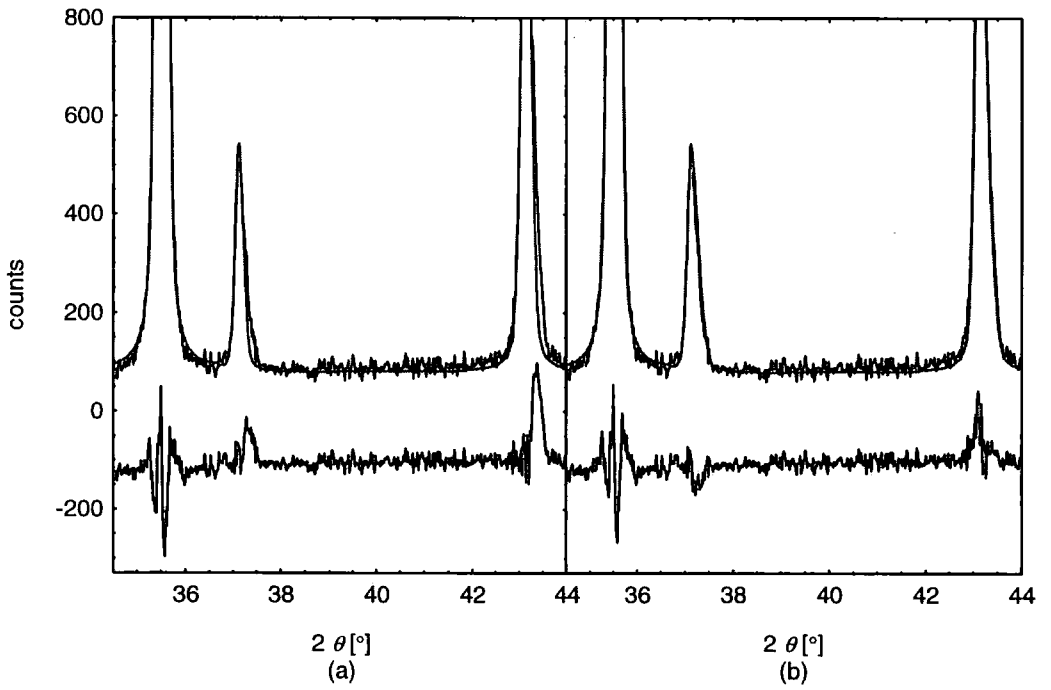

Figure 6.7. Detail of the data shown in Figure 6.5, and fit to this data after (a) cycle 7, and (b) cycle 8, and plots of the difference between the data and fit. This latter curve has been offset for clarity.

There are obvious discrepancies between the data and fit at $2\theta = 37.4$ °, and $2\theta = 43.4$ °. There is also a less pronounced feature centred at $2\theta = 75.5$ °. As

noted above, nickel oxide has previously been found as an impurity phase [6]. A diffraction pattern from nickel oxide can be found in Appendix 1. Some of the diffraction peaks from nickel oxide correspond to the discrepancies identified in Figure 6.7a. Therefore, nickel oxide was included as a second phase in the model used for Rietveld refinement. Sasaki *et al.*,[39] give the space group of nickel oxide as *Fm3m* (number 225 in the International Tables for X-ray crystallography [43]), and report a value of the lattice parameter of 4.178(1) Å. Adopting this information, and setting the profile coefficients of the nickel oxide phase the same as those of nickel manganite, the amount of nickel oxide (the scale factor) was refined. The results of this stage of refinement are presented in Table 6.5. The lattice parameter of nickel oxide was not refined.

	(Cycle 7)	Cycle 8
Scale ($NiMn_2O_4$) x 10^4	1.528(10)	1.4930(84)
Scale (NiO) x 10^4	0	1.399(77)
U	0.115(14)	0.120(11)
V	0.046(12)	0.353(97)
W	0.0042(23)	0.0063(20)
η_0	0.351(30)	0.371(25)
η_1	0.00256(57)	0.00151(48)
x (O)	0.26407(17)	0.26418(17)
B (8a)	0.554(26)	0.558(26)
B (16d)	0.373(21)	0.375(21)
B (32e)	0.827(54)	0.835(53)
R_p	5.96	5.91
R_{wp}	8.27	8.25
S	1.29	1.23

Table 6.5. Results from the 8th cycle of the Rietveld refinement of the data in Figure 6.5.

The proportion of the sample that was nickel oxide was calculated to be 1.09(6) %. The error on this is estimated to be approximately ± 1 %, due to a number of factors. Absorption effects, where scattered photons from one phase are re-absorbed by the other phase, phase concentration gradients [47], and effects due to different size grains at the sample surface are possible factors. The calculated value also does not take into consideration any amorphous content present, although this is estimated to be minimal due to the low incoherent scattering (background) in the data. Inspection of the data, a portion of which is shown in Figure 6.7b reveals that the discrepancies shown in Figure 6.7a have been eliminated almost entirely by the addition of a nickel oxide phase to the Rietveld refinement model. The *R* values, and goodness of fit indicator have also

fallen significantly as a result of this. A plot of the final (after Cycle 8) fitted data, and error on the fit is given in Figure 6.8. There are no further obvious discrepancies between the observed and calculated plots.

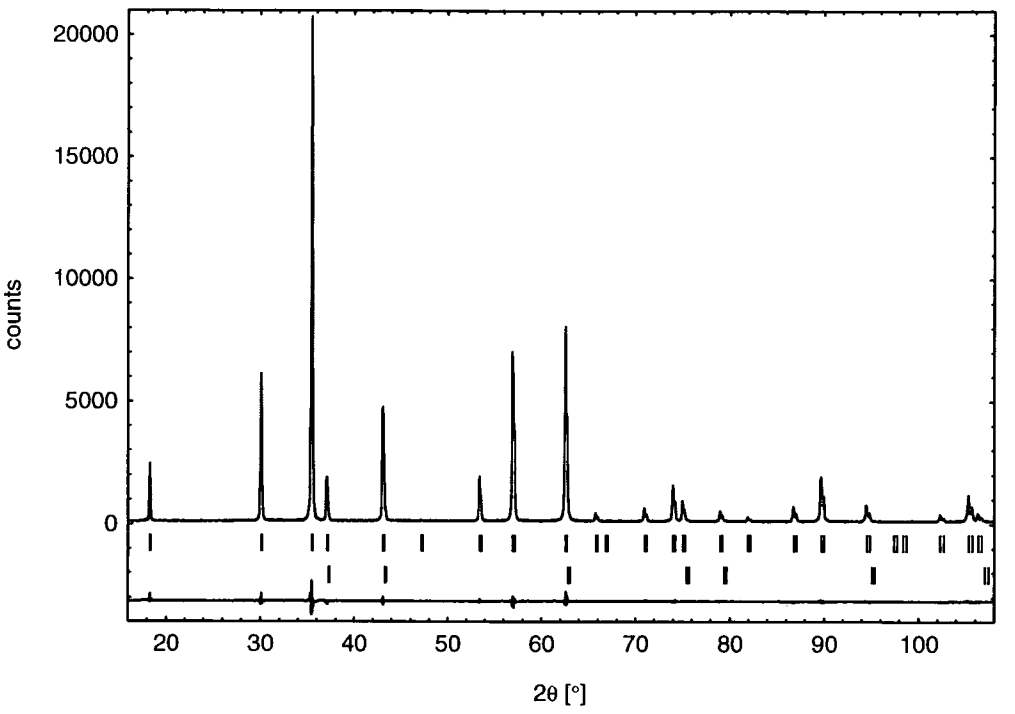

Figure 6.8. X-ray diffraction data collected on the sample fired at 800 °C, and a fit to the data using the Rietveld technique. The difference curve has been offset for clarity. The upper line of marked reflections correspond to the structure of $NiMn_2O_4$ and the lower line to that of NiO.

6.2.5 Validation of the Rietveld technique

In order to have any confidence in the results of the Rietveld refinement process, a number of tests were carried out using FULLPROF [44]. Included as one of the options in the program was the ability to generate simulated datasets using a set of input parameters identical to the set being refined. This facility incorporated the simulation of variations in the data due to the statistics of counting discrete events. A number of datasets were generated with a variety of input parameters, and then these simulated datasets were subjected to Rietveld analysis in a similar manner to the real data collected. 4 separate scenarios were considered;

1. No nickel oxide contamination present in the simulated data, but allowed for in the analysis.
2. No nickel oxide contamination present in the simulated data, nor allowed for in the analysis.

3. Nickel oxide present in the simulated data at 4%, and allowed for in the analysis.
4. Nickel oxide present in the simulated data at 4%,but not allowed for in the analysis.

The input parameters were chosen to be representative of those obtained from the refinements carried out on a number of nickel manganite samples. All of the initial parameters used in the refinement of the simulated datasets (except the nickel oxide percentage in runs 2 and 4) were identical to those used to generate the data. Despite this fact, considerable discrepancies became apparent due to the refinement process. In all 4 cases, the process of simulation and refinement was repeated 12 times, and the results averaged in order to determine the variation of the refined parameters. The initial parameters, and results from the refinements can be found in Appendix 2. By far the greatest differences between initial, and refined parameters were found in run 4, which also had a 'goodness of fit' indicator much higher than other runs. Unfortunately, run 4 represents the most likely scenario for much of the previous reported diffraction studies of nickel manganite. Only one of the literature reports (Wickham [6]) mentions the inclusion of nickel oxide as an impurity phase when refinements were carried out. Even the early (pre-Rietveld analysis) work, such as that of Boucher *et al.,* [9] may be suspect, as manual calculations were based upon observed integrated intensities of diffraction lines that were attributed entirely to a particular reflection of nickel manganite. The most serious errors present in the analysis of run 4 were an underestimate of the lattice parameter by 5 e.s.d.'s (estimated standard deviations), and the oxygen parameter by 3.6 e.s.d.'s. The cation temperature factors were also significantly wrong. The refined values were quite consistently in error, as indicated by the low values of the estimated error on the mean (based on 12 refinements).

Even in runs 1-3, where the 'goodness of fit', S = 1.01 indicated negligible differences between the simulated and refined datasets, there was a systematic bias evident in some of the refined parameters. In particular, the oxygen parameter was consistently underestimated by roughly 1 e.s.d., and all of the temperature factors were overestimated by varying amounts. The lattice parameter was reported with an acceptable level of accuracy in runs 1-3, in contrast with run 4. In the cases where the amount of nickel oxide was subject to

refinement, the results were consistently within 1 e.s.d., but with a small amount of systematic bias. The reported values for many of the parameters bear out the findings of Hill (Chapter 5, [41]), that e.s.d. values are only indicative of the measurement repeatability in a limited set of circumstances.

With the results from the validation experiments in mind, care was taken to identify any features possibly resulting from nickel oxide contamination when analysing both X-ray, and neutron diffraction data. This was done both by visual examination of the data at all stages of the analysis process, and the inclusion of nickel oxide as an additional phase present in Rietveld analysis. Even with this done, there remained the possibility that the e. s. d. values returned by the various Rietveld refinement software packages used, were insufficient to include the actual parameter values in the expected ranges. The severity of this effect was considered likely to be strongly dependent upon both the amount of nickel oxide present in a sample, and the accuracy to which this amount was determined.

6.2.6 Rietveld analysis of the samples fired at 700 °C to 1100 °C

All the datasets for the samples fired at different temperatures are shown in Figure 6.9. From this it can be seen that the impurity phases present in the sample fired at 600 °C are also present in some of the samples fired at higher temperatures. However, the impurity peak intensities quickly reduce in intensity as the firing temperature is increased. The peaks also become sharper, indicating an increase in crystallinity. The broad hump visible in the background data centred on $2\theta \sim 20$ ° diminishes, indicating a reduction of the amount of amorphous material present. The high temperature $Ni_{(1-\delta)}O$ impurities present in the sample fired at 1100 °C are to a lesser extent, also present in the samples fired at lower temperatures. This contamination is least visible in the data from the samples fired around 800 °C. Since the melting points of all the relevant phases are well above 1100 °C (see Appendix 2), it is unlikely that any metal is lost at the firing temperatures used (however see section 5.3). Therefore, the ratio of nickel to manganese should stay constant from sample to sample. The samples that show nickel oxide contamination are supposed to contain a nickel deficient spinel phase.

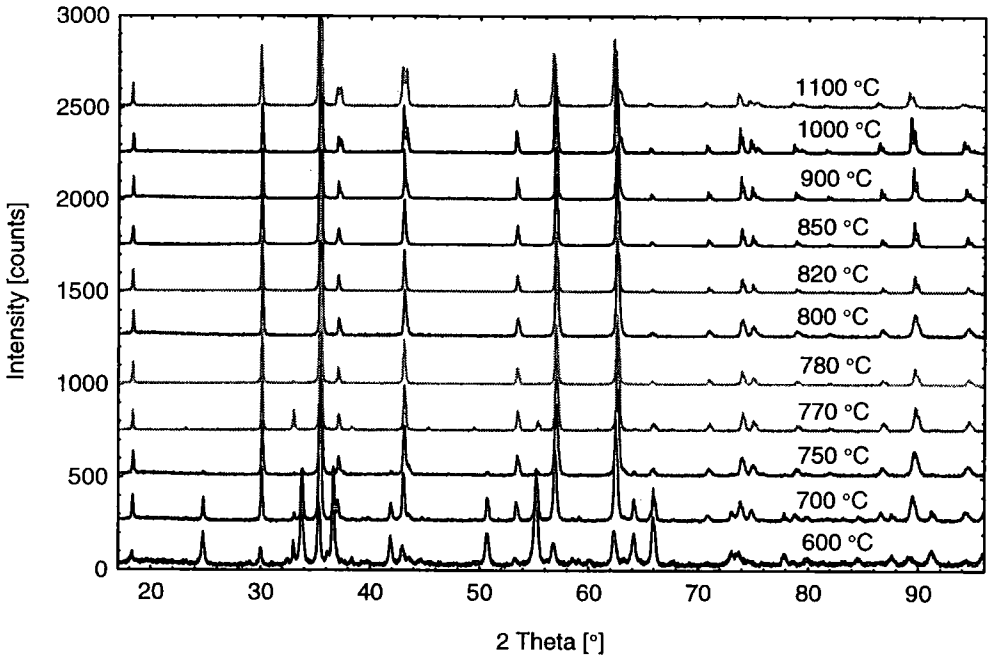

Figure 6.9. All of the X-ray diffraction patterns observed from samples fired at between 600 °C, and 1100 °C. All the datasets have been normalised to an intensity of 1000 for the strongest peak, and are offset for clarity.

In view of reports in the literature [6], the existence of a manganese deficient (nickel rich) spinel phase is considered unlikely at any temperature. Of the impurity phases identified in samples fired at temperatures below 800 °C, the most abundant can be indexed by the structure of $NiMnO_3$. In common with many of the other impurity compounds considered, this structure is believed [6] to be able to accommodate a considerable amount of non-stoichiometry. This of course will go virtually undetected by analysis of X-ray powder diffraction data, for the same reason that the inversion parameter of $NiMn_2O_4$ cannot be determined. Therefore, it is suggested that the actual impurity phase present at lower temperatures is;

$$Ni_{(1-\beta)}Mn_{(1+\beta)}O_3$$

with $0 \leq \beta \leq 1/3$. This, in combination with the spinel, NiO, and a small amount of α- Mn_2O_3 (as determined from inspection of the data, and as reported by Drouet *et al.*, [48]), allows the correct overall nickel to manganese ratio to be preserved in the low temperature samples.

Considering the phases identified at various firing temperatures (listed in Table 6.6), it can be seen that there is an overall loss of oxygen content as the

firing temperature is increased. This corresponds to an overall decrease in mass, as observed by previous authors in thermogravimetry and thermally programmed reduction experiments [49, 21, 23, 24, 28, 48, 34].

Phase	Temperature Region	Average Cation Charge	Oxygen atoms per Cation
NiO	> 800 °C	+2	1
$NiMn_2O_4$	800 °C	+2.67	1.33
$Ni_{(1-\delta)}Mn_{(1+\delta)}O_3$	< 800 °C	+3	1.5

Table 6.6 Cation charge, and oxygen content for the three crystalline phases found in samples fired at various temperatures.

If all of the oxygen is in the O^{2-} state, the average ionic charge of the nickel and manganese must therefore decrease with an increase in firing temperature.
The data fitting procedure by Rietveld analysis, as outlined above, was repeated for all of the datasets collected apart from that obtained from the sample fired at 600 °C. A mixture of different phases was included in the model where appropriate. Fitting to the 600 °C data was not attempted due to the large number of impurity phases identified, the limited angular range of the data (10° to 100°, instead of 10° to 120°), and the reduced data collection time (6 hours instead of 12 hours). Details of the crystallographic unit cells, and allowed reflections of all the phases considered are listed in Appendix 1. The detailed results from all of the Rietveld refinements, including a number of different *R*-factor values are to be found in Appendix 2. The amount of nickel oxide contamination found in the samples is shown in Figure 6.10. The expected standard deviations represented by the error bars on the nickel oxide amount shown in Figure 6.10 (in common with e.s.d. values for all other refined parameters) may be significantly underestimated, for reasons outlined in Appendix 2. Details of the variation in the lattice parameter of $NiMn_2O_4$, with firing temperature are also shown in Figure 6.10. The lattice parameter error bars represent an estimate of the total combined uncertainty, in accordance with UKAS, and BIPM guidelines [50, 51], however, the contribution to the combined uncertainty due to the statistical errors in the Rietveld refinement may be significantly underestimated, as highlighted by Young (p28, [41]). An example uncertainty budget for the lattice parameter of $NiMn_2O_4$ determined from X-ray diffraction data can be found in Appendix 3.

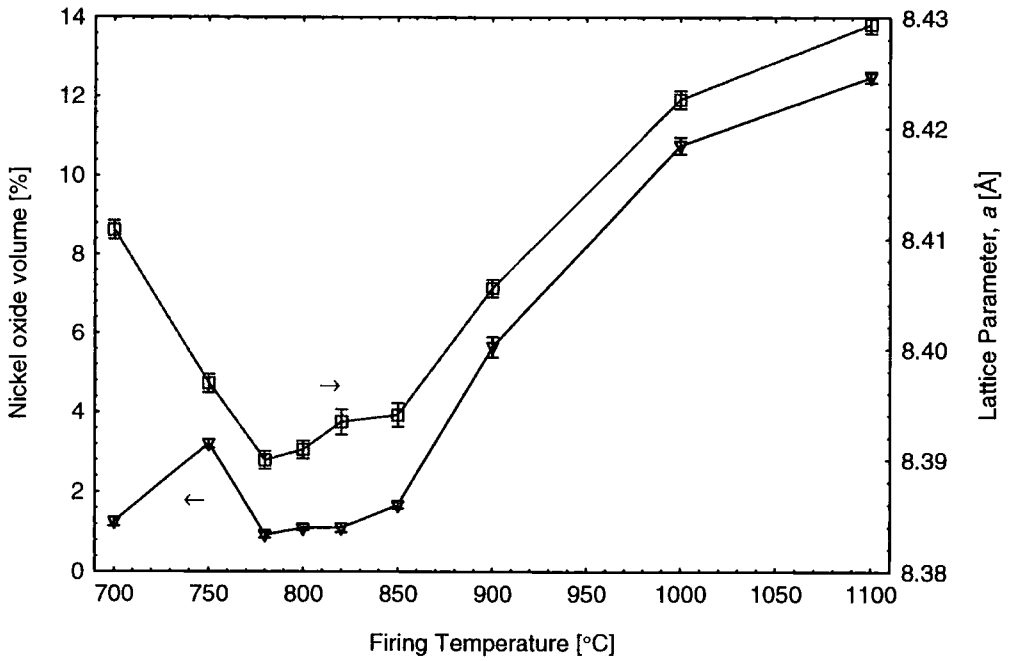

Figure 6.10. Amount of NiO present, and refined lattice parameter of $NiMn_2O_4$, in samples fired at various temperatures for 20 hours. The error bars represent only the statistical error reported from the fitting procedure, and do not take into account any systematic errors that may be present.

The minimum in the lattice parameter of $NiMn_2O_4$, centred on approximately 800 °C coincides with the region of lowest impurity content (the data shown in Figure 6.10 concerns NiO only, 27.29(42) % $NiMnO_3$ was found in the sample fired at 700 °C). The values of lattice parameter determined for the purest samples agree well with many of the values reported in the literature (as listed in Table 5.1). The fact that the observed lattice parameter increases sharply with increasing impurity content immediately raises doubts about the quality of the samples of those authors that reported lattice parameters significantly above the generally accepted value (Meenakshisundaram *et al.*, [17], Singh and Ram [32], Boucher [1]). There are a number of effects that contribute towards the observed minimum in the lattice parameter around 800 °C. As postulated above, $NiMn_2O_4$ may be nickel deficient above (and below) the temperature region where relatively pure samples were found. If the assumption is made that the majority of nickel in $NiMn_2O_4$ has a 2+ charge state, as has been reported in the literature (see section 5.3 for further details), then a nickel deficiency will result in a corresponding increase in the amount of Mn^{2+} present. Since the Mn^{2+} ion has a larger radius than Ni^{2+}, a larger value of the lattice parameter would be expected for a nickel deficient crystal. This is corroborated by Larson *et al.*, [5] in a study

of the $Ni_{(1-x)}Mn_{(2+x)}O_4$ system. Larson *et al.*, observed a distortion to tetragonal symmetry for values of x greater than 0.42. This distortion was large, (a = 8.320(2) Å, c = 8.703(2) Å at x = 0.50 [6]) and therefore would be readily apparent as a splitting of certain diffraction peaks. Since no peak splitting was observed in the data, x = 0.42 can be considered a lower limit on the amount of nickel present in the spinel phase. Assuming that no metal was lost from the samples during preparation, this implies an upper limit of 13.5 % (volume) on the amount of NiO present. The only sample approaching this limit was fired at 1100 °C, which contained 12.49(14) % NiO, corresponding to a nickel deficiency of x = 0.389(4).

Another effect on the lattice parameter, which may be important, is the possible formation of small regions of impurity phases within the $NiMn_2O_4$ crystallites. This would serve to create strain within the crystal, deforming it locally. Since the oxygen atoms in the spinel structure are in an approximately close packed lattice (face centred cubic, see section 4.1.1), any deformation from this would be expected to induce an increase in the unit cell volume, and therefore the lattice parameter.

Since the samples were quenched from the firing temperature, it was expected that the cation distribution of $NiMn_2O_4$ to be not much changed from the distribution at the firing temperature. This cation distribution has been shown to vary with firing temperature by a number of authors [12, 52, 19]. A change in cation distribution (note that the inversion parameter is only strictly valid for stoichiometric $NiMn_2O_4$) results in a change in lattice parameter, due to the differing effective ionic radii of the various ions present, when in tetrahedral, and octahedral sites. This behaviour is modelled in detail in section 4.2.3, and the models compared with published results as shown in Figure 4.4.

The behaviour of the refined oxygen position parameter with changes in firing temperature is shown in Figure 6.11. The values are slightly higher than most of those previously reported (as listed in Table 5.1), but nearer to those values predicted for the case of high spin manganese ions (as detailed in section 4.2.4).

During the validation testing of the FULLPROF refinement program (as detailed in section 6.2.4, and Appendix 2), it became apparent that the presence of nickel

oxide reflections caused the refined value of the oxygen position parameter to be underestimated.

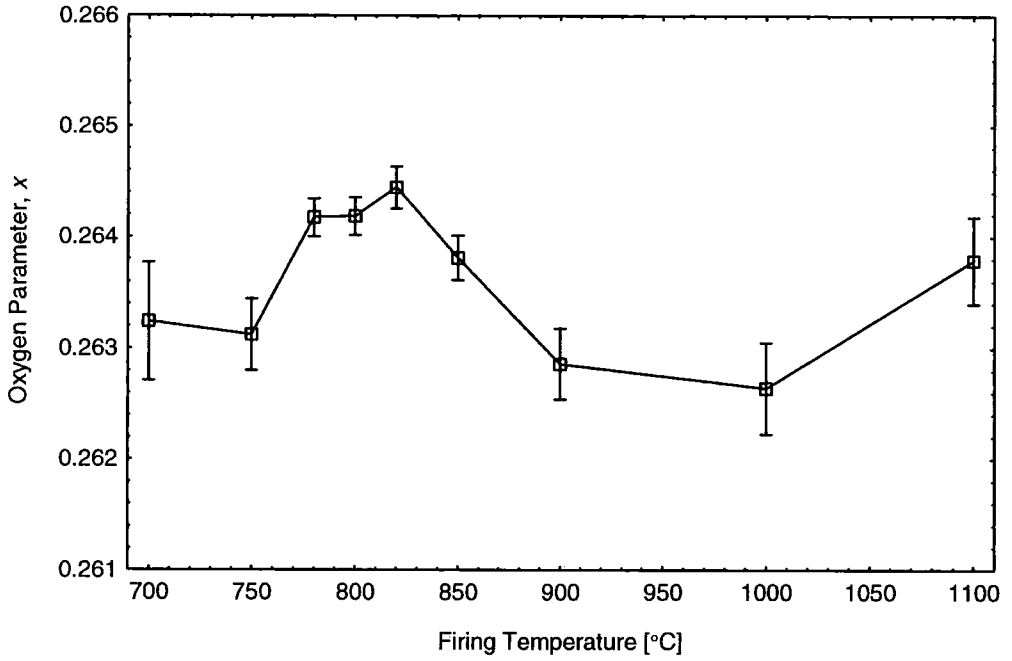

Figure 6.11. The variation in the refined oxygen position parameter of $NiMn_2O_4$ for samples fired at various temperatures. The error bars represent only the statistical error from the fitting procedure, and do not take into account any systematic errors that may be present.

This effect could account for the observed dependence upon firing temperature and therefore impurity content. In addition, the slight discrepancy with previous reports could be due to similar systematic underestimation of the oxygen parameter in previous Rietveld refinements (due to nickel oxide impurities). The metal ions, having many more electrons than the oxygen consequently have a higher scattering cross section, so any slight deviation from stoichiometry (such as oxygen vacancies) may have been interpreted as a change in oxygen position by the Rietveld analysis.

As has already been discussed, the presence of nickel oxide implies a variation of the cation distribution in $NiMn_2O_4$, and therefore a change in the average ionic size of the ions in the A, and B sites. The oxygen parameter is sensitive to the difference in the sizes of the ions, an increase in oxygen parameter being caused by an increase in the size of the A site, or a decrease in size of the B site (see section 4.2.4, Figure 4.5 for more details). Using the ionic radii given in section 4.2.3, and the cation distribution postulated by Brabers [52], it is predicted that an increase in oxygen parameter would result if Ni^{2+} was preferentially lost

from the A sites, to be replaced by the much larger Mn^{2+} ion. The proportion of nickel lost to NiO in the sample fired at 1100 °C was considerable, and so the increase in oxygen position parameter in this sample supports the prediction of preferential loss from A sites. The isotropic temperature factors (or *B* factors) of the various sites, obtained from Rietveld refinements are shown in Figure 6.12.

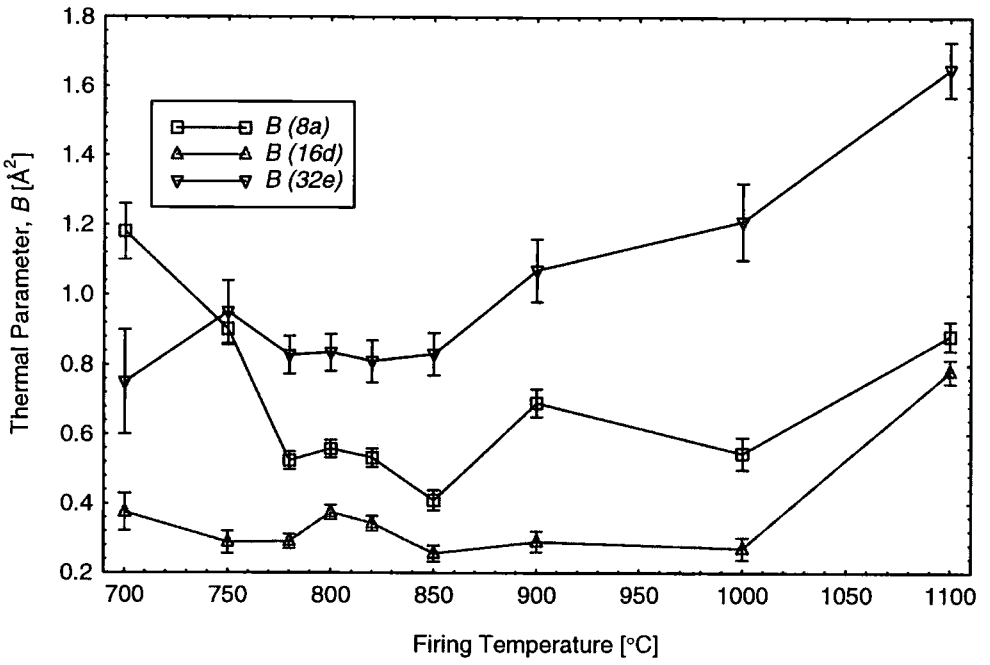

Figure 6.12. Refined Isotropic Temperature Factors for $NiMn_2O_4$ for samples fired at various temperatures. The lines are a guide to the eye.

The factors are labelled with their Wyckoff positions [53]. The 8a, 16d, and 32e sites correspond to A sites, B sites, and oxygen positions respectively. The *B* factors are related to σ, the mean displacement of the site occupants in Å;

$$B = 8\pi^2\sigma^2 .$$

This displacement is due to a number of factors, which unfortunately cannot be distinguished from one another using just room temperature X-ray diffraction data. The atomic displacements can be split into two types, static and dynamic. The static displacements are due to random effects in the crystal lattice, such as defects, impurity atoms, and local distortions of the crystal lattice (such as non co-operative local Jahn-Teller type distortions). The static displacements are generally unaffected by changes in temperature. The dynamic displacements (vibrations) can be further divided into temperature dependent, and temperature

independent (zero point motion) contributions. The temperature independent contribution is higher for lighter atoms (p397 [54]).

The larger error bars on the values from the 32e (oxygen) sites reflects the fact that oxygen is by far the lightest element present, and therefore the weakest scatterer of X-rays. This makes the position of the oxygen less certain, as statistical errors have a greater influence.

The oxygen *B* values are high, as has been observed previously [55]. Although this was expected due to the smaller atomic mass of oxygen compared to the metal cations, this was postulated to be partly due to local Jahn-Teller type distortions (see section 4.2.8). These distortions cause the octahedra of oxygen anions adjacent to an Mn^{3+} cation to be displaced from their mean positions. This distortion is non co-operative (in a random direction), due to the low concentration of Mn^{3+} (the Jahn-Teller active ion). For higher concentrations of Mn^{3+}, the mean distance between distorted octahedra becomes low enough that interactions between them become important. The effect of these interactions is to align the directions of distortion of the octahedra parallel to one another [56], causing a bulk distortion to tetragonal symmetry. The increase with increasing firing temperature, in the values arrived at for the 32e sites may be due to an increase in the proportion of the B sites occupied by Mn^{3+} ions. This is in accordance with reports of the cation distribution [15], and the change in inversion parameter with temperature [12, 19]. Any loss of nickel from nickel manganite (such as by segregation of nickel oxide), would also act to increase the amount of the B sites occupied by Mn^{3+}, to maintain charge neutrality. Loss of a significant amount of nickel will lead to bulk distortion to tetragonal symmetry, as observed by Larson *et al.*, [5].

All of the *B* factors may be additionally affected by strain broadening of the diffraction peaks, whereby local distortions due to intra-crystal impurities affect the atomic positions. It is also possible that errors will have been introduced due to the overestimation of the intensities of some of the $NiMn_2O_4$ diffraction peaks that overlap with NiO diffraction peaks. These effects may be responsible for the rise in *B* factors above a firing temperature of 900 °C, as this is where nickel oxide is found in significant quantities. Normally Rietveld analysis should be able to overcome this, as only some of the peaks are affected by overlap.

However, since both phases are cubic, the number of distinct peaks available is greatly reduced when compared to systems with lower symmetry.

6.2.7 Comparison of hydroxide, and oxide preparation routes

One of the problems commonly reported when previous authors have used the oxide preparation route, was the extreme slowness of the reaction between mechanically mixed oxides at 800 °C. The reported [3, 5, 57, 58, 35] way of overcoming this problem was to initially fire the oxides at a much higher temperature to enable the reaction to proceed much quicker, and then to anneal for an extended period of time at around 800 °C in order that any nickel oxide formed was re-absorbed. As a comparison this firing schedule with the hydroxide route, a sample was prepared at 1200 °C for 12 hours, followed by 800 °C for 155 hours, before quenching in a similar manner to the other samples. The precursor materials used were mixed hydroxides, similar to those used to study the effect of differing firing temperature. The resultant X-ray diffraction pattern is presented in Figure 6.13, together with the calculated fit from a Rietveld analysis carried out in a similar manner to those discussed in section 6.2.4. The results from the refinement are to be found in Appendix 2.

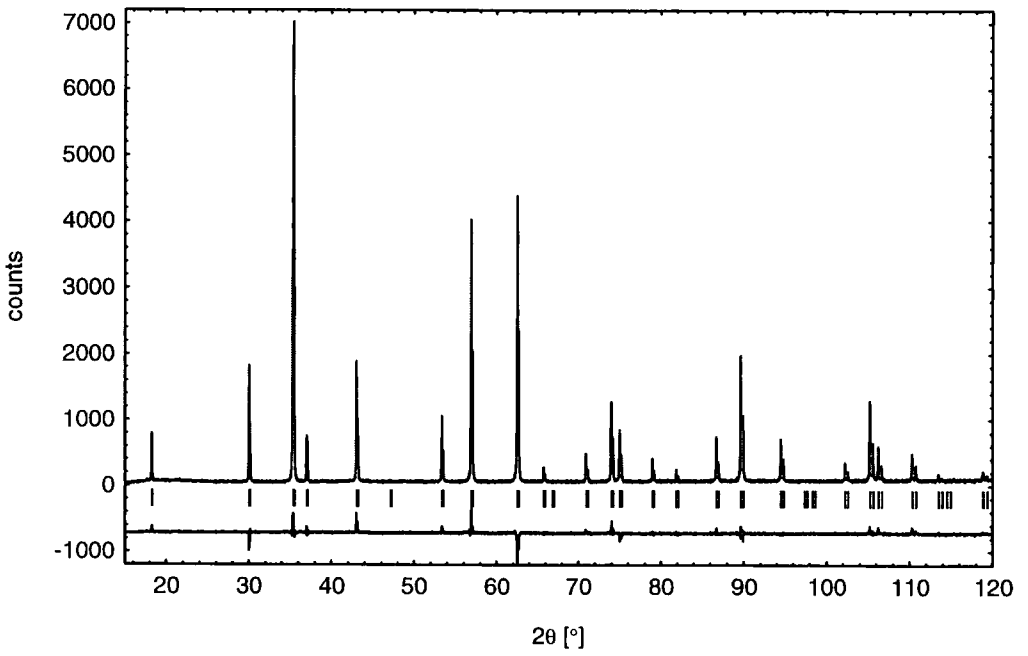

Figure 6.13. X-ray diffraction pattern for a sample fired at 1200 °C for 12 hours, followed by annealing at 800 °C for 155 hours.

The sample is very crystalline, as indicated by the $K_{\alpha 1}$, $K_{\alpha 2}$ splitting of the incident radiation, visible as a splitting of the diffraction peaks at angles as low as $2\theta = 35$ °. The background is much reduced, compared with the data in Figure 6.9, and no evidence of nickel oxide contamination was detected. The intensities of many of the peaks were not reproduced well in the model used for refinement, but their positions were. Manually altering the occupations of the A, and B sites did not appear to reduce the discrepancy between the data and model. For this reason, the fitted values of parameters that determine the integrated intensities (oxygen position, and isotropic temperature factors) may be seriously in error.

The lattice parameter obtained from the refinements was comparable to that from the sample fired at 800 °C for 20 hours (Figure 6.10), however the oxygen parameter, and oxygen site *B* factor were both higher. The behaviour of the oxygen is what would be expected for a sample that had a nickel deficiency. However, the alumina crucible used to hold the powder while in the furnace was found to be considerably stained after use. Fragments of the stained crucible, an unstained alumina crucible, and the sample were analysed using the EDAX (Energy Dispersive Analysis of X-rays) facility attached to an electron microscope. The results are shown in Figures 6.14 to 6.16.

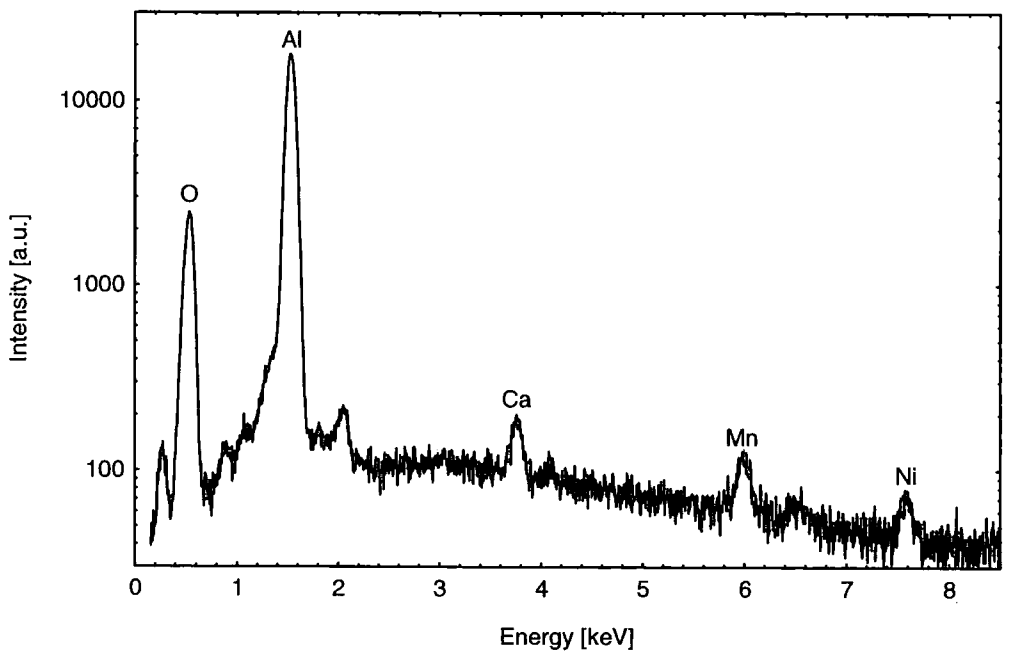

Figure 6.14. EDAX spectrum from an unstained crucible. The trace amounts of manganese and nickel present are due to the crucible having been used.

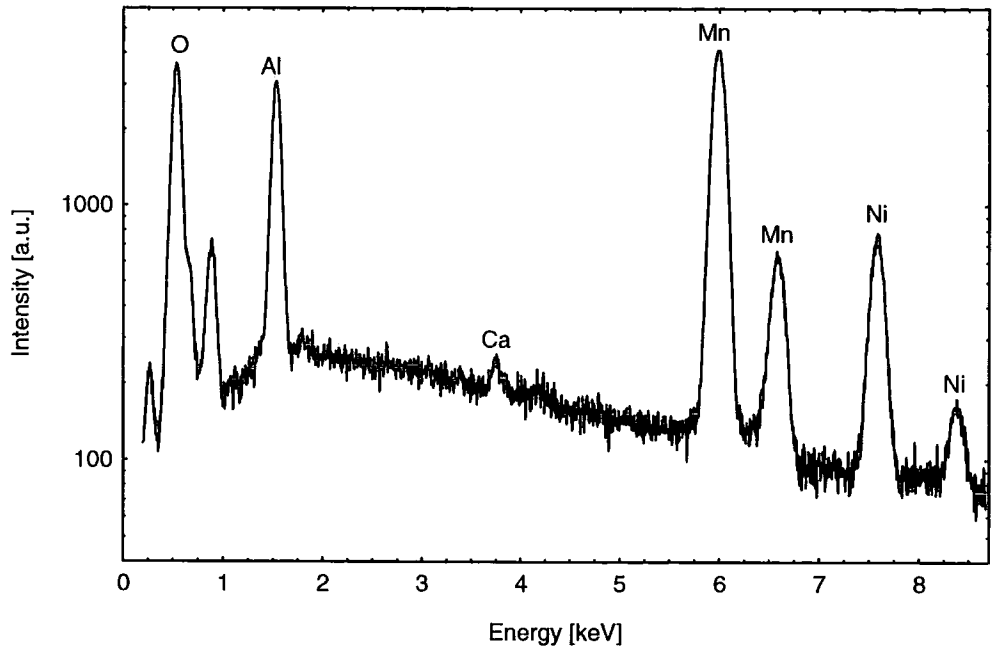

Figure 6.15. EDAX spectrum from a portion of the stained crucible.

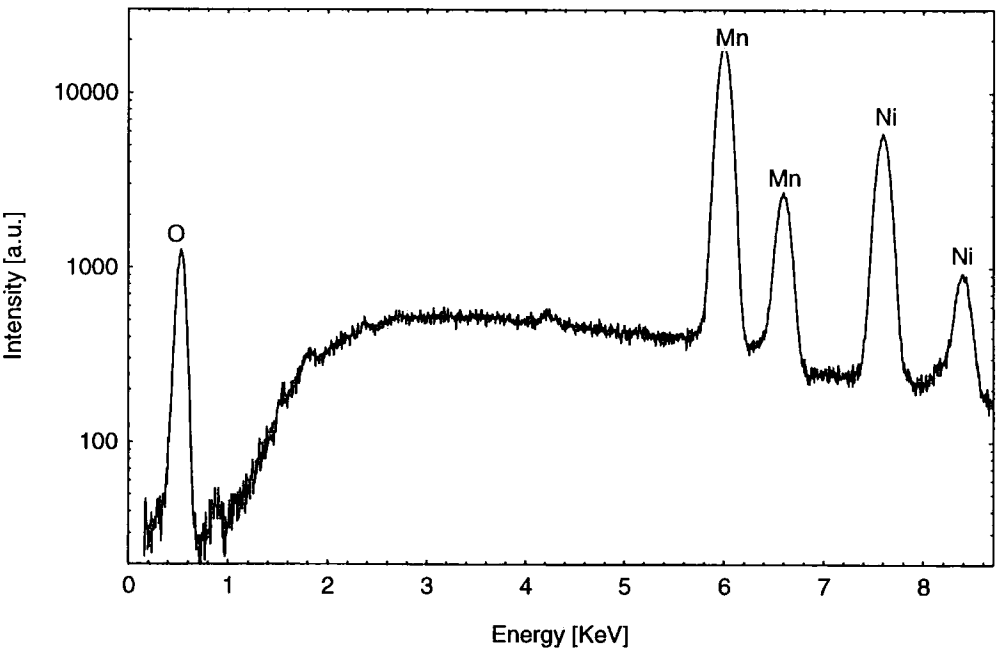

Figure 6.16. EDAX spectrum from the sample fired at 1200 °C, and annealed at 800 °C.

As can be seen the unstained crucible has a very small amount of nickel and manganese present, due to it having been used to produce $NiMn_2O_4$. The stained crucible shows considerable quantities of nickel and manganese, as expected. The ratio of the heights of the nickel and manganese peaks obtained from the stained crucible is considerably different to that obtained from the sample. The ratio of the main peak intensities are; $I_{Ni} / I_{Mn} = 0.188$, and 0.323 for the stained

crucible, and sample respectively. The conclusion drawn from this is that more manganese has been lost from the sample than nickel, leaving the sample non-stoichiometric. This is plausible, in view of the melting point of α-Mn_2O_3 being 1080 °C [36], however it contradicts the conclusion of nickel deficiency drawn from the X-ray diffraction analysis.

6.2.8 Scanning electron microscopy

Micrographs of the sample prepared at 1200 °C and annealed at 800 °C, and a sample fired at 800 °C for 20 hours, obtained using a SEM (Scanning electron microscope) in the Department of Physics, Durham University are shown in Figures 6.17, and 6.18. This instrument was a JEOL, JSM-IC848.

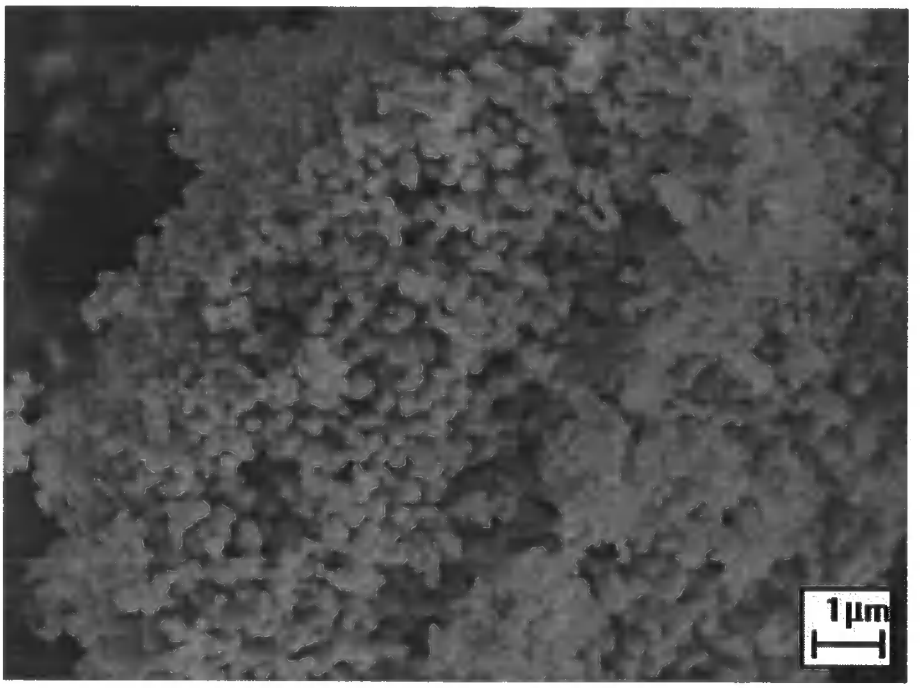

Figure 6.17. SEM image of $NiMn_2O_4$ prepared at 800 °C for 20 hours, taken at 7500 x magnification.

Note the difference in scale of the two images. As expected, the sample fired at higher temperature is much more densely sintered, with a larger grain size. This would obviously be an important consideration for utilisation of nickel manganite in devices, where repeatable, high density preparation routes are of prime interest. In the present work, this confirms that the mobility of the cations is strongly temperature dependent above the ideal firing temperature of 800 °C.

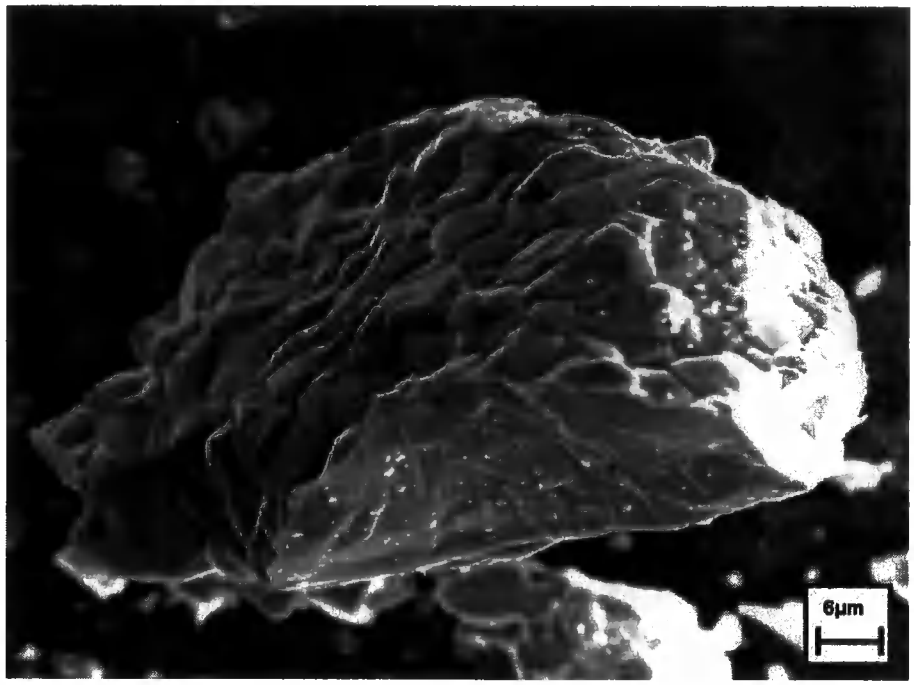

Figure 6.18. SEM image of $NiMn_2O_4$ prepared at 1200 °C for 12 hours, and annealed at 800 °C for 155 hours, taken at 1100 x magnification.

Presented in Figure 6.19, is a fluorescence map, taken at the same time as the image in Figure 6.18.

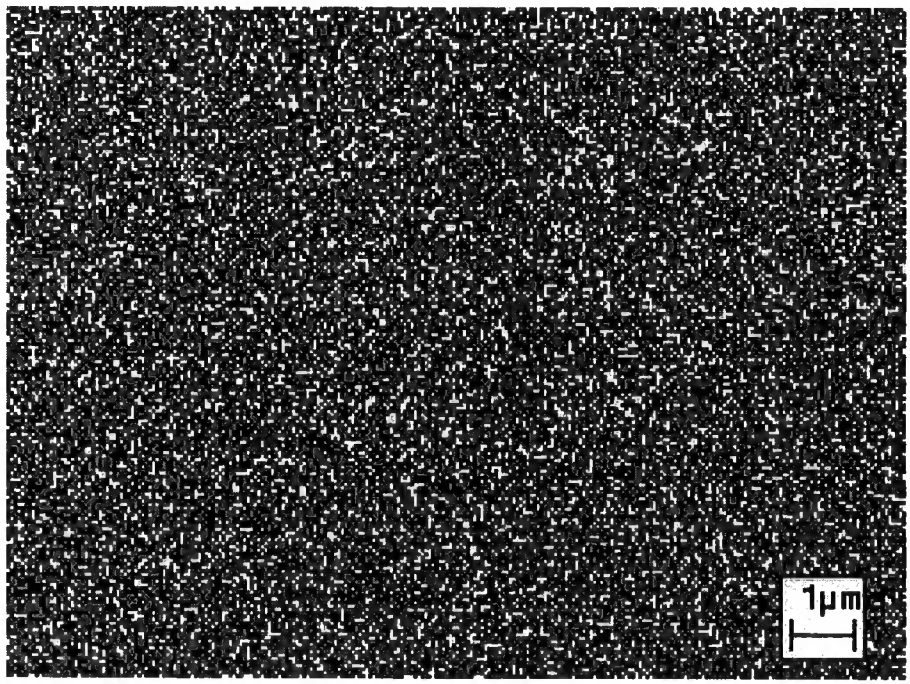

Figure 6.19. Spatially resolved fluorescence image of the sample shown in Figure 6.18.

The detector was tuned to the K emission line of manganese, thereby giving an image of the spatially resolved manganese concentration. As can be seen, there are no distinct features, or overall concentration gradient. Images obtained for

emission lines of nickel and oxygen, and for other samples are similarly featureless. The formation of crystalline impurities (such as nickel oxide) would show up as a region devoid of manganese.

6.3 Effects of differing firing times

Having determined the optimum preparation temperature for $NiMn_2O_4$ to be approximately 800 °C, and noting the increase in grain size and sintering observed for samples held at higher temperatures, the effect of firing time on sample properties was investigated. A number of samples were prepared, following the method set out in section 6.2, except that the firing temperature was always 800 °C, and the time that the sample was kept at this temperature before being quenched was varied between 1 hour, and 120 hours. The samples were again prepared in a random order, the precursor batches used given in Table 6.7.

Time at 800 °C [hours]	Precursor batch	Sample sequence number
1	3	2
20	1	1
48	3	3
120	3	4

Table 6.7. Firing schedule for time dependant experiment.

The X-ray diffraction patterns obtained from these samples are shown in Figure 6.20. As can be seen, the diffraction peak positions are nearly identical, the only change being the peak widths. The small peak at $2\theta = 33$ ° in the data from the sample fired for 1 hour can be attributed to the strongest [222] reflection from α- Mn_2O_3. Closer inspection of the (222), and the (400) peaks (shown in Figure 6.21 inset), in a similar manner to section 6.2.2, reveal a decrease in peak asymmetry as the firing time is extended. This asymmetry is again attributed to the presence of the (111), and (200) reflections of nickel oxide at $2\theta = 37.3$ ° and $2\theta = 43.3$ ° respectively. This is particularly the case for the sample fired for 1 hour, as the peak is broad enough for the two reflections to merge. There is no indication of any significant amounts of nickel oxide in the samples fired for 48, and 120 hours, as this would manifest as a separate peak (provided that the nickel oxide was also sufficiently highly crystalline).

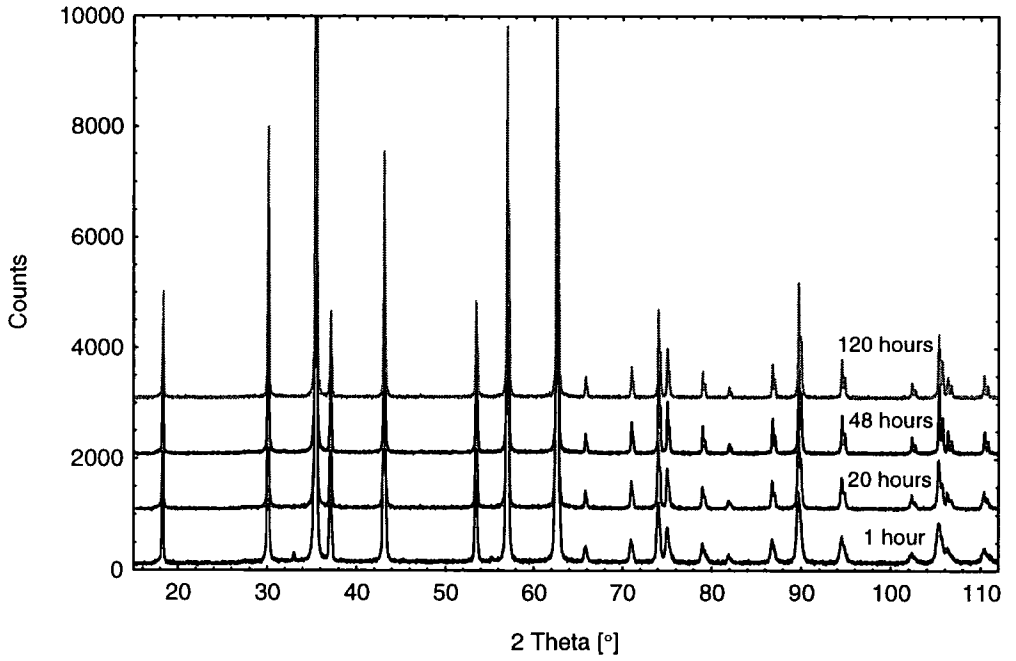

Figure 6.20. All of the X-ray diffraction patterns observed from samples fired for between 1 hour and 120 hours at 800 °C. The datasets have been offset for clarity.

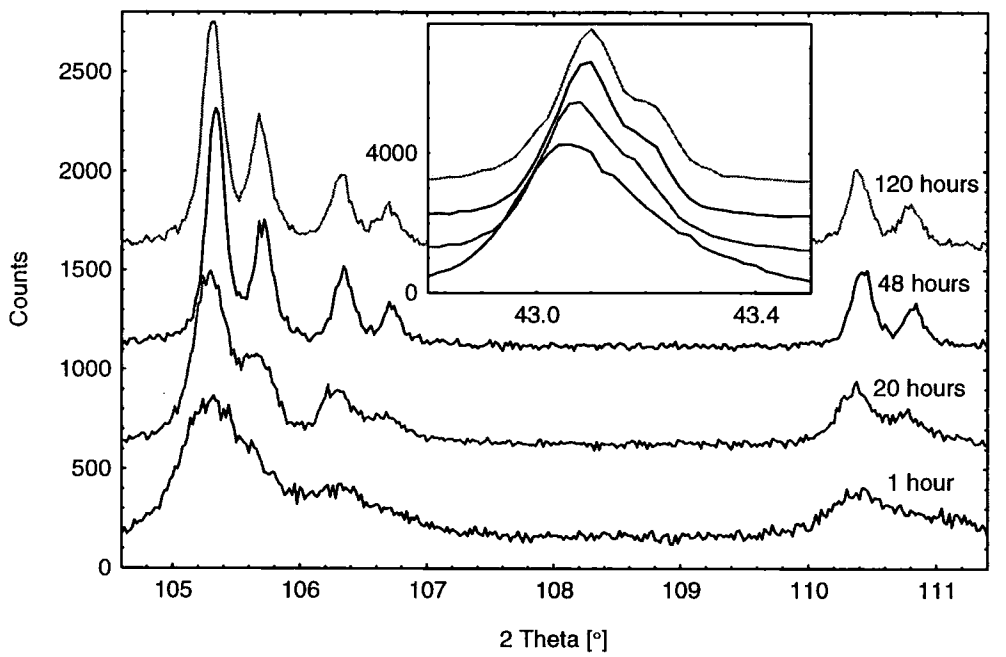

Figure 6.21. Detail of the X-ray diffraction patterns observed from samples fired for between 1 hour and 120 hours at 800 °C. The datasets have been offset for clarity.

Rietveld analysis was carried out on the datasets shown in Figure 6.20, in a similar manner to that described in section 6.2. The resulting fitted parameters, along with goodness of fit indicators are contained in Appendix 2, section A2.5. The $K_{\alpha 1}$, $K_{\alpha 2}$ splitting of the incident radiation is evident from the shape of the

peaks from the samples fired for 48, and 120 hours. The $K_{\alpha 1}$, $K_{\alpha 2}$ splitting is even more pronounced in the higher angle peaks, as shown in Figure 6.21. This indicates a higher crystallinity in these samples. The peak width was modelled as a function of diffraction angle, using the formula of Caglioti [42], as detailed in section 6.2. The resultant behaviour of I^2 as a function of *tan* θ, for varying firing temperatures is plotted in Figure 6.22.

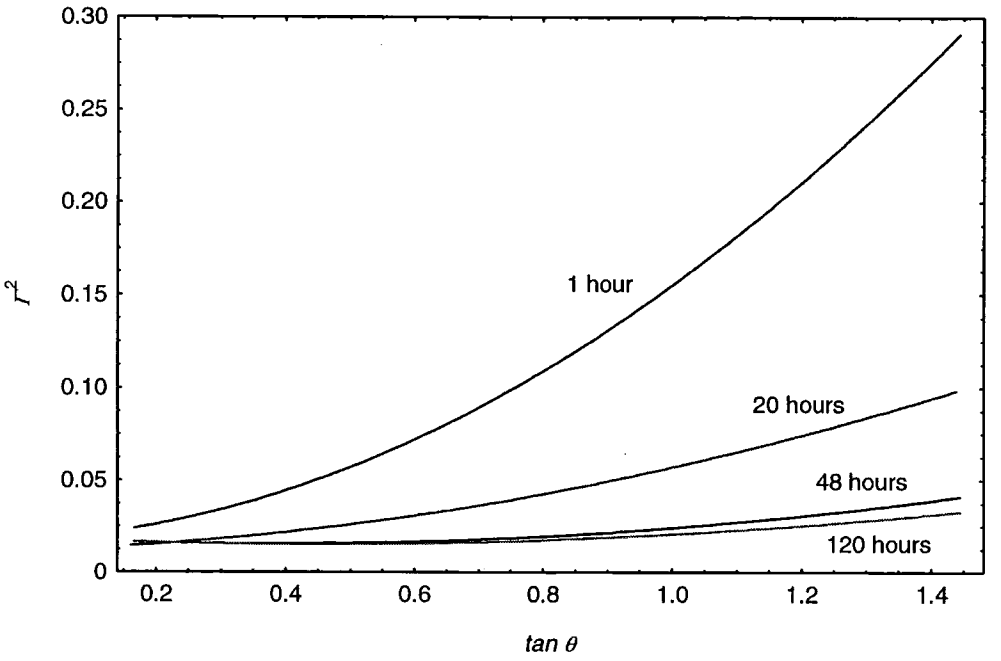

Figure 6.22. The Caglioti peak width function for samples fired for between 1 hour and 120 hours at 800 °C.

The reduction in peak width with increasing firing temperature (shown in Figure 6.21) is confirmed. There are a number of factors that contribute to the observed peak width [41], such as the instrument resolution function, sample microstrain, and crystallite size. Due to the cubic symmetry of nickel manganite, anisotropic profile broadening, and microstrain contributions were not expected. The variation in refined lattice parameter is shown in Figure 6.23. There is a small decrease with increasing firing time, which is statistically significant. The values for 1 hour, and 120 hours are separated by more than 4 times the estimated standard uncertainty. Assuming a coverage factor [50] of $k = 2$, such that a confidence level of approximately 95% is obtained at twice the estimated standard uncertainty, the probability that such a deviation arose by chance is less than 0.0625%.

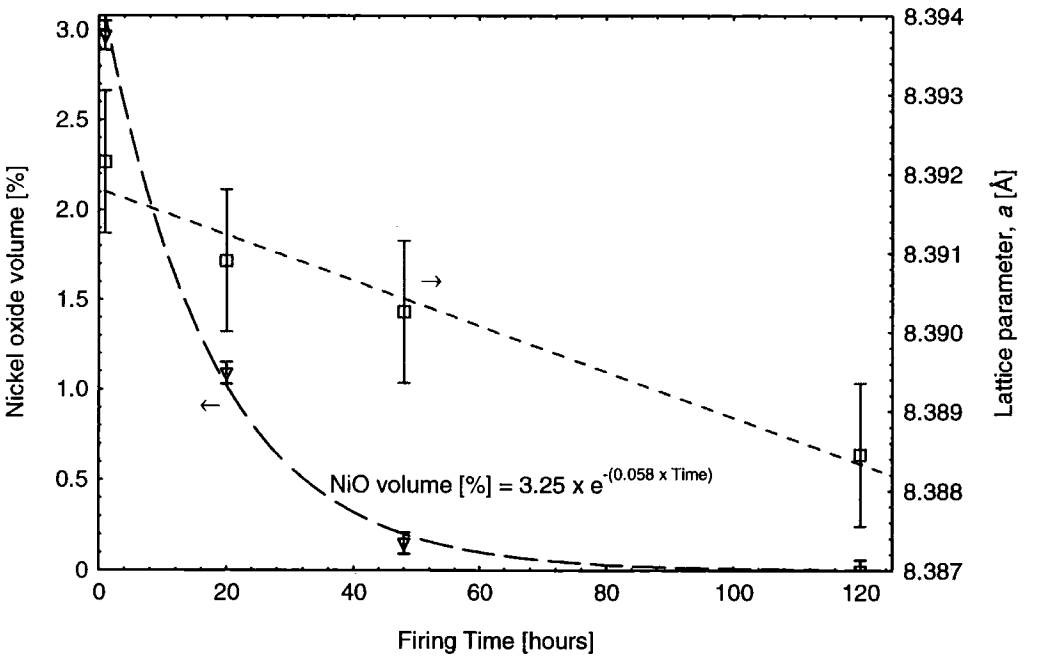

Figure 6.23. Amount of NiO present, and refined lattice parameter of $NiMn_2O_4$, in samples fired for various times at 800 °C. The lattice parameter error bars represent an estimate of the total combined uncertainty, in accordance with UKAS, and BIPM guidelines [50, 51], while the NiO amount error bars represent only the statistical error reported from the fitting procedure, and do not take into account any systematic errors that may be present. The dashed lines are fits to the data, with the NiO amount fitted to an exponential decay, and a linear fit to the lattice parameter.

The amount of nickel oxide present also decreased with an increase in firing time, as shown in Figure 6.23. It is noted that the correlation between lattice parameter, and nickel oxide amount is similar to that observed for samples with differing firing temperatures (Figure 6.10). Therefore, the mechanism for the change in lattice parameter was assumed to be the same as that postulated in section 6.2.6 (the Mn^{2+} ion having a larger radius than the Ni^{2+} ion). Since the error bars on the nickel oxide amount only take into account the statistics of the fitting process, the difference between the refined amount of nickel oxide contamination reported for samples fired for 48 hours, and 120 hours was estimated not to be significant at the 95% confidence level.

The fact that the samples have a higher purity with an increase in firing time suggests that nickel manganite is the thermodynamically stable crystallographic phase at 800 °C, and ambient pressure. The isotropic temperature factors (*B* factors) of the various sites, obtained from Rietveld refinements are shown in Figure 6.24. The factors are labelled with their Wyckoff positions [53]. The 8a, 16d, and 32e sites correspond to A sites, B sites, and oxygen positions respectively.

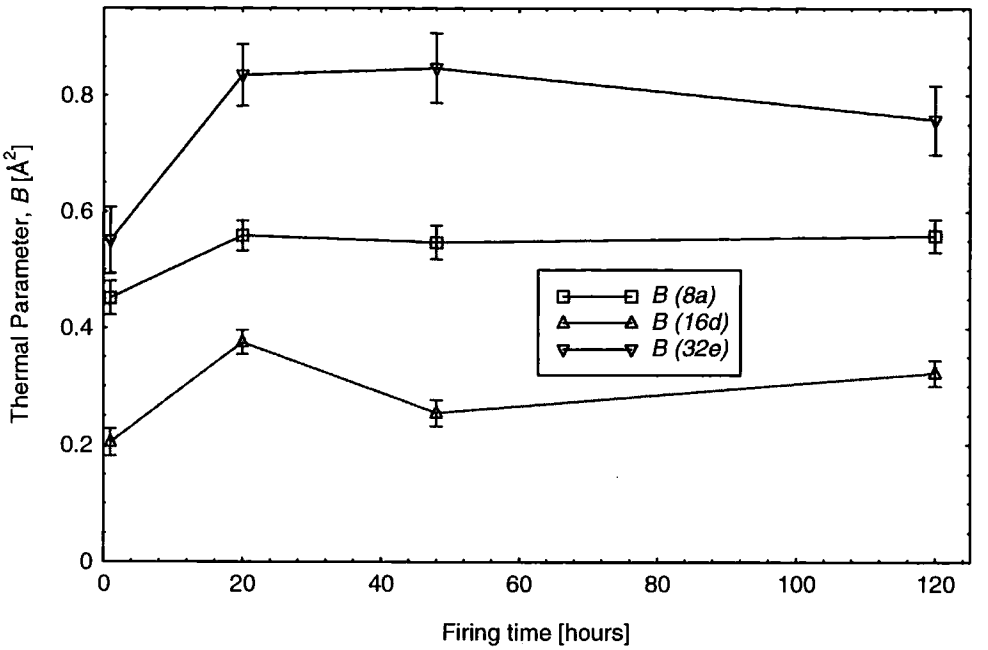

Figure 6.24. Refined Isotropic Temperature Factors for $NiMn_2O_4$ for samples fired for various times. The lines are a guide to the eye.

The values are broadly consistent from sample to sample, and agree well with other samples fired at temperatures around 800 °C. Due to the insignificant differences between the samples fired for 48, and 120 hours, it was concluded that 48 hours was an adequate firing time to produce well crystallised material. The SEM micrographs shown in Figures 6.25 to 6.27 support this conclusion. The grain size was noticeably larger in the sample fired for 48 hours (Figure 6.26), than it was in the sample fired for 20 hours (Figure 6.25). There was no significant increase in grain size when the firing time was further increased to 120 hours, indicating little further reaction having taken place.

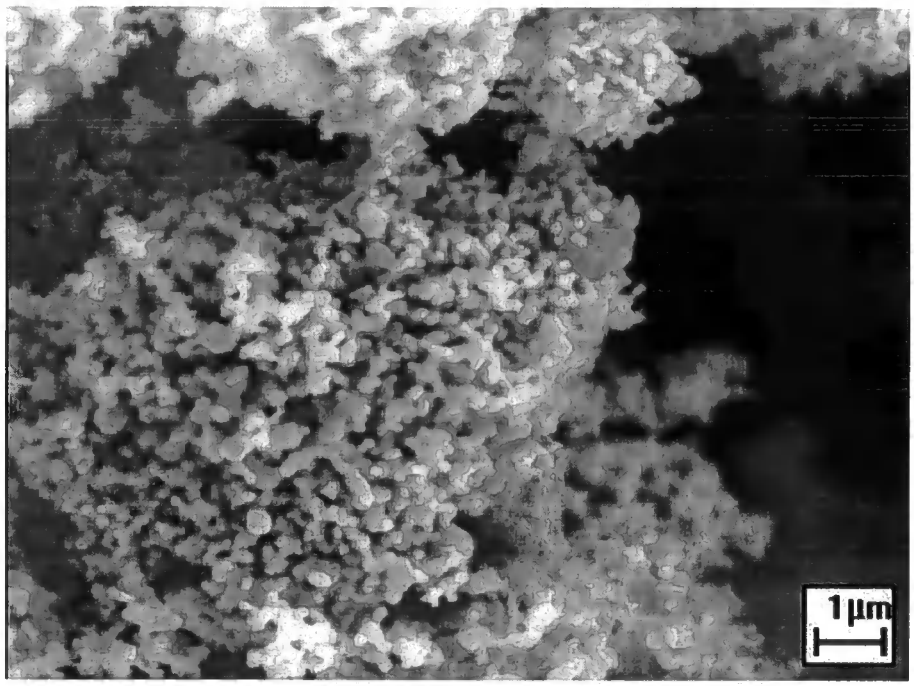

Figure 6.25. SEM image of $NiMn_2O_4$ prepared at 800 °C for 20 hours, taken at 7500 x magnification.

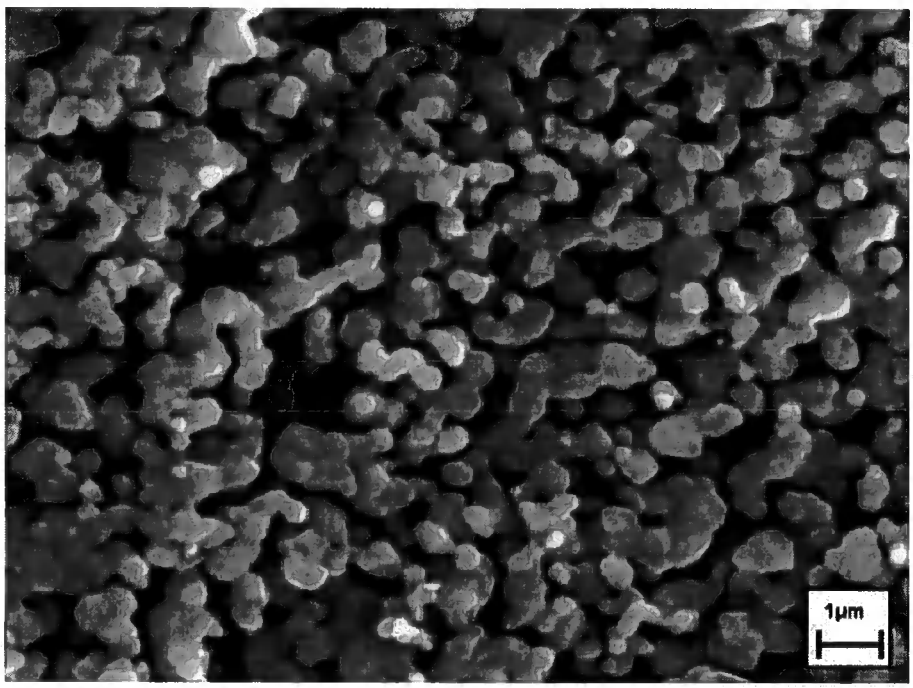

Figure 6.26. SEM image of $NiMn_2O_4$ prepared at 800 °C for 48 hours, taken at 7000 x magnification.

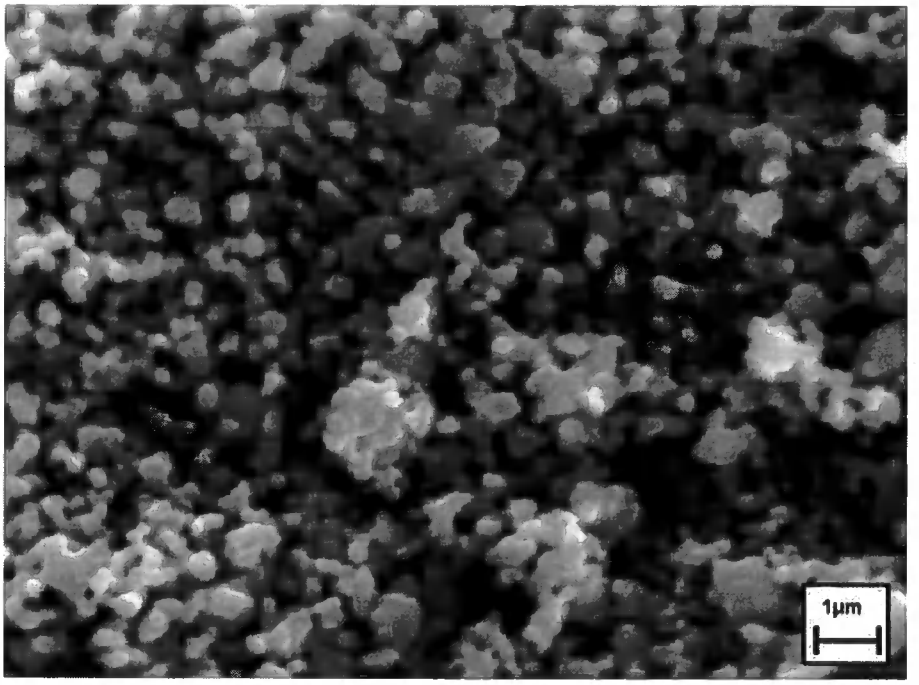

Figure 6.27. SEM image of $NiMn_2O_4$ prepared at 800 °C for 120 hours, taken at 7000 x magnification.

6.3.1 Effect of heating rate on sample properties

Due to reports in the literature of $NiMn_2O_4$ being unstable below a preparation temperature of 800 °C [5], and the experiments carried out at different firing temperatures confirming this, it was concluded that rapid heating and cooling is conducive to high sample purity. Accordingly, a heating rate of 10 K min^{-1} was used when raising samples to the firing temperature. This was the maximum heating rate available in the furnaces used. To test this supposition, a sample was prepared using a heating rate of 1 K min^{-1} to 800 °C, and held there for 48 hours. The starting materials were from batch 7. The choice of firing time enabled a direct comparison with the sample fired for 48 hours from the previous experiment. The X-ray diffraction data for both samples were almost identical, with all the expected reflections from $NiMn_2O_4$ present in both datasets. The $K_{\alpha 1}$, $K_{\alpha 2}$ splitting of the higher angle peaks was slightly greater in the sample with the higher heating rate, indicating a greater crystallinity. The only diffraction peak not common to both datasets is shown in Figure 6.28. This extra peak, at $2\theta = 33.1$ °, is attributed to the strongest (222) reflection from α-Mn_2O_3.

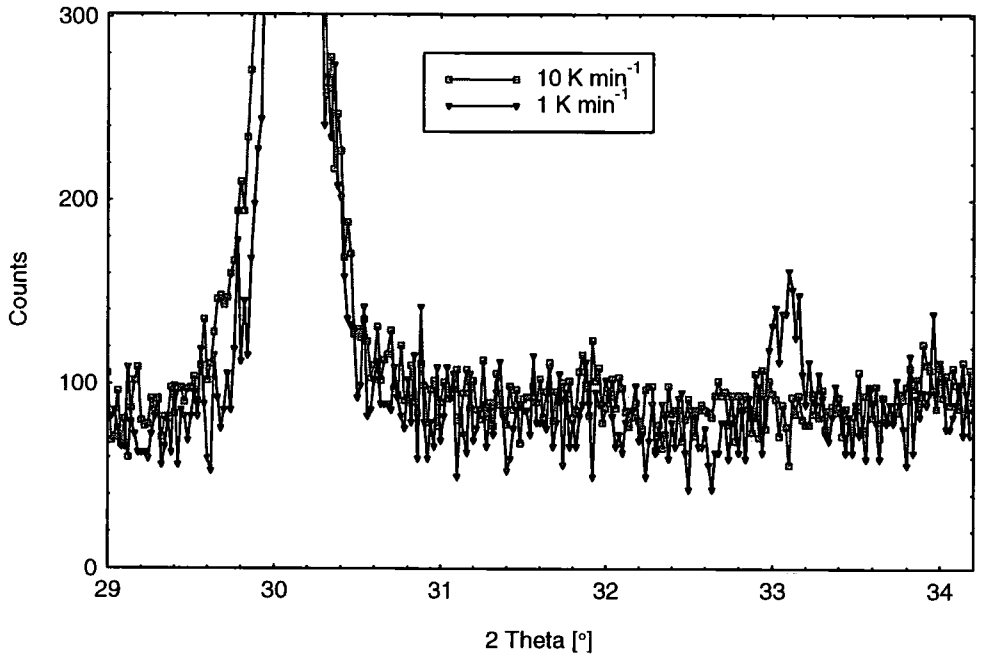

Figure 6.28. Comparison of the X-ray diffraction patterns obtained from 2 samples heated at different rates. All other preparation conditions were identical. The peak at $2\theta = 30.1$ ° is attributed to the (220) reflection of $NiMn_2O_4$, and the peak at $2\theta = 33.1$ °, to the strongest (222) reflection from α - Mn_2O_3.

The presence of small amounts of α - Mn_2O_3 indicates that the solid state reaction used to produce $NiMn_2O_4$ has not proceeded to completion in this sample, despite being held at the firing temperature for 48 hours. This may be due to α-Mn_2O_3 forming large crystals while the sample was being heated to 800 °C, and the manganese then only slowly diffusing away to form $NiMn_2O_4$. It is probable that regions of non-stoichiometric nickel manganite exist in this sample, adjacent to the remaining α-Mn_2O_3 crystallites. A SEM micrograph of this sample is shown in Figure 6.29. The presence of occasional larger crystals can be seen. These are not visible in the sample with a higher heating rate (Figure 6.26). The reason for these is unclear, particularly as the peak widths from X-ray diffraction data indicate that the crystallinity is reduced. Due to the obvious superiority of a higher heating rate for the formation of pure nickel manganite, and 10 K min^{-1} being the maximum heating rate available in the furnaces used, no further investigation of slower heating rates were attempted.

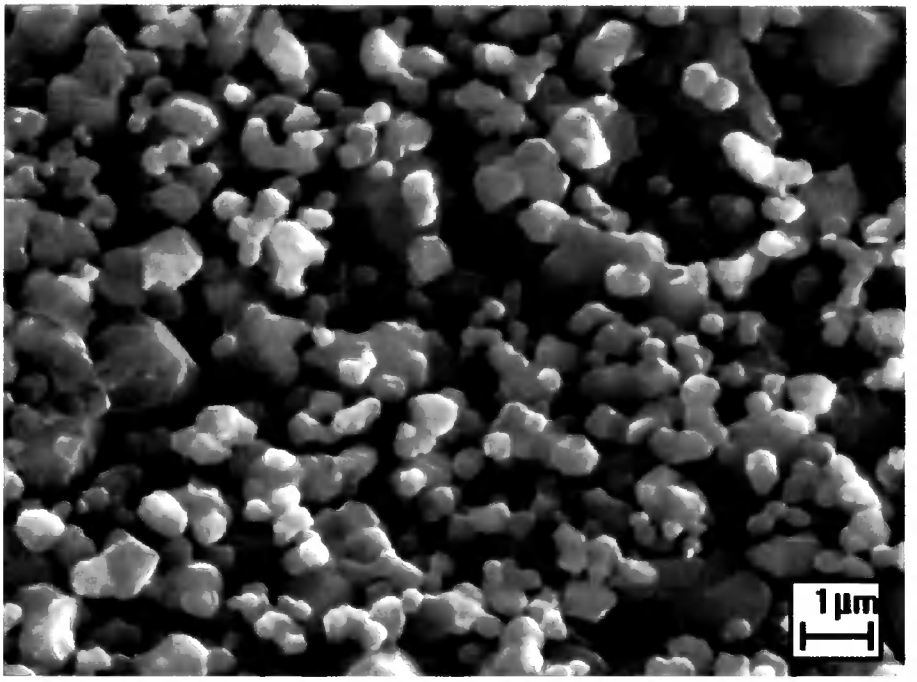

Figure 6.29. SEM image of $NiMn_2O_4$ prepared at 800 °C for 48 hours, with a heating rate of 1 K min^{-1}, taken at 7500 x magnification. Occasional larger crystallites are highlighted.

6.3.2 Crystal growth

An (unsuccessful) attempt was made to grow crystals of $NiMn_2O_4$, for electrical, and magnetic characterisation. Following reports in the literature [59], a sample of $NiMn_2O_4$ was prepared at 800 °C for 48 hours, then thoroughly ground in a pestle and mortar. This was then held at 800 °C for 168 hours, then removed from the furnace. 90 % of the sample was subjected to a further grinding, and then mixed with the remaining 10 % un-ground material. This was then left in a furnace at 800 °C for 1656 hours (just over 5 weeks), and then removed from the furnace, and allowed to cool naturally. The resulting powder was examined using an SEM, to see if any increase of crystallite size was evident. As can be seen from Figure 6.30, the crystallite size had not increased significantly, in comparison to samples fired for 120 hours (Figure 6.27). X-ray diffraction data did not reveal the presence of any impurities. The crucible used to prepare this sample did not show any signs of discoloration, leading to the conclusion that no metal content was lost during firing. Alternative methods using hydrogen chloride vapour as a transport agent (Brabers *et al.*, [15]) were not attempted due to health and safety considerations.

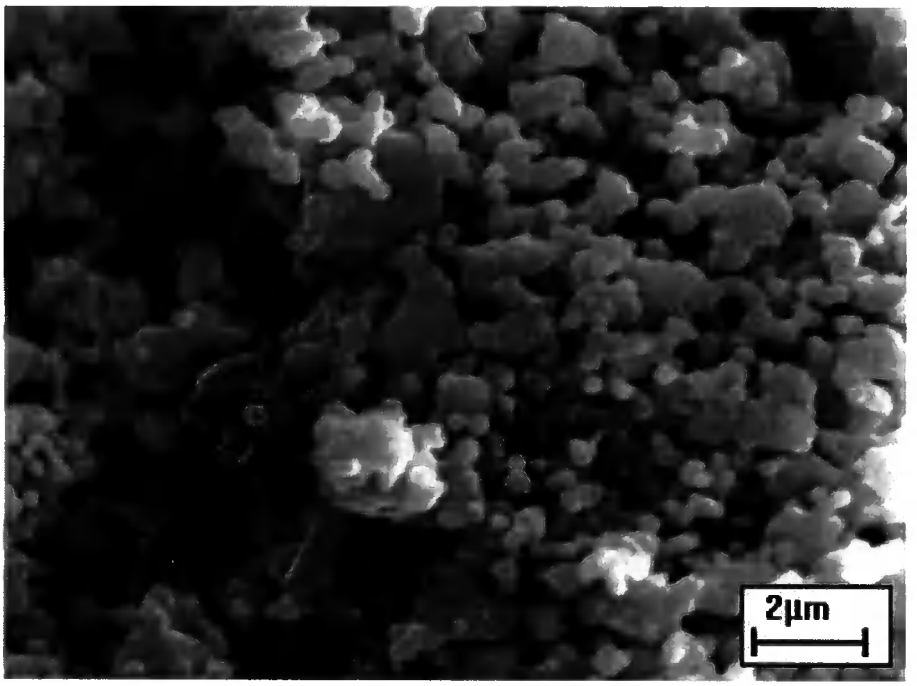

Figure 6.30. SEM image of $NiMn_2O_4$ prepared in an attempt to grow single crystals, taken at 6000 x magnification.

6.4 Effect of varying the firing temperature on inversion parameter.

In order to determine the inversion parameter of $NiMn_2O_4$ using diffraction, a technique other than X-ray diffraction had to be used. This was because X-rays scatter from electrons, and thus distinguishing between nickel and manganese ions is difficult due to the similar number of electrons they contain. Neutron diffraction gives much more contrast, as the scattering is from atomic nuclei, and the scattering factor of nickel and manganese (and oxygen) differ significantly. These are given in Table 6.8.

Atom	Scattering length, b [10^{-14}m]
Ni	1.030
Mn	-0.373
O	0.581

Table 6.8. Neutron scattering lengths reported by Koester *et al.*, [61].

In addition to nuclear scattering, neutrons interact with local magnetic moments present in the sample. This scattering becomes important when the sample is in an ordered magnetic state, giving rise to additional Bragg reflections ('magnetic reflections') [60]. Analysis of these can in some cases, give information about the magnetic structure present in the sample. Due to the much weaker scattering of neutrons compared with X-rays, it was necessary to prepare much larger

amounts of sample. Accordingly, each sample to be analysed by neutron diffraction was made from a batch of precursor hydroxides. It was decided to initially prepare 3 samples, fired for 48 hours, at 750 °C, 800 °C, and 850 °C respectively. These were chosen to be around the region of interest; that where $NiMn_2O_4$ was found to be stable (see section 6.2). In order that there be no variation due to differences in starting materials, the 3 batches of starting material (numbers 4, 5, and 6) were thoroughly mixed, and then weighed into 3 approximately equal portions. The sample preparation method outlined in section 6.2, was adhered to, apart from the firing time, which was increased to 48 hours. This was necessary as the results presented in section 6.3 indicated that this was adequate to reach chemical equilibrium at the firing temperature.

6.4.1 X-ray diffraction

Preliminary analysis by X-ray diffraction was carried out, before the samples were sent to be examined using neutron diffraction. This was carried out by Tadaaki Matsumura using Vega time of flight (TOF) diffractometer, at the KENS pulsed neutron source in the KEK laboratories, Tsukuba, Japan. Comparison of the X-ray diffraction data from these samples and samples from previous experiments are shown in Figures 6.31 to 6.33. As can be seen from the comparison in Figure 6.31, there is some difference in samples fired at 750 °C for differing times. The amounts of impurities present in the two samples are clearly different, which supports the conclusions drawn in section 6.3, that 20 hours is not long enough for a sample to reach chemical equilibrium. This is even more apparent at 750 °C, than 800 °C. There was some doubt as to whether the sample had reached equilibrium after 48 hours at 750 °C, but as the impurity content was increasing with firing time, this was not investigated further. In contrast to the comparison in Figure 6.31, the sample made for the neutron diffraction study at 800 °C was compared with a sample fired for the same time and at the same temperature. The datasets are shown in Figure 6.32. As can be seen, there is an excellent agreement between the two samples. Therefore, it can be concluded that there are no adverse effects from firing a much larger amount of material, in terms of phase purity. The reproducibility of the sample preparation technique is demonstrated.

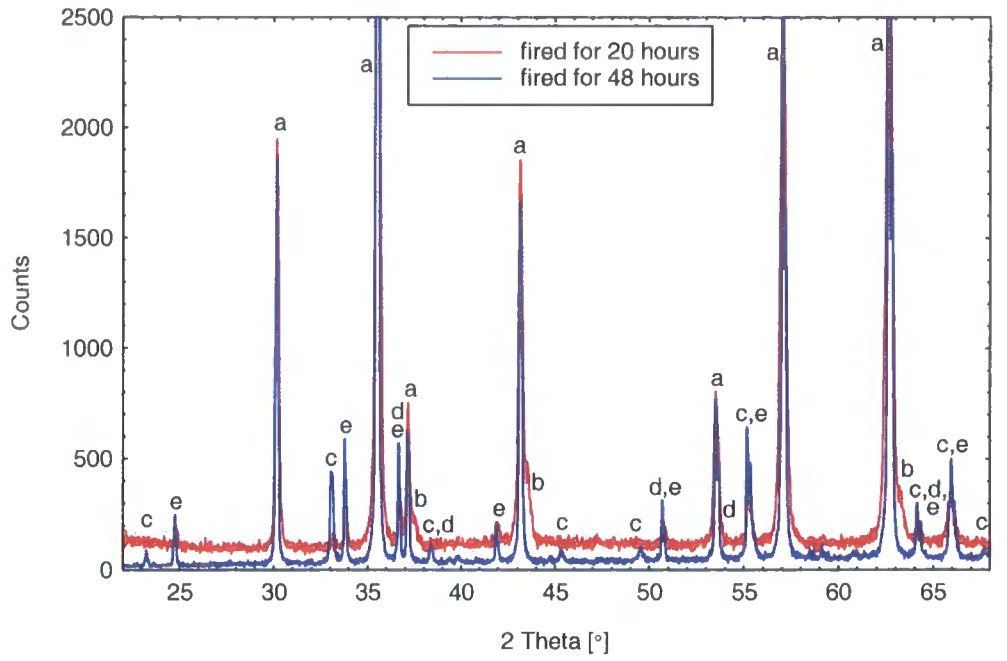

Figure 6.31. Comparison of the X-ray diffraction patterns from samples fired for 20 hours, and 48 hours at 750 °C. The data from the sample fired for 20 hours has been normalised to aid comparison. Peaks corresponding to the various phases present are labelled as follows; a - $NiMn_2O_4$; b - NiO; c - Mn_2O_3; d - Mn_3O_4; e - $NiMnO_3$. Note that the full peak heights are not shown.

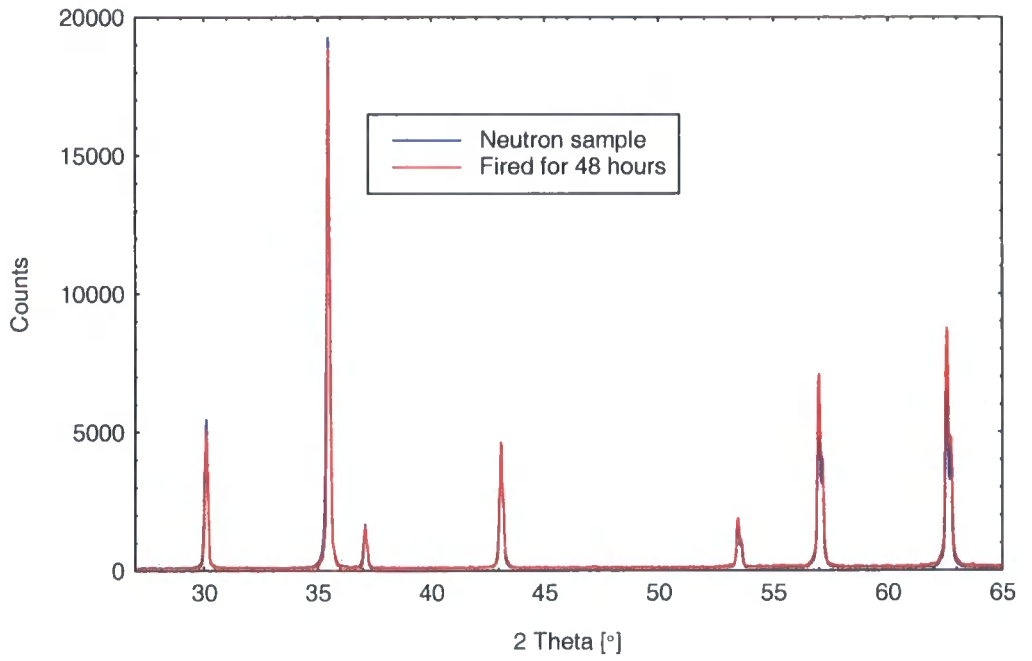

Figure 6.32. Comparison of the X-ray diffraction patterns from 2 samples fired for 48 hours at 800 °C, one from the firing time experiment, the other destined for neutron analysis.

The sample fired at 850 °C for 48 hours was compared with a sample fired at the same temperature for 20 hours. The datasets are shown in Figure 6.33. The

crystallinity has improved, as shown by the improved resolution of the $K_{\alpha 1}$, $K_{\alpha 2}$ split of the incident radiation.

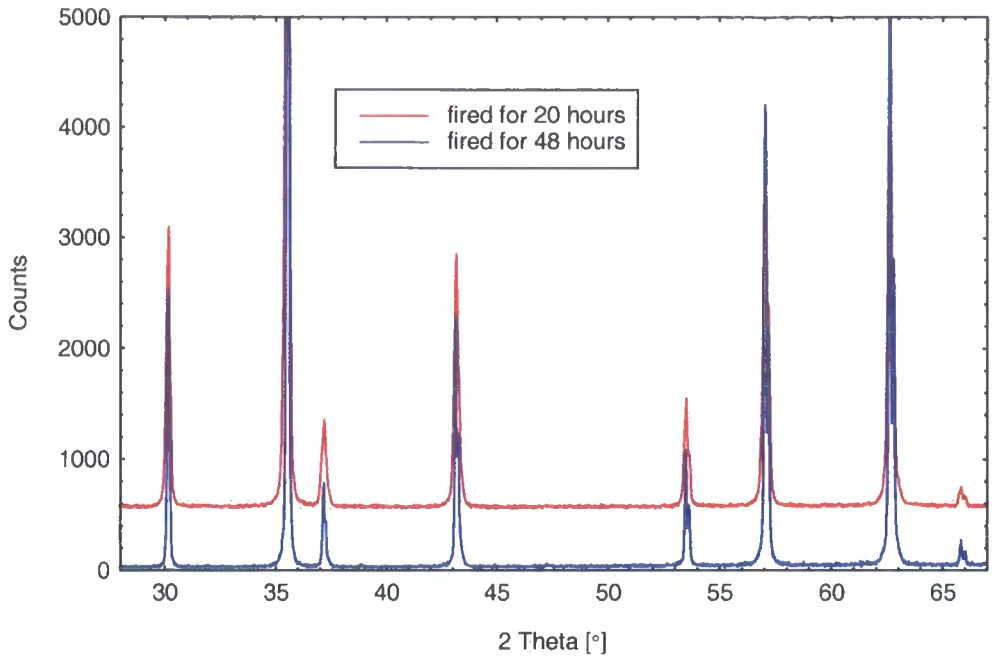

Figure 6.33. Comparison of the X-ray diffraction patterns from samples fired for 20 hours, and 48 hours at 850 °C. The data from the sample fired for 20 hours has been normalised and offset to aid comparison. Note that the full peak heights are not shown.

The amount of nickel oxide present in the sample fired at 850 °C for 20 hours was determined by Rietveld analysis, and found to be 1.66(7) % (volume). From an inspection of the data in Figure 6.33 the amount of nickel oxide did not vary greatly with a change in firing time to 48 hours. From this, and the results of the variable firing time experiments at 800 °C it was tentatively concluded that 48 hours was sufficient to reach equilibrium at 850 °C.

6.4.2 Scanning electron microscopy

The samples destined for neutron diffraction experiments were examined by SEM. The resulting micrographs are shown in Figures 6.34 to 6.36. As can be seen the crystallite size increases markedly between the samples. This seems to indicate that the atoms become much more mobile around 800 °C, enabling crystallite growth (see Figure 6.36), but also unfortunately leading to the segregation of nickel oxide as an impurity phase at 850 °C.

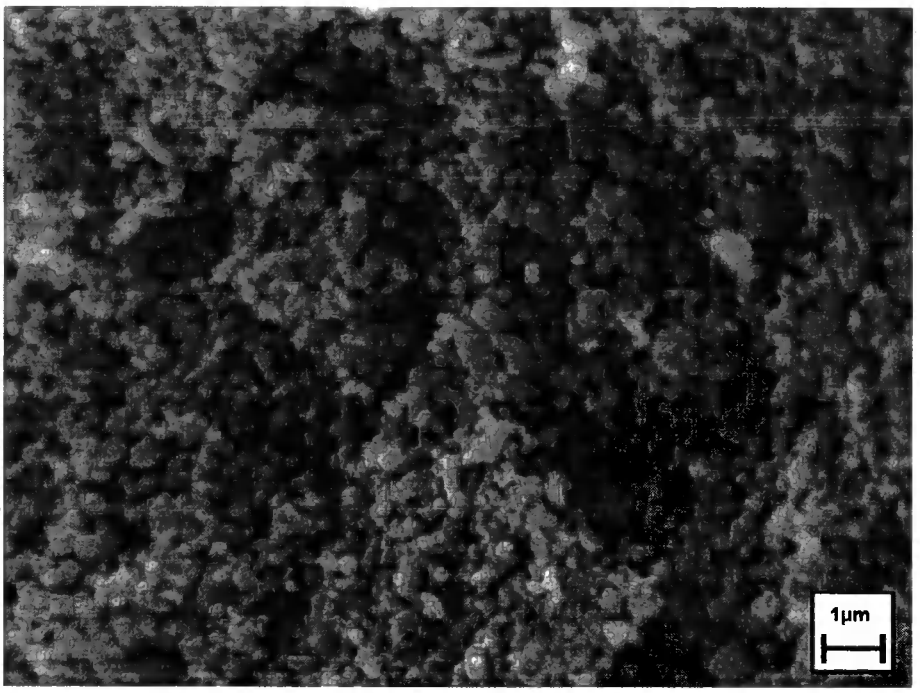

Figure 6.34. SEM image of $NiMn_2O_4$ prepared at 750 °C for 48 hours, taken at 6500 x magnification.

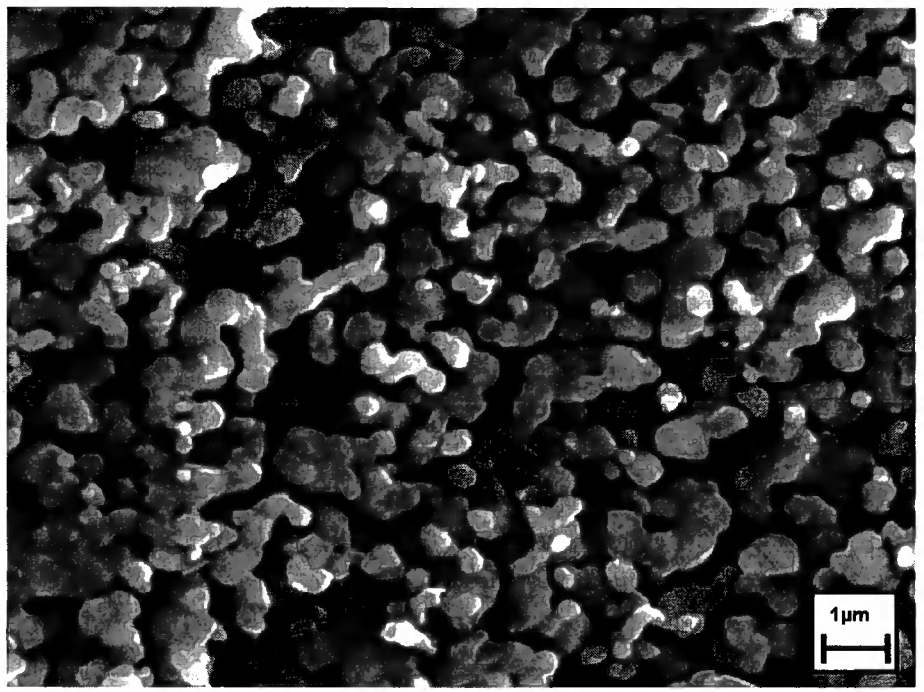

Figure 6.35. SEM image of $NiMn_2O_4$ prepared at 800 °C for 48 hours, taken at 7000 x magnification.

The samples were examined using spatially resolved fluorescence, to highlight any regions with a difference in concentration of nickel, manganese or oxygen. The images obtained were featureless, similar to Figure 6.19. This indicates that the impurities do not form large distinct crystallites.

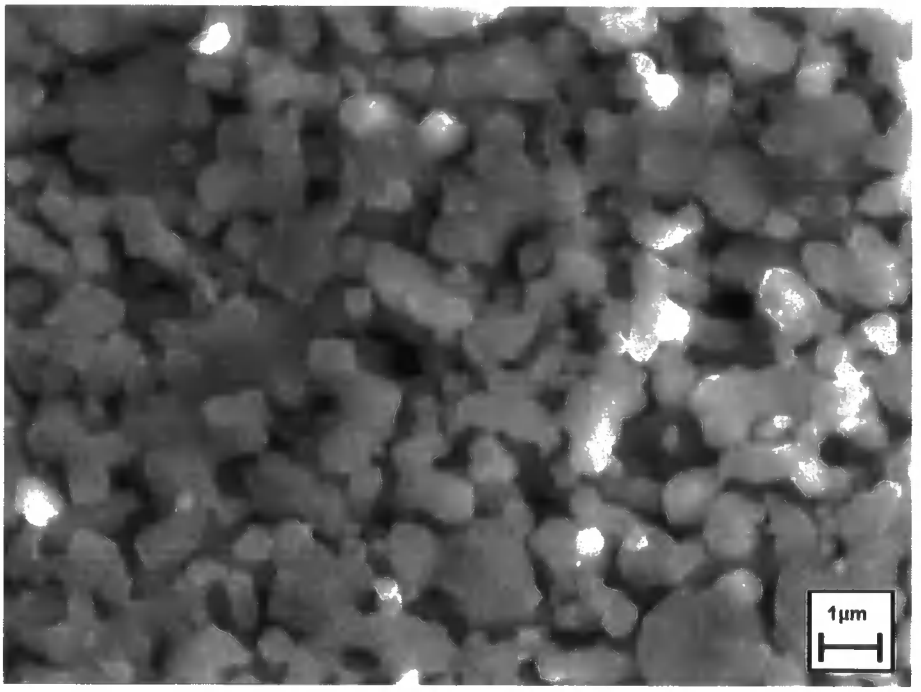

Figure 6.36. SEM image of $NiMn_2O_4$ prepared at 850 °C for 48 hours, taken at 6500 x magnification.

One of the phases ($NiMnO_3$) detected in the sample fired at 750 °C is reported to be a ferrimagnet at room temperature [62]. Any magnetic moment present in the sample would deflect the electron beam used to image the sample in a SEM. This manifests itself as a change in contrast, albeit a weak effect. There is no obvious contrast between grains in the micrograph of the sample fired at 750 °C, which reinforces the conclusion drawn above, of no large impurity crystallites. The sample fired at 850 °C looks to be much less porous than those fired at 750 °C or 800 °C.

6.4.3 Neutron diffraction

Neutron diffraction data was collected from 3 samples on the Vega time of flight (TOF) diffractometer, at the KENS pulsed neutron source in the KEK laboratories, Tsukuba, Japan. Shown on all the figures are fits produced by a Rietveld analysis of the data. The parameter lists, including *R* factors for the fits are to be found in Appendix 2. The data was analysed using the RIETAN2001T [46] program, running on a Macintosh computer. The fitting procedure was similar to that outlined in section 6.2. The number of crystal phases included in the fits varied, according to the peaks identified in the data. A particular phase was included only if peaks were visible that corresponded to that

phase. This excluded the possibility of false positive identification of impurities. There are a number of obvious errors in fitted peak intensities visible in Figure 6.37, all of which are peaks associated with various impurity phases.

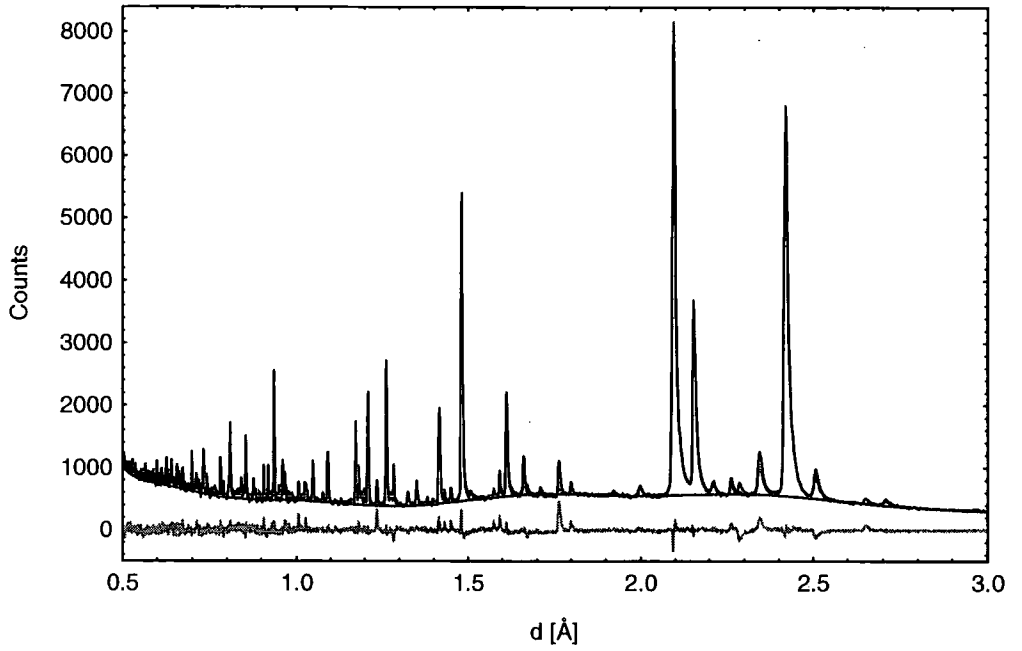

Figure 6.37. TOF neutron diffraction data collected from a sample fired at 750 °C for 48 hours. Also plotted is a fit to the data resulting from Rietveld analysis, the background function used, and the difference between fit and data.

The impurity phase $NiMnO_3$, displays antiferromagnetic order at 300 K [63, 38, 40]. The magnetic reflections due to this ordering [60] could not be included in the refinement due to limitations of the refinement software, time available and capabilities of the available computing hardware. In addition, the reported structure of Mn_2O_3 is complex [36], and may be influenced by small amounts of nickel. The calculated intensities of the diffraction peaks due to these impurities were obviously in error which is reflected in the high values of R_I for the impurity phases, and the goodness of fit indicator, S. The amounts of $NiMnO_3$, and Mn_2O_3 in the sample are almost certainly significantly different to those reported in Appendix 2. However the value of R_I for the nickel manganite phase is comparable to that obtained for the samples fired at 800 °C, and 850 °C, so there is no reason to suspect the parameters associated with this phase to be seriously in error. The data collected on the samples fired at 800 °C, and 850 °C is shown in Figures 6.38, and 6.39.

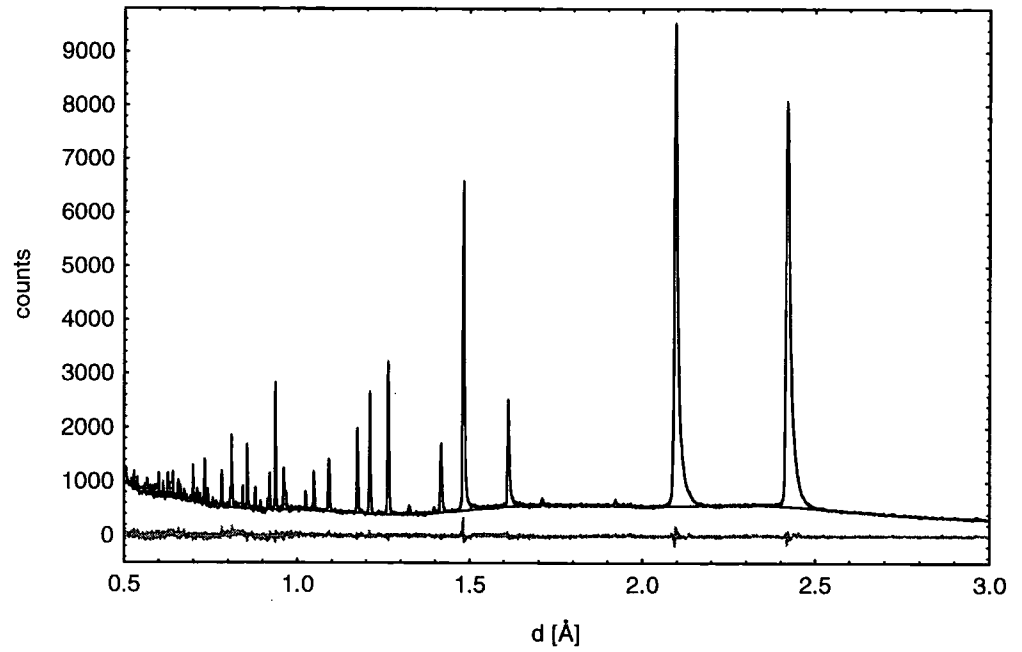

Figure 6.38. TOF neutron diffraction data collected from a sample fired at 800 °C for 48 hours. Also plotted is a fit to the data resulting from Rietveld analysis, the background function used, and the difference between fit and data.

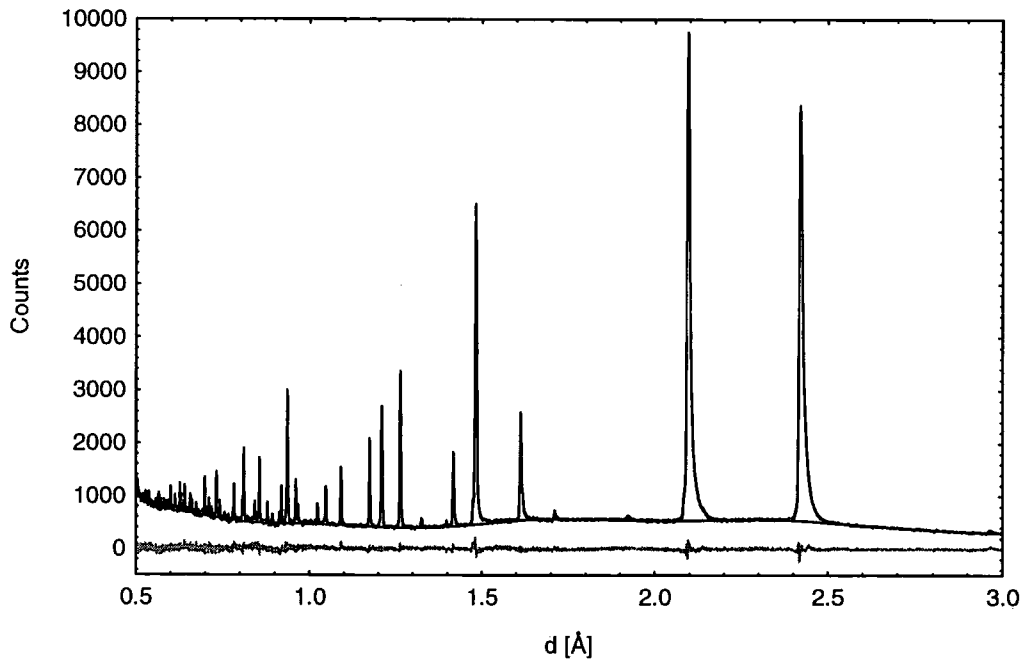

Figure 6.39. TOF neutron diffraction data collected from a sample fired at 850 °C for 48 hours. Also plotted is a fit to the data resulting from Rietveld analysis, the background function used, and the difference between fit and data.

The amount of nickel oxide found in the sample fired at 850 °C was 0.39(6) %, compared with 1.66(7) % found in the sample fired at the same temperature for 20 hours (as determined from X-ray diffraction – see section 6.2). It is unknown

if there are similar systematic inaccuracies in the analysis of T. O. F. neutron diffraction data, as there are in the analysis of X-ray diffraction data (see section 6.2).

Since the neutron scattering cross sections for nickel and manganese are appreciably different, the inversion parameter of nickel manganite was refined. The overall nickel to manganese ratio in nickel manganite was initially constrained to 2 to 1, so that only one parameter described the cation distribution over the A, and B sites. The results of the inversion parameter refinements are presented in Table 6.9.

Firing Temperature, [°C]	750	800	850
Inversion parameter, ν	0.840(5)	0.836(2)	0.833(2)
Expected value	0.725	0.7	0.675

Table 6.9. Results of refining the inversion parameter of samples fired at different temperatures, and calculated expected values.

The values are somewhat different to those of reports in the literature. Expected values are the equilibrium values at the firing temperature, calculated using the formula given by Macklen [19], based upon an oxygen loss study (see section 5.3). Not only are the absolute values different from predictions, but the change with the firing temperature is also different. The expected change in inversion parameter is 0.05 for 100 °C change in firing temperature, while that observed is only 0.007(5), 14 % of that expected. The value of the inversion parameter obtained by Boucher *et al.*, [9], for a sample quenched from 750 °C, was 0.76(4), which agrees with the predictions of Macklen. However, the change in inversion parameter per 100 °C derived from Boucher *et al.*, is only 0.011(9), calculated between 750 °C, and 940 °C. This is again much lower than expected from the predictions of Macklen. There are a number of possible explanations for this discrepancy. The reports in the literature could be at fault, which is unlikely given the reasonable agreement between them of the value expected at 750 °C. Alternatively, the preparation method could be at fault. The samples were cooled by removing them from the furnace and allowing them to cool naturally to ambient temperature. The cooling rate may not have been fast enough to preserve the thermodynamic equilibrium state at the firing temperature, allowing a degree of cation redistribution during cooling. If this was the case, the cooling rate throughout the sample was unlikely to have been

uniform, leading to a possible distribution of inversion parameter values. Diffraction experiments are expected not to be sensitive to this, as a powder average was sampled, and the samples were thoroughly ground prior to measurements being carried out on them. The inversion parameter obtained from diffraction data may therefore not be indicative of the thermodynamic equilibrium conditions at the firing temperature, but instead of some lower temperature. Calculations of what this lower temperature is, are presented in Table 6.10, based on the formula given by Macklen [19], and also the experimental data from Boucher *et al.*, [9].

Sample firing temperature [°C]	750	800	850
Measured inversion parameter, ν	0.840(5)	0.836(2)	0.833(2)
Equilibrium temperature (Macklen) [°C]	520(10)	528(4)	534(4)
Equilibrium temperature (Boucher *et al.*,) [°C]	501(12)	508(5)	513(5)

Table 6.10. Equilibrium temperatures calculated for the measured inversion parameters, after Macklen [19], and Boucher *et al.*, [9].

Available literature reports indicate that the cations become mobile above approximately 400 °C [9, 15]. There is not believed to be any abrupt change in equilibrium phase at these temperatures, and the mobility is due purely to thermodynamic reasons. In a series of thermally programmed reduction experiments [28], the time taken to reach equilibrium amongst the cations at temperatures between 400 °C, and 800 °C was observed to be strongly temperature dependent. At temperatures close to 400 °C, the timescales involved are considerable [19] (see section 5.3 for a fuller discussion). The temperature values in Table 6.10 would seem to indicate that the cooling rate obtained was indeed much too slow to retain the cation distributions at the firing temperature. As noted above, the neutron diffraction data for each of the 3 samples was fitted to a mixture of phases in some cases. The resultant mass fractions of the various phases present in the sample fired at 750 °C are very probably in error, for the reasons mentioned above, but undoubtedly constitute an appreciable fraction of the sample. This is confirmed from the X-ray diffraction data (Figure 6.31). This would be expected to result in a deviation from stoichiometry of the nickel manganite present. Accordingly, the inversion parameter was no longer considered to be adequate to describe the cation distribution in this sample. Therefore, the nickel to manganese ratios on the A, and B sites in nickel

manganite were allowed to vary independently when analysing the data. This was expressed by two site specific 'inversion parameters', ν_A, and ν_B, independent of one another. These parameters would be equal for a stoichiometric sample. The values arrived at by Rietveld analysis for the samples fired at 750 °C, and 850 °C are presented in Table 6.11. The fit to the data of the sample fired at 800 °C did not improve when ν_A, and ν_B were allowed to vary independently.

Sample firing temperature [°C]	Overall inversion parameter, ν	A site inversion parameter, ν_A	B site inversion parameter, ν_B	Manganese to Nickel ratio
750	0.840(5)	0.838(6)	0.841(3)	1.992(13)
850	0.833(3)	0.840(2)	0.829(2)	2.033(6)

Table 6.11. Site specific inversion parameters, as determined by Rietveld analysis, for samples with different firing temperatures.

The deviation of nickel manganite from stoichiometry was 0.4(7) % in the sample fired at 750 °C, and 1.6(3) % in the sample fired at 850 °C. A similar analysis was carried out by Boucher *et al.*, [9], on samples quenched from a wide range of different temperatures. These samples were reported to be consistently manganese rich, by between 2 and 7 %, indicating an appreciable amount of nickel oxide impurity present.

Using the values reported above for the non-stoichiometry of nickel manganite, and the mass fractions of the various phases present, it was possible to obtain the ratio of manganese to nickel for the entire sample. For the sample fired at 750 °C, this was calculated to be 2.22(5), bearing in mind the impurity phase concentrations determined were almost certainly in error. There was no evidence of loss of either metal by staining of the crucible in which the sample was fired, and the firing temperature was well below the melting points of all the phases present. There are a number of possible explanations for this result. In common with nickel manganite, the two impurity phases present can both accommodate some non-stoichiometry [36, 40]. However, the relatively small amounts of these phases present in the sample precluded any meaningful determination of the non-stoichiometry from analysis of the diffraction data. The calculated manganese to nickel ratio for the sample fired at 850 °C was 2.007(8), as expected.

The lattice parameters were also obtained from the Rietveld refinement of the neutron diffraction data. These are compared with values obtained from X-ray data in Figure 6.40.

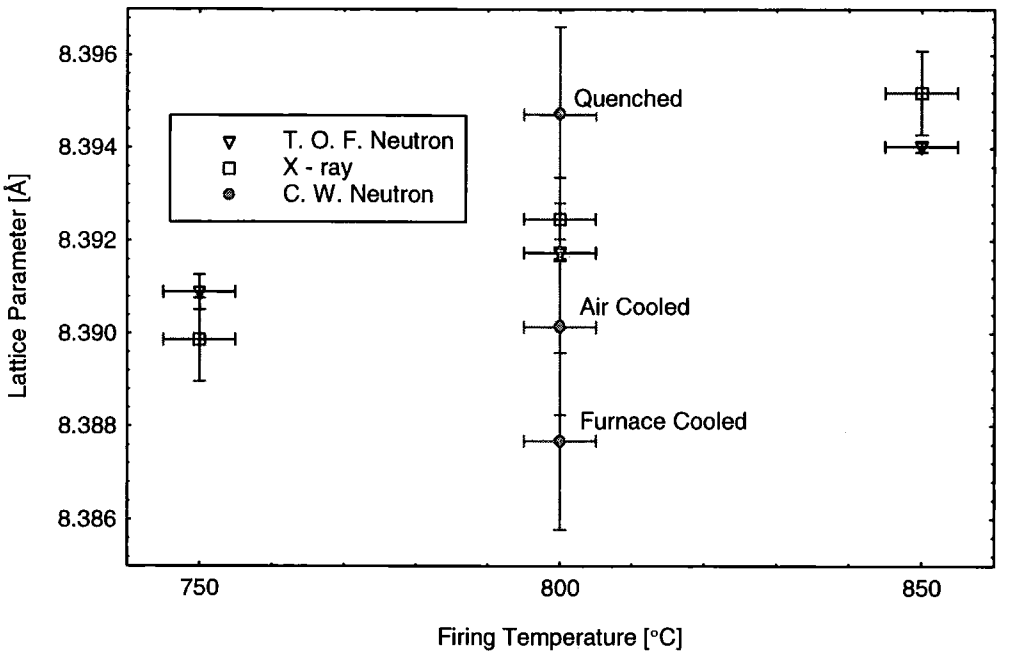

Figure 6.40. Lattice parameters of nickel manganite fired at different temperatures, obtained from fitting to neutron, and X-ray diffraction data. The green points were obtained from samples subjected to different cooling rates, as detailed in section 6.5.

There is an acceptable agreement between lattice parameters determined from the two different diffraction techniques. The values in Figure 6.40 are also in agreement with the values obtained in earlier experiments (Figure 6.10, and Figure 6.23). The isotropic temperature factors (or *B* factors) obtained from the Rietveld refinements are presented in Figure 6.41. In comparison with those obtained from X-ray data (Figure 6.12, and Figure 6.24), the values obtained here are higher for all the sites. The values for the oxygen sites are still significantly higher than for the cations. Due to the neutron scattering length of oxygen being comparable to those of nickel and manganese (see Table 6.8), the ability to resolve the positions of the oxygen atoms should be good. This is not the case using X-rays, as the scattering amplitude is dependent on atomic number. The improved resolution of the oxygen atoms is manifest as smaller statistical uncertainties of the oxygen temperature factors, relative to those of the cations. This can clearly be seen when comparing the relative error bar sizes in Figure 6.12, and Figure 6.24, with those in Figure 6.41.

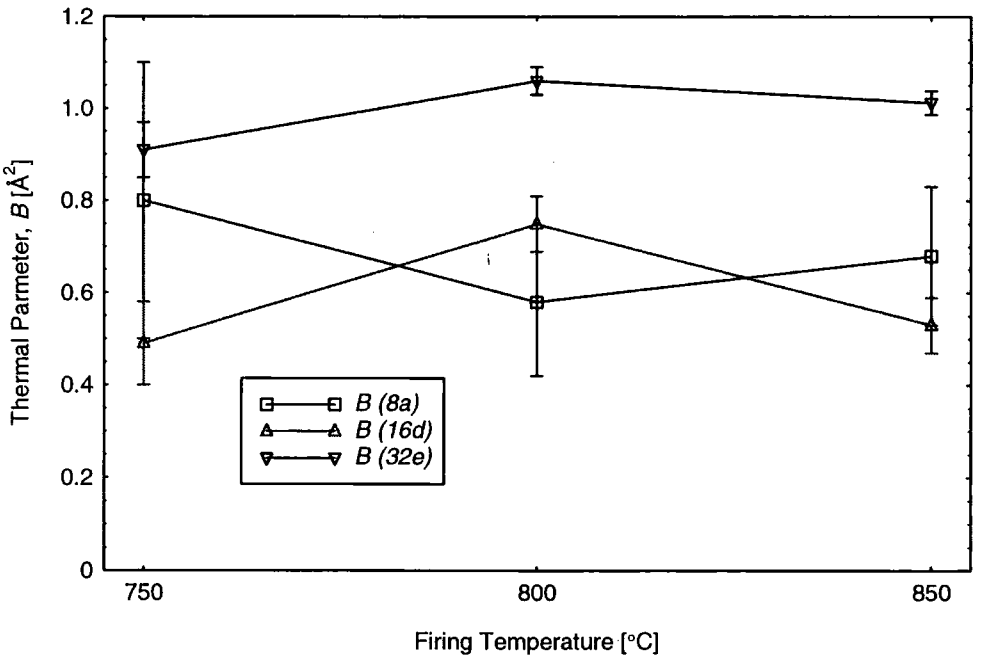

Figure 6.41. Isotropic temperature factors nickel manganite fired at different temperatures, obtained from fitting to neutron diffraction data.

In conclusion, altering the firing temperature is not a satisfactory way to vary the inversion parameter of nickel manganite. The temperature region in which nickel manganite is stable as a pure phase is too small to obtain any significant change in inversion parameter. The cooling rate of the samples made was probably too slow to preserve the cation distribution at the firing temperature.

6.5 Effect of varying the cooling rate on inversion parameter

As shown in section 6.3, the time it takes for sample precursor material to react completely at 800 °C is approximately 48 hours. It is to be expected that the timescale for decomposition of nickel manganite into a mixture of oxides as it is cooled, is also of this order. A comparison of literature values, and the data presented in section 6.4 indicates that the cation redistribution reaction takes place much more rapidly, such that an appreciable change in inversion parameter occurs within a few minutes. Therefore, an obvious method of obtaining samples with differing inversion parameters is to alter the cooling rate from the firing temperature. Provided that nickel manganite is stable as a pure compound at the firing temperature, and the cooling rate is not too slow, the purity of the samples should be high. All the results obtained thus far indicate that 800 °C is the optimum temperature at which to prepare samples to ensure minimal impurities.

6.5.1 Sample preparation

Three different methods of cooling samples were investigated; quenching into liquid nitrogen, cooling in air at ambient temperature (as used for all previous samples), and furnace cooling at a rate of 1 K minute^{-1}. A quench into liquid nitrogen requires that the sample be in pellet form since the rapid production of nitrogen gas would disperse a powdered sample. Therefore, to aid in comparison, all the samples were made into pellets. It was found that any attempt to make the mixed hydroxide precursor into pellet form was difficult to extract from the pellet press used, and produced extremely friable pellets. In view of this, the following preparation route was employed.

The use of neutron diffraction again meant that large amounts of sample had to be produced. Five batches of precursor material (numbers 8 to 12) were prepared, mixed and then divided into 4 approximately equal portions of 8.9 g. These samples were then individually fired as powders at 800 °C for 48 hours, to convert them to high purity nickel manganite. The heating rate used was 10 K minute^{-1}, and the samples were allowed to cool at ambient temperature when removed from the furnace. The samples were then pressed into a number of pellets using a 13 mm diameter steel pellet press with a force of 20 kN (2 metric tons). The pellets were then fired again for 48 hours at 800 °C and then subjected to one of a number of heat treatments. These are outlined in Table 6.12, along with the identifying numbers of the samples. The pellets were then ground to powders, as required for neutron diffraction.

Sample number	Heat treatment
1	Removed from furnace, and immediately quenched into liquid nitrogen.
2	Removed from furnace, and allowed to cool in air at ambient temperature.
3	Slow cooled in the furnace, at a rate of 1 °C per minute.
4	Transferred into second furnace at 1150 °C for 90 seconds, then quenched into liquid nitrogen.

Table 6.12. Heat treatments applied to the samples.

6.5.2 Neutron diffraction

Neutron diffraction measurements were taken on the instrument D1A, at the Institute Laue – Languevin (ILL), Grenoble, France. Data was collected for 8 hours, at 3 different temperatures (2 K, 105 K, and 300 K) for each sample.

The wavelength of the incident neutrons was 1.9404 Å, and data was collected in the angular range $10\ ° \leq 2\theta \leq 150\ °$.

6.5.3 300 K data

A portion of the data collected at room temperature (300 K), is shown in Figure 6.42.

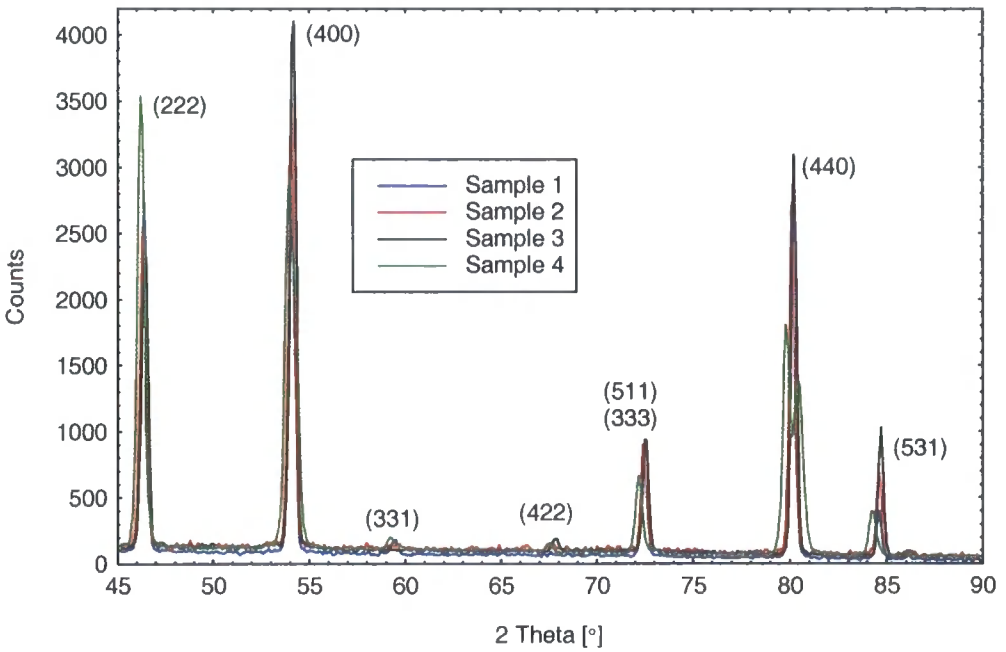

Figure 6.42. Some of the neutron diffraction data collected on all 4 samples at room temperature.

The only sample to exhibit any reflections attributable to impurity phases is sample 4. The (222), (400), (440), and (444) peaks of this sample are all contaminated by nickel oxide reflections. As can be seen from the data, the heights of all peaks change from sample to sample. This is attributed to a change in inversion parameter, as the neutron scattering factors of nickel and manganese are dissimilar. Due to the different symmetries of the A, and B sites, only certain reflections are allowed from them. This dependency is listed in Appendix 1, for different reciprocal lattice vectors, *hkl*. The oxygen sites, having a lower symmetry than either cation site, contribute to all allowed reflections for the space group (see section 4.1.1). All the peaks shown in Figure 6.42 are allowed reflections for the B sites, apart from (220), and (422) peaks. Since these are very weak reflections, no definite trends can be observed. The only peak not affected by the A sites is the (222) peak. The trend in this peak is opposite to the

trend in all the other peaks, lending weight to the contention that this is caused by a change in inversion parameter.

Rietveld analysis was carried out on the data as shown in Figure 6.42. This was carried out using the programs FULLPROF, and WinPLOTR [44], in a similar manner to the analysis of the X-ray diffraction data presented in section 6.2. Detailed results from all of the refinements can be found in Appendix 2. A representative dataset is presented in Figure 6.43, showing the data, fit, and difference curves.

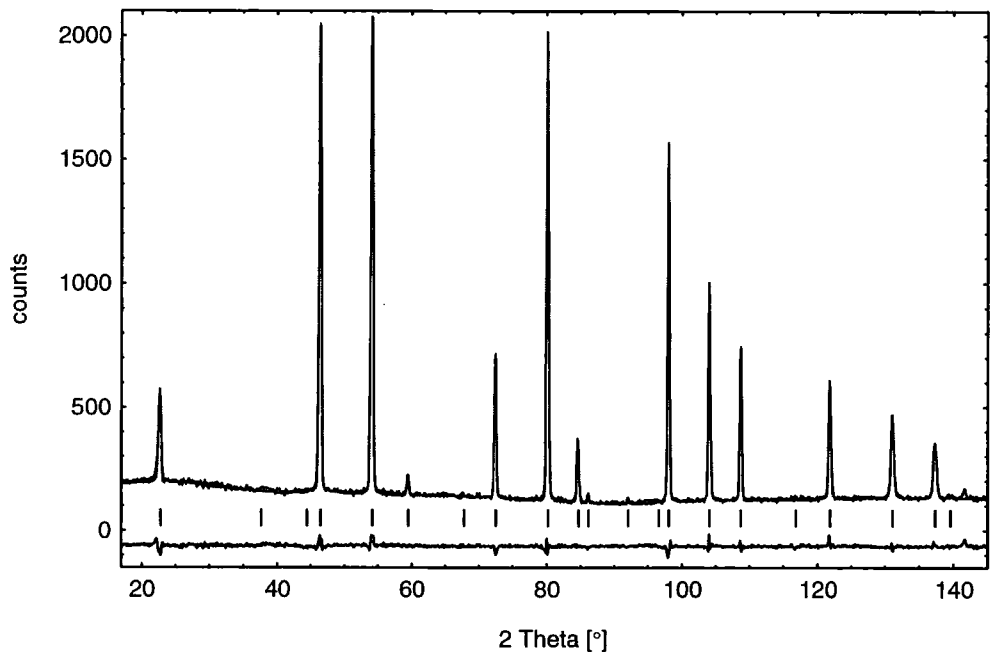

Figure 6.43. Graphical results of the Rietveld analysis of the data collected from sample 1, at 300K. The data, fit, difference curve, and allowed reflections for nickel manganite are shown.

The model fitted to data from samples 1 – 3 included only a nickel manganite phase, but an additional nickel oxide phase was included when analysing data from sample 4. As was the case for the analysis reported in section 6.2, the lattice parameter, oxygen position, and inversion parameters were refined for all samples. Peak profile parameters and scale factors were also refined, as before. In some cases it was found that the *16d* (A site) isotropic temperature factor was unstable in the refinement. In these cases, it was fixed at a value of 0.65, in accordance with the findings presented in Figure 6.41. In the case of the nickel oxide present in sample 4, the occupancy factor of nickel was refined. This sample was found to contain 11(4) % nickel oxide by volume. In view of the large amount of nickel segregated as nickel oxide in sample 4, it was not

surprising that using a single inversion parameter to describe the cation distribution in nickel manganite did not give a satisfactory fit to the data in this case. Therefore, following the procedure outlined in section 6.4.3, separate inversion parameters were refined for the A, and B sites in this sample. The values arrived at are reported in Table 6.13, and indicate a substantial deviation from stoichiometry.

Sample no.	Lattice parameter, a [Å]	Oxygen parameter, x	Overall Inversion Parameter, ν	A site Inversion Parameter, ν_A	B site Inversion Parameter, ν_B
3	8.38768(12)	0.26357(7)	0.8830(22)	0.8868(29)	0.8714(50)
2	8.39014(26)	0.26368(10)	0.8177(29)	0.8215(38)	0.8090(72)
1	8.39472(16)	0.26314(9)	0.7483(19)	0.7558(26)	0.7306(46)
4	8.42315(25)	0.26371(8)	-	0.89(33)	0.62(18)

Table 6.13. Various refined parameters arrived at from the neutron diffraction data in Figure 6.47.

However, the estimated standard deviations are considerable, reflecting the fact that the determination of site specific occupation parameters in a high symmetry crystal structure depends on the relative intensities of quite a small number of peaks. The relevant chemical formula for this phase was calculated to be;

$$Ni_{0.73(38)}Mn_{2.27(38)}O_4.$$

The value of δ for the nickel oxide (chemical formula $Ni_{(1-\delta)}O$ [39]) present in sample 4, was determined as 0.112(17). Using these values from the refinement, the overall manganese to nickel ratio for the sample was 2.2(4). Even though Nickel oxide is an antiferromagnet at room temperatures [64], and therefore additional scattering from the ordered moments would be expected [60], the cubic symmetry, and random orientation result in a lack of observable magnetic Bragg reflections [65].

In common with the Rietveld refinements carried out on the data in section 6.4.3, once a value of the inversion parameter had been obtained for samples 1-3, the site occupancy constraints were made independent, and inversion parameters for the A, and B sites were refined seperately. All of the values arrived at are also reported in Table 6.13. During this extra stage in the data refinement, all of the other structural parameters were also refined. None of these varied significantly from the values obtained when refining a single inversion parameter. The A site inversion parameters are consistently larger than the B site inversion parameters. The difference is small for all samples, except sample 4, for reasons outlined

above. This small deviation indicates there is a slight nickel deficiency in the nickel manganite of the samples, of about 2 %. The same trend was seen in a similar analysis carried out by Boucher *et al.,* [9], where the deficiency values reported therein are in the range of 2 % to 7 %. The lack of any detectable nickel oxide does not mean that the samples are necessarily nickel deficient overall. The precursor materials were suitably fine as to present little in the way of Bragg reflections. It is possible that a small portion of this amorphous material remained, or had been segregated from the nickel manganite crystallites in sufficiently small concentrations to be non-crystalline. The lattice parameter obtained for different inversion parameters is shown in Figure 6.44, in comparison with values found in the literature (see section 5.2 for more details).

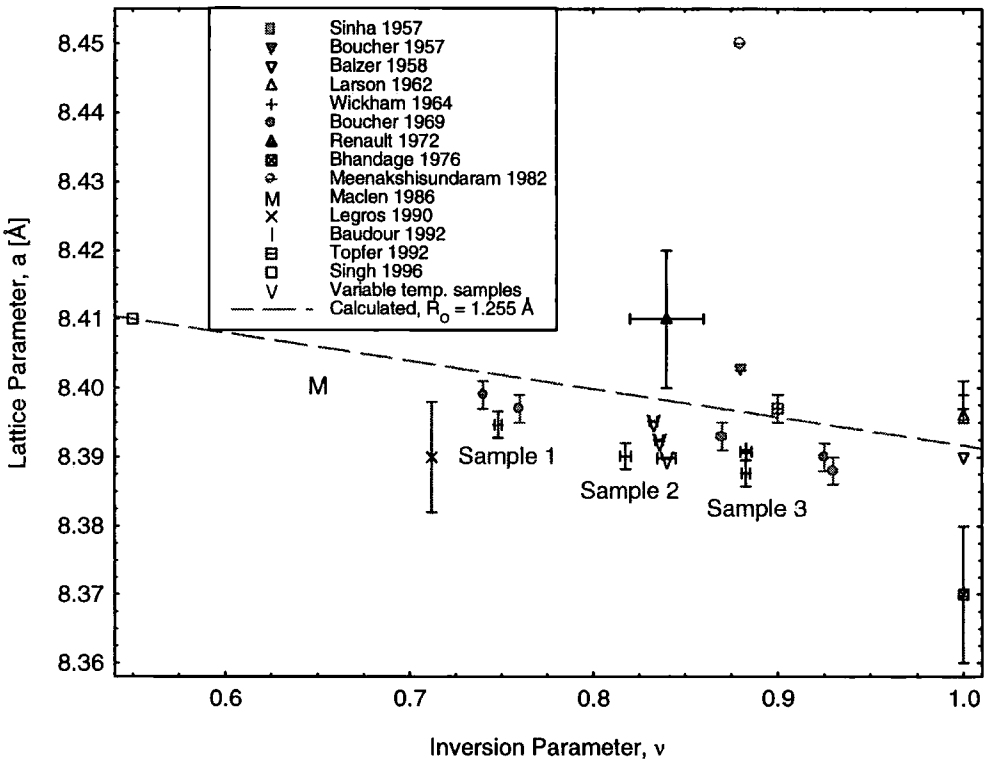

Figure 6.44. Comparison of lattice parameters and inversion parameters reported in the literature, and those obtained in this work, labelled Sample 1, 2, and 3 (see text for details). Results obtained in section 6.4 are also shown. The line is from a predictive model (see section 4.2).

The dashed line plotted in Figure 6.44 is a prediction based upon ionic radii calculations, and assuming the cation distribution postulated by Brabers *et al.,* [15]. The calculation is based upon an oxygen radius of 1.255 Å, and all the cations being in high spin states (see section 4.2.3 for more details). The trend of the lattice parameter for samples 1-3 is in agreement with the

predictions, and literature values. The values are a little lower than expected, but not unreasonably so. This could be due to differences in the preparation conditions between this study, and other workers. There has been quite a variation in the precursor materials, temperatures, and firing times used to produce nickel manganite. More details are given in chapter 5, and section 6.1. There is also the possibility of systematic errors in the diffractometer used. The values of lattice parameter determined for the samples studied in section 6.4 are also plotted for comparison. The trend observed in these datapoints is attributed to stoichiometry changes, rather than lattice parameter variation.

It is worthwhile noting that the value of lattice parameter for sample 4 (8.42315(25) Å) is significantly higher than all but one (Meenakshisundaram *et al.*, [17]) of the reported literature values. The fact that this sample is appreciably non-stoichiometric, and all the stoichiometric samples have much lower lattice parameters casts doubt on the purity of the sample measured by Meenakshisundaram *et al.*,. An increase in lattice parameter with decreasing nickel content was noted by Wickham [6]. The data for sample 4 is not shown in either Figure 6.44, or 6.45, due to the lack of a definable inversion parameter. Comparison of the oxygen position (shown in Figure 6.45) also reveals an agreement between this, and earlier works. The values of x from Table 6.13 have been converted to the u parameter used in earlier works. The lines are again predictions that are based upon ionic radii calculations, for high spin and low spin cations. There are several shortcomings to the model used for predictions (see section 4.2.4 for more details). In particular, the presence of any Mn^{3+} ions on the A sites has a large effect on the expected oxygen position, reducing it from the predictions plotted. The decrease in oxygen parameter at high values of the inversion parameter, ν, is noticeable both in results from this work, and data from Boucher *et al.*, [12]. This decrease at high inversion parameter may be less pronounced in the data from Boucher *et al.*,, but a comparison is difficult due to the large error bars reported, and the lack of a sample with a high enough inversion parameter in the present study. In contrast to the case for lattice parameter, non-stoichiometry does not seem to contribute greatly to deviations from expected oxygen parameter. The value obtained from sample 4 (appreciably non-stoichiometric) is (within experimental error) identical to that

for sample 2 (~ 2 % nickel rich). Although it is noted that the value reported by Meenakshisundaram *et al.*, [17] is again an extreme value.

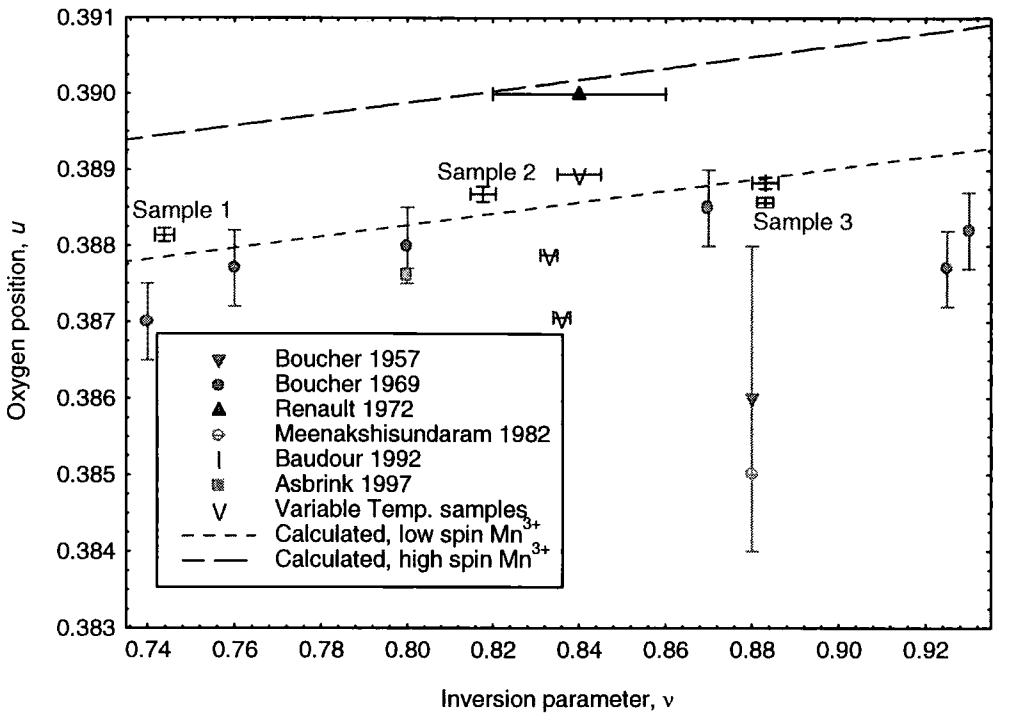

Figure 6.45. Comparison of oxygen positions and inversion parameters reported in the literature, and those obtained in this work, labelled Sample 1, 2, and 3 (see text for details). Results obtained on samples fired at various temperatures (section 6.4) are also shown. The lines are from a predictive model (see section 4.2).

6.5.4 Low temperature (2 K and 105 K) Data

In addition to the room temperature data discussed above, diffraction patterns at low temperatures were obtained with the use of a cryostat mounted on the diffractometer. The cryostat was a liquid helium continuous flow type, and was fabricated in the workshops at the ILL. Plots of part of the datasets obtained for samples 1-4 at various temperatures, are shown in Figures 6.46 to 6.49. The 3 measurement temperatures were chosen to lie in the 3 regions of different magnetic behaviour, as reported by Boucher *et al.*, [12]. These were; a paramagnetic regime at room temperature, a collinear ferrimagnetic regime at 105 K, and a complex canted spin arrangement at 2 K. The collinear region was reported to exist between a lower transition at approximately 80 K and the Curie temperature, which was reported to vary between 115 K and 160 K, depending on the inversion parameter.

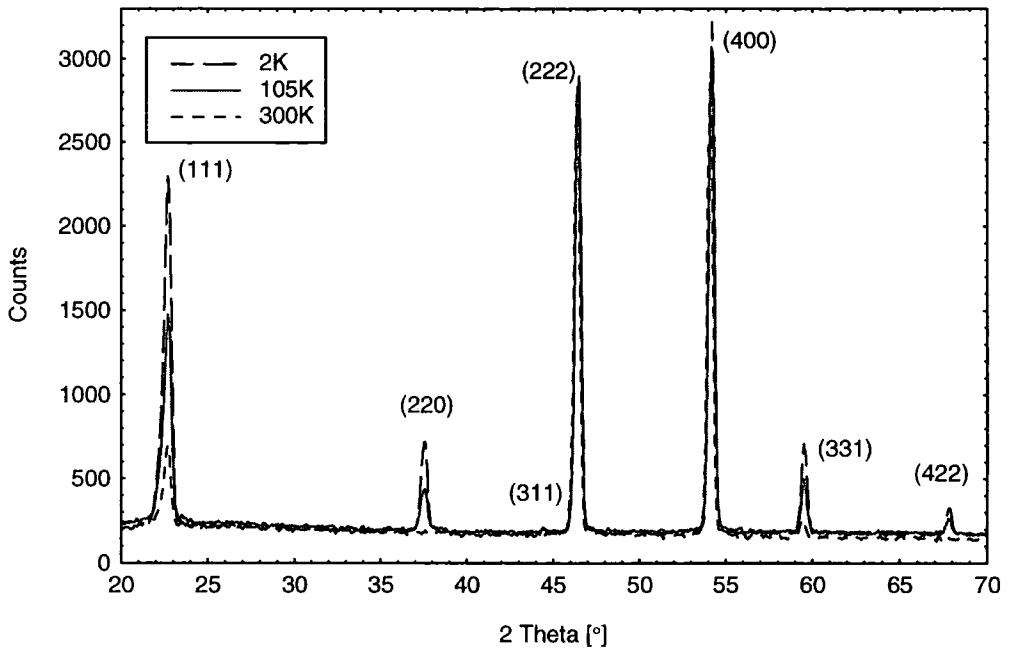

Figure 6.46. Comparison of neutron diffraction patterns obtained from sample 1 at 2 K, 105 K, and 300 K. The relevant reciprocal lattice vectors are given for reflections from nickel manganite. Only a part of the datasets are shown.

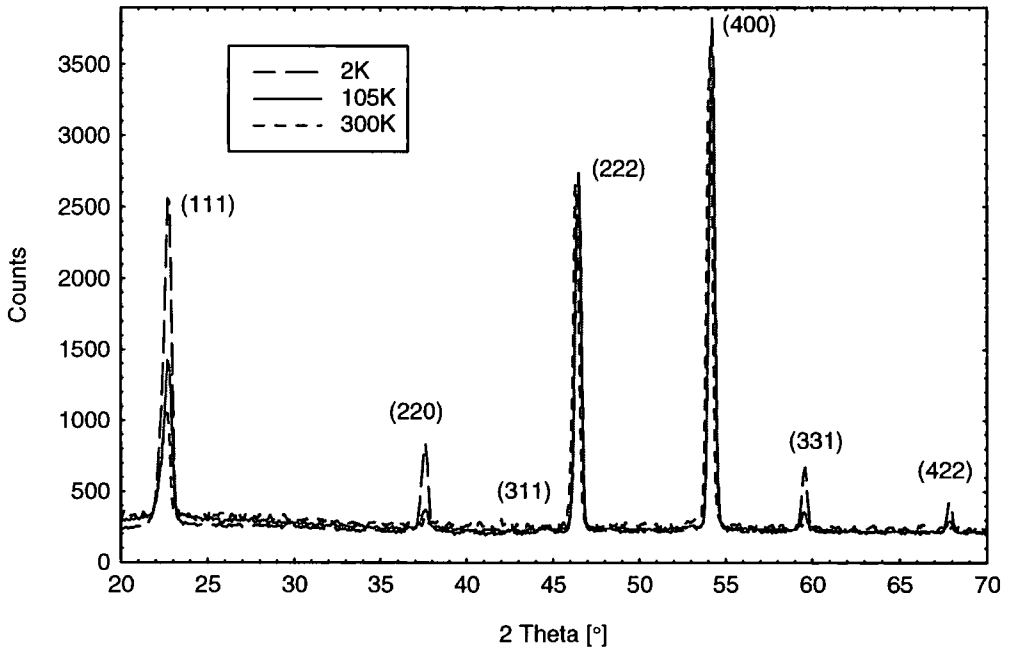

Figure 6.47. Comparison of neutron diffraction patterns obtained from sample 2 at 2 K, 105 K, and 300 K. The relevant reciprocal lattice vectors are given for reflections from nickel manganite. Only a part of the datasets are shown.

In all the samples measured there was a noticeable change in the diffraction pattern obtained at low temperatures, compared with the room temperature data. This change manifest as the appearance of diffraction peaks that were formerly absent, or very weak, and a change in height of existing peaks. These changes

were concentrated at lower values of 2θ, with higher angle peaks not displaying any noticeable change.

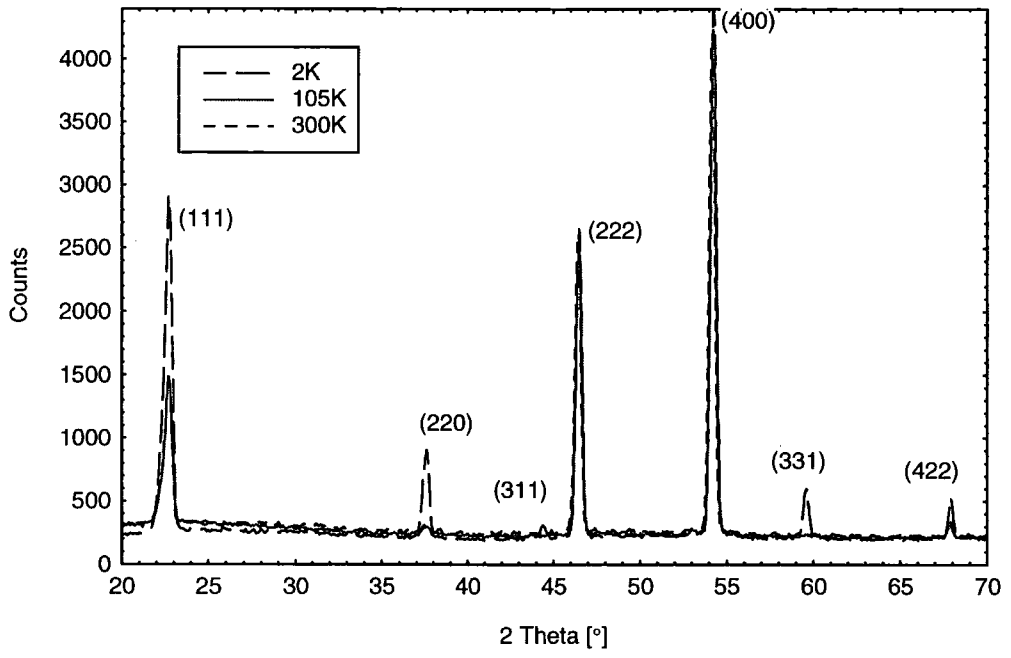

Figure 6.48. Comparison of neutron diffraction patterns obtained from sample 3 at 2 K, 105 K, and 300 K. The relevant reciprocal lattice vectors are given for reflections from nickel manganite. Only a part of the datasets are shown.

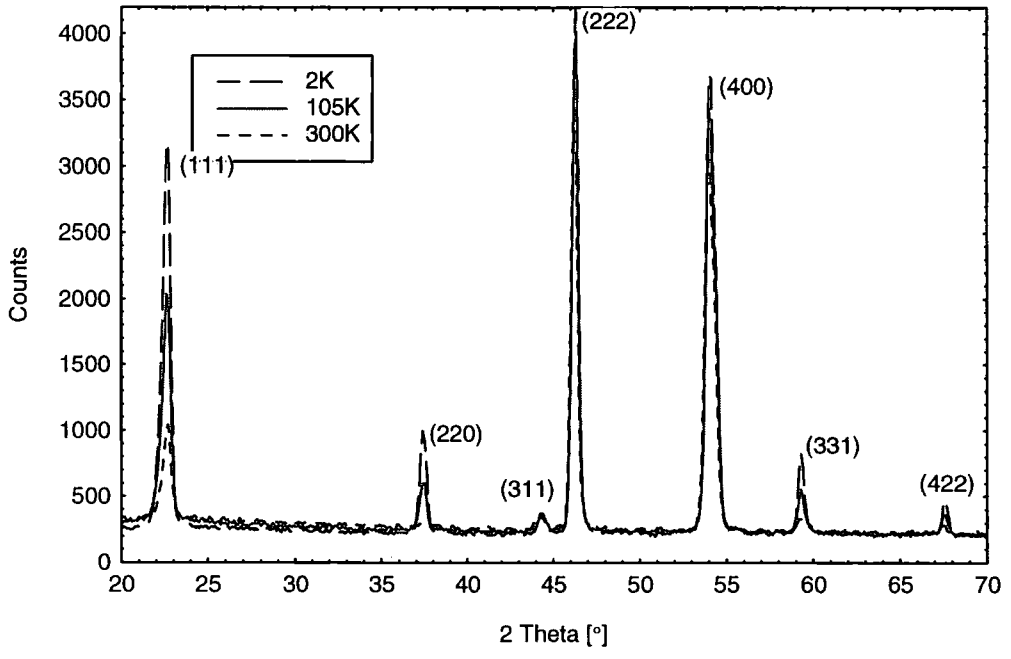

Figure 6.49. Comparison of neutron diffraction patterns obtained from sample 4 at 2 K, 105 K, and 300 K. The relevant reciprocal lattice vectors are given for reflections from nickel manganite. Reflections due to nickel oxide are not indexed. Only a part of the datasets are shown.

All of the peaks appearing were at the positions of allowed reflections from the spinel structure (see section 4.1 for a discussion of allowed reflections, and Appendix 1 for a list).

These factors all indicated that the onset of magnetic ordering was responsible for this effect. The strength (peak height) of magnetic reflections decreases rapidly with increasing Bragg angle [60]. This angular dependency is described by the magnetic form factor, which varies for different magnetic species. The fact that there were no emergent peaks that corresponded to fractional values of *hkl* indicates that the magnetic unit cell is the same size as the crystallographic unit cell. Examination of the dependencies of certain reflections on the contents of either the A, or B site, indicates that magnetic ordering is present on both sites. The (220) reflection is sensitive to only the A sites, and increases massively at 2 K. The (222) reflection sensitive to only the B sites [43], and shows slight changes with temperature for all samples. There is not believed to be any change in the crystallographic structure, or cation distribution below room temperature. Contradictory reports in the literature exist on this issue, with Brabers *et al.*, [15] asserting that cation mobility ceases around 400 °C, and Åsbrink *et al.*, [59] reporting a change in inversion parameter between room temperature and 115K. The conclusions of Åsbrink *et al.*, are far from certain however, as the reported error on their inversion parameter at 115 K was larger than the change observed. The character of the changes observed upon cooling to 105 K, and 2 K, is broadly the same for all the samples except sample 3. For this sample, there is little change in the diffraction patterns collected at 300 K, and 105 K. This implies either weak, or an absence of magnetic order at 105 K. Sample 3 has the highest inversion parameter of all the samples produced, as it was slow cooled from the firing temperature. According to the findings of Boucher *et al.*, [12], the Curie temperature decreases as inversion parameter increases, but the lowest value reported was 113 K, for a sample with an inversion parameter of 0.93. This sample was also slow cooled from the firing temperature. There are a number of possible explanations for this discrepancy, such as the Curie temperature depending upon other factors as well as the inversion parameter. The degree of non-stoichiometry reported for the Boucher *et al.*, sample was 5 %, whereas the value for our sample is 2.5(12) %, which may have some

bearing. In the extreme case of nickel deficiency, the mineral Hausmannite (Mn_3O_4), an ordering temperature of 80 K is observed [64], so smaller deficiencies may also result in a change in Curie temperature. Another possibility is that the sample temperature may have been inaccurate for either or both measurements.

Rietveld analysis of the low temperature neutron diffraction data was attempted. This was achieved by adding the magnetic scattering as an additional component to the model used. The results of the 300 K refinements for each sample were used as a starting point for the low temperature model. It was assumed that the inversion parameter, nickel oxide content (where applicable) and oxygen parameter remained constant upon cooling below 300 K. The lattice parameter was allowed to vary, to account for the thermal expansion coefficient of nickel manganite. The refined values of the lattice parameter are plotted in Figure 6.50.

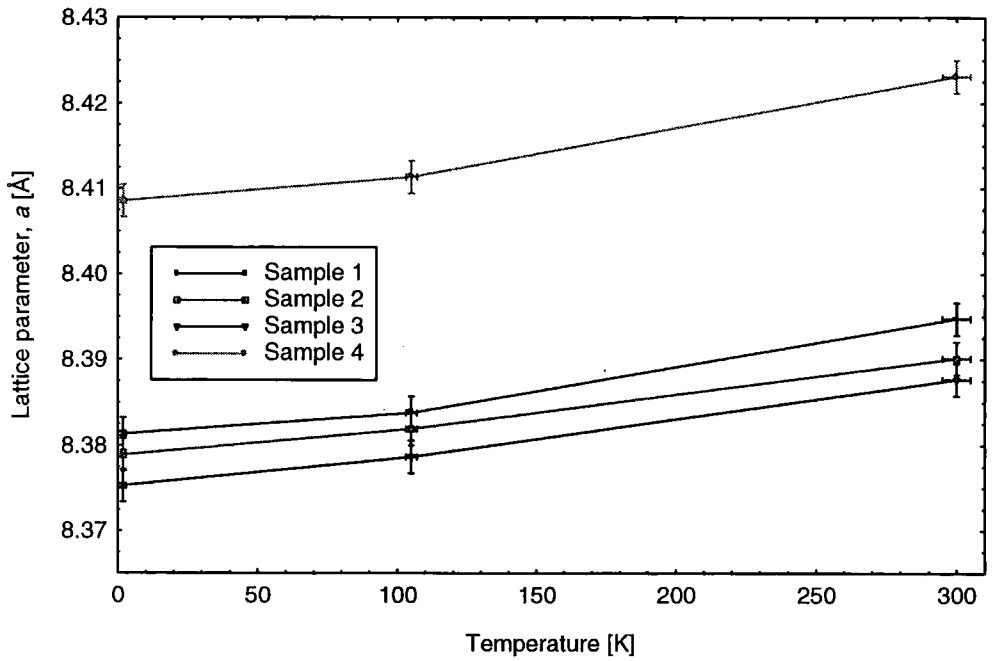

Figure 6.50. Refined lattice parameters, obtained from Rietveld analysis of neutron diffraction data from samples 1 - 4.

The behaviour of the lattice parameter with temperature is broadly the same for all 4 samples, and is what would be expected due to thermal contraction. There is no evidence of any structural phase change at low temperature.

There were limitations imposed upon the complexity of the model used for the magnetic structure. The most serious of these was that, due to the cubic crystal

structure, it was not possible to determine in which direction the magnetisation vector pointed [65]. The magnetisation direction was arbitrarily chosen to lie along the (100) direction in order to simplify calculations. In addition, the cubic unit cell, and the rapid decrease in magnetic form factors with increasing diffraction angle meant that the number of diffraction peaks showing a significant magnetic contribution was limited to 5 or 6. Because of this, the number of refined parameters used to describe the magnetic structure had to be limited in order to preserve an adequate over-determination ratio. The magnetic model used was that of a collinear ferrimagnet, with the moments on the A sites in the (100) direction, and the moments on the B sites antiparallel to this. An average magnetic moment was refined for each sublattice, as trying to model each ion species individually would have involved too many additional parameters. The results of these refinements can be found in Appendix 2. A plot of the data collected from sample 2 at 2 K, and the refinement fit is shown in Figure 6.51.

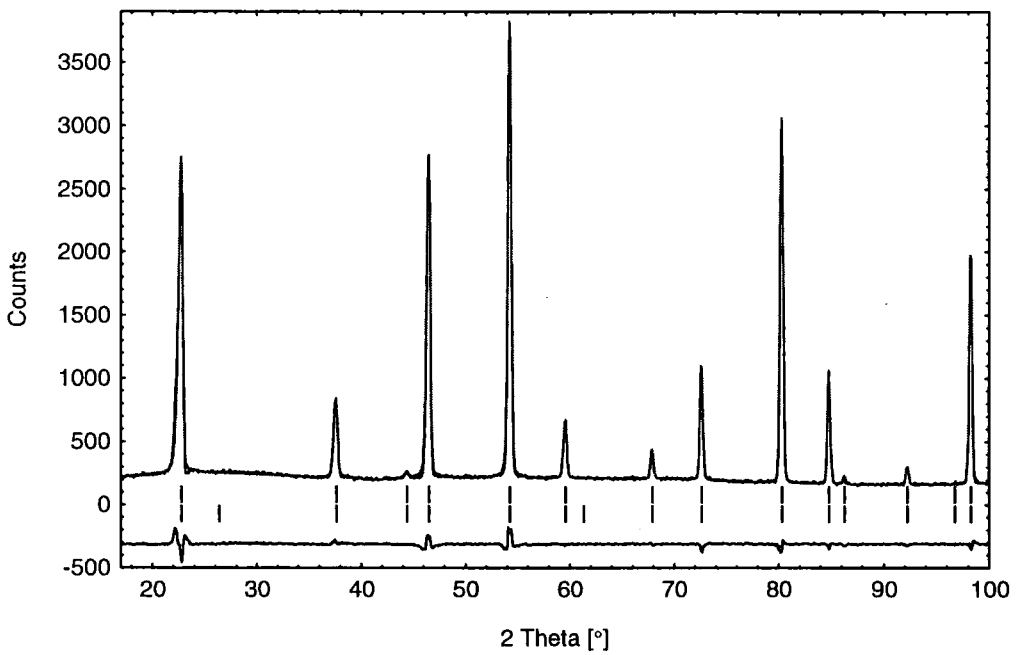

Figure 6.51. Graphical results of the Rietveld analysis of the data collected from sample 2, at 2 K showing data, fit and difference curves. The allowed nuclear reflections for nickel manganite are marked in the upper line, and the allowed magnetic reflections in the lower line.

The agreement between the integrated areas of the peaks in the data and fit is good. The resulting magnetic moments from the Rietveld refinements are shown in Figure 6.52.

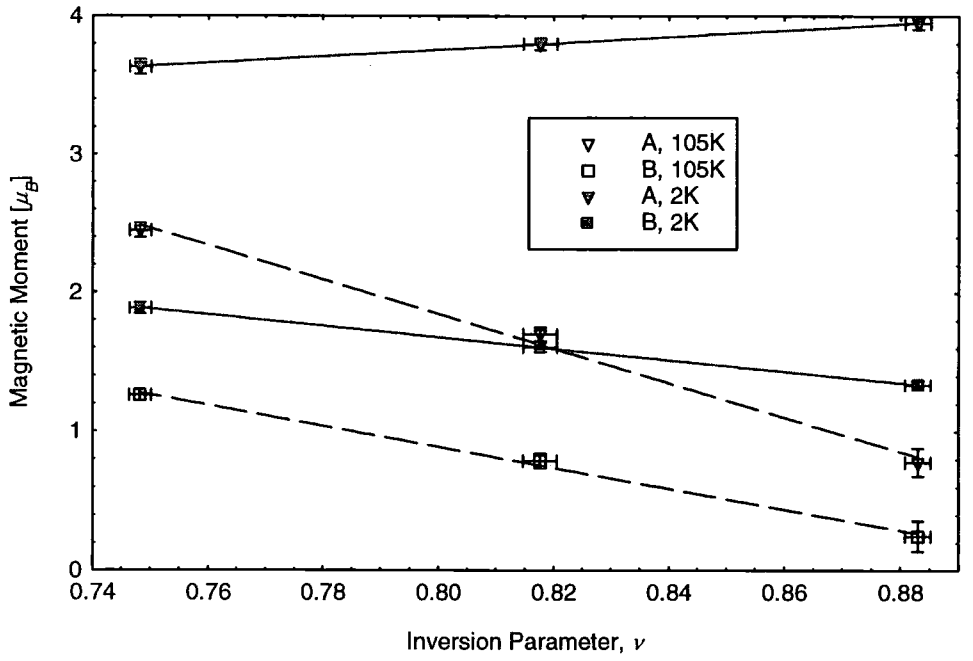

Figure 6.52. Refined average magnetic moments per cation for the A, and B sites, at 2 K, and 105 K, plotted against the refined inversion parameter. The straight lines are fits to the data.

The refined values from sample 3 at 105 K are non-zero, despite there being little apparent change in diffraction pattern between 300 K, and 105 K. The magnetic moments arrived at for sample 3, are in agreement with the trend observed for the other samples. The resultant magnetic moments per formula unit (AB_2O_4), and per kilogram have been calculated, and are presented in Table 6.14.

	Inversion Parameter, ν	Moment at 105 K [μ_B]	Moment at 105 K [J T^{-1} kg^{-1}]	Moment at 2 K [μ_B]	Moment at 2 K [J T^{-1} kg^{-1}]
Sample 1	0.7483(19)	-0.069(64)	-1.7(1.5)	-0.135(69)	-3.2(1.7)
Sample 2	0.8177(29)	0.120(72)	2.9(1.7)	0.585(54)	14.1(1.3)
Sample 3	0.8830(22)	0.28(15)	6.7(1.8)	1.275(53)	30.6(1.3)
Sample 4	-	0.120(76)	2.9(1.8)	0.095(75)	2.3(1.8)

Table 6.14. Calculated magnetic moments per formula unit, and per kilogram.

The negative moment values in Table 6.14 for sample 1 signify that the resultant moment lies antiparallel to the moment on the A sites, whereas for all other samples it is parallel. This reversal of the total moment would not be apparent in conventional magnetisation data. The trends in the moments with changing inversion parameter are similar to those already reported in the literature (Table 5.2, [8]). The values in Table 6.14 for a temperature of 105 K are in good agreement with the values obtained from magnetisation measurements at 77 K, given in Figure 6.65, and Table 6.21. Sample 4 is the only one that is

significantly different. It is interesting to note that, according to the values in Table 6.14, the saturation magnetisation of sample 4 is no larger at 2 K, than at 105 K, in contrast to all the other samples.

Assuming that the moments vary linearly with inversion parameter (as the lines shown in Figure 6.52), there will be a compensation point (zero total moment) at an inversion parameter of 0.761(6), calculated using the 2 K moments. A similar calculation using the moments at 105 K gives a compensation point at an inversion parameter of 0.774(16), which agrees with the 2 K value. These values are similar to the expected positions of the compensation point, as calculated in section 4.3.3 for different moment configurations. Since the inferred value lies approximately midway between the predicted values, it is not possible to draw any definite conclusions as to the moment arrangement from this data alone.

All of the values in Table 6.14, and the calculation of the compensation points, assume that the angle between the moments on the A, and B sites is 180°.

The reduction of the moments with increasing inversion parameter at 105 K is consistent with an approaching Curie temperature, so that the thermal excitations serve to reduce the apparent moments. The moments at 2 K are unlikely to be affected by a changing Curie temperature to any great extent, so can be taken as indicative of the saturation moments of the sublattices. From the slope and intercept of the lines in Figure 6.52, the moments of the ion species present on each site can be deduced in some cases. The nickel A site moment is calculated to be 1.878(22) μ_B, which suggests that the nickel ion is in a 2+ state, and that the orbital component of angular momentum is completely quenched, in contrast to the findings of Mehandjiev [66] (see section 4.3, and Table 4.12 for more details). The A site manganese moment is calculated to be 4.224(35) μ_B, which is slightly lower than the 4.6 μ_B quoted by Wickham [67] for Mn^{2+} in a tetrahedral environment. This is consistent with there being a small amount of Mn^{3+} present on the A sites, as this should have a lower moment than Mn^{2+}.

The B sites are more complex, as there is generally agreed to be a number of different charge states of manganese present, to account for the transport properties (see section 5.3 for more details). Taking the cation distribution of Brabers [52];

$$Ni^{2+}_{1-v}Mn^{2+}_{v}[Ni^{2+}_{v}Mn^{3+}_{2-2v}Mn^{4+}_{v}]O_4,$$

the moment of the Mn^{3+} ions on the B sites is 4.923(34) μ_B, in excellent agreement with the Mehandjiev [66] value of 4.9 μ_B. However the individual moments of the Ni^{2+}, and Mn^{4+}, cannot be determined using this approach, only their sum, which is 1.73(11) μ_B. This value is much lower than would be expected from the previously reported values in Table 4.12. This would suggest either that the cation distribution of Brabers is in error, or that the moments of the various ions on the B sites are other than collinear. This second possibility was put forward by Boucher [1], in order to explain a neutron diffraction pattern collected at 4.2 K, and developed in later work (see section 5.6 for more details). An antiparallel arrangement of the nickel and manganese as suggested by Boucher, gives an expected value of the B site moment which agrees with the data in Figure 6.52. The later works of Boucher reported that the total moment of the A sites, and the B sites were not exactly antiparallel, deviating by between 3.4 °, and 21.5 ° [68]. In order to test whether this deviation would be observable in the data presented in Figures 6.46 to 6.49, a series of simulated datasets were generated. These were based upon the parameters from the refinement of the 2 K data from sample 1. The only thing varied in the simulations, was the angle of the A site moments away from the (100) direction. The results of the simulations are plotted in Figure 6.53.

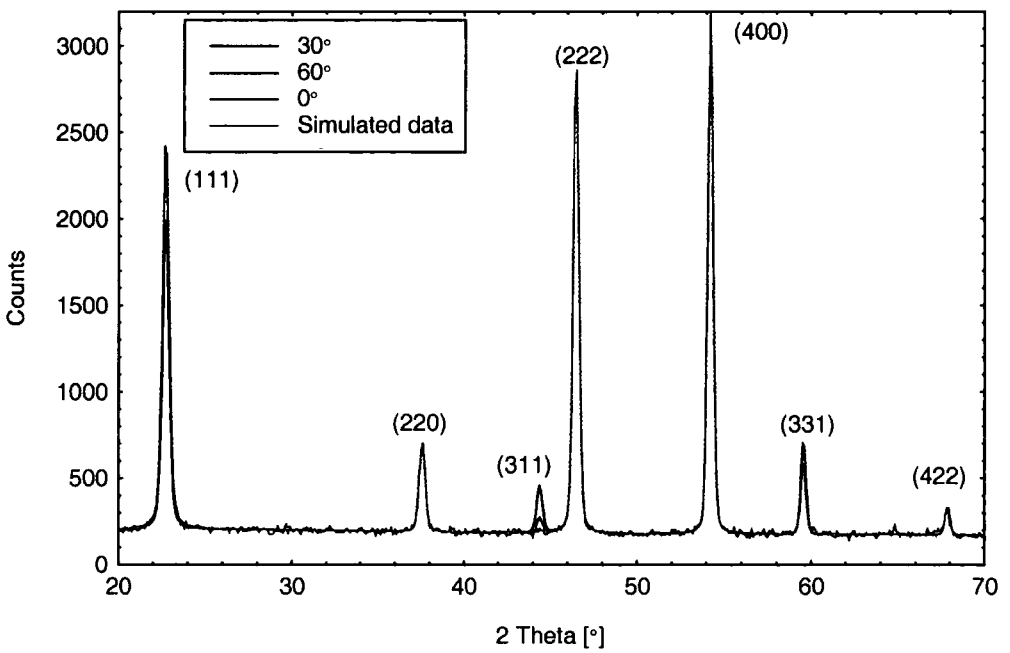

Figure 6.53. Calculated diffraction patterns for various deviations from collinear moments. The green curve shows the scatter that would be expected due to statistical fluctuations.

It should be noted that the angles used (30 °, and 60 °) were much larger than the angles reported by Boucher *et al.*, [68] in order to exaggerate the differences in Figure 6.53. The feature most noticeable is the increase of the (311) diffraction peak from nearly zero intensity. There are also changes to a number of other peaks, but these are small relative to the peak intensities. However, a deviation of the order of those observed by Boucher *et al.*, [68], for samples with low inversion parameters would be lost in the scatter of the datapoints. The only sample which showed any increase in the (311) diffraction peak as the temperature was lowered, was sample 3 (Figure 6.48). This sample had the highest inversion parameter, and so should have the largest deviation from a collinear moment arrangement according to Boucher *et al.*, [68]. An attempt to include this deviation from collinearity in the magnetic model used in the refinements failed, giving unstable parameter values, or obviously incorrect patterns.

A modulation of the background intensity for all the diffraction patterns collected was noted. This modulation appeared at the same angular values, independent of sample or temperature, an example of which is given in Figure 6.54.

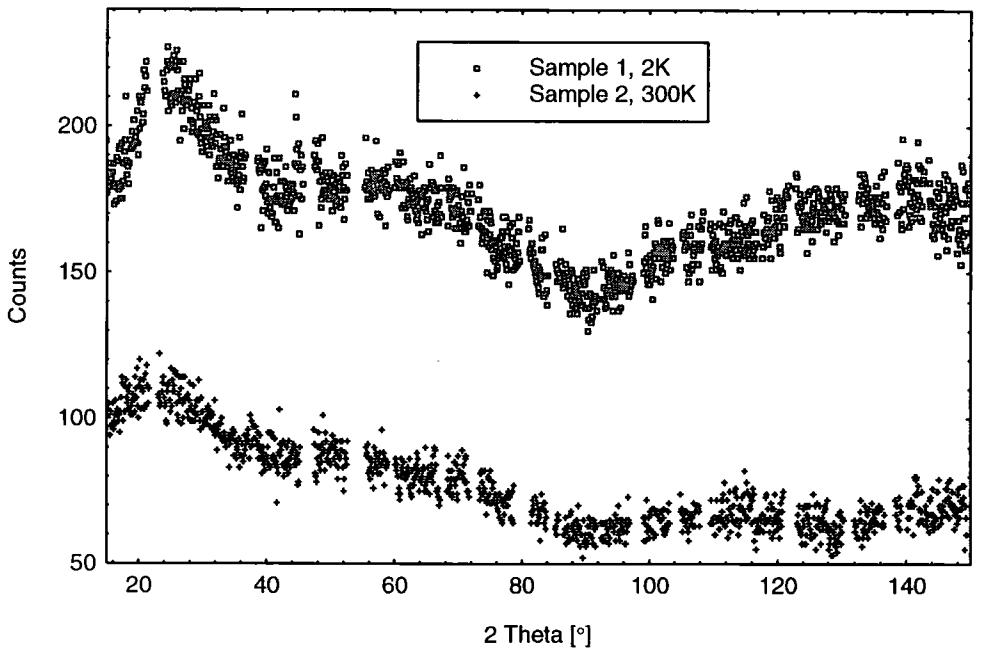

Figure 6.54. Comparison of background signals from datasets collected on different samples, at different temperatures.

This has been attributed to the presence of short range order on the B sites, as the period of modulation corresponds to the B-B nearest neighbour distance. An analysis of similar modulations observed for nickel manganite samples has been carried out by Boucher *et al.*, [9], and Elbadraoui *et al.*, [34], to yield the Warren-Cowley parameters (see section 5.7). However, there are a number of other contributions to the background signal, which have to be accounted for, which can cause significant errors in any analysis. This fact and the lack of a background trace for the instrument meant that this analysis was not carried out. The possible contributions to the background include scattering from amorphous content in the sample, contamination of the incident neutron beam with non-monochromatised components, diffuse scatter from magnetic atoms (with strong form factor dependence), multiple scattering events, etc.

6.6 Magnetic measurements

A variety of different instruments were used to study the magnetic properties of nickel manganite samples. The majority of the magnetic measurements on bulk nickel manganite samples were carried out in the Physics Department, University of Durham, using a VSM designed and built in the department's workshop. The operation of the VSM is described in section 1.5.1. The resolution in magnetic moment obtained was approximately 9 x 10^{-8} J T^{-1}. Measurements were taken of samples selected from those reported in sections 6.2 (variable firing temperature), 6.4 (variable firing temperature), and 6.5 (variable cooling rate). Measurements using a SQUID magnetometer were also carried out on a few samples. The SQUID measurements were carried out by Dr. Chris Leighton, at the Department of Chemical Engineering and Materials Science, University of Minnesota, Minneapolis. The AGFM described earlier was also used to study one sample.

6.6.1 Variable firing temperature (600 °C to 1000 °C)

A number of samples were chosen as representative from those listed in Table 6.1. These were the samples fired at; 600 °C, 750 °C, 800 °C, 900 °C, and 1000 °C, each for 20 hours. The magnetic properties at ambient temperature (298(3) K) were investigated by measuring the magnetic moments of the samples

as the applied magnetic field was cycled to produce a full hysteresis loop. The resulting data is shown in Figure 6.55.

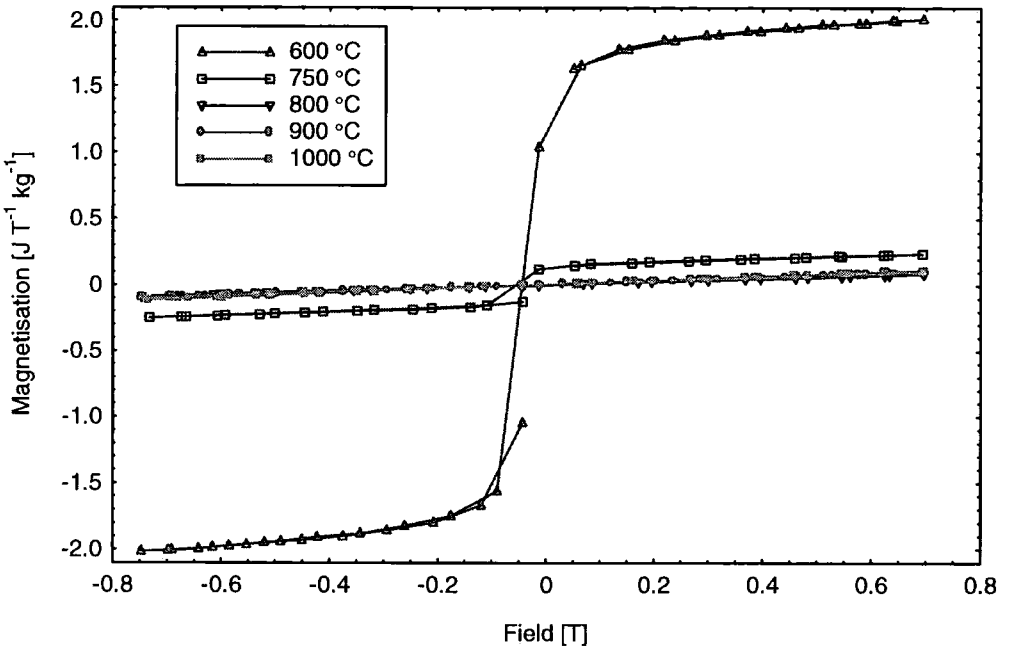

Figure 6.55. *m-H* loops collected at 298(3) K for samples fired at 600 °C to 1000 °C.

There are some immediately apparent differences between the behaviour of the samples fired at different temperatures. The samples fired at 800 °C and over show a linear dependence of magnetic moment with applied field, indicating a paramagnetic (non ordered) state. The samples fired at 600 °C, and 750 °C show a more complex behaviour, indicating that there is some magnetic ordering present in the samples leading to the formation of a magnetic domain structure. The slope of the magnetisation curve at applied field strengths sufficient to achieve saturation (alignment of all of the magnetic domains) was found non-zero. This feature is indicative of ferrimagnetic ordering, as the magnetic moment slowly increases above saturation due to the rotation of the sublattice magnetisation vectors towards the applied field direction. This non-zero slope can be expressed as a differential susceptibility, in a similar manner to the slope due to a paramagnetic specimen. The differential susceptibilities, and values of saturation magnetisation extrapolated back to zero applied field, obtained from the data shown in Figure 6.55, are given in Table 6.15. The errors quoted in Table 6.15 (and in all other tables in the present section) refer only to the

uncertainties reported from the process of fitting a linear dependence to the data in Figure 6.55, and take no account of any other sources of error.

Firing Temperature [°C]	Saturation Magnetisation [J T^{-1} kg^{-1}]	Differential Susceptibility [$10^{-7}m^3$ kg^{-1}]
600	1.785(8)	4.10(18)
750	0.1507(20)	1.71(5)
800	-	1.561(5)
900	-	1.784(4)
1000	-	2.037(5)

Table 6.15. Saturation magnetisation, and differential susceptibility at 298(3) K for samples fired at temperatures of 600 °C to 1000 °C, as determined from the data shown in figure 6.55.

The appearance of ferrimagnetic order at 298(3) K in the samples fired at 600 °C, and 750 °C implies the presence of impurity phases, as nickel manganite is a paramagnet at this temperature [1]. Of the impurity phases likely to be found in these samples, $NiMn_2O_3$ is the only one that displays ferrimagnetic order at 298(3) K (Appendix 1 contains a list of impurity phases, and details of their properties). Comparing the values of saturation magnetisation in Table 6.15, with the reported value for $NiMnO_3$, (22 J T^{-1} kg^{-1}, [64]), enables estimates of the amount of $NiMnO_3$ present to be made. The values arrived at are 8.1%, and 0.7% (mass fraction), for the samples fired at 600 °C, and 750 °C respectively. These values should be treated with some caution, as $NiMn_2O_3$ can accommodate a considerable degree of non-stoichiometry, which would be expected to have an effect on the value of the saturation magnetisation. These values are consistent with the analysis presented in section 6.2, as the amount of $NiMnO_3$ in the sample fired at 750 °C is too small to be detected from X-ray data, and reflections attributed to $NiMnO_3$ were observed from the sample fired at 600 °C (shown in Figure 6.4). The increase in the paramagnetic susceptibility as the firing temperature was increased from 800 °C to 1000 °C, is thought not to be due to additional contributions from impurities. The major impurity found in these samples was nickel oxide (see section 6.2, and Appendix 2 for more details), which has a susceptibility of 1.11 x 10^{-7} m^3 kg^{-1}, lower than that measured for all the samples. The presence of nickel oxide implies a non-stoichiometry in the remaining nickel manganite present, which is considered the most likely cause of the increase in susceptibility. The moments of the two sublattices, and the interactions between them will have an influence upon the

susceptibility, and are expected to be strongly affected by changes in cation distribution.

Similar measurements of magnetisation as a function of applied field for all the samples were carried out at a temperature of 76(2) K, and are shown in Figure 6.56.

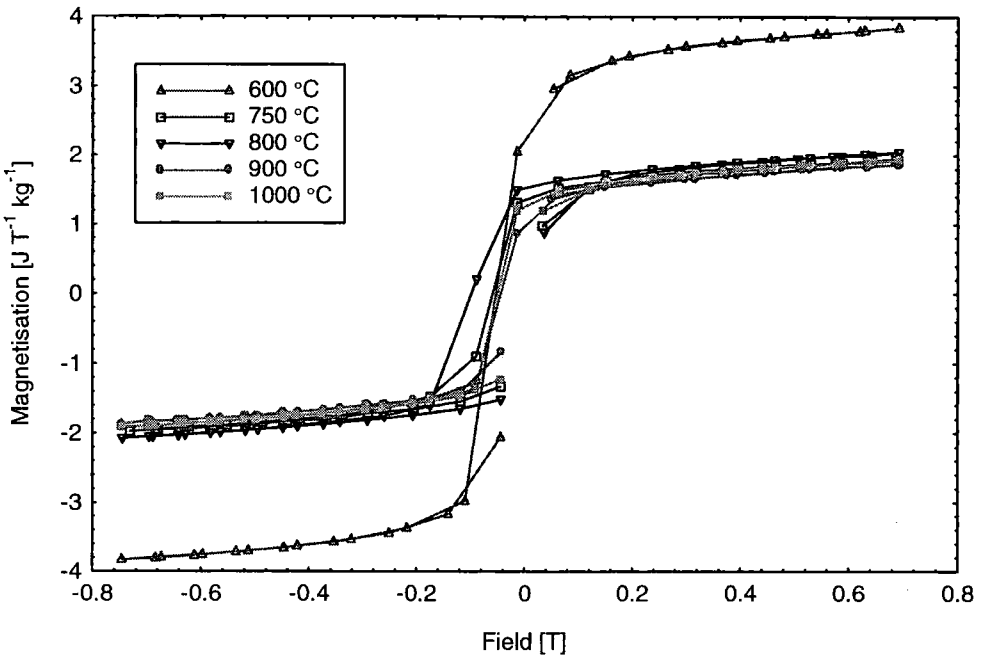

Figure 6.56. *m-H* loops collected at 76(2) K for for samples with differing firing temperatures.

The data collected at 76(2) K shows an ordered phase present in all samples. The saturation magnetisation is approximately the same for all the samples, except the one fired at 600 °C, which is again consistent with the presence of $NiMnO_3$ in this sample, which has a much higher saturation magnetisation than nickel manganite. The differential susceptibilities, and values of saturation magnetisation extrapolated back to zero applied field, obtained from the data shown in Figure 6.56, are given in Table 6.16.

Firing Temperature [°C]	Saturation Magnetisation [J T^{-1} kg^{-1}]	Differential Susceptibility [10^{-7} m^3 kg^{-1}]
600	3.351(15)	8.63(35)
750	1.579(17)	6.75(40)
800	1.660(11)	7.07(26)
900	1.782(13)	6.84(30)
1000	1.544(10)	6.75(24)

Table 6.16. Saturation magnetisation, and differential susceptibility at 77(2) K for samples fired at temperatures of 600 °C to 1000 °C, as determined from the data shown in Figure 6.56.

The fact that the saturation moments at 76(2) K, and differential susceptibilities, are similar for all samples fired at 750 °C or above implies that the inversion parameter of all of these samples is approximately the same, in as far as the inversion parameter is valid for non-stoichiometric samples. It should be noted that the differential susceptibilities at 76(2) K are all considerably higher than the paramagnetic susceptibilities measured at 298(3) K, which is consistent with the ferrimagnetic ordering observed previously in nickel manganite [1].

In addition to the samples measured with the VSM, a sample fired at 700 °C for 20 hours was measured using the AGFM described in earlier chapters. The resulting data, collected at 77(4) K, and 298(4) K is presented in Figure 6.57.

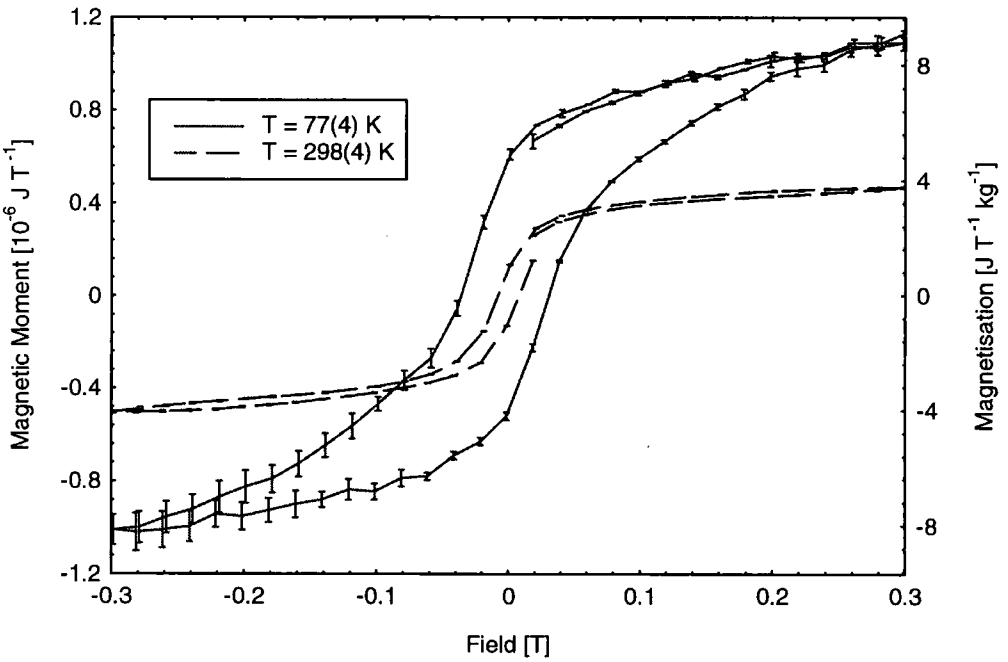

Figure 6.57. AGFM *m-H* data from a sample fired at 700 °C for 20 hours.

This powdered sample was mounted on the AGFM with the aid of a small amount of vacuum grease mixed with the sample. For this reason, an accurate measurement of the amount of sample being measured was not available. The saturation magnetic moment of the sample, obtained from the data collected at 298(4) K in a similar manner to the values in Tables 6.15, and 6.16, is 3.72(11) x 10^{-7} J T^{-1}. If it is assumed that the only phase showing magnetic ordering at 298(4) K is $NiMnO_3$, the reported value of saturation magnetisation (22 J T^{-1} kg^{-1}, [64]), and the mass fraction determined from Rietveld refinement (27.29(42)%, from Appendix 2), an approximate sample mass of 0.12 mg can be

estimated. Following from this, magnetisation can be calculated, shown on the right hand axis in Figure 6.57. The magnetisation exhibited by this sample was much higher than for any of the other samples fired at different temperatures, as expected from the much higher proportion of $NiMnO_3$ in the sample. Plots of magnetisation as a function of temperature were obtained by applying a constant magnetic field of 442(4) mT, and varying the sample temperature inside the cryostat attached to the VSM. The data has been corrected for the slightly differing sample masses used. All data were collected in the same manner, by slowly heating the cryostat from the base temperature of approximately 77 K, over a period of between 4 and 6 hours. Data points were taken continuously as the sample temperature was monitored with a thermocouple in direct contact with the sample holder. As can be seen from the data in Figure 6.58, there is a rapid increase in magnetisation upon cooling, beginning at approximately 113 K for all the samples measured.

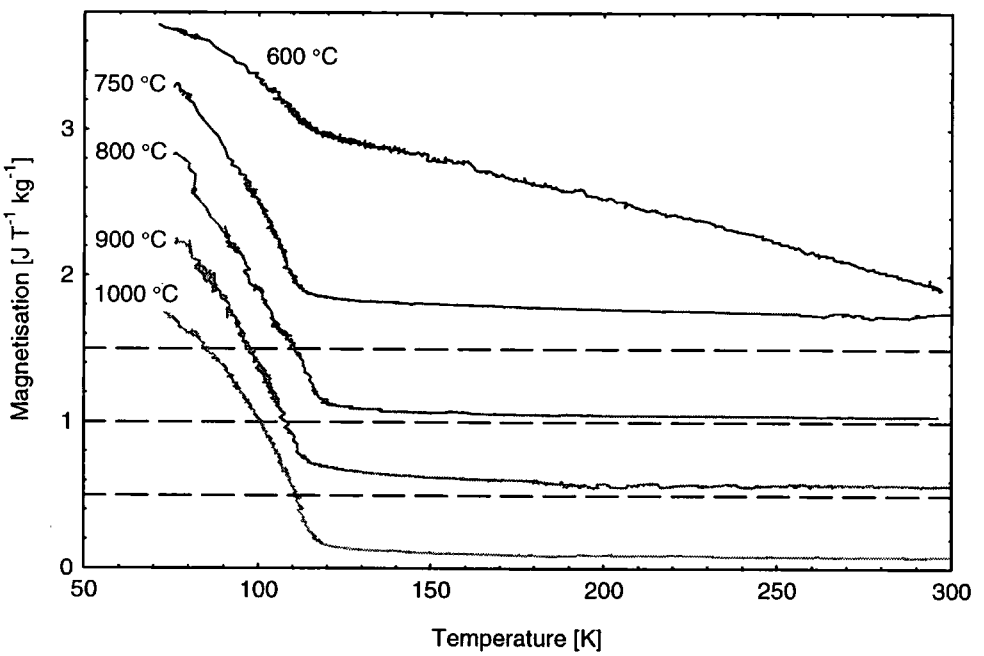

Figure 6.58. Plot of magnetisation as a function of temperature for samples fired at temperatures of 600 °C to 1000 °C. The curves for the samples fired at 750 °C, 800 °C, and 900 °C are offset for clarity, by the amounts indicated by the dashed lines. The data from the sample fired at 600 °C has not been offset.

The increase in magnetisation corresponds to the paramagnetic to ferrimagnetic phase transition of nickel manganite [69]. This Curie temperature can be

determined by a fit to the curve just below the transition. A typical fitting curve is shown in Figure 6.59, for data collected from the sample fired at 750 °C.

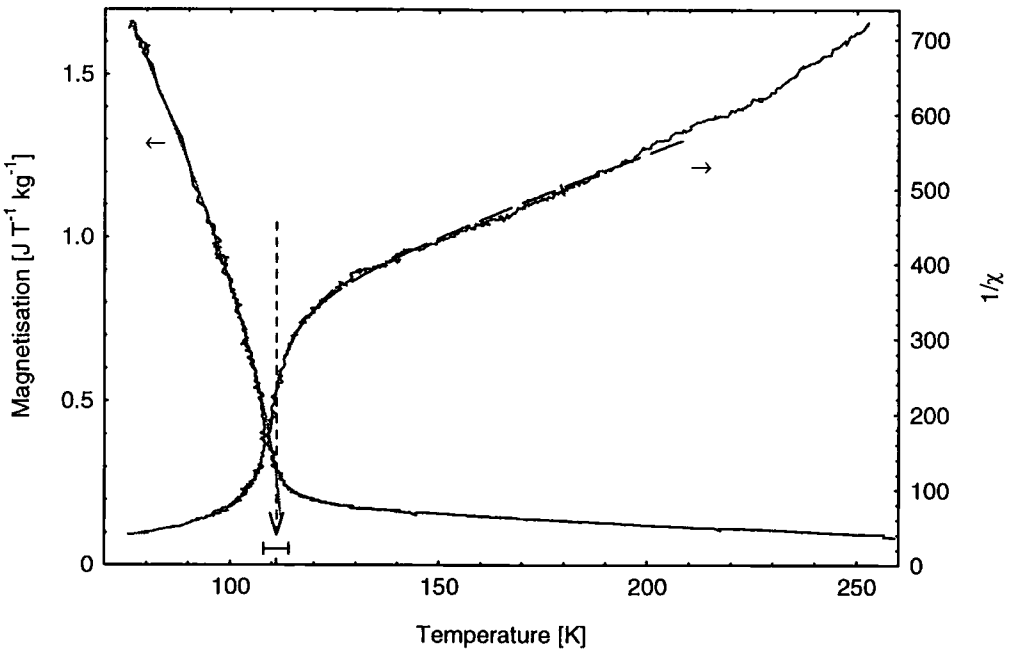

Figure 6.59. Plot of magnetisation as a function of temperature for the sample fired at 750 °C for 20 hours. The solid curve is a fit to the low temperature magnetisation data, while the dashed curve is a fit to the inverse susceptibility (dimensionless) in the paramagnetic regime. The arrow marks the transition temperature. The susceptibility curve has been corrected for the saturation magnetisation of the ilmenite phase.

In the Bethe approximation of the behaviour of ferromagnetic materials, the temperature dependence of the saturation magnetisation, M_S just below the Curie temperature is given by the following expression (equation 6.39 from [69]);

$$M_S(T) \propto (T_C - T)^{\beta}, \tag{6.1}$$

where T_C is the Curie temperature, and β is one of the critical exponents. The saturation magnetisation can be approximated by the magnetic moment in a (moderate) applied field, as measured by the VSM. By reducing the applied field, the rounding observed at the Curie temperature would also be reduced, but the paramagnetic susceptibility would become much more difficult to measure. Therefore, the choice of field applied involved a compromise between the sharpness in the transition region, and the resolution of the paramagnetic behaviour.

The fit to the saturation magnetisation, M_S shown in Figure 6.59, was to a modified form of equation 6.1;

$$M_S = a + b(T_C - T)^{\beta}, \tag{6.2}$$

where a, b, T_C, and β were variable parameters. The inclusion of a, the constant term was necessary to account for the saturation magnetisation of the $NiMnO_3$ present in some of the samples, which has a reported Curie temperature of 437 K (or 164 °C) [64]. The magnetic impurity present also manifests as the large, weakly temperature dependent, component above the Curie transition in the sample fired at 600 °C, as shown in Figure 6.58 (note that the curve from this sample has not been offset). As has been shown above, a considerable proportion of this sample was impurity phases (see section 6.2 for more details of the X-ray measurements). The values of the parameters in equation 6.2, obtained from the data shown in Figure 6.59, were; a = 0.15(7) J T^{-1} kg^{-1}, b = 0.123(3) J T^{-1} kg^{-1}, T_C = 111.9(1.6) K, and β = 0.700(5).
The value of a agrees with the measured room temperature saturation magnetisation value (Table 6.15) for this sample. The value of the critical exponent, β, is slightly larger than that reported for ferromagnetic metals. Values of the Curie temperature for the other samples measured were obtained as well, and are reported in Table 6.17.

Firing Temperature [°C]	600	750	800	900	1000
Curie Temperature [K]	115(5)	111(3)	115(3)	112(4)	114(4)

Table 6.17. Ferrimagnetic Curie temperatures for samples fired at temperatures of 600 °C to 1000 °C for 20 hours.

Errors have been estimated from the spread of the datapoints, and the sharpness of the transition in each case. There is no trend observed in the Curie temperature as the firing temperature is varied. This reinforces the conclusion drawn from the data in Table 6.16, that the inversion parameter does not vary greatly between samples, as the Curie temperature has been reported to be sensitive to the cation distribution [12]. The values in Table 6.17 are at the lower limit of those reported by Boucher *et al.*, [12], and suggest an inversion parameter of approximately 0.93. This value was obtained from a slow cooled sample, whereas the samples reported here were cooled relatively rapidly.

In contrast to the case for ferromagnetic, and antiferromagnetic materials, the paramagnetic susceptibility above the Curie temperature does not exhibit a Curie-Weiss type behaviour near the transition for ferrimagnetic materials. A brief explanation is offered in section 1.3.5, along with a model for the behaviour observed, which approaches the Curie-Weiss law at higher temperatures. The inverse susceptibility curve in Figure 6.59 was fitted to using the equation reported by Chikazumi [69];

$$\frac{1}{\chi} = \frac{T}{C} + \frac{1}{\chi_0} + \frac{A}{(T-\theta)}. \qquad (6.3)$$

The values obtained were; C = 0.477(6) K, χ_0 = 7.41(25) x 10^{-3}, A = -695(32) K, and θ = 105.85(13) K. From these values, it can be deduced (see section 1.3.5), that the intra-sublattice interactions are mainly of positive sign, the inter-sublattice interaction is negative (antiferromagnetic), and there is a significant difference between the two intra-sublattice interactions.

None of the other datasets shown in Figure 6.58 was of sufficient quality to enable any meaningful fitting procedure. The model in equation 6.3 assumes that the susceptibility is due entirely to the nickel manganite component of the sample. This was not the case for the sample fired at 750 °C, as discussed above, and demonstrated in Figure 6.57. Therefore, the fit parameters obtained should be treated with some caution. In addition, the susceptibility was calculated assuming that the density of the sample was that of polycrystalline nickel manganite, as determined from X-ray diffraction measurements (see section 6.2). The densities of the impurity phases differ from that of nickel manganite by up to 30 % (see Appendix 2).

6.6.2 Variable firing temperature (750 °C to 850 °C)

The samples fired for 48 hours at 750 °C, 800 °C, and 850 °C to try to change the inversion parameter, were also measured with the VSM. The magnetic properties at ambient temperature (298(3) K), and at 75.5(12) K, were investigated by measuring a full hysteresis loop, in a similar manner to the data shown in Figures 6.55, and 6.56. The resulting data is shown in Figure 6.60 for all 3 samples, showing differences between the behaviour of the samples fired at various temperatures.

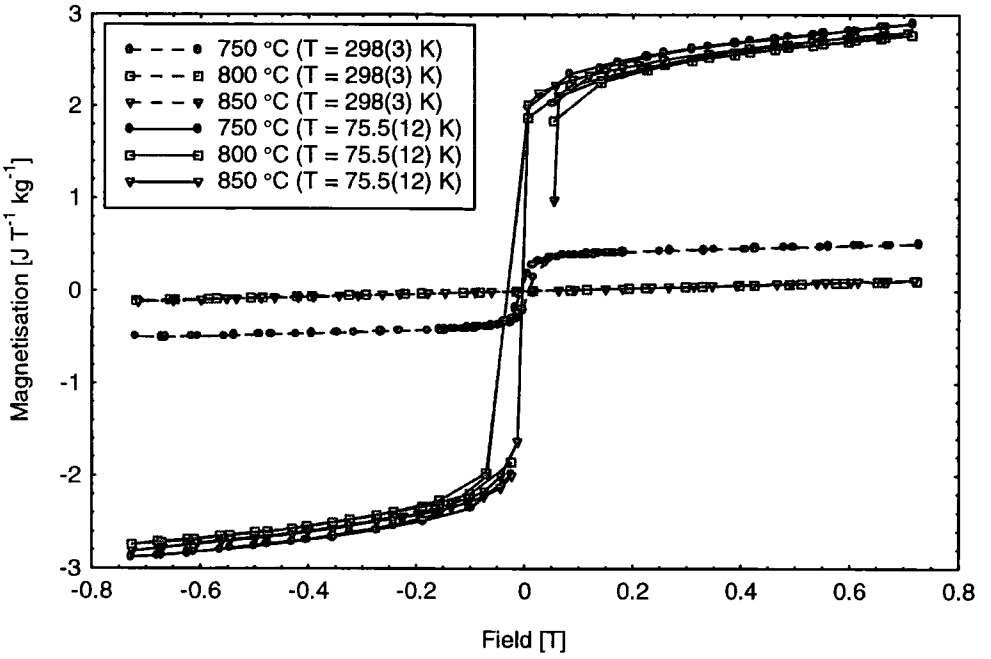

Figure 6.60. *m-H* loops collected at 298(3) K, and 75.5(1.2) K for samples fired for 48 hours at 750 °C, 800 °C, and 850 °C.

The samples fired at 800 °C and 850 °C show a paramagnetic (non ordered) state at 298(3) K. The non-zero slope of the magnetisation curve at applied field strengths sufficient to achieve saturation was again taken to be indicative of ferrimagnetic ordering. The differential susceptibilities, and saturation magnetisation extrapolated back to zero applied field, obtained from the data shown in Figure 6.60, are given in Table 6.18.

Firing Temperature [°C]	Saturation Magnetisation at 75.5(1.2) K [J T^{-1} kg^{-1}]	Saturation Magnetisation at 298(3) K [J T^{-1} kg^{-1}]	Differential Susceptibility at 75.5(1.2) K [10^{-7} m^3 kg^{-1}]	Differential Susceptibility at 298(3) K [10^{-7} m^3 kg^{-1}]
750	2.402(12)	0.3938(22)	8.85(30)	2.016(53)
800	2.258(14)	-	9.10(35)	1.9470(26)
850	2.297(12)	-	9.32(31)	2.123(33)

Table 6.18. Saturation magnetisation, and differential susceptibility at 75.5(1.2) K and 298(3) K, for samples fired for 48 hours at temperatures of 750 °C to 850 °C, as determined from the data shown in Figure 6.60.

These values are consistently slightly higher than those reported in Tables 6.15, and 6.16, and may be due to a number of factors. A change in the instruments, sample positioning, amorphous content, crystal size, shape demagnetising corrections, Curie temperature (measured values are similar, as shown in

Table 6.19), cation distribution (which would affect the Curie temperature), or non magnetic impurity content, could all be responsible.

Using the value of saturation magnetisation at 298(3) K, of the sample fired at 750 °C, and assuming that this is due to $NiMn_2O_4$ impurities only, a mass fraction of 1.79% can be estimated for this phase. The corresponding amount as determined from analysis of neutron diffraction data (see section 6.4, and Appendix 2), was 4.91(43)%, but this is undoubtedly an over estimate for the reasons outlined in Appendix 2.

Plots of magnetisation as a function of temperature were obtained by applying a constant magnetic field of 442(4) mT, and varying the sample temperature inside the cryostat attached to the VSM, in a similar manner to the data shown in Figure 6.58. The data has been corrected for the slightly differing sample masses used, and is shown in Figures 6.61 to 6.63.

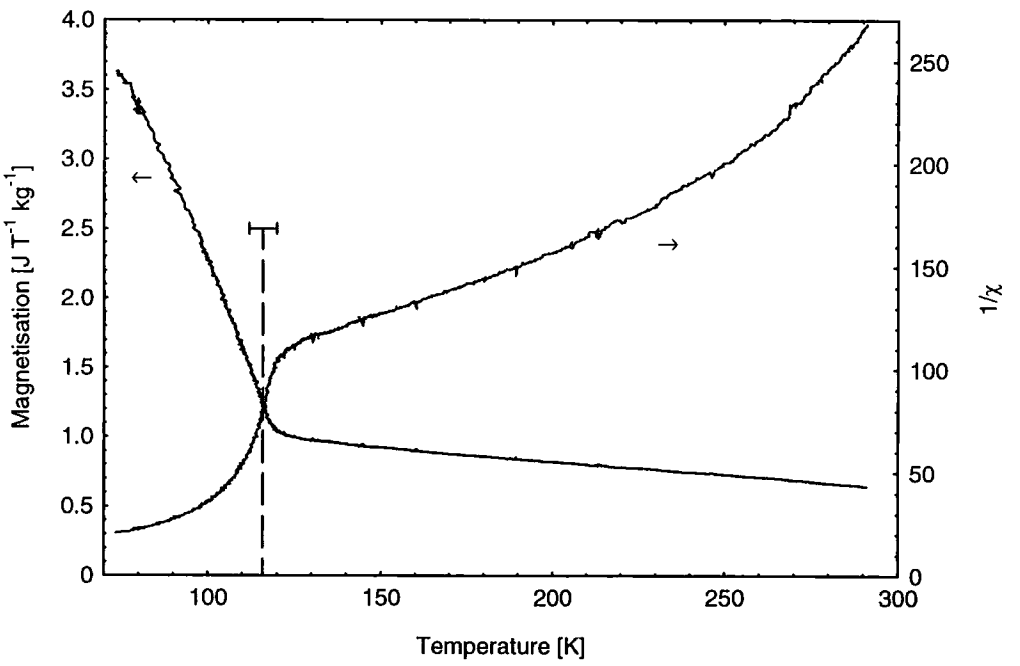

Figure 6.61. Plot of magnetisation as a function of temperature for the sample fired at 750 °C for 48 hours. The dashed line marks the transition temperature. A correction due to the saturation magnetisation of the ilmenite phase was carried out when calculating the susceptibility.

The behaviour of the magnetisation was broadly the same for all the three samples, apart from a much larger susceptibility above the Curie temperature observed in the sample fired at 750 °C. This was undoubtedly a contribution from the ilmenite phase, $NiMnO_3$. In this case, no attempt was made to fit to the high temperature paramagnetic data from the sample fired at 750 °C.

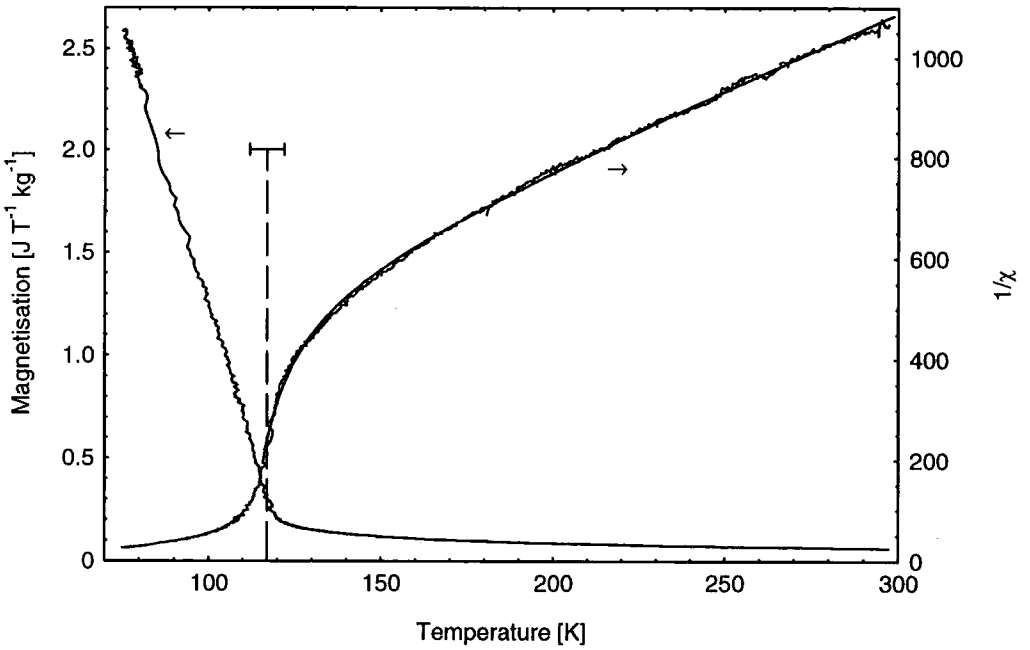

Figure 6.62. Plot of magnetisation as a function of temperature for the sample fired at 800 °C for 48 hours. The solid black curve is a fit to the inverse susceptibility in the paramagnetic regime. The dashed line marks the transition temperature.

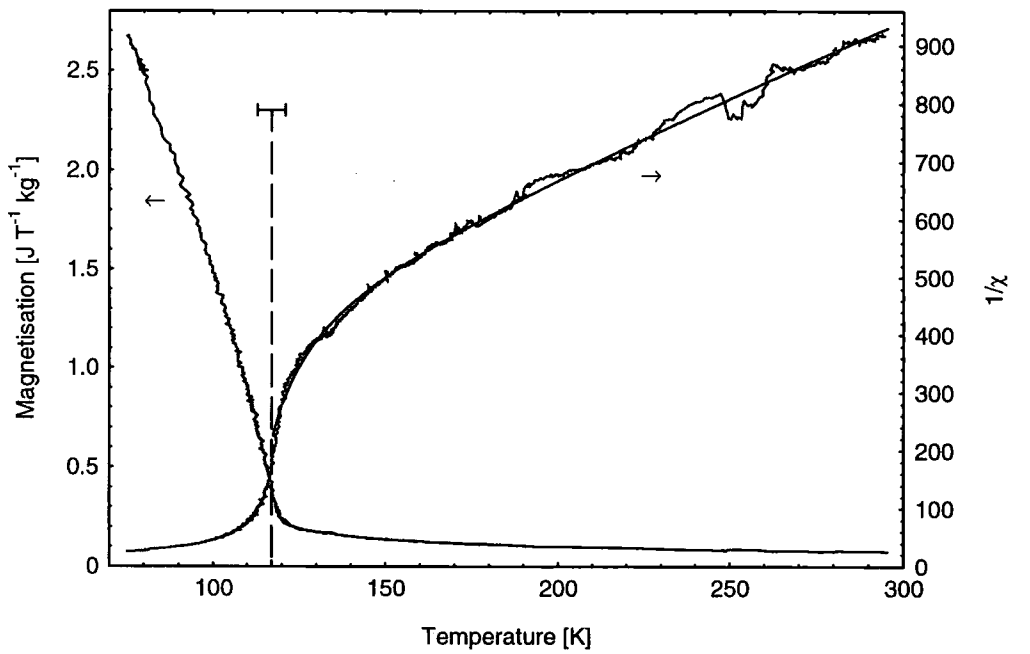

Figure 6.63. Plot of magnetisation as a function of temperature for the sample fired at 850 °C for 48 hours. The solid black curve is a fit to the inverse susceptibility in the paramagnetic regime. The dashed line marks the transition temperature.

Values of the Curie temperature for these samples were obtained, as in section 6.6.1, and are presented in Table 6.19.

Firing Temperature [°C]	750	800	850
Curie Temperature [K]	116(4)	117(5)	117(4)

Table 6.19. Ferrimagnetic Curie temperatures for samples fired at various temperatures for 48 hours.

In agreement with the results obtained for samples fired for 20 hours, there was no significant difference in the Curie temperatures with changing firing temperature.

The non stoichiometry determined from neutron diffraction analysis was 0.4(7) % for the sample fired at 750 °C, and 1.6(3) % for the sample fired at 850 °C. This reinforces the conclusion that a small degree of non-stoichiometry has little effect on the Curie temperature. The inversion parameters obtained for these samples were almost identical. The values of the Curie temperatures of these samples are slightly higher than those obtained for the samples fired for 20 hours. The reason for this is unknown, but may be due to the larger sample masses involved requiring slightly longer to cool to room temperature. This change in cooling rate has an effect on the inversion parameter, as demonstrated in section 6.4.

The high temperature data was fitted to, using the model in equation 6.3. The values of the parameters obtained are reported in Table 6.20, and are similar for both samples.

Firing Temperature [°C]	C[K]	χ_0	A [K]	θ[K]
800	0.3356(18)	$4.69(9)\times10^{-3}$	-3700(110)	105.6(3)
850	0.3880(24)	$5.35(11)\times10^{-3}$	-3350(130)	104.7(4)

Table 6.20. Model fitting parameters for equation 6.3, obtained from high temperature susceptibility data.

These samples had no detectable ferrimagnetic contaminants, and so the values obtained were considered more reliable than those obtained from the data in Figure 6.63, where impurities were observed. None of the parameters has changed sign, and so the conclusions drawn in section 6.6.1, about the relative strengths of the various interactions remain valid. Section 1.3.5 contains an explanation of the dependencies of the parameters upon the interactions present within the sample. The A parameter has increased, lending more significance to the difference between the two intra-sublattice interactions.

6.6.3 Variable cooling rate

The 4 samples detailed in section 6.5.1 were measured in the VSM, along with a 5th sample. This sample was prepared in the same manner as sample 4 (see Table 6.11), except the temperature at which it was quenched from was 1350 °C, instead of 1150 °C. This sample was not measured by neutron diffraction, due to a lack of time, and preliminary X-ray diffraction measurements indicating a significant amount of nickel oxide present (more than that present in sample 4). Nevertheless, it was thought worth reporting magnetic measurements on this sample for comparison. Details of the preparation conditions of sample 1-4 can be found in section 6.5.1, Table 6.12. Measurements using a SQUID magnetometer were carried out on samples 2, and 3. The magnetic properties at ambient temperature (298(3) K), and at 75.5(12) K, were investigated by measuring full hysteresis loops. The resulting data is shown in Figure 6.64, and Figure 6.65, for all 5 samples.

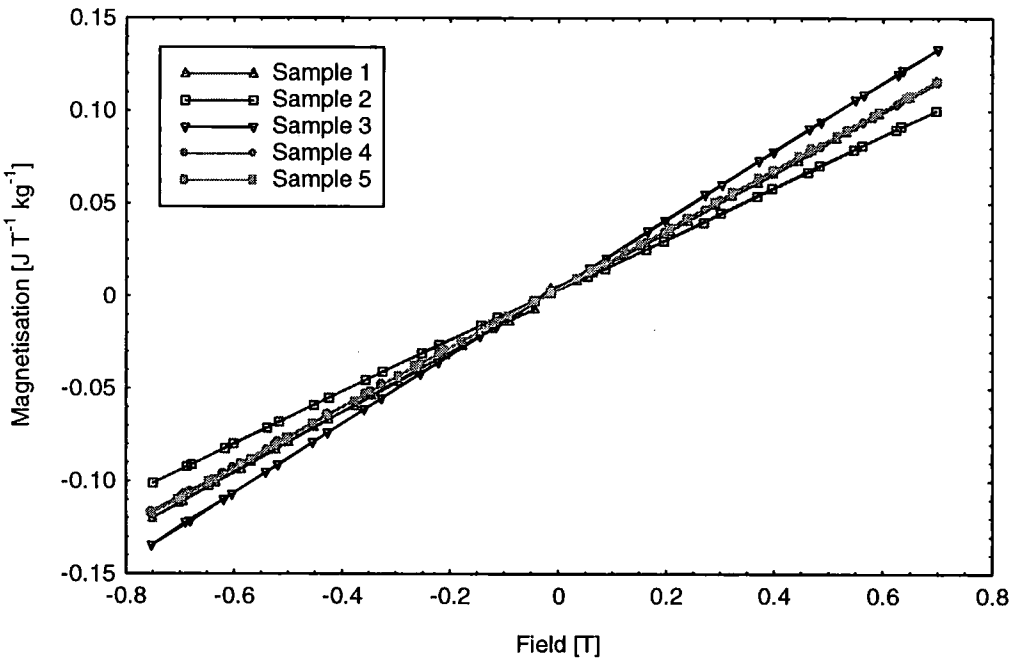

Figure 6.64. *m-H* loops collected at 298(3) K, for samples 1 - 5.

There is no evidence for an ordered magnetic state at 298(3) K, as all the magnetisation datasets in Figure 6.64 follow a linear dependence on applied field. In contrast to the samples fired at different temperatures (Figure 6.60), the saturation magnetisation below the Curie temperature (shown in Figure 6.65) varies significantly from sample to sample.

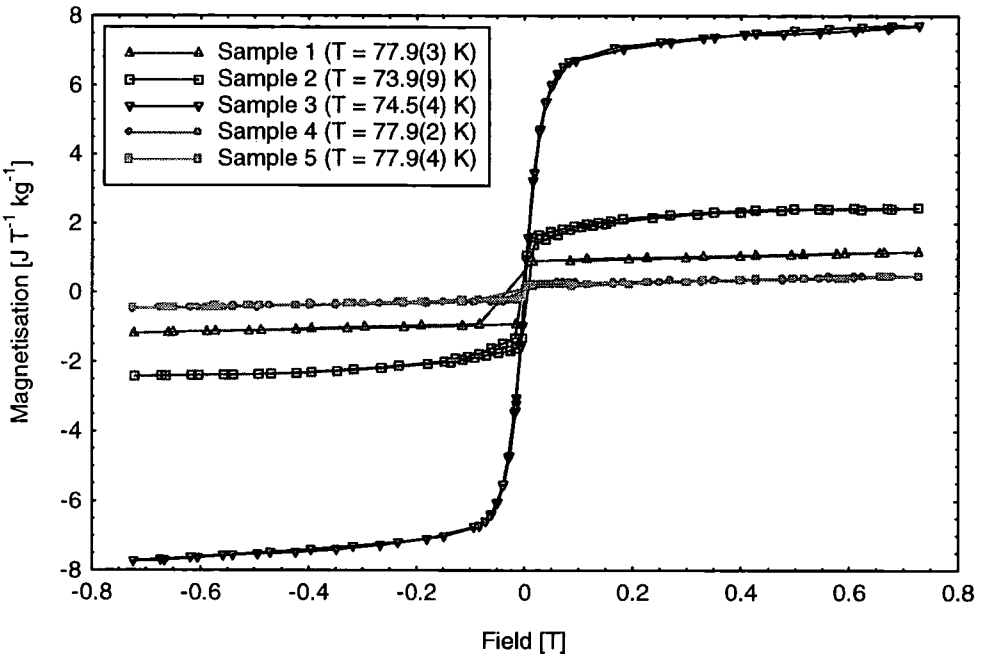

Figure 6.65. *m-H* loops collected at approximately 77 K, for samples 1 - 5.

The differential susceptibilities, and values of saturation magnetisation extrapolated back to zero applied field, obtained from the data shown in Figures 6.64, and 6.65, are given in Table 6.21.

	Saturation Magnetisation [J T^{-1} kg^{-1}]	Differential Susceptibility at 77 K [10^{-7} m^3 kg^{-1}]	Differential Susceptibility at 298(3) K [10^{-7} m^3 kg^{-1}]
Sample 1	0.9022(19)	5.00(25)	2.0400(41)
Sample 2	2.170(29)	4.95(68)	1.7393(24)
Sample 3	7.067(39)	11.57(89)	2.3161(16)
Sample 4	0.228(11)	4.51(28)	2.0007(20)
Sample 5	0.2219(78)	4.41(19)	2.0203(15)

Table 6.21. Saturation magnetisation and differential susceptibility at approximately 77 K, and differential susceptibility at 298(3) K for samples 1 - 5, as determined from the data shown in Figure 6.64, and Figure 6.65.

Sample 2 was cooled in the same manner as those samples studied in sections 6.61, and 6.62. The values of the saturation magnetisation, and susceptibility at 298(3) K for this sample are similar to those reported in Tables 6.15, 6.16, and 6.18 for samples fired at 800 °C. The values of saturation magnetisation for samples 1-3 agree well with the values obtained from Rietveld refinement of neutron diffraction data taken at 105 K (Table 6.14). However, the values for sample 4 are at odds, with the 105 K neutron diffraction value significantly larger than the 77.9(2) K value in Table 6.21. The change in the

magnetisation with temperature for sample 4 (shown in Figure 6.69) is considerable, which may account for some of the discrepancy.

The differential susceptibility at 73.9(9) K for sample 2 is significantly lower than for previous samples. The reason for this is unknown, but may be again due to slight differences in cooling rate, as this has a large effect as the values in Table 6.21 show. The inversion parameter of samples 1 – 3 varies over the range 0.7483(19) to 0.8830(22). This has an effect on the relative contributions of each sublattice to the total magnetic moment, as revealed by analysis of neutron diffraction data (see Appendix 2, and section 6.5 for details). The trend, of total magnetic moment increasing as inversion parameter increases, is confirmed by the magnetisation data at 77 K. Samples 4, and 5 have a very similar magnetic behaviour to each other, despite their differing preparation conditions. This may be due to the relative insensitivity of the magnetism to deviations from stoichiometry, as seen in previous samples. As shown in the analysis of neutron diffraction data in Appendix 2, sample 4 is significantly non-stoichiometric.

Plots of magnetisation as a function of temperature were obtained from all 5 samples, and are shown in Figures 6.66, to 6.70.

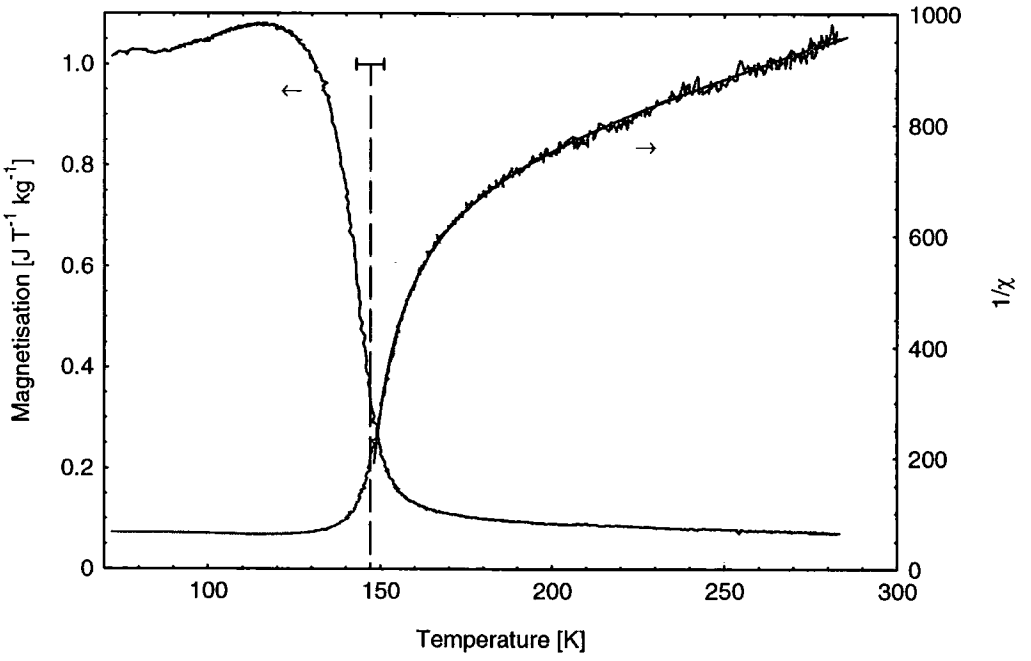

Figure 6.66. Plot of magnetisation as a function of temperature for sample 1. The solid black curve is a fit to the inverse susceptibility in the paramagnetic regime. The dashed line marks the transition temperature.

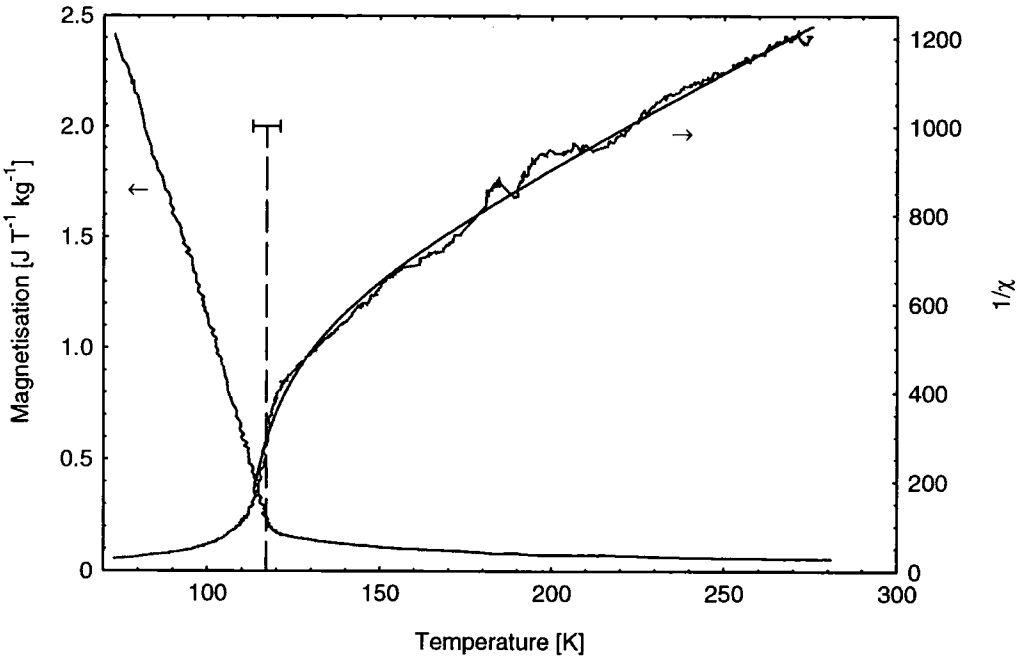

Figure 6.67. Plot of magnetisation as a function of temperature for sample 2. The solid black curve is a fit to the inverse susceptibility in the paramagnetic regime. The dashed line marks the transition temperature.

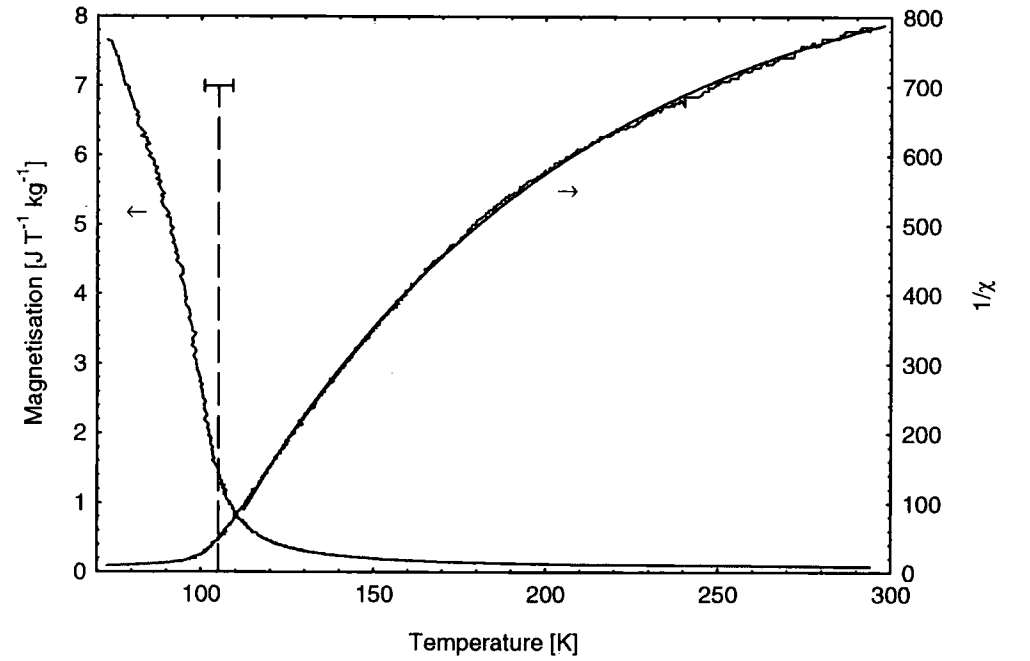

Figure 6.68. Plot of magnetisation as a function of temperature for sample 3. The solid black curve is a fit to the inverse susceptibility in the paramagnetic regime. The dashed line marks the transition temperature.

The most striking differences between the data in Figures 6.66 to 6.70, are the variation in Curie temperatures, and the behaviour of the saturation

magnetisation at low temperatures. High temperature fits to the paramagnetic susceptibility are shown where relevant.

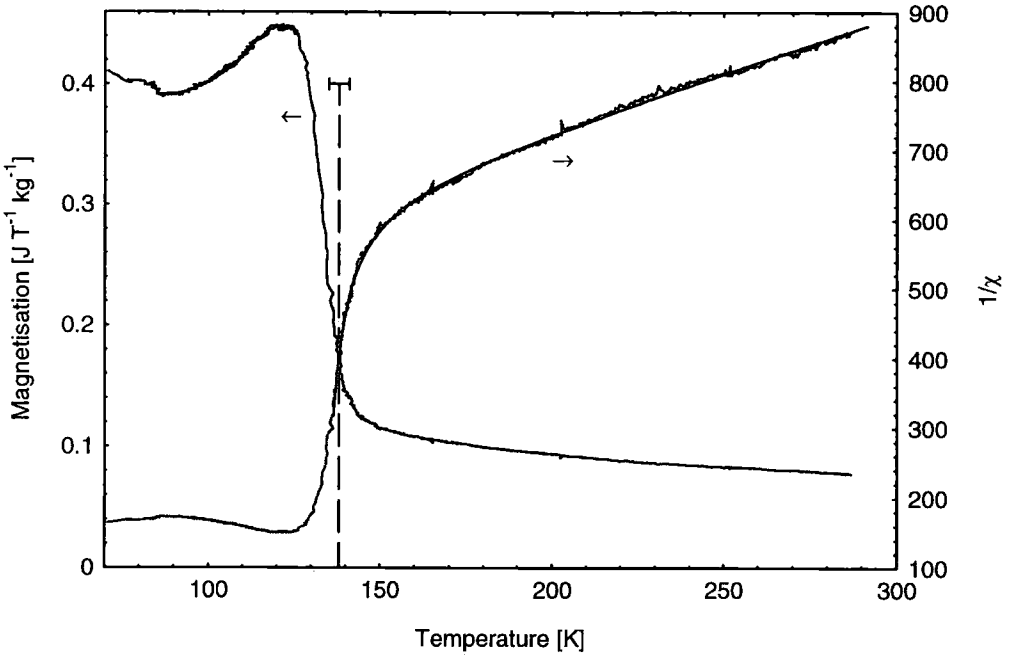

Figure 6.69. Plot of magnetisation as a function of temperature for sample 4. The solid black curve is a fit to the inverse susceptibility in the paramagnetic regime. The dashed line marks the transition temperature.

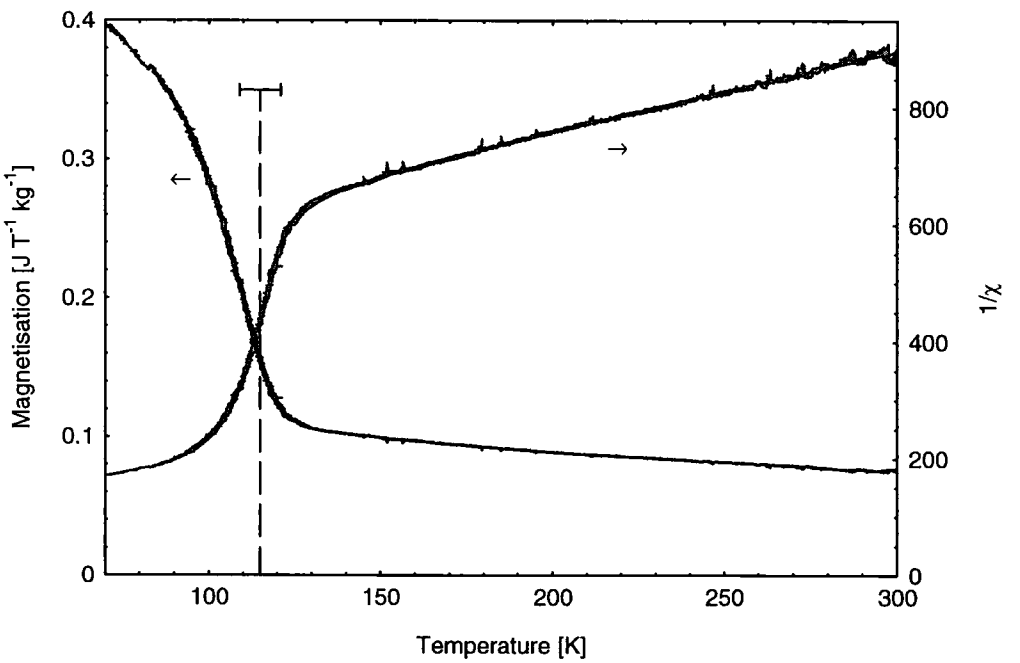

Figure 6.70. Plot of magnetisation as a function of temperature for sample 5. The solid black curve is a fit to the inverse susceptibility in the paramagnetic regime. The dashed line marks the transition temperature.

In all cases, the transition temperatures determined as shown in section 6.6.1, are marked in the figures. The values of the Curie temperatures obtained from the datasets in Figures 6.66 to 6.70, are shown in Table 6.22.

Sample number	1	2	3	4	5
Curie Temperature [K]	147(4)	117(4)	105(4)	138(3)	115(6)

Table 6.22. Curie temperatures obtained from VSM data for samples cooled at various rates.

The low value of the Curie temperature for sample 3 explains the lack of obvious magnetic diffraction peaks at 105 K (see section 6.5). It should be noted at this point, that the lack of sharpness in the transitions observed in the curves of susceptibility as a function of temperature, may not be caused purely by the use of a finite applied magnetic field. Another possible cause may be a spread in Curie temperatures, due to a corresponding distribution of inversion parameters around some mean value. The cause of this could be a non-uniform cooling rate from the firing temperature, as discussed in section 6.2. However, distinguishing these two contributions to the blurring of the transition temperature would have required a great deal more data collection at a variety of applied fields, which was not possible due to financial and schedule constraints. The fitted parameters from the high temperature susceptibility model, obtained for samples 1, 2, 4, and 5 are given in Table 6.23. The fitted values for the data in Figure 6.68 (sample 3), were unphysical, and therefore have not been reported. The reason for the failure to adequately model the data for sample 3, was that the approximately linear region of the inverse susceptibility curve had not been reached at room temperature, despite this sample having the lowest Curie temperature measured.

Sample number	C[K]	χ_0	A [K]	θ[K]
2	0.251(3)	$6.2(6)\times10^{-3}$	-5520(460)	100.6(9)
1	0.550(8)	$2.10(3)\times10^{-3}$	-5390(140)	138.4(2)
4	0.623(3)	$2.37(1)\times10^{-3}$	-1410(23)	132.16(7)
5	0.7535(9)	$1.99(2)\times10^{-3}$	-737(5)	113.43(3)

Table 6.23. Model fitting parameters for equation 6.3, obtained from high temperature susceptibility data.

The conclusions drawn in section 6.6.1, about the relative strengths of the interactions remain valid (see section 1.3.5 for a fuller discussion). The trend observed in the combined Curie constant, C, agrees with the increase in

saturation moment observed in the order Sample 5, 4, 1, 2, in VSM data (Figure 6.65), and analysis of neutron diffraction data (Appendix 2). Similarly, the trends in χ_0, and θ, imply a smaller inter-sublattice interaction in sample 2 than sample 1, which manifests as a lower Curie temperature. The A parameter in Table 6.23 is a measure of how much curvature is evident in the inverse susceptibility, due to competition between the various intra-site interactions, and this stays roughly constant between the two stoichiometric samples (1 and 2), but is much lower for the nickel deficient samples. This, and the finding that nickel is preferentially lost from the B sites in non-stoichiometric samples, implies that some of the interactions of nickel on the B sites may be acting in opposition to a simple ferrimagnetic configuration. A similar prediction was made by Boucher *et al.*, [12], when they suggested that the moments of the nickel ions on the B sites were oriented parallel to the moments on the A sites.

SQUID magnetometer measurements on samples 2, and 3 were carried out by Dr Chris Leighton at the University of Minnesota, and are presented in Figure 6.71, and Figure 6.72 respectively.

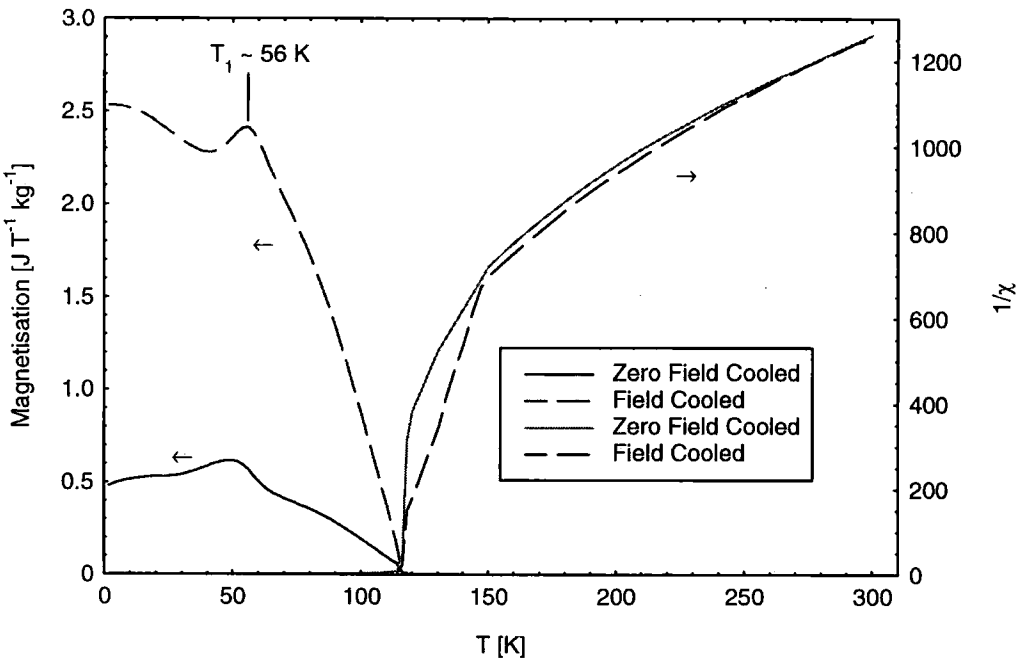

Figure 6.71. Plot of magnetisation as a function of temperature for sample 2, and the inverse susceptibility in the paramagnetic regime.

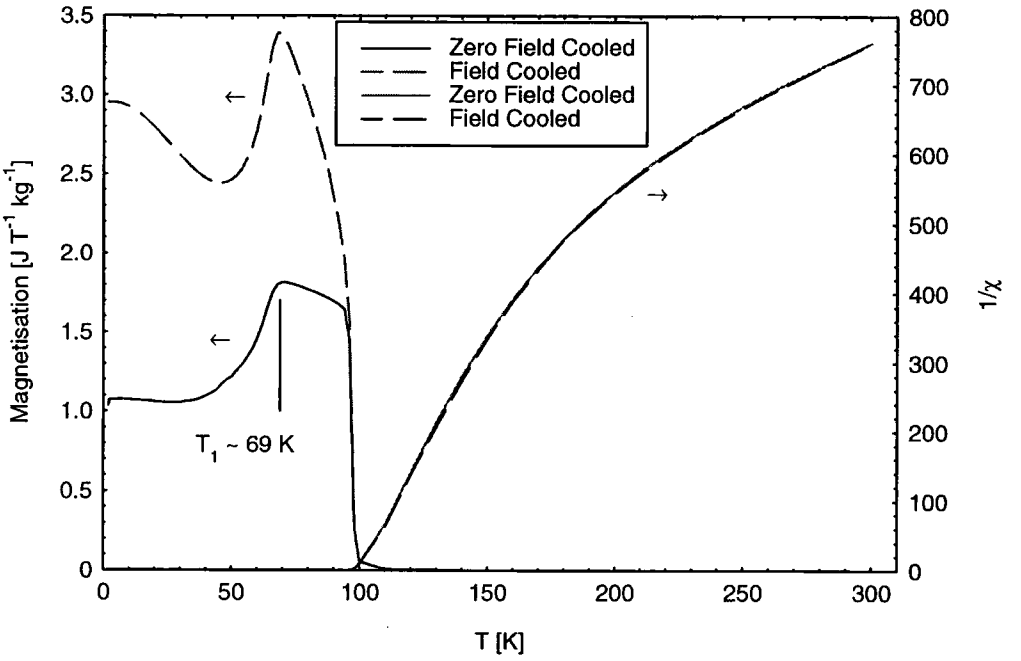

Figure 6.72. Plot of magnetisation as a function of temperature for sample 3, and the inverse susceptibility in the paramagnetic regime.

The SQUID data was taken in an applied field of 1 mT, warming from the base temperature of the instrument, with the sample cooled in fields of 0 mT, or 1 mT, labelled 'Zero Field Cooled', and 'Field Cooled' respectively. The inverse susceptibility curves plotted in Figure 6.67, and Figure 6.68, are in good agreement with those obtained from SQUID measurements. Since the applied field used for SQUID magnetometry was much smaller than that used for the VSM measurements, the Curie transition observed was much sharper. Estimates of the Curie temperature for samples 2, and 3 were 116(1) K, and 100(2) K respectively, which are in agreement with the values obtained from VSM data (and in agreement with the values from μSR measurements in section 6.8). The relationship between inversion parameter, and Curie temperature is plotted in Figure 6.73, along with other reports in the literature, and the results obtained in section 6.6.2 for samples fired at different temperatures. The values of Curie temperature were taken from VSM data (Table 6.22) for sample 1, and SQUID data for samples 2, and 3. Sample 4 was found to be so far from stoichiometry that a single inversion parameter was meaningless, and therefore it has not been included in Figure 6.73. The cation distribution in sample 5 was not determined, but is likely to be even further from stoichiometry than sample 4.

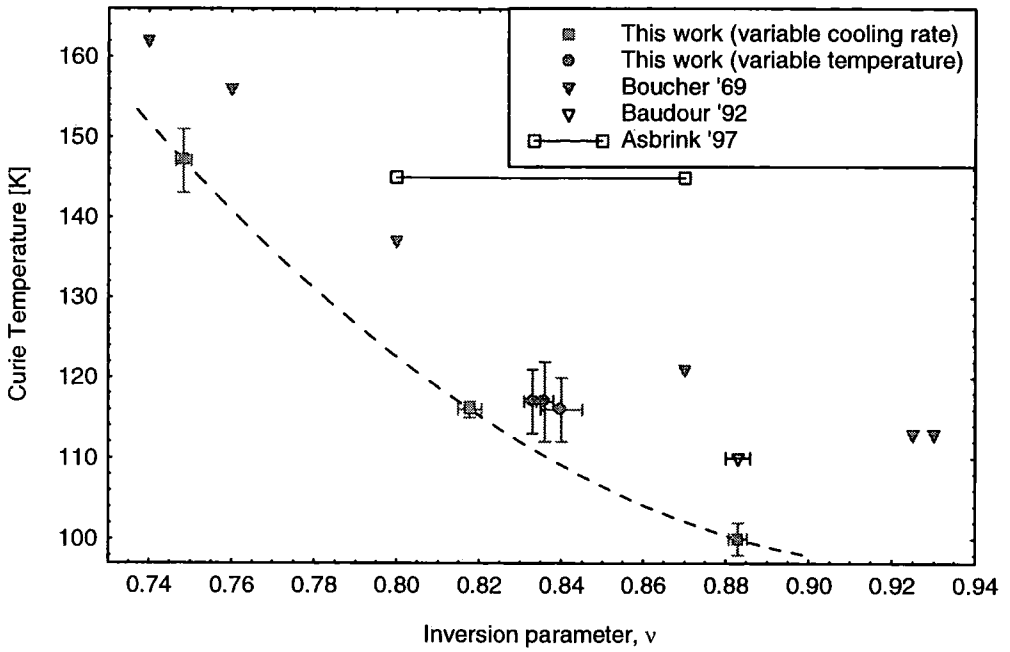

Figure 6.73. The Curie temperature as a function of inversion parameter, for samples cooled at different rates, and fired at different temperatures. Values reported in the literature are shown for comparison. The purple curve is a quadratic fit to the variable cooling rate data.

The trend observed in the data from samples 1-3 is similar to that found by Boucher *et al.*, [12], but the Curie temperatures are lower by 10 ~ 15 K. The more recent value from Baudour *et al.*, [26] is in better agreement with the present work. It is unknown why the values obtained from the variable firing temperature study are slightly offset from those from samples 1-3. This could have something to do with the differing preparation conditions, as the variable temperature samples were fired as powders, whereas samples 1-3 were fired for an additional period in pellet form, before heat treatment, giving a total firing time of 96 hours.

The inversion parameter may not be the only factor affecting the Curie temperature. The presence of short range ordering (see section 5.7), or variable amounts of Mn^{3+} ions on the A sites (see section 5.3) may also be contributory factors. Studying the separate dependencies would be extremely difficult, as all factors are altered by a variation in the cooling rate of the samples [12, 52, 34], which is the only method found for appreciably altering the inversion parameter without affecting stoichiometry.

The features labelled T_l in the field cooled magnetisation curves in Figures 6.71, and 6.72, are believed to be at, or near to, the transition from a collinear ferrimagnetic phase to a more complex canted moment arrangement.

Corresponding features were observed in μSR data on the same samples (see section 6.8). Similar features were also observed by Boucher *et al.*, [12], in neutron diffraction, and specific heat data (see section 5.6 for a fuller discussion of the results of Boucher *et al.*,). The transition temperatures of Boucher *et al.*, were reported to be approximately 84 K, and largely independent of the inversion parameter. The features observed for samples 2, and 3 were at approximately 56 K, and 69 K respectively, in both SQUID, and μSR data. Sample 3 was the only one which showed any evidence of a non-collinear moment arrangement at low temperatures, as shown in section 6.5.3.

From inspection of the data in Figures 6.66, 6.69, 6.71, and 6.72, it can be seen that samples 1-4 exhibit *P* type ferrimagnetic behaviour (see section 1.3.5 for details). This implies that the sublattice with the smaller moment is more easily thermally disturbed in these samples [69]. It has been claimed [70, 71] that the presence of either *N*, *P*, or *R* type behaviour (see section 1.3.5, figure 1.6) in spinel oxides implies the presence of magnetic frustration on at least one sublattice. *P* type behaviour was not observed for any values of ν in the samples studied by Boucher *et al.*, [12]. The arrangement of B sites in the spinel structure, that of corner-shared tetrahedra, is analogous to the crystal structure if water ice, which was the first system where frustration was identified, by Pauling [72].

6.7 Nickel manganite thin films

A number of nickel manganite thin films were grown by electron beam evaporation in the Physics Department, University of Durham by Rainier Schmidt. The details of the growth process is reported elsewhere [35, 73]. The target material used was nickel manganite, and was produced by the mixed oxide route. A mixture of NiO, and Mn_2O_3 was fired at 1200 °C, and annealed at 800 °C for up to 50 hours. A small excess of Mn_2O_3 was used, in order to counteract the loss of manganese observed at 1200 °C. This preparation route was employed in order to try to reproduce the properties of industrially produced thermistor devices.

6.7.1 Room temperature magnetisation

All of the films were measured at room temperature using the AGFM detailed in chapters 2 and 3. For comparative purposes, a sample of the target material was measured as well. The *m-H* curve measured is presented in Figure 6.74, along with a curve corrected for the instrument background, which is also shown.

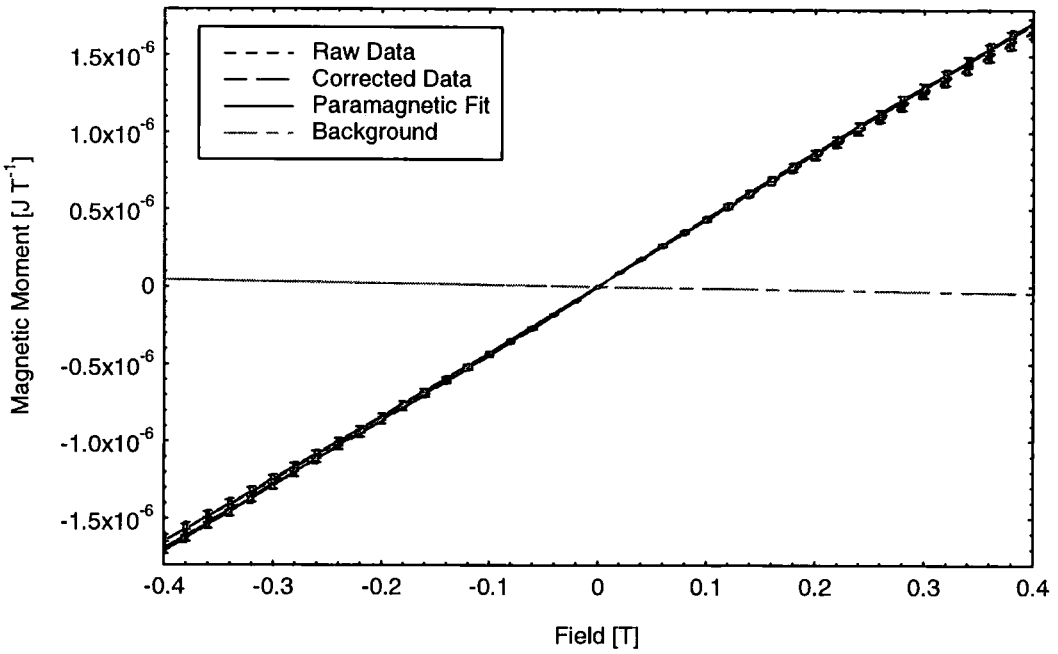

Figure 6.74. AGFM *m-H* data from a sample of 12.3 mg nickel manganite target material + 12.1 mg vacuum grease at T = 300(5) K.

The AGFM sample holder was simply a piece of microscope cover slide on the end of the resonant element, unsuitable for measuring loose powders. However, the target material was in powder form, so was mixed with vacuum grease in a known weight ratio to enable sample mounting. The entire probe assembly was weighed with and without sample to ensure accuracy. The contribution due to the grease was also removed. A separate AGFM measurement produced a mass susceptibility for the grease of; χ_p = - 4.52(4) x 10^{-9} m^3 kg^{-1}. The resultant susceptibility of the target nickel manganite sample was found to be χ = 2.32(2) x 10^{-3}, using a density of 5231 kg m^{-3} as determined from a measurement of the lattice parameter in section 6.2.2. This value is approximately twice that observed in samples made by the hydroxide route (Table 6.21). The sample shows no traces of impurities that have a spontaneous

magnetisation at room temperature (such as $NiMnO_3$). However, paramagnetic or antiferromagnetic impurities may be present, such as NiO, Mn_2O_3, and Mn_3O_4. A series of 5 films of varying thickness' were deposited onto glass substrates of varying size. The nominal thickness and area of the films deposited are given in Table 6.24.

Sample	Thickness [μm]	Area [mm^2]	Volume [10^{-12} m^3]
Film 1	4	9.72	38.8
Film 2	58	1.51	103
Film 3	2.34	13.9	32.4
Film 4	6.4	13.9	88.7
Film 5	2.83	13.9	39.2

Table 6.24. Details of the nickel manganite thin film samples.

Magnetisation data collected at room temperature on all of the thin films is shown in Figures 6.75 to 6.79.

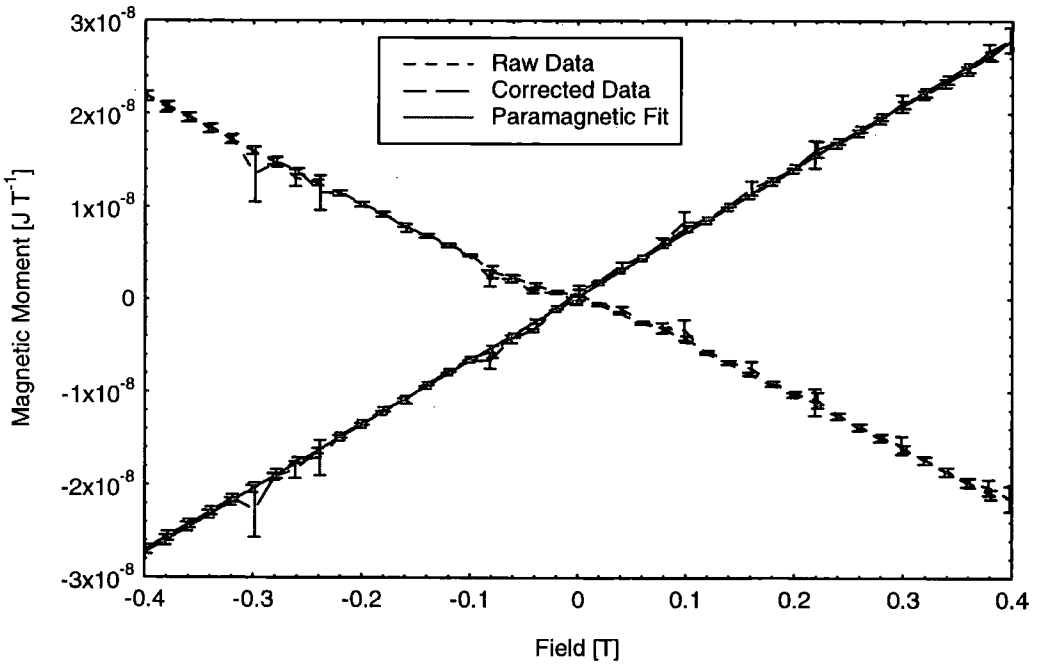

Figure 6.75. AGFM *m-H* data for thin film 1 (thickness = 4 μm), T = 300(5) K .

The film thickness was measured using an Alpha-Step stylus profileometer. In most cases, there was a variation in film thickness found across a sample, so there may be considerable errors on the computed volumes. All the films were deposited onto glass substrates, which were thoroughly cleaned before use. The substrates were cleaned using a detergent, decon 90, an ultrasonic water bath, and refluxing with hot isopropyl-alcohol for 4 hours respectively.

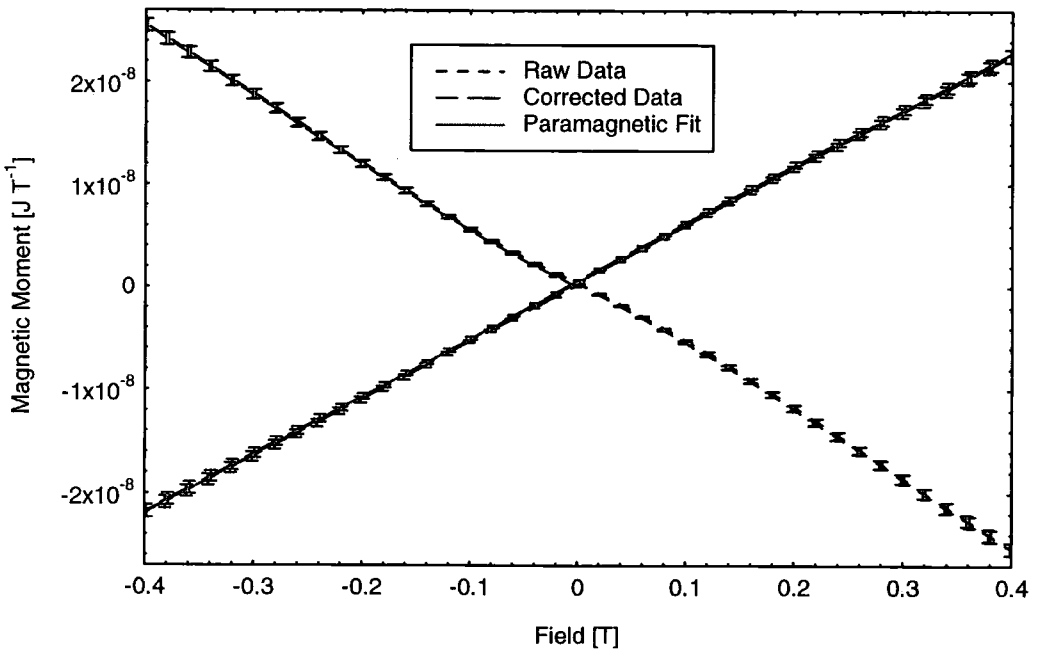

Figure 6.76. AGFM *m-H* data for thin film 2 (thickness = 58 μm), T = 300(5) K.

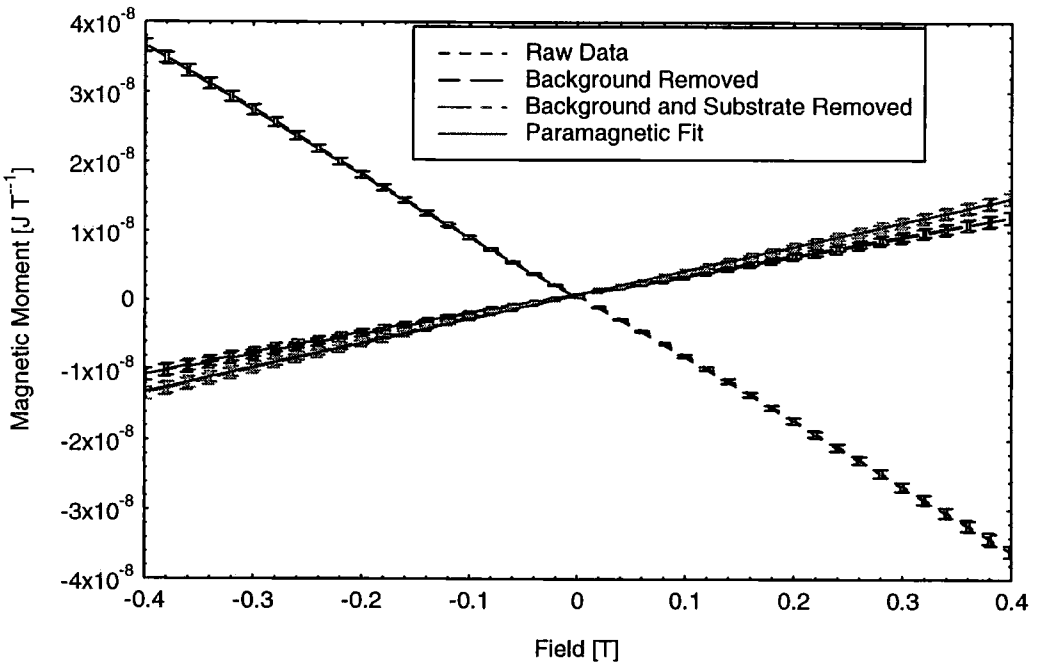

Figure 6.77 AGFM *m-H* data for thin film 3 (thickness = 2.34 μm), T = 300(5) K.

In some cases, the magnetic responses of the glass targets were measured before deposition. As can be seen from the data, the films are all paramagnetic at room temperature, the only one showing any sign of contamination being film 5. All of the data has been corrected for the diamagnetic background of the AGFM sample holder.

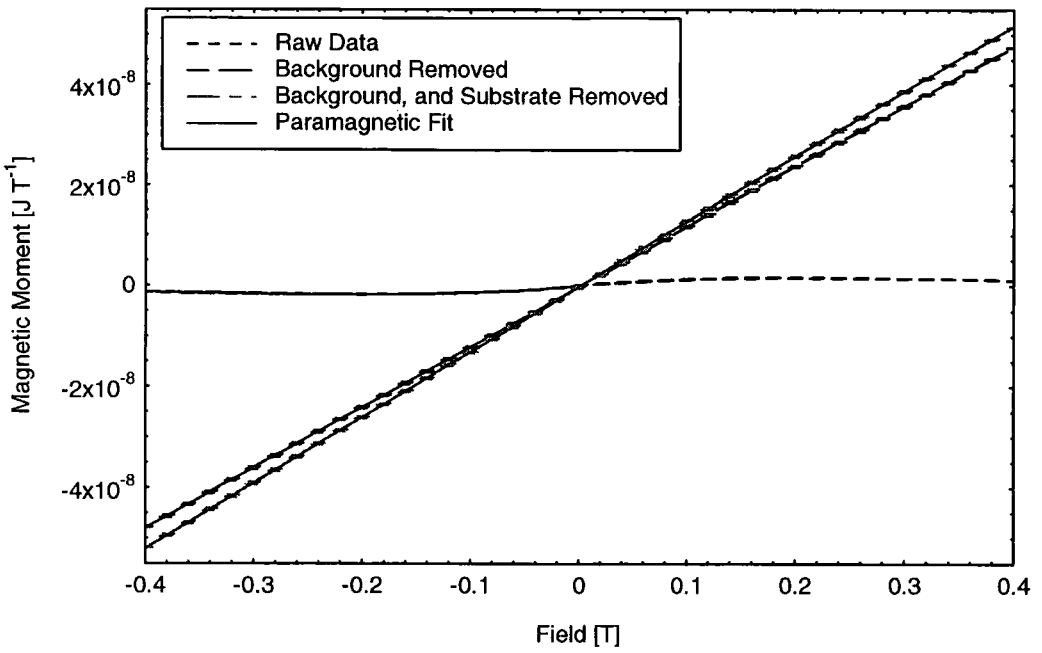

Figure 6.78. AGFM *m-H* data for thin film 4 (thickness = 6.4 μm), T = 300(5) K.

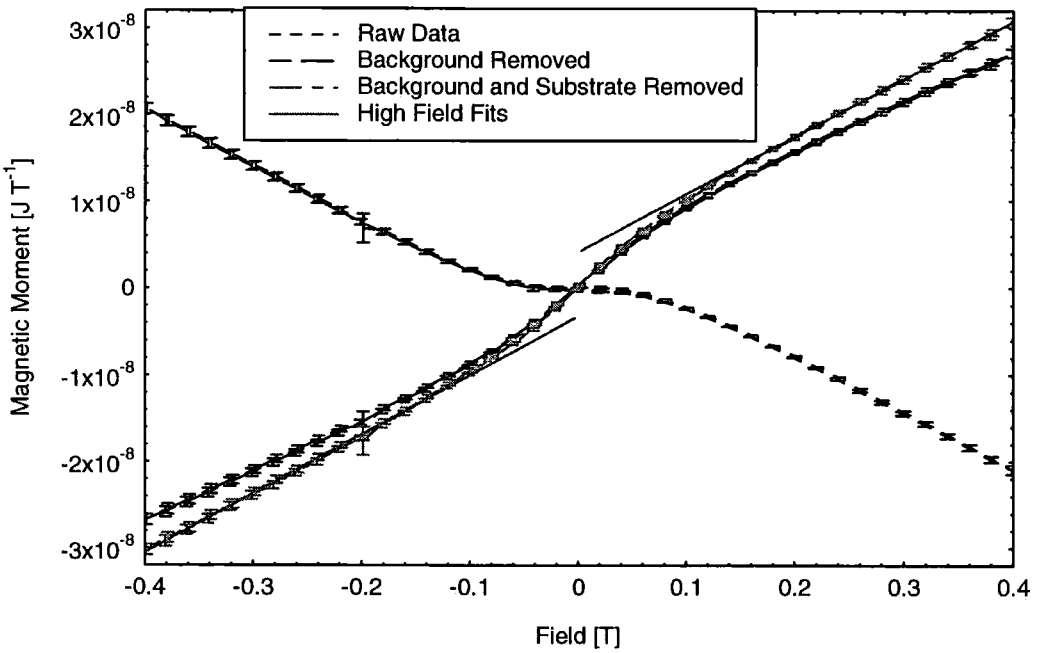

Figure 6.79. AGFM *m-H* data for thin film 5 (thickness = 2.83 μm), T = 300(5) K.

In addition, the contributions due to the glass substrates have been accounted for. In the case of films 1, and 2 (Figure 6.75, and 6.76), which were deposited onto relatively thick substrates, the substrates were not measured on the AGFM before deposition. Therefore, a piece of the same glass was measured, yielding a susceptibility of; $\chi_p = 2.71(4) \times 10^{-10}$ m^3 kg^{-1}. This value was then used to

calculate the contribution of the substrate for films 1 and 2. The mass of the film was negligible in comparison to the mass of the substrate.

It soon became apparent that the susceptibility of the glass used as substrate varied slightly between samples, so that a general substrate correction, as applied to the AGFM data from films 1 and 2 led to inaccuracies. Therefore, for all subsequent films, the actual piece of glass used was measured directly before deposition took place. The glass pieces used for samples 3, 4, and 5 were also much thinner, to reduce mass, and therefore the amount of noise on the AGFM measurements.The values of volume susceptibility calculated for all the films are reported in Table 6.25.

Sample	Thickness [μm]	Volume Susceptibility (dimensionless) x 10^{-3}
Bulk	-	2.32(2)
Film 1	4	1.934(8)
Film 2	58	1.131(3)
Film 3	2.34	1.934(4)
Film 4	6.4	1.839(7)
Film 5	2.83	2.16(3)

Table 6.25. Volume susceptibilities calculated from AGFM measurements for all films, and a bulk sample of target material.

The error values quoted do not take into account the possible errors in the volume of the sample, which may be considerable. The susceptibility value for film 5 was obtained by fitting a straight line to the high field regions of the data, as shown in Figure 6.79. The fits obtained were good, as the contribution from the ordered component saturated in a relatively low field. The values of the thin film susceptibility in Table 6.25 were calculated assuming that the density of the films was the same as the crystalline density, i.e. there were no voids in the film. This assumption was not made for the bulk powder, since the value was calculated from the sample mass. This may account for the lower values reported for the films, especially the thicker ones. An alternative is that the effective magnetic moment of the nickel manganite has changed due to the deposition process. This may be due to a change in stoichiometry of the deposited material, if nickel or manganese is lost during deposition. Alternatively the inversion parameter may have changed, thereby altering the population of the various cations in the structure.

As noted above, there is evidence of contamination in film 5. This manifests as a non-linearity in the *m-H* loop. This shape is characteristic of materials that exhibit a spontaneous magnetisation, ferromagnets, and ferrimagnets (see section 1.3). This contamination was not present when the substrate was measured, so was introduced either during deposition, or in subsequent storage. As demonstrated in chapter 3, the smallest amounts of dust sometimes give rise to large impurity signals, so as a precaution, film 5 was cleaned as thoroughly as possible, and re-measured. There was no change observable after cleaning. The saturation moment of the impurity was found to be 3.68(14) x 10^{-9} J T^{-1}, from the offsets on the high field fits to the data (see Figure 6.79). The only impurity phase expected in nickel manganite that shows ordering at room temperatures is the ilmenite type phase, $NiMnO_3$. This has a reported saturation moment of 22 J T^{-1} kg^{-1} at 300 K [64]. If the saturation moment observed is attributed entirely to this, and all the phase is saturated, then the amount of $NiMnO_3$ present in film 5 is 167(6) ng, or 3.39(12) x 10^{-14} m^3. This corresponds to approximately 0.1 % of the film by volume. It is unknown why this sample alone shows an ordered component. One possibility was that the target material was impure, due to an incorrect ratio of the precursor oxides, or annealing at too low a temperature.

6.7.2 Variable temperature magnetisation

Magnetisation measurements at variable temperature were made using the AGFM described in chapter 2, modified so that the sample probe was in a temperature-controlled environment. The resonant probe, biomorph, and a modified damping weight were inserted into a modified Oxford instruments continuous flow cryostat. Details of characterisation in this configuration are included in chapter 3. The cryostat, connected to an Oxford Instruments temperature controller model ITC4, enabled the temperature of the sample to be held at a controlled temperature between 77 K, and 300 K. This could be maintained indefinitely. The temperature of the sample was monitored using a miniature platinum resistance thermometer. This was suspended next to, but not touching, the sample by an additional quartz fibre, somewhat thicker than the one used to mount the sample on. Temperature readings were taken in zero applied magnetic field. Because the cryostat was metallic, eddy currents due to the

alternating gradient field coils (external to the cryostat) were formed in the cryostat tail. These, and the large magnetic moment associated with so much steel, contributed to a large background signal. The resonant peak observed was no longer recognisable as due to a single mode of vibration, so the fitting and correction procedures outlined in sections 2.3.2, and 2.3.3 could not be implemented. This necessitated taking frequency scans at a fixed temperature, and trying to determine which features were due to the resonance of the sample probe that was being excited by the magnetic moment of the sample. The phase of the signal was unpredictable as the sample temperature changed, so the only the magnitude of the signal obtained was considered. Representative frequency scans are shown in Figure 6.80. These were taken in a field of 0.2 T, measured outside the cryostat. The system was allowed to stabilise at the set temperature for up to 30 minutes before measurements were taken. Unless this was done, it was found that the signal changed appreciably as a frequency scan was underway.

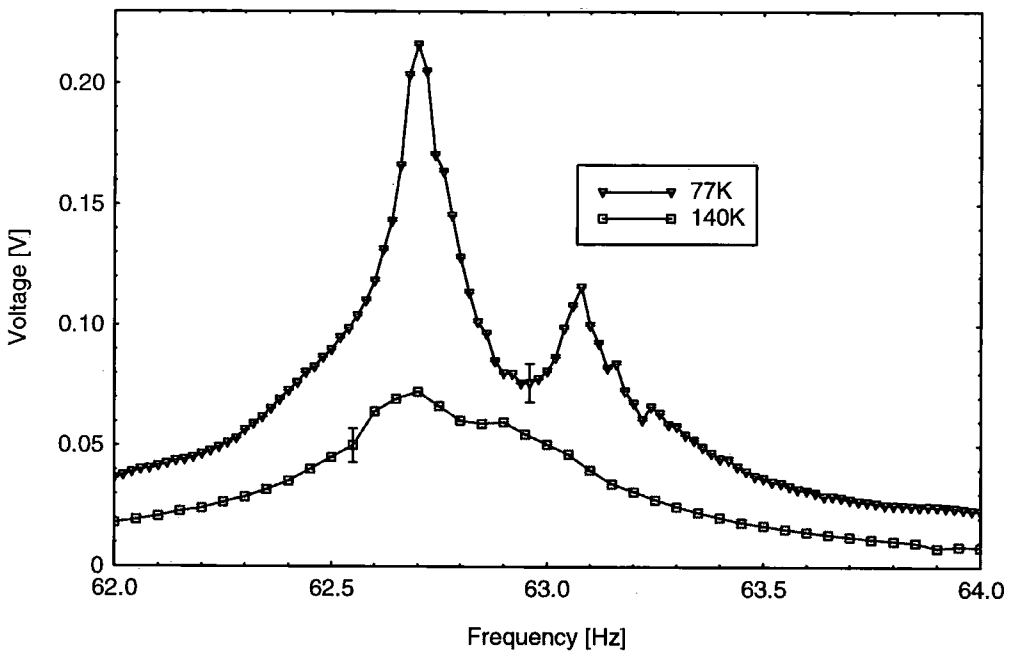

Figure 6.80. Low temperature AGFM frequency response, at different temperatures. Data is shown for film 3, at 0.2 T. Representantive error bars are shown.

The feature at 62.75 Hz was identified as most probably due to the changing sample magnetisation. The height of this feature was taken from a number of frequency scans at temperatures between 77 K, and room temperature. The height of this peak at room temperature was referenced to the calibrated signal

obtained from film 3 measured in the room temperature AGFM (Figure 6.77). With this known, a magnetic moment was calculated for all the other peaks observed at different temperatures. No correction was made for any changes in the background signal with temperature, or changes in the sensitivity of the biomorph [74]. The heights of the 62.75 Hz feature as a function of temperature are plotted in Figure 6.81.

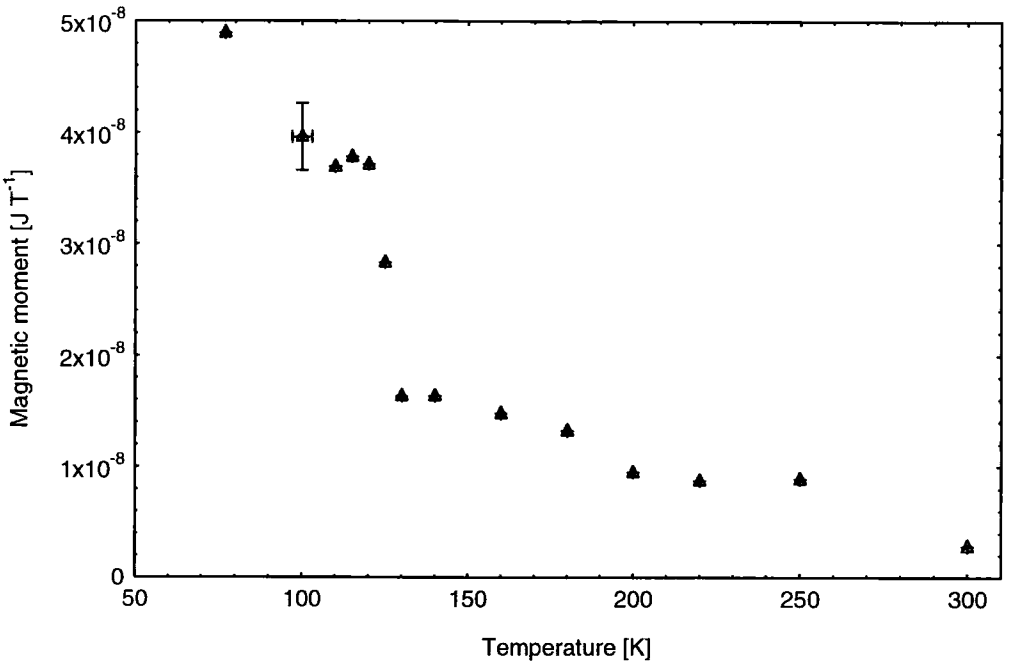

Figure 6.81. Temperature dependance of the magnetic moment of film 3, at 0.2 T. Representantive error bars are shown.

No attempt to remove the magnetic contribution from the substrate was made. In comparison with Figure 1.5 (VSM data on a sample of bulk nickel manganite), the background is much larger, as expected. However a clear feature is observed at a temperature of between 125 K and 130K. The similarities between this, and the transition observed in the bulk sample are clear. Taking the observed feature to be the paramagnetic-ferrimagnetic phase transition in nickel manganite, and assuming that the material is approximately stoichiometric, an inversion parameter of $\nu = 0.788(8)$ can be estimated for this film sample from the relationship plotted in Figure 6.72. This value of inversion parameter is indicative of a sample that has been cooled quite rapidly, but not quenched. The substrate temperature during evaporation was lower than 400 °C at all times, so material deposited would be expected to cool to the substrate temperature almost

instantaneously. Therefore, it is probable that the inversion parameter of the thin films is at least partly determined by the inversion parameter of the target material used.

6.8 Muon spin relaxation experiments

A number of samples of $NiMn_2O_4$ were studied using the Muon Spin Relaxation (μSR) spectrometer at the ISIS facility [75], housed at the Rutherford Appleton Labs, Didcot. The samples used were those made for study by neutron diffraction at the ILL, numbered 2 and 3. These are detailed in Table 6.12, section 6.5.1. The aim of this work was to study the low temperature magnetic transitions in nickel manganite, and the effect of short-range order on the magnetic properties. μSR is a powerful technique in that it is a sensitive probe of the local magnetism.

All the recorded data extend to longer times than displayed, as the muon pulse rate was fixed, but this was not considered useful. Only data within a time window of $0.2\ \mu s < t < 20\ \mu s$ was analysed, using the WiMDA [76] utility, which provided for the correct propagation of counting uncertainties through the least squares fitting procedure. Figure 6.82 shows the behaviour of the asymmetry observed for sample 2 at room temperature, with a magnetic field of 2 mT applied at right angles to the initial muon spin vector. This illustrates coherent precession, as the local field experienced was almost identical for all muons. The asymmetry at $t = 0$ represents the degree of spin polarisation of the muons, once they have been implanted into the sample. The oscillations in Figure 6.82 are approximately centred on an asymmetry of zero, which indicates that the efficiency of the two detector banks were similar. The efficiency ratios were calculated for each sample studied, and used to correct the subsequent data before analysis. Since oscillations are clearly visible in Figure 6.82, and decay only slightly, it can be concluded that the local field disturbances are small compared with the applied field. This is to be expected for a paramagnetic material. In contrast, there were no oscillations visible when no applied field was present, as shown in Figure 6.83. This indicates a very rapid dephasing, again characteristic of a paramagnetic material.

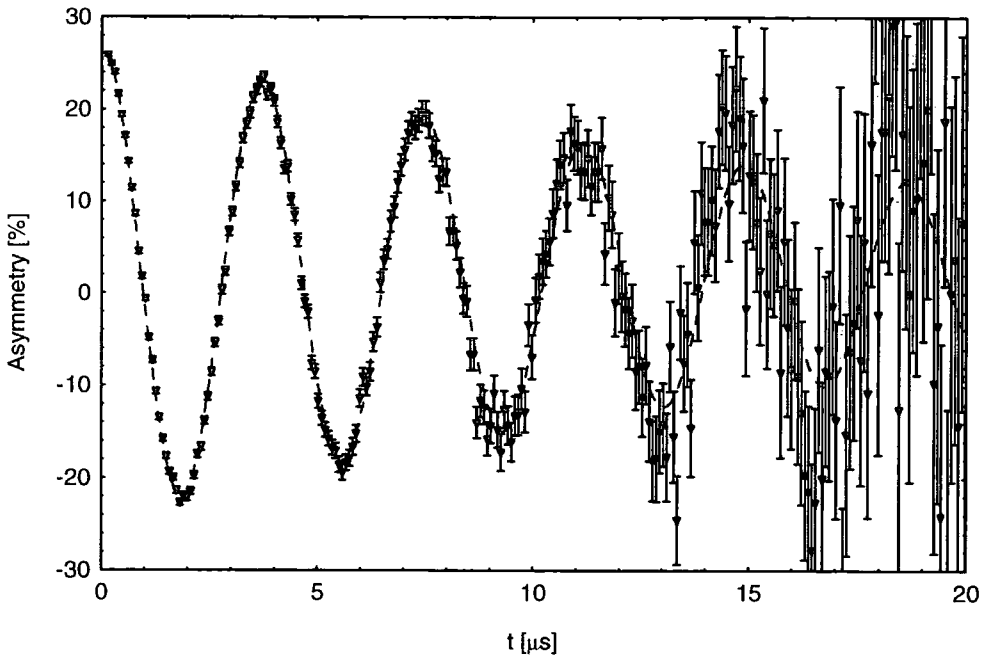

Figure 6.82. μSR asymmetry data from sample 2 at room temperature, with a transverse magnetic field of 2 mT applied. The dashed line is a fit to the data, giving a field of 1.979(3) mT, and a dynamical depolarisation rate λ=0.048(3).

The application of a longitudinal (parallel to muon beam vector) field of 2 mT, in order to decouple the nuclear moments had no measurable effect on the recorded data, indicating that the signals detected were due to the electronic magnetisation, and the dynamic nature of the fields at the muon sites [77]. Measurements on both samples were therefore taken in the range 10.5 K < T < 295 K, in zero applied magnetic field. A selection of the collected data in the different magnetic regimes is shown in Figure 6.83 for sample 2, and Figure 6.84 for sample 3. All the data has been corrected for the slightly different detector efficiencies, and sample absorption. It was found that all the zero field datasets from both samples could be modelled with a stretched exponential function [78];

$$a_0(t) = Ae^{-(\lambda t)^{\beta}}.$$

The stretched exponential form for the data results from a wide variation of the magnetic moment fluctuation rate, ν (not to be confused with the inversion parameter) [78]. This function is useful in cases intermediate to the Gaussian spin ($\beta = 1$) or Lorentzian spin ($\beta = 0.5$) distributions. The Gaussian distance distribution is appropriate to a concentrated spin system, such as a strong

paramagnet, whereas dilute spin systems such as the canonical spin glasses obey a Lorentzian distance distribution [78].

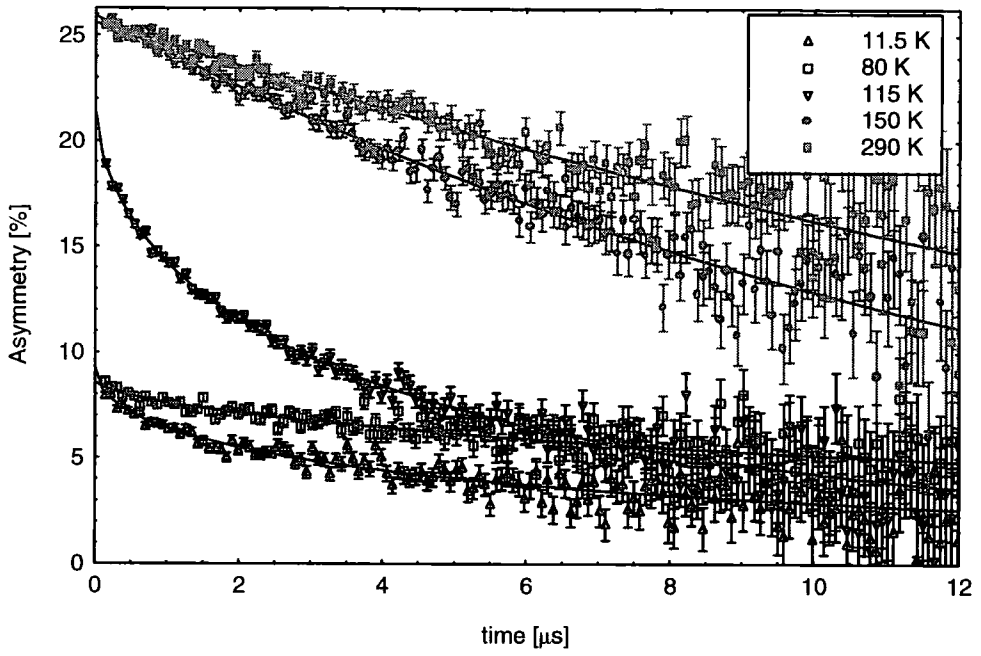

Figure 6.83. Asymetry data collected from sample 2, at between 11.5 K, and 290 K in zero applied field. Also plotted are stretched exponential fits to the datasets.

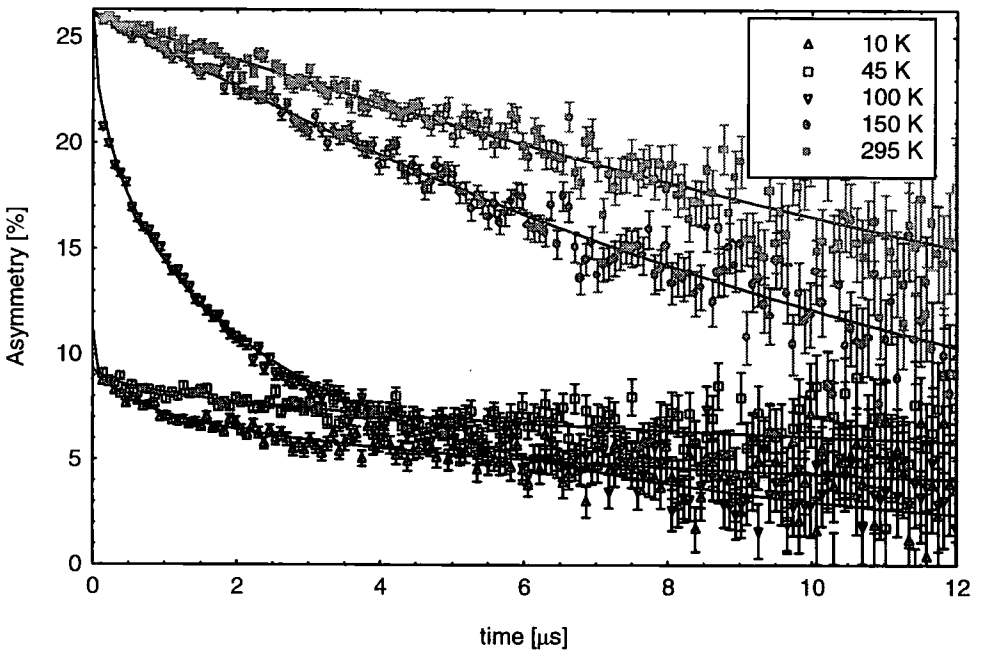

Figure 6.84. Asymetry data collected from sample 3, at between 10 K, and 295 K in zero applied field. Also plotted are stretched exponential fits to the datasets.

For each dataset plotted in Figures 6.83, and 6.84, the fitted stretched exponential function has also been plotted. In all cases the agreements are very good, with

the average value of χ^2 (least squares fitting residual) = 1.13 for all the datasets in Figures 6.83, and 6.84. Plots of the fitted values of the relaxation exponent β, the dynamical depolarisation rate λ, and the initial asymmetry (A) are shown in Figures 6.85 to 6.87, for both samples. The error bars shown in Figures 6.85 to 6.87 were those reported by the data analysis program WiMDA, and so are due solely to the uncertainties in the curve fitting procedure. There may be other significant sources of uncertainty, such as changes in detector efficiencies, timing variations, and changing contributions from the cryostat at different temperatures.

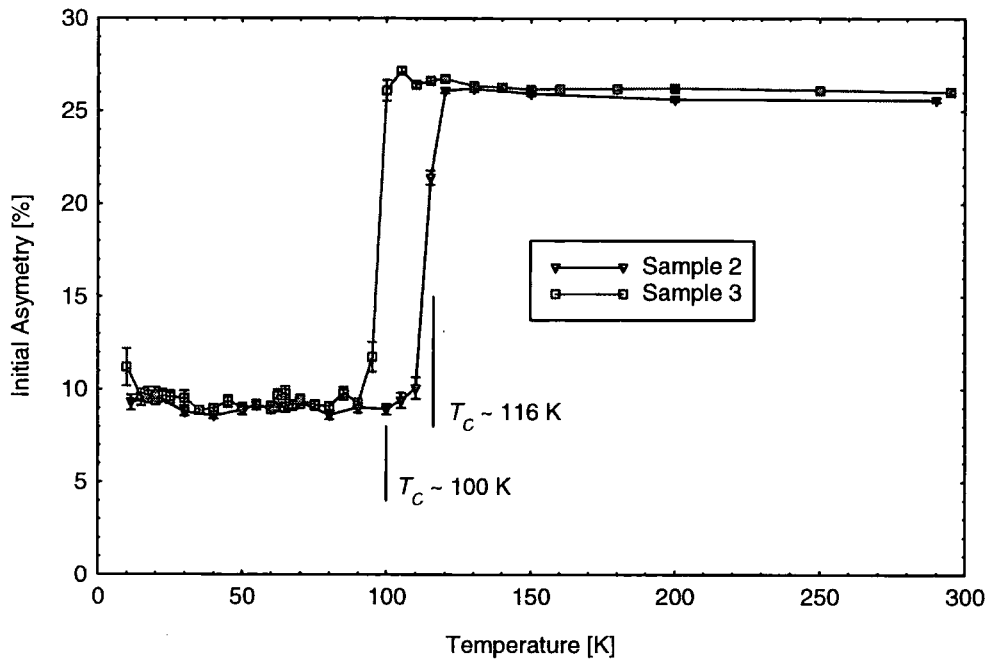

Figure 6.85. Initial Asymetry fitted to μSR data. The Curie temperatures determined from SQUID magnetometer measurements (section 6.6) are marked for both samples.

The high temperature value of the initial asymmetry, A (shown in Figure 6.85) agrees well with that determined from the initial run obtained in a transverse field of 2 mT (Figure 6.82). This indicated that no rapid muon de-phasing was occurring at room temperature. The initial asymmetry drops at temperatures that correspond to the T_C *'s* determined from both VSM (Table 6.22), and SQUID magnetometer (section 6.6) data. This is expected because at the onset of magnetic ordering, the static local fields cause extremely rapid precession of the muon spin, similar to that observed in Figure 6.82 for a field of just 2 mT. In contrast to the data in Figure 6.82, the oscillations are rapid enough such that

they are shorter than the sampling time, and therefore cannot be resolved by the spectrometer. The effect of this is to average the oscillations, giving 1/3 of the 'true' initial asymmetry. The bulk magnetic ordering is therefore 'decoupled' from the spectrometer below T_C. This has the effect of enabling small fluctuations superimposed on the magnetic ordering to be observed quite easily. This decoupling characteristic is confirmed by the behaviour of the exponent β, shown in Figure 6.86.

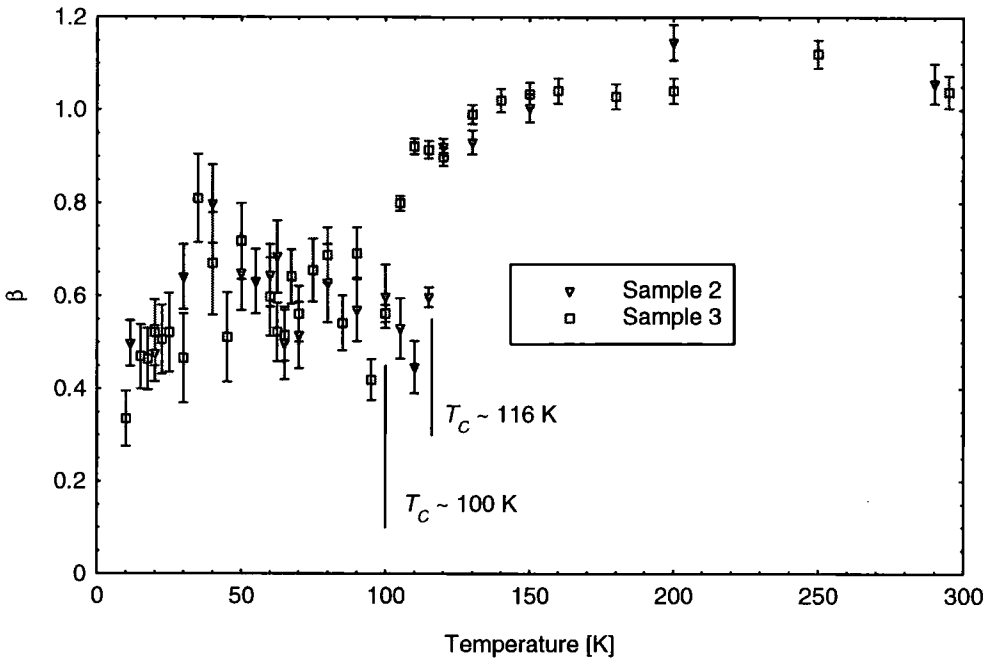

Figure 6.86. Relaxation exponent β fitted to μSR data. The Curie temperatures determined from SQUID magnetometer measurements (section 6.6) are marked for both samples.

The exponent β drops from approximately 1 above T_C, to 0.5 below T_C, indicating a change in character from a Gaussian to a Lorentzian distribution. Since below T_C nickel manganite is clearly not a dilute spin system, the muons must be sensitive only to deviations from the bulk order, confirming the 'decoupling' behaviour, as discussed above. The deviations from bulk order, such as thermal excitations, spin waves, etc., have the characteristics of a predominantly dilute magnetic system. The slight increase in β around 50 K indicates an increase in the concentration of spin fluctuations. This is around the same temperature as the features observed in magnetisation data (see Figures 6.71,and 6.72), which have been interpreted as a transition to an ordered

canted spin arrangement by Boucher *et al.*, [12]. The increase in β is consistent with this additional ordering.

The behaviour of the dynamic depolarisation rate, λ as the sample temperature is changed is plotted Figure 6.87 for both samples.

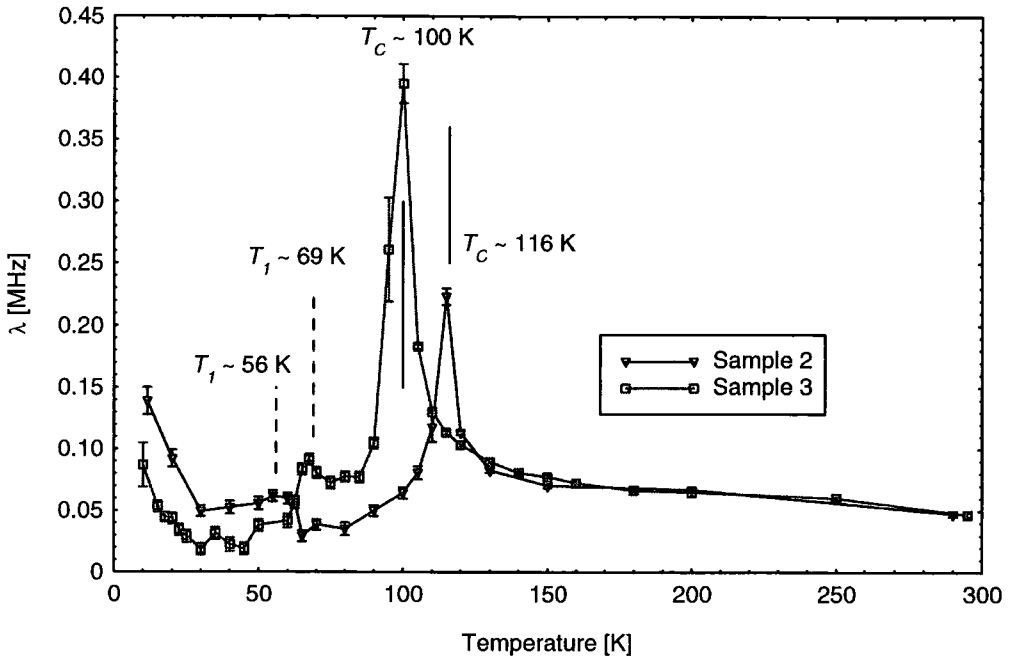

Figure 6.87. Dynamic depolarisation rate λ fitted to μSR data. The Curie temperatures determined from SQUID magnetometer measurements (section 6.6) are marked for both samples, as are the positions of the features labelled T_1 in Figures 6.71, and 6.72.

There are several features immediately obvious from the behaviour of λ with changing temperature. The positions of the large peaks in λ, agree well with the features observed in A, and β, and the Curie temperatures from SQUID magnetometer data. Due to the decoupling of the muons from bulk magnetic ordering below T_C, additional features were observable in λ. The features labelled T_1 in the field cooled magnetisation curves in Figures 6.71, and 6.72, correspond to similar features in the behaviour of λ (labelled in Figure 6.87). These are believed to be at, or near to, the transition from a collinear ferrimagnetic phase to a more complex canted moment arrangement, at ~ 56 K, and ~ 67 K in samples 2, and 3 respectively. These temperatures are lower than the previously reported [12] values of 82-84 K (section 6.6.3). This suggests that the exchange energy causing the (presumed) canting is smaller for the present samples compared to those of Boucher [9]. This could be due to differences in

charge state or bond angle as the present samples are of higher purity. There is also a pronounced increase in λ below 30 K, observed for both samples. This increase continues to the lowest temperatures achieved in the experiment. Further lower temperature experiments [79] have confirmed this increase, finding a further peak in λ just below 10 K. This has been interpreted as evidence for a previously unknown magnetic transition at this temperature. There are no corresponding features visible in the SQUID magnetisation data down to these temperatures, and no previous reports in the literature. The only published magnetisation data that extends to low enough temperatures is that of Boucher *et al.,* [12], and this also shows no features around 10 K. The specific heat data of Boucher *et al.,* that identifies the higher temperature transitions extends only down to 20 K, while their temperature dependent neutron diffraction data is similarly featureless around 10 K. The magnetic structure at 4.2 K as determined from neutron diffraction data by Boucher *et al.,* may therefore evolve from a collinear structure in 2 steps rather than 1, however some accompanying feature in the magnetisation or neutron data is to be expected. The other possibility is that the transition below 10 K is not due to an additional ordered magnetic state, but a local disorder superimposed upon the already established long range ordering. This would be consistent with the lack of evidence of a change in long range ordering in neutron and magnetisation data. Support for this proposal can also be found from the calculations of Goodenough [80, 81] upon the relative strengths and signs of the various interactions present in spinels (summarised in Tables 4.8, and 4.9 for the relevant ions). These show that for nickel manganite there is expected to exist a number of interactions between adjacent B site ions that conflict with each other, and the dominant A – B site superexchange interactions. These interactions are predicted to be much weaker and therefore will only become important at low temperatures. This frustration has been proposed [70, 71] as the cause of the decrease in saturation magnetisation observed below the Curie temperature in samples 1 – 4. Since the cation distribution amongst the B sites has a variable proportion of the 3 proposed constituent ions (Ni^{2+}, Mn^{3+}, Mn^{4+}), which in general precludes a complete geometrical ordering, an element of spatial disorder is inevitable. This, and the proposed multiple interactions present, make it highly

unlikely that many individual B site ions will experience identical environments, and a degree of disorder in the moment directions is to be expected, termed a Localised Canted State (LCS) [82]. Arrangements of this type have been found in a number of other systems, such as $Ni_xCd_{1-x}Mn_2O_4$ ($0.2 < x < 0.8$) [83], and $Mg_{1+x}Fe_{2-2x}Ti_xO_4$ ($x > 0.83$) [82]. These types of partially disordered system are particularly amenable to study by μSR, as the technique is insensitive to the bulk ordering below the Curie temperature. Similar increases in λ have been observed in a number of other disordered systems ([84, 85] and references therein) as the fluctuation rate decreases upon approach to a freezing temperature.

The behaviour of the dynamic depolarisation rate, λ as the sample temperature is changed can be explained by the relationship;

$$\lambda = \frac{4a^2}{\nu},$$

where a is the dynamic field spread, a measure of the distribution of local field direction and magnitude, or width of the distribution function, and ν is the fluctuation rate of the local fields. The peaks in λ are noticeably asymmetric, due to the differing mechanisms at work above and below the transitions. The rapid increase as the ordering temperature is approached from above is due to a slowing down of spin fluctuations (decrease in ν) as the material becomes ordered. The decrease below the ordering temperature is due to a sharp drop in the dynamic field spread, a as all the domains achieve a similar saturation magnetisation state. There are several approaches which attempt to describe the behaviour of spin dynamics near magnetic ordering transitions, both phenomenological, and theoretical. The dynamical scaling theory of Hohenberg and Halperin [86] predicts such a slowing down of the fluctuating moments above T_C. This was formulated in terms of the correlation time, $\tau_c = 1/\nu$;

$$\tau_c = \tau_0 \left[\frac{T}{T - T_C} \right]^n$$

Since the dynamical depolarisation rate, λ is proportional to the correlation time, and the dynamic field spread, a is not believed to change appreciably above T_C, a formulation in λ is equally valid. This is illustrated in the log-log plot of Figure 6.88, which shows the dependence of λ on the inverse reduced temperature, $1-T_C/T$ in the temperature range $T_C \leq T \leq 260$ K for both samples.

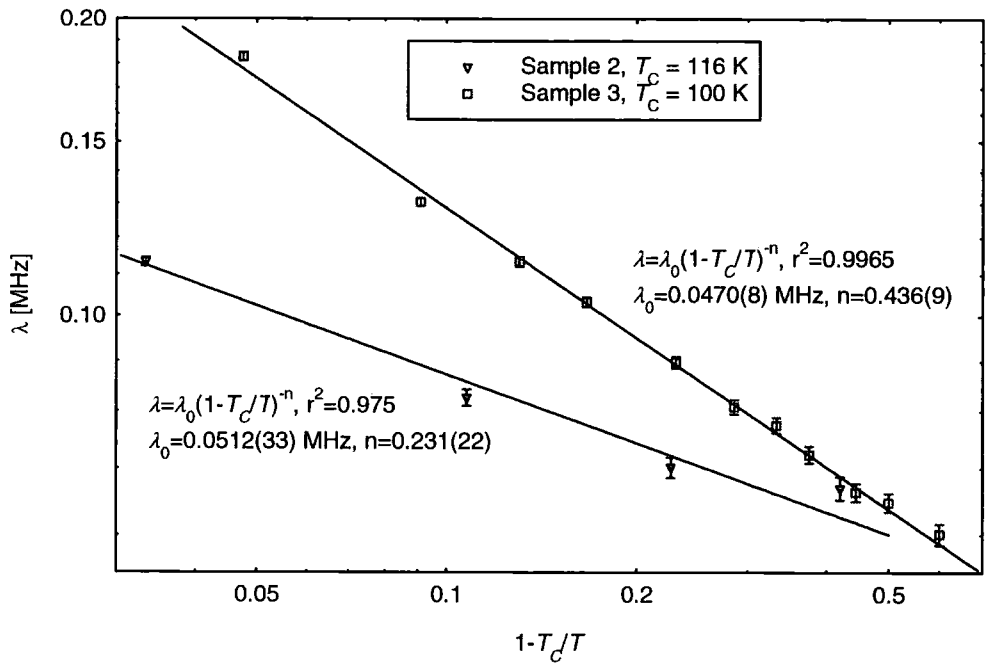

Figure 6.88. Log-log plot of the dependence of the fitted dynamic depolarisation rate, λ on the inverse reduced temperature. Also plotted are least squares fits to the data corresponding to the equations shown.

The straight lines in Figure 6.88 are fits to a modified form of the above equation, which show excellent agreement with the data. Values of the exponent, n were realistic, although considerably different for the two samples. Attempts to fit the increase in λ below 30 K to a similar expression did not provide a satisfactory agreement between model and data, for any transition temperature in the region 0.5 K < T < 10 K. Such a failure of this model has also been noted by Lappas *et al.*, [85], when attempting to model μSR data just above a disorder freezing temperature. The procedure adopted was to use the standard Arrhenius law;

$$\tau_c = \tau_0 e^{\left(E_a/k_B T\right)},$$

appropriate to thermally activated processes with approximately constant energy barriers. Accordingly, a similar approach was tried with the increase in λ below 30 K in the present data, illustrated in the Arrhenius plot of Figure 6.89. The agreement of data and model is good for sample 3. The 3 datapoints in the temperature region of interest collected from sample 2 are not considered enough to confirm or deny any particular functional form, however the activation energy obtained from both samples are strikingly similar. Similar Arrhenius behaviour

has also been observed in purely disordered systems such as $Cu_{0.95}Mn_{0.05}$, and amorphous cobalt aluminosilicate ([85], and references therein).

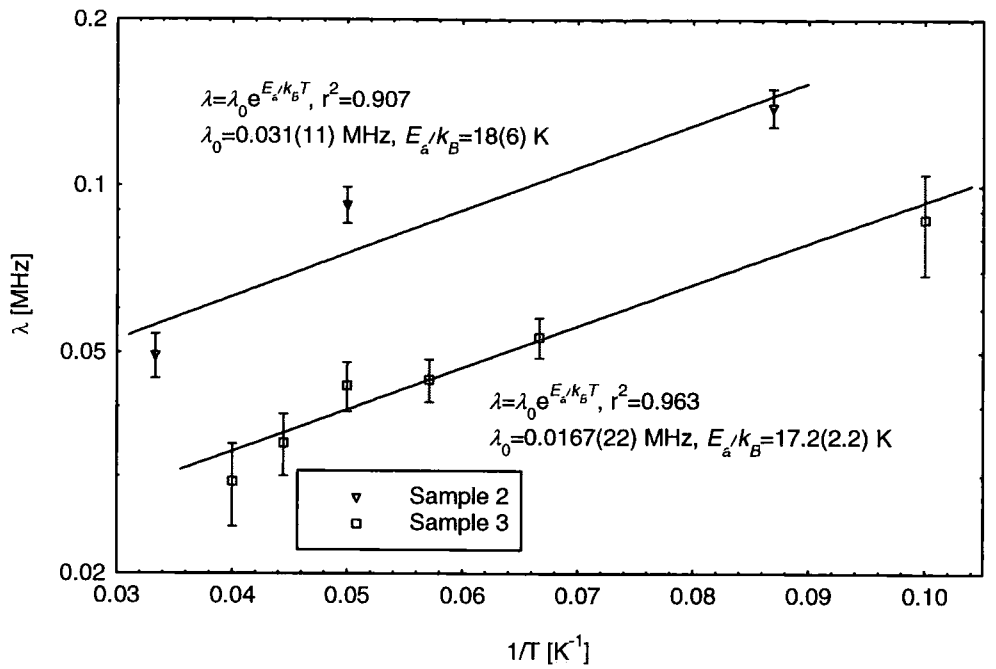

Figure 6.89. Arrhenius plot of the fitted dynamic depolarisation rate, λ vs inverse temperature. Also plotted are least squares fits to the data corresponding to the Arrhenius equations shown.

6.9. Summary

The optimum preparation conditions for the production of pure nickel manganite have been studied. The mixed oxide route has been found unsuitable, due to the presence of persistent impurities, and loss of manganese at the high firing temperatures (up to 1200 °C) necessary. Accordingly, the hydroxide route, using coprecipitated precursor material was adopted for all further work. The finely divided state of these precursors has been confimed. The optimum preparation temperature was investigated in the region 600 °C to 1100 °C. A minimum in the lattice parameter coincided with a minimum impurity content at 800 °C. Lattice parameter and oxygen parameter values were found to agree well with previously reported values. These were determined from analysis of X-ray diffraction data, using a standardised procedure. Rietveld refinement was used, utilising the FULLPROF [44] analysis program, and the peak with dependence of Caglioti *et al.*, [42]. Impurity phases were included in the analysis as appropriate. The procedure was validated using simulated datasets, which highlighted

errors when nickel oxide impurities were present but not accounted for. This situation gives estimates of lattice parameter and oxygen parameter that are much too low. Even when the simulated data and model were identical, a statistically significant reduction in refined oxygen parameters was observed.

The effect of varying the firing time and heating rate were investigated, and findings were that impurity content decreased with increasing firing time at 800 °C, and a slow heating rate gave rise to an increased amount of α-Mn_2O_3. A firing time of 48 hours was found to be an adequate compromise to reduce the level of impurities to low enough levels. Attempts to stimulate the growth of macroscopic crystals with extended firing times were unsuccessful. Likewise attempts to alter the cation distribution by slight changes in the firing temperature around 800 °C were of limited success. The variation in inversion parameter, as measured using time of flight (TOF) neutron diffraction was approximately 1%, for a temperature difference of 100 °C.

Altering the inversion parameter by controlling the cooling rate from the firing temperature was much more successful. A range of $0.7483(19) \leq \nu \leq 0.8830(22)$ was obtained, enabling further experiments on these samples to study the effect of the change in ν on various other properties. The dependence of the lattice and oxygen parameters was measured, and found to be in agreement with the trends in the literature, and the predictions made in section 4.2.1. Constant wavelength neutron diffraction data at a range of temperatures was obtained, and features indicative of magnetic ordering at low temperature were noted. These were subjected to Rietveld analysis, and the average moments of the ions on the A, and B sites were obtained. The A site moment was seen to increase with increasing ν, while the opposite trend was seen in the B site moments. From these dependencies, an number of things were calculated; a compensation point at $\nu = 0.761(6)$, and in some cases the moments of the various ions present. Both of these agreed with expected values, and supported the contention of Boucher *et al.*, [12], that the magnetic moments of the manganese and nickel on the B sites are in opposition at low temperature. Evidence of a canting angle between the total moments on the A, and B sites was observed in the form of a non-zero amplitude for the (311) diffraction peak at low temperatures in the sample with the highest inversion parameter. Unfortunately this angle could not

be determined, due to a lack of resolution. Similarly qualatative evidence of short range ordering was observed in the diffuse neutron scattering background. Magnetic measurements were made on the same samples, and good agreement was found with the moments determined by neutron diffraction. The Curie temperatures were found to be lower than previously reported values, although the dependence on inversion parameter was broadly similar. *P* type behaviour was noted in the low temperature magnetisation for all values of inversion parameter, which is indicative of magnetic frustration. From study of samples known to be non-stoichiometric, it was concluded that nickel ions on the B sites take part in interactions that are in opposition to a simple ferrimagnetic ordering. An additional magnetic transition below the Curie temperature was found in both magnetisation and μSR data, between 56 K and 69 K. These temperatures are lower than previously reported.

The AGFM detailed in chapters 2 and 3 was used to collect variable temperature magnetisation data on a thin film nickel manganite sample produced from the mixed oxide route. By comparison of the determined Curie temperature to the behaviour of bulk material, an inversion parameter of 0.788(8) was estimated. μSR data was obtained on 2 samples with differing inversion parameter. The temperatures of the various magnetic transitions already observed were confirmed, and an additional transition at approximately 10 K was discovered. This transition has not been observed previously, despite several previous neutron diffraction experiments covering the relevant temperature interval. This lower transition is postulated to be a further canting transition, not necassarily displaying any long range ordering. The behaviour of the spin fluctuation rate agrees with a dynamical scaling theory on approach to the Curie temperature from above, whereas an Arrhenius behaviour was observed for the transition at 10 K. This behaviour is indicative of a disorder freezing transition superimposed on bulk long range magnetic ordering.

References

1. Boucher, B., *C. R. Hebd. Seances Acad. Sci.* **249** (1957) 514.
2. Sinha, A. P. B., Sanjana, N. R. and Biswas, A. B., *Acta Cryst.* **10** (1957) 439.
3. Baltzer, P. K. and White, J. G., *J. App. Phys.* **29** (1958) 445.
4. Azaroff, L. L., *Z. Kristallographie* **112** (1959) S33.
5. Larson, E. G., Arnott, R. J. and Wickham, D. G., *J. Phys. Chem. Solids* **23** (1962) 1771.

6. Wickham, D. G., *J. Inorg. Nucl. Chem.* **26** (1964) 1369.
7. Villers, G. and Buhl, R., *C. R. Hebd. Seances Acad. Sci.* **260** (1965) 3406.
8. Boucher, B., Buhl, R. and Perrin, M., *C. R. Hebd. Seances Acad. Sci.* **263** (1966) 344.
9. Boucher, B., Buhl, R. and Perrin, M., *Acta Cryst.* **B25** (1969) 2326.
10. Brabers, V. A. M., *Phys. Stat. Sol.* **33** (1969) 563.
11. Buhl, R., *J. Phys. Chem. Solids* **30** (1969) 805.
12. Boucher, B., Buhl, R. and Perrin, M., *J. Phys. Chem. Solids* **31** (1970) 363.
13. Renault, N., Baffier, N. and Huber, M., *J. Solid State Chem.* **5** (1972) 250.
14. Bhandage, G. T. and Keer, H. V., *J. Phys. C* **9** (1976) 1325.
15. Brabers, V. A. M. and Terhell, J. C. J. M., *Phys. Stat. Sol. A* **69** (1982) 325.
16. Devale, A. B. and Kulkarni, D. K., *J. Phys. C* **15** (1982) 899.
17. Meenakshisundaram, A., *et al.*, *Phys. Stat. Sol. A* **69** (1982) K15.
18. Brabers, V. A. M., Van Setten, F. M. and Knapen, P. S. A., *J. Solid State Chem.* **49** (1983) 93.
19. Macklen, E. D., *J. Phys. Chem. Solids* **47** (1986) 1073.
20. Islam, M. S. and Catlow, C. R. A., *J. Phys. Chem. Solids* **49** (1988) 119.
21. Gillot, B., *et al.*, *Mat. Chem. Phys.* **24** (1989) 199.
22. Tang, X., Manthiram, A. and Goodenough, J. B., *J. Less Comm. Metals* **156** (1989) 357.
23. Gillot, B., *et al.*, *Mat. Chem. Phys.* **26** (1990) 395.
24. Jung, J., *et al.*, *J. Eur. Ceramic Soc.* **6** (1990) 351.
25. Legros, R., Metz, R. and Rousset, A., *J. Mat. Sci.* **25** (1990) 4410.
26. Baudour, J. L., *et al.*, *Physica B* **180 & 181** (1992) 97.
27. Feltz, A., Topfer, J. and Schirrmeister, F., *J. Eur Ceramic Soc.* **9** (1992) 187.
28. Gillot, B., *et al.*, *Solid State Ionics* **58** (1992) 155.
29. Topfer, J., *et al.*, *Phys. Stat. Sol. A* **134** (1992) 405.
30. Lindner, F. and Feltz, A., *J. Eur. Ceramic Soc.* **11** (1993) 269.
31. Martin de Vialdes, J. L., *et al.*, *Mat. Res. Bulletin* **29** (1994) 1163.
32. Singh, J. and Ram, R. S., *Phys. Stat. Sol. A* **158** (1996) 73.
33. Asbrink, S., *et al.*, *Phys. Rev. B* **57** (1998) 4972.
34. Elbadraoui, E., *et al.*, *Phys. Stat. Sol. B* **212** (1999) 129.
35. Schmidt, R. and Brinkman, A. W., *Int. J. Inorg. Mat.* (2002) 1.
36. Geller, S., *Acta. Cryst. B* **27** (1971) 821.
37. Jarosch, D., *Mineralogy and Petrology* **37** (1987) 15.
38. Cloud, W. H., *Phys. Rev.* **111** (1958) 1046.
39. Sasaki, S., Fujino, K. and Takeuchi, Y., *Proc. Japan Acad.* **55** (1979) 43.
40. Mehandjiev, D., *Applied Catalysts A* **206** (2001) 13.
41. Young, R. A., ed. *The Rietveld Method.* 1st Edition. IUCr Monographs on Crystallography. Vol. 5 Published by; Oxford University Press, Oxford (1993)
42. Caglioti, G., Paoletti, A. and Ricci, F. P., *Nucl. Instrum. Methods* **35** (1958) 223.
43. International Union of Crystallography, *International Tables for X - Ray Crystallography.* Vol. 1, ed. Henry, N.F.M. and Lonsdale, K. Published by; Kynoch Press, Birmingham (1952)
44. Roisnel, T. and Rodriguez-Carvajal, J., Computer Program; *WinPLOTR,* Laboratoire Leon Brillouin, Centre d'Etudes de Saclay, Gif-sur-Yvette (2001)
45. Larson, A. C. and Von Dreele, R. B., Computer Program; *General Structure Analysis System,* University of California, Los Alamos (1985)
46. Ohta, T., *et al.*, *Physica B* **234-236** (1997) 1093.
47. Drouet, C., *et al.*, *Int. J. Inorg. Mat.* **2** (2000) 419.
48. Drouet, C., Alphonse, P. and Rousset, A., *Solid State Ionics* **123** (1999) 25.
49. Golestani, F., Azimi, S. and Mackenzie, K. J. D., *J. Mat. Sci.* **22** (1987) 2847.
50. BIPM, I., IFCC, ISO, IUPAC, IUPAP, OIML, *Guide to the Expression of Uncertainty in Measurement.* 1st Edition Published by; International Organisation for Standardisation, Geneva (1993)
51. UKAS, *M3003; Uncertainty and Confidence in Measurement.* 1st Edition Published by; UKAS, (1997)
52. Brabers, V. A. M., *Phys. Stat. Sol. A* **12** (1972) 629.
53. Wyckoff, R. W. G., *Crystal Structures.* 2nd Edition. Vol. 1-4 Published by; Wiley, New York (1962-1966)
54. Ashcroft, N. W. and Mermin, N. D., *Solid State Physics.* 1st Edition Published by; W. B. Saunders Company, Philadelphia (1976)

55. Cervinka, L., *J. Phys. Chem. Solids* **26** (1965) 1917.
56. Novak, P., *J. Phys. Chem. Solids* **30** (1969) 2357.
57. Padalia, B. D. and Krishnan, V., *Phys. Stat. Sol. A* **25** (1974) K177.
58. Csete de Gyorgyfalva, G. D. C., *et al.*, *J. Eur. Ceramic Soc.* **19** (1999) 857.
59. Asbrink, S., *et al.*, *J. Phys. Chem. Solids* **58** (1997) 725.
60. Koester, L., Raunch, H. and Seyman, E., *Atomic Data and Nuclear Data Tables 49*, . 1991.
61. Bacon, G. E., *Neutron Diffraction.* 3rd Edition. Monographs on the Physics and Chemistry of Materials, ed. Bawn, C.E.H., *et al.*,. Published by; Clarendon Press, Oxford (1975)
62. Schieber, M. M., *Experimental Magnetochemistry; Nonmetallic Magnetic Materials.* 1st Edition. selected Topics in Solid State Physics. Vol. 8, ed. Wohlfarth, E.P. Published by; North - Holland Publishing Company, Amsterdam (1967)
63. Gorter, E. W., *Phillips Res. Rep.* **9** (1954) 295.
64. Goodenough, J. B., *Magnetism and the Chemical Bond.* 1st Edition. Interscience Monographs on Chemistry. Vol. 1, ed. Cotton, A.F. Published by; Interscience Publishers, John Wiley and Sons, New York (1963)
65. Shirane, G., *Acta Cryst.* **12** (1959) 282.
66. Mehandjiev, D. and Angelov, S., *Magnetochemistry of Solid State.* Published by; Nauka; Ikustro, Sofia (1979)
67. Wickham, D. G. and Goodenough, J. B., *Phys. Rev.* **115** (1959) 1156.
68. Boucher, B., Buhl, R. and Perrin, M., *J. Phys. Chem. Solids* **30** (1969) 2467.
69. Chikazumi, S., *Physics of Ferromagnetism.* 2nd Edition. The International Series of Monographs on Physics, ed. Birman, J., *et al.*,. Published by; Clarendon Press, Oxford (1997)
70. Coey, *J. App. Phys.* **49** (1978) 1646.
71. Antoshina, L. G., *et al.*, *J. Phys: Condens. Matter* **14** (2002) 8103.
72. Pauling, L., *The Nature of the Chemical Bond.* 3rd Edition Published by; Cornell University Press, New York (1960)
73. Schmidt, R., *et al.*, *Key Engineering Materials* **206-213** (2002) 1417.
74. Spassov, L., *et al.*, *Sensors and Actuators A* **62** (1997) 484.
75. King, P., http://www.isis.rl.ac.uk/muons/muonsIntro/isisMuons/isisMuons.htm (Accessed on; 20/10/2001)
76. Pratt, F., Computer Program; *WiMDA*, Oxford Version 1.132 (2001)
77. Kilkoyne, S. H., *Lecture notes from the Training Course in Pulsed mSR techniques*, . 1996, CCLRC.
78. Lee, S. L., Kilkoyne, S. H. and Cywinski, R. *Muon Science: muons in physics, chemistry and materials.* in *Proceedings of the Fifty First Scottish Universities Summer School in Physics.* 1998. St Andrews, Scotland: IOP Publishing, Edinburgh, (July 1999)
79. Giblin, S., *To be published* (2003)
80. Goodenough, J. B. and Loeb, A. L., *Phys. Rev.* **98** (1955) 391.
81. Goodenough, J. B., *Phys. Rev.* **117** (1960) 1442.
82. Brabers, V. A. M., *Progress in Spinel Ferrite Research*, in *Handbook of Magnetic Materials*, Buschow, K.H., Editor. 1995, Elsevier Science: Amsterdam. p. 189.
83. Bhandage, G. T., *et al.*, *J. Magn. Magn. Mater.* **166** (1997) 141.
84. Dormann, J. L., *Hyperfine Interact.* **68** (1991) 47.
85. Lappas, A., *et al.*, *J. Sol. State. Chem.* **145** (1999) 587.
86. Hohenberg, P. C. and Halperin, B. I., *Rev. Mod. Phys.* **49** (1977) 435.

Chapter 7
Conclusions and further work

7.1 Conclusions

Nickel manganite crystallises in the spinel structure, and is of considerable commercial interest, due to the useful temperature dependent electrical transport properties. Previous work [1-4] has shown that the transport mechanism is variable range phonon assisted hopping between manganese ions. The negative temperature coefficient of resistivity that results from this mechanism is advantageous for thermistor device properties. The transport mechanism is dependent upon the relative concentrations of Mn^{3+}, and Mn^{4+} cations on the spinel B sites, which is in turn dependent upon the inversion parameter. The cation distribution has been shown to be influenced by the cooling rate from the firing temperature, and relatively insensitive to changes in firing temperature. However nickel manganite can only be produced without a significant amount of impurity, by firing within a small temperature region centred on 800 °C. This region turned out to be smaller than that reported in the available literature. The purity is also influenced by the firing time, and type of precursor materials used. In particular, producing nickel manganite from mixed oxides has been shown to lead to significant impurity phases. The mixed oxide route was used in many previous investigations of the properties of nickel manganite, leading to possible errors in the conclusions drawn. A procedure for producing nickel manganite from a mixture of co-precipitated hydroxides has been thoroughly investigated, and developed to provide material with no detectable impurity phases. Little work has been previously reported on this preparation technique.

There is a variation in the position of the oxygen ions in nickel manganite, driven by the differing ionic radii of the cation species present. In section 4.2.1, a new relationship between the lattice parameter, and bond lengths has been derived, and used to draw predictions from published data. Various material parameters, such as the average oxygen radius, and that the majority of the Mn^{3+} on the octahedral (B) sites was in a high spin state were concluded. As far as the author is aware, calculations of this type concerning nickel manganite are not found elsewhere in the published literature. The cation distribution of Brabers [1],

which is generally accepted to be approximately correct, agrees well with reported values of site preference energies. The possible amount of Mn^{3+} ions on the tetrahedral (A) sites is limited by the lack of a co-operative Jahn-Teller type distortion.

The lattice parameter determined from X-ray diffraction data was strongly correlated with the amount of nickel oxide impurity phase present (shown in Figure 6.10). Other impurities such as $NiMn_2O_3$ were detectable from magnetisation measurements at 300 K, as shown in Figure 6.55. The presence of nickel oxide is difficult to detect from diffraction data, but has been shown to lead to significant errors if its presence is not accounted for in Rietveld analysis.

The cation distribution has been determined by Rietveld refinement of neutron diffraction data for a number of samples cooled at different rates from the firing temperature. The range of inversion parameters achieved by this method was $0.75 < \nu < 0.88$. Attempts to prepare material with lower inversion parameters, by quenching from higher temperatures resulted in partial sample decomposition. These samples have been extensively characterised, exploring the relationships between the cation distribution and various material parameters. These derived relationships can henceforth be used to gain information about the cation distribution without directly measuring it. This would be advantageous in many cases, such as thin films, and mass produced devices, as direct determination of the cation distribution by neutron diffraction is time consuming, expensive, and requires a considerable amount of material.

The magnetic behaviour of nickel manganite is dominated by a superexchange interaction between the A, and B sites, giving ferrimagnetic ordering, with a Curie temperature in the range 100 K to 147 K, depending upon inversion parameter. The relationship between Curie temperature and inversion parameter is shown in Figure 6.73. The values of Curie temperature obtained for various values of inversion parameter were lower than early reports [5], but are in agreement with the sample measured in a more recent study [6]. The observed trend in Curie temperature with inversion parameter was not consistent with the various interactions expected in nickel manganite. The saturation magnetisation at 77 K was also found to change significantly with inversion parameter, as shown in Figure 6.65. Low temperature magnetisation measurements are

feasible for thin films, as demonstrated in section 6.7, and could potentially be used in an industrial environment. Using the relationship established between the ferrimagnetic Curie temperature and inversion parameter, established for bulk material, the inversion parameter of this thin film sample was estimated to be $\nu = 0.788(8)$. Other material parameters, such as the lattice parameter, and oxygen position were either not as strongly correlated with changes in the inversion parameter, or not as easy to measure as the magnetisation. The magnetisation measurements on thin films were made using a variable temperature AGFM.

This instrument was originally developed for the study of dilute magnetic semiconductor materials, but has been equally applicable to measurements of nickel manganite. Details of the AGFM design are reported in chapter 2. Extensive characterisation has been carried out, in order to evaluate the performance of this instrument for samples of differing mass, magnetic moment, etc. The noise base of this instrument was determined as 1.4×10^{-11} JT^{-1} under ideal conditions, and a field of 0.4 T was attainable. Representative magnetisation data on a range of materials were collected, and are all presented in chapter 3.

Nickel manganite exhibits complex magnetic properties at low temperatures. The material goes through a transition to a collinear ferrimagnetic state, as mentioned above, also a second transition at lower temperature, interpreted to be the onset of a more complex non-collinear magnetic arrangement. The inversion parameter has a bearing on low temperature magnetic properties, as both neutron diffraction, and SQUID magnetometer measurements have shown. *P* type ferrimagnetic behaviour was observed below the Curie temperature in nickel manganite, in contrast to reports in the literature [5], which is evidence for frustration in one or both cation sublattices. Evidence for a third magnetic transition at approximately 10K, is evident in muon spin relaxation data. This transition is conjectured to be to a local canted state (LCS), as has been observed in other spinel systems. It is believed that nickel manganite is the only system to show evidence of LCS behaviour emerging from a non collinear magnetic state.

7.2 Further work

In order to fully understand the low temperature magnetic state of nickel manganite, some further study is required. There is scope for further work using the same samples that were fabricated with a range of inversion parameters by cooling at varying rates, as detailed in section 6.5. AC susceptibility measurements to temperatures below the postulated disorder freezing temperature (~10 K) would be useful, as conventional spin glass materials exhibit a characteristic cusp in the AC susceptibility at the disorder freezing temperature [7], and materials exhibiting a LCS are expected to do likewise. In addition, additional temperature dependent neutron diffraction experiments to study the behaviour of the moments on the A, and B sites as a function of temperature, for differing values of inversion parameter. The use of a neutron diffractometer optimised for a high count rate, and relatively quick temperature changes would allow diffraction patterns to be collected with a much finer temperature resolution than the 3 points obtained so far. An example of such in instrument is D20, at the Institute Laue-Languevin, Grenoble, France. Neutron diffraction experiments with an applied magnetic field parallel to the diffraction vector should give more information about the direction of the magnetic moments occurring on the cation sublattices. A similar experiment was carried out by Boucher *et al.*, [8], but the samples used were of dubious quality by modern standards, and the method of Rietveld was not used to analyse the data. All of these techniques, taken together should give a much more complete picture of the nature and strength of the low temperature interactions between the magnetic ions in nickel manganite.

Further attempts to obtain samples with a wider range of inversion parameters would be a useful exercise, to gain additional knowledge of the relationship with the Curie temperature. A sample with an inversion parameter of 0.77, where there is believed to be a compensation point (equal moments on the A, and B cation sublattices), should behave like an antiferromagnet above the canting transition, but possess a finite saturation magnetisation below. The magnitude of this magnetisation, coupled with neutron diffraction measurements of the moments of the sublattices would allow verification of the nature of the moment canting. The possibility of doping nickel manganite with non-magnetic cations of similar ionic radii to nickel and manganese, but different charge states would

open up a large number of further research possibilities. This approach would allow the cation distribution, and the magnetic interaction strengths to be altered, and their influence on the magnetic and transport properties to be studied. Continued development of the AGFM may address some of the problems encountered while trying to perform sensitive magnetic measurements at low temperatures, such as the increase in background signal associated with a cryostat, and the increased mechanical noise caused by cryogen flows. A new method of vibration isolation has been suggested, which should go some way towards alleviating the problems with mechanical noise.

References

1. Brabers, V. A. M. and Terhell, J. C. J. M., *Phys. Stat. Sol. A* **69** (1982) 325.
2. Csete de Gyorgyfalva, G. D. C., *et al.*, *J. Eur. Ceramic Soc.* **19** (1999) 857.
3. Elbadraoui, E., *et al.*, *Phys. Stat. Sol. B* **212** (1999) 129.
4. Basu, A., *et al.*, *J. App. Phys.* **92** (2002) 4123.
5. Boucher, B., Buhl, R. and Perrin, M., *J. Phys. Chem. Solids* **31** (1970) 363.
6. Baudour, J. L., *et al.*, *Physica B* **180 & 181** (1992) 97.
7. Mydosh, J. A., *Spin Glasses, An Experimental Introduction.* Published by; Taylor and Francis, London (1993)
8. Boucher, B., Buhl, R. and Perrin, M., *Acta Cryst.* **B25** (1969) 2326.
9. Lappas, A., *et al.*, *J. Sol. State. Chem.* **145** (1999) 587.

Appendix 1

Phase information

$NiMn_2O_4$

Space Group: *Fd-3m* (#227)	a = 8.390 Å
V = 590.59 Å^3	Formula Mass = 232.57 g
Unit cell = 8 * F. M.	Density = 5231 kg m^{-3}
Volume/metal ion = 24.6 Å^3	

Atom	fraction	x	y	z
Ni	1 - v	0.125	0.125	0.125
Mn	v	0.125	0.125	0.125
Ni	v/2	0.5	0.5	0.5
Mn	1 - v/2	0.5	0.5	0.5
O	1	0.26	0.26	0.26

Table A1.1. Atom site positions for $NiMn_2O_4$, origin choice 2.

[*hkl*]	$\|hkl\|^2$	Multiplicity	2 Theta [°]	Site Sensitivity
111	3	8	18.3	A, B, O
220	8	12	30.1	A, O
311	11	24	35.5	A, B, O
222	12	8	37.1	B, O
400	16	6	43.1	A, B, O
331	19	24	47.2	A, B, O
422	24	24	53.5	A, O
511	27	24	57.0	A, B, O
333	27	8	57.0	A, B, O
440	32	12	62.6	A, B, O
531	35		65.8	A, B, O
442	36		66.9	O

Table A1.2. The first 12 allowed reflections for $NiMn_2O_4$, assuming a radiation wavelength of 1.54056 Å.

$Ni_{(1-\delta)}O$ Bunsenite [1]

Space Group: *Fm-3m* (#225)	a = 4.178(1) Å
V = 72.93 Å^3	Formula Mass = (58.69(1 - δ)+16) g
Unit cell = 4 * F. M.	Density = 6802 kg m^{-3}
Volume/metal ion = 18.2 Å^3	
Antiferromagnetic	T_N = 523 K, spins in (111) planes [2]
$\chi_{298\ K}$ = 7.55 x 10^{-4} [3]	Melting point = 1984 °C

Atom	x	y	z
Ni	0	0	0
O	0.5	0.5	0.5

Table A1.3. Atom site positions for $Ni_{(1-\delta)}O$.

[*hkl*]	Multiplicity	2 Theta [°]
111	8	37.3
200	6	43.3
220	12	62.9
311	24	75.5
222	8	79.5
400	6	95.1
331	24	107.1
420	24	111.2
422	24	129.2
511	24	146.7
333	8	146.7

Table A1.4. The first 8 allowed reflections for $Ni_{(1-\delta)}O$, assuming a radiation wavelength of 1.54056 Å.

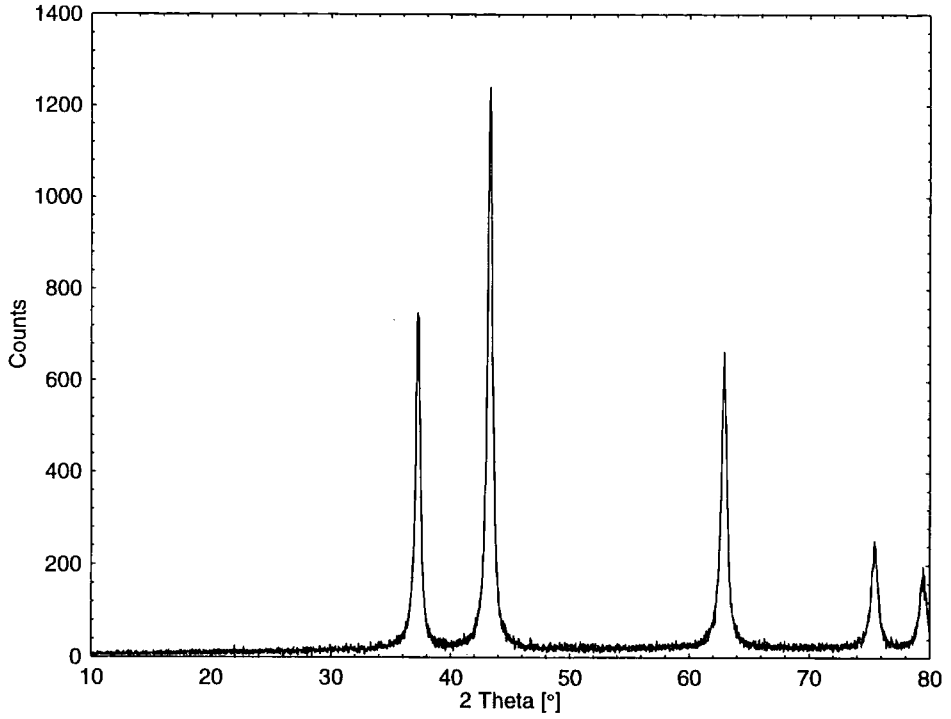

Figure A1.1. X-ray diffraction pattern for NiO.

α-Mn_2O_3 Bixbyite [4]

Space Group: *Pbca* (#61)	a = 9.4157(3) Å	b = 9.4233(3) Å c = 9.4047(3) Å
V = 834.45 Å^3		Formula Mass = 157.88 g
Unit cell = 16 * F. M.		Density = 5027 kg m^{-3}
Volume/metal ion = 52.1 Å^3		
Antiferromagnetic	T_N = 80 K	Paramagnetic T_C = -121 K
$\chi_{298\,K}$ = 5.64 x 10^{-4} [3]		n_{eff} = 4.87 μ_B [2]
	Melting point (loss of oxygen) = 1080 °C	

Atom	x	y	z
Mn1	0	0	0
Mn2	0	0	0.5
Mn3	0.28479(10)	0.25253(5)	-0.00590(5)
Mn4	0.00462(5)	0.28507(10)	0.24564(5)
Mn5	0.25301(5)	0.00130(4)	0.28533(10)
O1	0.13299(32)	-0.08466(35)	0.15030(33)
O2	0.14435(33)	0.12989(34)	-0.08507(35)
O3	-0.08038(35)	0.14693(33)	0.12412(31)
O4	-0.37447(31)	0.41757(34)	-0.35569(31)
O5	-0.35081(32)	-0.37238(33)	0.41947(35)
O6	0.41306(34)	-0.35285(33)	-0.36751(35)

Table A1.5. Atom site positions for α-Mn_2O_3.

[*hkl*]	Multiplicity	2 Theta [°]
211	24	23.1
222	8	32.9
400	6	38.1
332	24	45.1
431,341	24, 24	49.2
440	12	55.0
541,451	24, 24	63.9
622	24	65.6
631, 361	24, 24	67.3
444	8	68.9
662	24	90.8
840, 480	12, 12	93.9
10.2.2, 666	24, 8	116.2
10.6.2, 6.10.2	24, 24	150.3

Table A1.6. The 14 most intense allowed reflections for α-Mn_2O_3, assuming a radiation wavelength of 1.54056 Å.

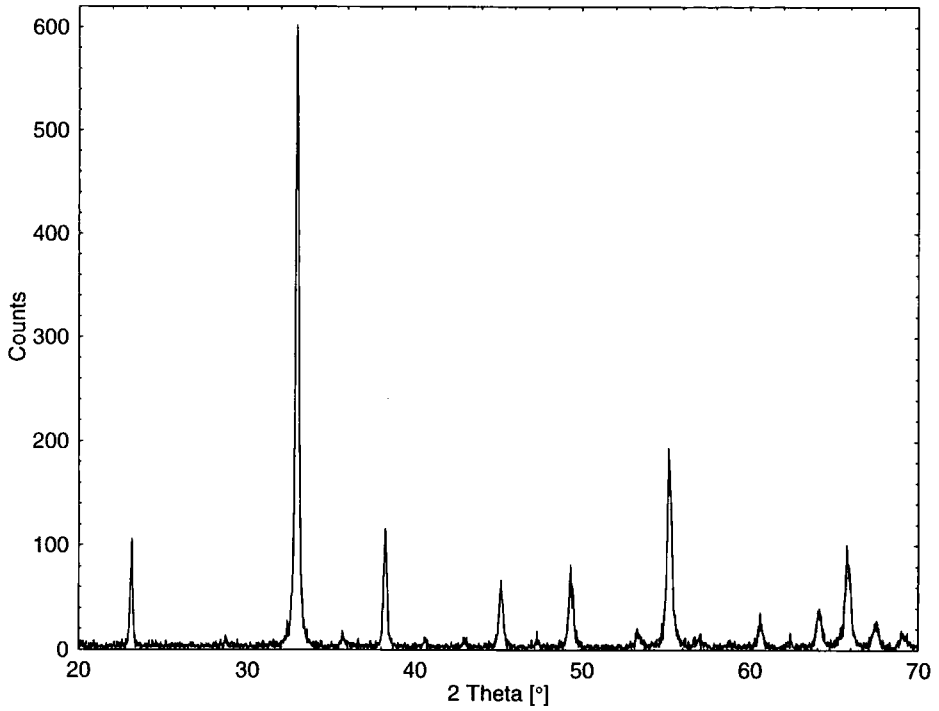

Figure A1.2. X-ray diffraction pattern for α-Mn_2O_3.

Mn3O4 Hausmannite [5].

Space Group: *I41/amd* (#141)	$a = b = 5.765(1)$ Å $\quad c = 9.442(2)$ Å
$V = 313.81$ Å^3	Formula Mass = 228.82 g
Unit cell = 4 * F. M.	Density = 4843 kg m^{-3}
Volume/metal ion = 26.2 Å^3	
Ferrimagnetic, high crystalline anisotropy [6]	$M_{SAT} = 45.2$ JT^{-1}kg^{-1} at 300 K
$\chi_{298\ K} = 3.30 \times 10^{-3}$ [3]	Melting point = 1564 °C

Atom	*x*	*y*	*z*
Mn1	0	0.25	0.875
Mn2	0	0.5	0.5
O	0	0.4722(2)	0.2589(2)

Table A1.7. Atom site positions for Mn_3O_4.

[*hkl*]	Multiplicity	2 Theta [°]
101	8	18.0
112	8	28.9
200	4	31
103	8	32.4
211	16	36.1
202	8	36.5
004	2	38.1
220	4	44.4
105	8	50.8
312	16	53.9
321	16	58.5
224	8	59.9
400	4	64.6
413	16	74.1

Table A1.8. The 14 most intense allowed reflections for Mn_3O_4, assuming a radiation wavelength of 1.54056 Å.

$NiMnO_3$ Ilmenite [7]

Space Group: *R–3R* (#148) $a = b = 4.905$ Å $c = 13.59$ Å $\alpha = 90°\ \beta = 90°\ \gamma = 120°$	
$V = 326.96$ Å^3	Formula Mass = 161.63 g
Unit cell = 6 * F. M.	Density = 4925 kg m^{-3}
Volume/metal ion = 27.2 Å^3	
Ferrimagnetic, alternate layers AF coupled (p279, [8]), spins in (111) planes [2]	$T_N = 437$ K
$M_{SAT} = 22$ JT^{-1}kg^{-1} at 300 K	$n_B = 0.7\ \mu_B$ at 0K

Atom	*x*	*y*	*z*
Ni^{2+}	0	0	0.333
Mn^{4+}	0	0	0.166
O^{2-}	0.310	0	0.25

Table A1.9. Atom site positions for $NiMnO_3$.

[*hkl*]	Multiplicity	2 Theta [°]
012	6	24.7
104	6	33.8
110	6	36.6
006	2	39.8
113	6	41.9
11-3	6	41.9
202	6	44.7
024	6	50.6
116	6	55.2
11-6	6	55.2
018	6	58.5
12-4	6	64.1
214	6	64.1
300	6	65.9

Table A1.10. The 12 most intense allowed reflections for $NiMnO_3$, assuming a radiation wavelength of 1.54056 Å.

References

1. Sasaki, S., Fujino, K. and Takeuchi, Y., *Proc. Japan Acad.* **55** (1979) 43.
2. Goodenough, J. B., *Magnetism and the Chemical Bond.* 1st Edition. Interscience Monographs on Chemistry. Vol. 1, ed. Cotton, A.F. Published by; Interscience Publishers, John Wiley and Sons, New York (1963)
3. CRC, *The CRC handbook.* 89th Edition Published by; The Chemical Rubber Company, (2000)
4. Geller, S., *Acta. Cryst. B* **27** (1971) 821.
5. Jarosch, D., *Mineralogy and Petrology* **37** (1987) 15.
6. Larson, E. G., Arnott, R. J. and Wickham, D. G., *J. Phys. Chem. Solids* **23** (1962) 1771.
7. Cloud, W. H., *Phys. Rev.* **111** (1958) 1046.
8. Schieber, M. M., *Experimental Magnetochemistry; Nonmetallic Magnetic Materials.* 1st Edition. selected Topics in Solid State Physics. Vol. 8, ed. Wohlfarth, E.P. Published by; North - Holland Publishing Company, Amsterdam (1967)

Appendix 2

Rietveld refinement results

A2.1 Numerical criteria of fit, and estimated standard deviations [1].

In common with other users of Rietveld refinement, the conventional goodness of fit indicators (R values) are quoted in the refinement results below. A brief explanation of these is presented here. In all cases, values are expressed as a percentage, and a lower value indicates a better agreement between observed and calculated data.

R – Pattern

$$R_P = \frac{\sum |y_{oi} - y_{ci}|}{\sum y_{oi}}$$

R – Weighted pattern

$$R_{WP} = \sqrt{\frac{\sum w_i (y_{oi} - y_{ci})^2}{\sum w_i y_{oi}^2}}$$

R – Expected

$$R_E = \sqrt{\frac{(N-P)}{\sum w_i y_{oi}^2}}$$

R – Intensity (Bragg factor)

$$R_I = \frac{\sum \left| \sqrt{I_{oK}} - \sqrt{I_{cK}} \right|}{\sum \sqrt{I_{oK}}}$$

S – 'Goodness of fit'

$$S = R_{WP} / R_E$$

In all of the above equations;

I_K = intensity of the K^{th} reflection
y_i = counts at the i^{th} angle
$w_i = 1/y_{oi}$
N = number of observations
P = number of parameters adjusted

The subscripts o, and c, refer to observed and calculated quantities respectively. The indicators R_P, R_{WP}, R_E, and S all refer to the entire diffraction pattern, including background contributions, so can be affected by factors such as incomplete fitting to the background function, peak profile functions, and impurity phases present. Of these indicators, R_{WP} is probably the most meaningful, as it is the quantity that is minimised in a least-squares refinement procedure. If there are a number of different crystallographic phases present in the sample, and the diffraction peaks are well enough defined as to be unambiguously assigned to one or other of the phases, then separate values of R_I can be calculated for each phase. This is useful in the case of a sample containing minority impurity phases, as these may unduly affect the values of R_P, R_{WP}, R_E, and S.

The reported values of the estimated standard deviations (e.s.d.) were calculated using;

$$\sigma_j = S\sqrt{M_{jj}^{-1}}$$

Where S is the 'Goodness of fit' indicator, and M_{jj}^{-1} is a diagonal element of the inverse matrix obtained from the normal matrix used in the least squares fitting process. The normal matrix has elements approximated as;

$$M_{jk} = \sum_i 2w_i \left(\frac{\partial y_{ci}}{\partial x_j}\right)\left(\frac{\partial y_{ci}}{\partial x_k}\right)$$

An e. s. d. calculated using this method only takes into account statistical errors due to counting statistics of discrete events, and does not include any contributions due to possible systematic errors, or the repeatability of the measurement. A consequence of these definitions is that the e. s. d. can be made arbitrarily small by increasing the counting time, or number of observations. According to R. J. Hill (Chapter 5, [1]), the calculated e. s. d. is only a good approximation of the measurement repeatability when the step width is as large, or larger than the FWHM of the narrowest diffraction peak. Therefore, many of the e. s. d. values reported below (especially for samples fired at low temperatures, or for short times) may significantly underestimate the actual experimental repeatability.

A2.2 X-ray data, Firing temperatures 700 °C to 1100 °C.

Firing Temperature = 700 °C		Firing time = 20 hours	
a = 8.41079(27) Å		x = 0.26324(53)	
B *(8a)* = 1.18(8) Å^2	B *(16d)* = 0.375(54) Å^2	B *(32e)* = 0.75(15) Å^2	
U = 0.101(24)	V = 0.033(21)	W = 0.0079(43)	
η_0 = 0.681(54)		η_1 = -0.0004(10)	
NiO Amount = 1.25(11) %		$NiMnO_3$ Amount = 27.29(42) %	
R_p = 12.3 %	R_{wp} = 18.4 %	R_e = 8.48 %	S = 2.17

Firing Temperature = 750 °C		Firing time = 20 hours	
a = 8.39687(19) Å		x = 0.26312(32)	
B *(8a)* = 0.902(45) Å^2	B *(16d)* = 0.288(32) Å^2	B *(32e)* = 0.95(9) Å^2	
U = 0.175(17)	V = 0.029(14)	W = 0.0093(29)	
η_0 = 0.534(32)		η_1 = -0.0025(6)	
NiO Amount = 3.20(11) %			
R_p = 8.52 %	R_{wp} = 12.2 %	R_e = 8.53 %	S = 1.43

Firing Temperature = 780 °C		Firing time = 20 hours	
a = 8.38994(13) Å		x = 0.26417(17)	
B (8a) = 0.524(26) Å^2	B (16d) = 0.291(21) Å^2		B (32e) = 0.828(54) Å^2
U = 0.0518(39)	V = -0.0006(42)		W = 0.0179(10)
η_0 = 0.407(17)		η_1 = 0.00181(34)	
NiO Amount = 0.92(7) %			
R_p = 6.06 %	R_{wp} = 8.27 %	R_e = 6.36 %	S = 1.30

Firing Temperature = 800 °C		Firing time = 20 hours	
a = 8.39090(12) Å		x = 0.26418(17)	
B (8a) = 0.558(26) Å^2	B (16d) = 0.375(21) Å^2		B (32e) = 0.835(53) Å^2
U = 0.120(11)	V = 0.0353(97)		W = 0.0063(20)
η_0 = 0.371(25)		η_1 = 0.00151(48)	
NiO Amount = 1.09(6) %			
R_p = 5.91 %	R_{wp} = 8.25 %	R_e = 6.71 %	S = 1.23

Firing Temperature = 820 °C		Firing time = 20 hours	
a = 8.3934(8) Å		x = 0.26444(19)	
B (8a) = 0.532(27) Å^2	B (16d) = 0.343(21) Å^2		B (32e) = 0.81(6) Å^2
U = 0.0247(23)	V = -0.0030(26)		W = 0.0139(7)
η_0 = 0.429(19)		η_1 = 0.00307(37)	
NiO Amount = 1.10(11) %			
R_p = 6.71 %	R_{wp} = 8.78 %	R_e = 6.18 %	S = 1.42

Firing Temperature = 850 °C		Firing time = 20 hours	
a = 8.3995(7) Å		x = 0.26381(20)	
B (8a) = 0.410(29) Å^2	B (16d) = 0.257(23) Å^2		B (32e) = 0.831(61) Å^2
U = 0.0225(23)	V = -0.0394(36)		W = 0.0447(12)
η_0 = 0.181(17)		η_1 = 0.00541(35)	
NiO Amount = 1.66(7) %			
R_p = 7.18 %	R_{wp} = 9.32 %	R_e = 6.47 %	S = 1.44

Firing Temperature = 900 °C		Firing time = 20 hours	
a = 8.40551(7) Å		x = 0.26286(32)	
B *(8a)* = 0.691(40) Å^2	B *(16d)* = 0.290(30) Å^2		B *(32e)* = 1.07(9) Å^2
U = 0.0129(20)	V = 0.0001(23)		W = 0.0074(7)
η_0 = 0.450(32)		η_1 = 0.0045(6)	
NiO Amount = 5.65(26) %			
R_p = 7.77 %	R_{wp} = 10.30 %	R_e = 8.31 %	S = 1.24

Firing Temperature = 1000 °C		Firing time = 20 hours	
a = 8.42258(14) Å		x = 0.26264(41)	
B *(8a)* = 0.544(47) Å^2	B *(16d)* = 0.27 Å^2		B *(32e)* = 1.21(11) Å^2
U = 0.0180(31)	V = -0.0105(39)		W = 0.0152(12)
η_0 = 0.277(40)		η_1 = 0.0062(7)	
NiO Amount = 10.76(21) %			
R_p = 9.84 %	R_{wp} = 12.6 %	R_e = 9.02 %	S = 1.40

Firing Temperature = 1100 °C		Firing time = 20 hours	
a = 8.42937(15) Å		x = 0.26379(39)	
B *(8a)* = 0.883(42) Å^2	B *(16d)* = 0.781(34) Å^2		B *(32e)* = 1.65(8) Å^2
U = -0.028(7)	V = 0.121(8)		W = -0.0007(17)
η_0 = 0.339(24)		η_1 = 0.0044(5)	
NiO Amount = 12.49(14) %			
R_p = 7.36 %	R_{wp} = 9.56 %	R_e = 6.83 %	S = 1.40

A2.3 FULLPROF Validation testing results, Runs 1 – 4.

Simulated Data, Runs 1 - 2		
$NiMn_2O_4$ Scale = 0.0002000	ν = 0.800	
a = 8.40000 Å	x = 0.26400	
B *(8a)* = 0.300 Å^2	B *(16d)* = 0.600 Å^2	B *(32e)* = 0.900 Å^2
U = 0.120	V = 0.350	W = 0.0050
η_0 = 0.400	η_1 = 0.0050	
NiO Scale = 0.0000	NiO Amount = 0.00 %	
a = 4.17800 Å	B = 0.600 Å^2	

Simulated Data, Runs 3 - 4			
$NiMn_2O_4$ Scale = 0.0002000		ν = 0.800	
a = 8.40000 Å		x = 0.26400	
B *(8a)* = 0.300 Å^2	B *(16d)* = 0.600 Å^2		B *(32e)* = 0.900 Å^2
U = 0.120	V = 0.350		W = 0.0050
η_0 = 0.400		η_1 = 0.0050	
NiO Scale = 0.0004080		NiO Amount = 4.00 %	
a = 4.17800 Å		B = 0.600 Å^2	

Presentation of the results of refinements of the simulated data is given in the following format;

Parameter = Mean(FULLPROF e.s.d.) ± Estimated error on the mean

The mean, and estimated error on the mean have been calculated from the results of 12 identical refinements on datasets generated from the same initial parameters listed above. Where the mean refined value varies from the initial parameter by more than twice the standard deviation as estimated by the FULLPROF program, the standard deviation is given in a **bold** typeface. The same criterion applies to the estimated error on the mean.

Refinement Results, Simulated Run 1			
a = 8.40003(20) ± 0.00004 Å		x = 0.26383(20) ± **0.00005**	
B *(8a)* =	B *(16d)* =		B *(32e)* =
0.327(26) ± **0.008** Å^2	0.653(**21**) ± **0.004** Å^2		0.974(58) ± **0.012** Å^2
U = 0.120(30) ± 0.008	V = 0.357(26) ± 0.008		W = 0.0039(53) ± 0.0017
η_0 = 0.406(20) ± 0.004		η_1 = 0.00462(39) ± **0.00008**	
NiO Amount = 0.07(11) ± **0.03** %			
R_p = 5.93(2) %	R_{wp} = 8.06(2) %	R_e = 7.99 %	S = 1.01

Refinement Results, Simulated Run 2			
a = 8.39989(20) ± 0.00006 Å		x = 0.26382(19) ± **0.00005**	
B *(8a)* =	B *(16d)* =		B *(32e)* =
0.319(25) ± **0.007** Å^2	0.645(**20**) ± **0.007** Å^2		0.941(58) ± **0.007** Å^2
U = 0.123(30) ± 0.006	V = 0.357(25) ± 0.005		W = 0.0028(52) ± **0.0010**
η_0 = 0.409(20) ± 0.006		η_1 = 0.00455(39) ± **0.00010**	
R_p = 5.93(1) %	R_{wp} = 8.03(2) %	R_e = 7.99 %	S = 1.01

Refinement Results, Simulated Run 3			
a = 8.40009(20) ± 0.00006 Å		x = 0.26387(20) ± **0.00005**	
B (8a) =	*B (16d)* =		*B (32e)* =
0.340(26) ± **0.008** Å^2	0.636(21) ± **0.005** Å^2		0.971(59) ± **0.015** Å^2
U = 0.116(30) ± 0.006	V = 0.367(26) ± **0.004**		W = 0.0007(53) ± 0.0036
η_0 = 0.413(20) ± **0.004**		η_1 = 0.00450(39) ± **0.00009**	
NiO Amount = 3.91(12) ± **0.03** %			
R_p = 5.88(2) %	R_{wp} = 7.96(2) %	R_e = 7.92 %	S = 1.01

Refinement Results, Simulated Run 4			
a = 8.39890(**22**) ± **0.00005** Å		x = 0.26320(**22**) ± **0.00006**	
B (8a) =	*B (16d)* =		*B (32e)* =
0.523(**28**) ± **0.006** Å^2	0.499(**21**) ± **0.004** Å^2		0.921(63) ± 0.017 Å^2
U = 0.156(35) ± **0.005**	V = 0.365(29) ± **0.007**		W = 0.0000(59) ± **0.0013**
η_0 = 0.409(22) ± 0.005		η_1 = 0.00456(42) ± **0.00010**	
R_p = 6.61(1) %	R_{wp} = 8.86(2) %	R_e = 7.92 %	S = 1.12

A2.4 X-ray data, Oxide precursors.

Firing Temperature = 1200 °C		Firing time = 12 hours	
Firing Temperature = 800 °C		Firing time = 155 hours	
a = 8.392930(80) Å		x = 0.26484(43)	
B (8a) = 0.432(44) Å^2	*B (16d)* = 0.105(38) Å^2		*B (32e)* = 1.77(12) Å^2
U = 0.0066(11)	V = -0.0077(16)		W = 0.00925(57)
η_0 = 0.362(34)		η_1 = 0.00418(58)	
NiO Amount = 0.00(0) %			
R_p = 9.50 %	R_{wp} = 12.2 %	R_e = 9.20 %	S = 1.33

A2.5 X-ray data, Firing times 1 hour to 120 hours.

Firing Temperature = 800 °C		Firing time = 1 hour	
a = 8.39212(19) Å		x = 0.26493(17)	
B (8a) = 0.451(29) Å^2	*B (16d)* = 0.264(23) Å^2		*B (32e)* = 0.550(57) Å^2
U = 0.1163(94)	V = 0.0219(80)		W = 0.0170(17)
η_0 = 0.438(18)		η_1 = 0.00161(39)	
NiO Amount = 2.97(8) %			
R_p = 6.34 %	R_{wp} = 8.59 %	R_e = 6.32 %	S = 1.36

Firing Temperature = 800 °C		Firing time = 48 hours	
a = 8.390254(86) Å		x = 0.26423(20)	
B (8a) = 0.547(29) Å^2	B (16d) = 0.254(22) Å^2		B (32e) = 0.847(60) Å^2
U = 0.0228(17)	V = -0.0175(23)		W = 0.01876(75)
η_0 = 0.546(21)		η_1 = 0.00186(40)	
NiO Amount = 0.15(6) %			
R_p = 6.13 %	R_{wp} = 8.63 %	R_e = 6.44 %	S = 1.34

Firing Temperature = 800 °C		Firing time = 120 hours	
a = 8.388457(81) Å		x = 0.26459(19)	
B (8a) = 0.559(28) Å^2	B (16d) = 0.323(22) Å^2		B (32e) = 0.758(59) Å^2
U = 0.0179(15)	V = -0.0161(21)		W = 0.01878(67)
η_0 = 0.413(19)		η_1 = 0.00356(37)	
NiO Amount = 0.00(6) %			
R_p = 6.10 %	R_{wp} = 8.43 %	R_e = 6.44 %	S = 1.31

A2.6 Time Of Flight neutron data, Samples fired at 750 °C, 800 °C and 850 °C.

Firing Temperature = 750 °C		Firing time = 48 hours	
a = 8.39099(10) Å		x = 0.263399(79)	
ν = 0.840(5)	ν_A = 0.8386(60)		ν_B = 0.8406(39)
B (8a) = 0.86(33) Å^2	B (16d) = 0.489(89) Å^2		B (32e) = 0.910(35) Å^2
$NiMnO_3$ Amount = 9.37(39) %		Mn_2O_3 Amount = 4.91(43) %	
R_I ($NiMn_2O_4$) = 2.71%	R_I ($NiMnO_3$) = 7.79%		R_I (Mn_2O_3) = 8.83%
R_p = 4.43%	R_{wp} = 6.09 %	R_e = 2.66 %	S = 2.29

N. B. The impurity phase $NiMnO_3$, displays antiferromagnetic order at 300 K [2-4], the magnetic component of which could not be included in the refinement due to limitations of the refinement software, time available and capabilities of the available computing hardware. In addition, the reported structure of Mn_2O_3 is complex [5], and may be influenced by small amounts of nickel. The calculated intensities of the diffraction peaks due to these impurities were obviously in error (see figure 6.42), which is reflected in the high values of R_I for the impurity phases, and the goodness of fit indicator, S. The amounts of $NiMnO_3$, and Mn_2O_3 in the sample are almost certainly significantly different to those reported above. However the value of R_I for the nickel manganite phase is comparable to that obtained for the samples fired at 800 °C, and 850 °C, so there is no reason to suspect the parameters associated with this phase to be seriously in error.

Firing Temperature = 800 °C		Firing time = 48 hours	
a = 8.39174(12) Å		x = 0.263508(40)	
ν = 0.8363(23)	ν_A = 0.8371(27)		ν_B = 0.8330(34)
B (8a) = 0.58(16) Å^2	B (16d) = 0.746(59) Å^2		B (32e) = 1.064(26) Å^2
R_I ($NiMn_2O_4$) = 2.72%			
R_p = 3.05 %	R_{wp} = 3.44 %	R_e = 2.70 %	S = 1.27

Firing Temperature = 850 °C		Firing time = 48 hours	
a = 8.39404(12) Å		x = 0.263491(43)	
ν = 0.8330(24)	ν_A = 0.8396(30)	ν_B = 0.8289(37)	
B *(8a)* = 0.68(15) Å^2	B *(16d)* = 0.534(62) Å^2	B *(32e)* = 1.012(26) Å^2	
NiO Amount = 0.39(6) %			
R_I ($NiMn_2O_4$) = 3.48%		R_I (NiO) = 2.14%	
R_p = 3.24%	R_{wp} = 3.70 %	R_e = 2.73 %	S = 1.36

A2.7 Constant Wavelength neutron data, Samples 1 – 4.

Sample Number 1			
a (300 K) = 8.39472(12) Å		x = 0.26314(6)	
a (105 K) = 8.38378(12) Å		ν = 0.7483(19)	
a (2 K) = 8.38134(13) Å			
B *(8a)* = 0.65 Å^2	B *(16d)* = 0.94(12) Å^2	B *(32e)* = 1.458 Å^2	
U = 0.1205(44)	V = -0.2617(95)	W = 0.2364(50)	
η_0 = 0.264(35)		η_1 = -0.00059(47)	
M_A (105 K) = 2.447(51) μ_B		M_B (105 K) = -1.258(39) μ_B	
M_A (2 K) = 3.633(55) μ_B		M_B (2 K) = -1.884(41) μ_B	
R_p = 3.70 %	R_{wp} = 4.63 %	R_e = 3.42 %	S = 1.35

Sample Number 2			
a (300 K) = 8.39014(19) Å		x = 0.26368(10)	
a (105 K) = 8.38190(13) Å		ν = 0.8177(29)	
a (2 K) = 8.37889(13) Å			
B *(8a)* = 0.65 Å^2	B *(16d)* = 0.80(13) Å^2	B *(32e)* = 1.495(60) Å^2	
U = 0.1497(81)	V = -0.316(16)	W = 0.2555(83)	
η_0 = 0.376(47)		η_1 = -0.00093(63)	
M_A (105 K) = 1.700(50) μ_B		M_B (105 K) = -0.790(51) μ_B	
M_A (2 K) = 3.799(43) μ_B		M_B (2 K) = -1.607(33) μ_B	
R_p = 5.75 %	R_{wp} = 7.01 %	R_e = 5.22 %	S = 1.34

Sample Number 3			
a (300 K) = 8.38768(12) Å		x = 0.26357(7)	
a (105 K) = 8.37868(12) Å		ν = 0.8830(22)	
a (2 K) = 8.37528(12) Å			
B (8a) = 0.65 Å^2	B (16d) = 0.834(80) Å^2	B (32e) = 1.356(42) Å^2	
U = 0.1449(51)	V = -0.315(11)	W = 0.2577(54)	
η_0 = 0.373(30)		η_1 = -0.000246(41)	
M_A (105 K) = 0.78(10) μ_B		M_B (105 K) = -0.25(11) μ_B	
M_A (2 K) = 3.949(42) μ_B		M_B (2 K) = -1.337(33) μ_B	
R_p = 3.97 %	R_{wp} = 5.05 %	R_e = 3.22 %	S = 1.57

Sample Number 4			
a (300 K) = 8.42315(25) Å		x = 0.26371(8)	
a (105 K) = 8.41133(26) Å		ν_A = 0.89(33)	
a (2 K) = 8.40854(27) Å		ν_B = 0.62(18)	
B (8a) = 1.95(30) Å^2	B (16d) = 0.74 Å^2	B (32e) = 1.507(54) Å^2	
U = 0.217(14)	V = -0.326(24)	W = 0.2723(97)	
η_0 = 0.133(40)		η_1 = 0.00307(57)	
M_A (105 K) = 2.786(54) μ_B		M_B (105 K) = -1.333(54) μ_B	
M_A (2 K) = 4.027(54) μ_B		M_B (2 K) = -1.966(52) μ_B	
NiO Amount = 10.7(38) %			
R_p = 4.01 %	R_{wp} = 5.27 %	R_e = 3.13 %	S = 1.68

References

1. Young, R. A., ed. *The Rietveld Method.* 1st Edition. IUCr Monographs on Crystallography. Vol. 5 Published by; Oxford University Press, Oxford (1993)
2. Gorter, E. W., *Phillips Res. Rep.* **9** (1954) 295.
3. Cloud, W. H., *Phys. Rev.* **111** (1958) 1046.
4. Mehandjiev, D., *Applied Catalysts A* **206** (2001) 13.
5. Geller, S., *Acta. Cryst. B* **27** (1971) 821.

Appendix 3

Uncertainty budgets

All the following uncertainties have been evaluated in accordance with UKAS guidelines [1], as abridged from the BIPM Guide to the expression of uncertainty in measurement [2].

Estimated uncertainty in the measurement of Lattice Parameter, *a*, using C. W. neutron diffraction data from instrument D1A at the Institut Laue - Languevin							
Source of Uncertainty	Reference	Value [Å]	Probability distribution	Divisor	c_i	u_i [Å]	V_i or V_{eff}
Fitting to Pattern	FULLPROF results	0.0002	normal	1	1	0.0002	∞
Thermal Expansion Coefficient of nickel manganite	FULLPROF results at 300K, and 105K, assuming ± 5 K	0.0003	rectangular	1.7321	1	0.00017	∞
Thermal Expansion Coefficient of Diffractometer (Aluminium)	Ashcroft & Mermin, assuming ± 5 K	0.001	rectangular	1.7321	1	0.00057	∞
Calibration of Diffractometer	Estimated	0.0005	normal	2	1	0.00025	∞
Resolution of Diffractometer	± 0.05 °, at 2 theta = 140 °	0.003	rectangular	1.7321	1	0.00173	∞
Combined uncertainty			**normal**			**0.00186**	
Expanded uncertainty			**normal**	**k=2**		**0.0037**	

Estimated uncertainty in the measurement of Lattice Parameter, *a*, using C. W. X-ray diffraction data from a Siemens D5000 diffractometer							
Source of Uncertainty	Reference	Value [Å]	Probability distribution	Divisor	c_i	u_i [Å]	V_i or V_{eff}
Fitting to Pattern	FULLPROF results	0.00027	normal	1	1	0.00027	∞
Repeatability of Fitting to Pattern	Appendix 2	0.0002	normal	1	1	0.0002	11
Systematic Error in Fitting to Pattern	Appendix 2	0.0011	rectangular	1.7321	1	0.00064	∞
Thermal Expansion Coefficient of nickel manganite	FULLPROF results at 300K, and 105K, assuming ± 2 K	0.00012	rectangular	1.7321	1	0.000069	∞
Thermal Expansion Coefficient of Diffractometer (Aluminium)	Ashcroft & Mermin, assuming ± 2 K	0.0004	rectangular	1.7321	1	0.00023	∞
Calibration of Diffractometer	Estimated	0.0002	normal	2	1	0.0001	∞
Resolution of Diffractometer	± 0.01 °, at 2 theta = 140 °	0.0006	rectangular	1.7321	1	0.00034	∞
Combined uncertainty			**normal**			**0.00084**	**379**
Expanded uncertainty			**normal**	**k=2**		**0.0017**	

1. UKAS, *M3003; Uncertainty and Confidence in Measurement.* 1st Edition Published by; UKAS, (1997)
2. BIPM, I., IFCC, ISO, IUPAC, IUPAP, OIML, *Guide to the Expression of Uncertainty in Measurement.* 1st Edition Published by; International Organisation for Standardisation, Geneva (1993)